Alma Mater Studiorum – Università di Bologna

DOTTORATO DI RICERCA IN

TECNOLOGIE DELL'INFORMAZIONE

Ciclo XXIV

Settore Concorsuale di afferenza: 09/E

Settore Scientifico disciplinare: ING-INF/01

TITOLO TESI

ADVANCED NUMERICAL SIMULATION OF SILICON-BASED SOLAR CELLS

Presentata da: **Mauro Zanuccoli**

Coordinatore Dottorato **Relatore**

Prof. Claudio Fiegna **Prof. Claudio Fiegna**

Esame finale anno 2012

Acknowledgements

During my doctoral course period I have been constantly supported and advised by several people. I want to express my gratitude to all of them. I am deeply grateful to my supervisor, Prof. Claudio Fiegna and to Prof. Enrico Sangiorgi for the opportunity and the support. I would like to thank all my colleagues who have supported the activity with helpful discussions, Dr. Paolo Magnone and Raffaele De Rose. During the three-year period I had the great opportunity to visit scientific and technological partners like Applied Material, Inc. in Santa Clara, CA, USA (AMAT) Minatec Grenoble-Inp., France and the Institute of Physics and Technology of the Russian Academy of Sciences (FTIAN-RAS), Moscow. My work has been supported by all these partners, therefore I would like to thank Dr. Michel Frei and Dr. Mukul Agrawal (AMAT), Dr. Igor Semenikhin, Prof. Vladimir Vyurkov (FTIAN-RAS) and Prof. Anne Kaminski, Prof. Mirelle Mouis and Prof. Davide Bucci (IMEP-LAHC) for the support and inputs on technological aspects.

Publications of the author

Journals

M. Zanuccoli, R. De Rose, P. Magnone, E. Sangiorgi and C. Fiegna
Performance analysis of rear point contact solar cells by three-dimensional numerical simulation.
IEEE Trans. Elec. Devices, vol. 59 (5), DOI: 2012, 10.1109/TED.2012.2187297

I. Semenikhin, M. Zanuccoli, M. Benzi, V. Vyurkov, E. Sangiorgi and C. Fiegna
Computational efficient RCWA method for simulation of thin film solar cells.
Optical and Quantum Electronics, DOI: 10.1007/s11082-012-9560-5

International workshops and conferences

M. Zanuccoli, R. De Rose, P. Magnone, M. Frei, H.-W. Guo, M. Agrawal, E. Sangiorgi and C. Fiegna
Numerical simulation and modeling of rear point contact contact solar cells.
Conference Records of 37th IEEE Photovoltaic Specialist Conference (PVSC), Seattle, Washington, US, 2011

P. Magnone, R. De Rose, M. Zanuccoli, D. Tonini, M. Galiazzo, G. Cellere, H.-W. Guo, M. Frei, E. Sangiorgi and C. Fiegna
Understanding the impact of Double Screen-Printing on Silicon Solar Cells by 2-D Numerical Simulations.
Conference Records of 37th IEEE Photovoltaic Specialist Conference (PVSC), Seattle, Wash-

ington, US, 2011

R. De Rose, M. Zanuccoli, P. Magnone, D. Tonini, M. Galiazzo, G. Cellere, M. Frei, H.-W. Guo, C. Fiegna and E. Sangiorgi
2-D numerical analysis of the impact of the highly-doped profile on selective emitter solar cell performance.
Conference Records of 37th IEEE Photovoltaic Specialist Conference (PVSC), Seattle, Washington, US, 2011

M. Zanuccoli, H.-W. Guo, E. Sangiorgi, C. Fiegna
Three-dimensional numerical simulation of rear point contact crystalline silicon solar cells.
Renewable Energy & Power Quality Journal, No.9, 12th May 2011 ISSN 2172-038X

M. Zanuccoli, P.F. Bresciani, M. Frei, H.-W. Guo, H. Fang, M. Agrawal, C. Fiegna, E. Sangiorgi
2-D numerical simulation and modeling of monocrystalline selective emitter solar cells.
Conference Records of 35th IEEE Photovoltaic Specialist Conference (PVSC), Honolulu, Hawaaii, US, 2010

M. Zanuccoli, P.F. Bresciani, M. Frei, H.-W. Guo, H. Fang, M. Agrawal, C. Fiegna, E. Sangiorgi
2-D numerical simulation and modeling of monocrystalline selective emitter solar cells.
Conference Records of 35th IEEE Photovoltaic Specialist Conference (PVSC), Honolulu, Hawaaii, US, 2010 pp. 2262 - 2265, DOI: 10.1109/PVSC.2010.5617010, ISSN : 0160-8371, Print ISBN: 978-1-4244-5890-5

I. Semenikhin, M. Zanuccoli, M. Benzi, V. Vyurkov, E. Sangiorgi and C. Fiegna
Application of a computationally efficient implementation of the RCWA method to numerical simulations of thin film amorphous solar cells.
Proceedings of 11th International Conference on Numerical Simulation of Optoelectronic Devices (NUSOD), 2011 pp. 117 - 1185, DOI: 110.1109/NUSOD.2011.6041168, ISSN : 2158-3234, Print ISBN: 978-1-61284-876-1

R. De Rose, M. Zanuccoli, P. Magnone, E. Sangiorgi and C. Fiegna

Open issues for the numerical simulation of silicon solar cells.

Proceedings of 12th International Conference on Ultimate Integration on Silicon (ULIS), 2011 pp. 1 - 4, DOI: 1110.1109/ULIS.2011.5757961, E-ISBN : 978-1-4577-0089-7, Print ISBN: 978-1-4577-0090-3

I. Semenikhin, V. Vyurkov, M. Zanuccoli, E. Sangiorgi and C. Fiegna

Efficient implementation of the Fourier modal method (RCWA) for the optical simulation of optoelectronics devices.

Proceedings of 114th International Workshop on computational Electronics (IWCE), 2010 pp. 1 - 4, DOI: 10.1109/IWCE.2010.567798, Print ISBN: 978-1-4244-9383-8

I. Semenikhin, M. Zanuccoli, V. Vyurkov, E. Sangiorgi and C. Fiegna

Application of RCWA method to optoelectronic numerical simulations of 2D nanostructures.

Proceedings of 14th International Workshop on computational Electronics (IWCE), 2010 pp. 1 - 2, DOI: 110.1109/INEC.2011.5991728, ISSN: 2159-3523, Print ISBN: 978-1-4577-0379-9

List of Symbols

Symbol	Unit	Name or description
A	$[cm^2]$	area of the solar cell
B	$[cm^3 \quad s^{-1}]$	radiative recombination coefficient
c	$[m \quad s^{-1}]$	speed of light in vacuum
C_n	$[cm^6 \quad s^{-1}]$	material-specific Auger coefficient for electrons
C_p	$[cm^6 \quad s^{-1}]$	material-specific Auger coefficient for holes
D_n	$[cm^2 \quad s^{-1}]$	diffusion coefficient for electrons
D_p	$[cm^2 \quad s^{-1}]$	diffusion coefficient for holes
E	$[eV]$	energy
E_0	$[V \quad m^{-1}]$	electric field strength
E_C	$[eV]$	bottom edge of the conduction band
E_V	$[eV]$	top edge of the valence band
E_g	$[eV]$	energy band-gap
$E_{0,A}$	$[eV]$	position of the minimum for the acceptor-like exponential-tail states
$E_{0,D}$	$[eV]$	position of the minimum for the donor-like exponential-tail states
E_A	$[eV]$	energy slope for acceptor-like exponential-tail states
E_D	$[eV]$	energy slope for donor-like exponential-tail states
$E_{A,MG}(E)$	$[eV]$	energy position of Gaussian acceptor-like mid-gap states
$E_{D,MG}(E)$	$[eV]$	energy position of Gaussian donor-like mid-gap states
E_F	$[eV]$	Fermi level
E_{F_i}	$[eV]$	intrinsic Fermi level
E_{ph}	$[eV]$	photon energy
E_t	$[eV]$	energy trap level
$f_A(E)$	-	probability of occupation of acceptor-like states
$f_D(E)$	-	probability of occupation of donor-like states
FF	-	Fill Factor

Symbol	Unit	Name or description
$g(E)$	$[cm^{-3}]$	total density of states
$g_A(E)$	$[cm^{-3}]$	total density of acceptor-like states
$g_D(E)$	$[cm^{-3}]$	total density of donor-like states
$g_A^{BT}(E)$	$[cm^{-3}]$	density of acceptor-like exponential-tail states
$g_D^{BT}(E)$	$[cm^{-3}]$	density of donor-like exponential-tail states
$g_A^{MG}(E)$	$[cm^{-3}]$	density of acceptor-like mid-gap states
$g_D^{MG}(E)$	$[cm^{-3}]$	density of donor-like mid-gap states
$G_{A,BT}(E)$	$[cm^{-3}]$	minimum value of acceptor-like exponential-tails states
$G_{D,BT}(E)$	$[cm^{-3}]$	minimum value of donor-like exponential-tails states
G_{OPT}	$[cm^{-3} \quad s^{-1}]$	optical generation rate
h	$[J \quad s]$	Planck constant
H	$[A \quad m^{-1}]$	magnetic field strength
H_R	-	Haze parameter for reflected light
H_T	-	Haze parameter for transmitted light
J_{sc}	$[A \quad cm^{-2}]$	short-circuit current density
J_{ph}	$[A \quad cm^{-2}]$	photo-generated current density
J_0	$[A \quad cm^{-2}]$	diode saturation current density
J_n	$[A \quad cm^{-2}]$	electron current density
J_p	$[A \quad cm^{-2}]$	hole current density
K_B	$[J \quad K^{-1}]$	Boltzmann constant
k	-	extinction coefficient (imaginary part of the complex refractive index)
I_0	$[W \quad m^{-2}]$	Input irradiance
I_{MPP}	$[A]$	Maximum Power-Point Current
L_n	$[cm]$	diffusion length of electrons
L_p	$[cm]$	diffusion length of holes
L_T	$[cm]$	transport length
n	-	real part of the complex refractive index
$\tilde{n}$	-	complex refractive index
n_{n_0}	$[cm^{-3}]$	electron conc. in n-type semiconductors in equilibrium
n_{p_0}	$[cm^{-3}]$	electron conc. in p-type semiconductors in equilibrium
$n(P)$	$[cm^{-3}]$	concentration of free electrons
n_i	$[cm^{-3}]$	intrinsic carrier density concentration
$n_{i,eff}$	$[cm^{-3}]$	effective intrinsic carrier concentration
n_T	$[cm^{-3}]$	total concentration of trapped electrons

Symbol	Unit	Name or description
N	$[cm^{-3}]$	net doping concentration
N_A	$[cm^{-3}]$	acceptor doping concentration
N_C	$[cm^{-3}]$	effective density of states in conduction band
N_D	$[cm^{-3}]$	donor doping concentration
$N_A^{MG}(E)$	$[cm^{-3}]$	total number of acceptor-like mid-gap states
$N_D^{MG}(E)$	$[cm^{-3}]$	total number of donor-like mid-gap states
N_T	$[cm^{-3}]$	total concentration of traps
N_{sub}	$[cm^{-3}]$	substrate doping concentration
N_V	$[cm^{-3}]$	effective density of states in valence band
p_{n_0}	$[cm^{-3}]$	hole conc. in n-type semiconductors in equilibrium
p_{p_0}	$[cm^{-3}]$	hole conc. in p-type semiconductors in equilibrium
$p(P)$	$[cm^{-3}]$	concentration of hole
p_T	$[cm^{-3}]$	total concentration of trapped hole
R_{net}	$[cm^{-3} \quad s^{-1}]$	Net recombination rate per time and volume unit
R_S	Ω	series resistance
R_{SH}	Ω	shunt resistance
q	C	elementary charge
S	$[W \quad m^{-2}]$	Poynting vector strength
S_{e_0}	$[cm \quad s^{-1}]$	surface recombination velocity for electrons
S_{h_0}	$[cm \quad s^{-1}]$	surface recombination velocity for holes
$S(E)$	$[Wm^{-2} \quad nm^{-1}]$	spectral irradiance
t	$[s]$	time
T	$[K]$	absolute temperature
v_{th}	$[cm \quad s^{-1}]$	thermal velocity of carriers
V_A	$[V]$	applied voltage
V_{MPP}	$[V]$	Maximum Power-Point Voltage
V_0	$[V]$	Built-in potential
V_{OC}	$[V]$	open-circuit voltage
W	$[\mu m]$	wafer thickness
W_{DEP}	$[\mu m]$	depletion region width
W_M	$[\mu m]$	front finger width
W_{SE}	$[\mu m]$	lateral extension of the HDOP region
W_{SUB}	$[\mu m]$	front contact pitch

Symbol	Unit	Name or description
α	$[cm^{-1}]$	absorption coefficient of the radiation
ε	$[F \quad cm^{-1}]$	electromagnetic permittivity
ε_0	$[F \quad cm^{-1}]$	permittivity of vacuum
η	-	conversion efficiency
η_C	-	carrier collection efficiency
θ	$[^\circ]$	angle of incidence of the radiation
λ	$[nm]$	wavelength of the radiation
μ	$[H \quad cm^{-1}]$	magnetic permeability
μ_0	$[H \quad cm^{-1}]$	magnetic permeability in vacuum
μ_n	$[cm^2 \quad V^{-1} \quad s^{-1}]$	electron mobility
μ_p	$[cm^2 \quad V^{-1} \quad s^{-1}]$	hole mobility
$\rho(\mathbf{r})$	$[C \quad cm^{-3}]$	charge density
ρ_{BC}	$[\Omega \quad cm^2]$	specific back contact resistivity
ρ_c	$[\Omega \quad cm^2]$	specific contact resistivity
ρ_m	$[\Omega \quad cm]$	metal resistivity
ρ_S	$[\Omega \quad cm]$	substrate resistivity
σ_A	$[eV]$	standard deviation of Gaussian mid-gap acceptor-like states
σ_D	$[eV]$	standard deviation of Gaussian mid-gap donor-like states
$\sigma_{A,n}$	$[cm^2]$	capture cross-section of acceptor-like traps for electrons
$\sigma_{A,p}$	$[cm^2]$	capture cross-section of acceptor-like traps for holes
$\sigma_{D,n}$	$[cm^2]$	capture cross-section of donor-like traps for electrons
$\sigma_{D,p}$	$[cm^2]$	capture cross-section of donor-like traps for holes
σ_{RMS}	$[cm^2]$	root mean square value of surface heights (for rough interfaces)
τ_e	$[s]$	carrier lifetime for electrons
τ_h	$[s]$	carrier lifetime for holes
$\phi(\lambda)$	$[Photons \quad s^{-1} \quad m^{-2}]$	incident photon flux
$\phi(\mathbf{r}, t)$	$[V]$	electrostatic potential
ϕ_n	$[eV]$	Quasi-Fermi levels for electrons
ϕ_p	$[eV]$	Quasi-Fermi levels for holes
ω	$[rad \quad s^{-1}]$	angular frequency

List of Abbreviations

ADF	Angular Distribution Function
AFM	Atomic Force Microscopy
ARC	Anti-Reflection Coating layer
ARS	Angular Resolved Scattering
a-Si	amorphous silicon
a-Si:H	hydrogenated amorphous silicon
BSF	Back Surface Field
BSRV	Back Surface Recombination Velocity
BSRV_{eff}	Effective Back Surface Recombination Velocity
BSRV_{pass}	Back Surface Recombination Velocity at passivated interface
c-Si	crystalline silicon
CdTe	Cadmium Telluride
CIGS	Copper Indium Gallium Diselenide
CPV	Concentrator PhotoVoltaic
CPW	cells per wavelength
Cz	Czochralski
DOS	density of states
FDTD	Finite Difference Time Domain
EMA	Effective Media Approximation
EQE	External Quantum Efficiency
FZ	Floating Zone
HE	Homogenous Emitter
HDOP	heavy and deep phosphorus diffusion
IBR	Internal Bottom Reflectivity
IBR_{eff}	Effective Internal Bottom Reflectivity
IQE	Internal Quantum Efficiency
LDOP	lowly-doped and shallow diffusion
LFC	Laser Firing Contact
MCz	Magnetic Czochralski
PDE	Partial Differential Equation
PERC	Passivated Emitter and Rear Cell
PERL	Passivated Emitter, Rear Locally diffused cell
RCWA	Rigorous Coupled-Wave Analysis
RPC	Rear Point Contact
RT	Ray Trace

SE	Selective Emitter
SEM	Scanning Electron Microscopy
SiN	Silicon Nitride
SR	Spectral Response
SRH	Shockley Read Hall
SLT	Single Level Trap
TCAD	Technology Computer-Aided Design
TCO	Transparent Conductive Oxide
TE	Transverse Electric
TEM	Transverse Electro Magnetic
TIS	Total Integrating Scattering
TM	Transverse Magnetic
TMM	Transfer Matrix Method

Contents

List of Figures **xix**

1 Introduction **1**

2 Solar cell device physics and technology review **7**

2.1 Absorption of light in semiconductors 7

2.2 Recombination mechanisms 12

2.2.1 Radiative recombination 12

2.2.2 Auger recombination 12

2.2.3 Trap-assisted recombination 13

2.2.4 Effettive carrier lifetime 14

2.3 Semiconductor Model Equations 15

2.3.1 Drift-Diffusion Transport Model 15

2.3.2 Semiconductor equations 16

2.3.3 1-D single-junction silicon solar cell model 17

2.3.4 Output characteristic and figures of merit 23

2.3.5 Other figures of merit 25

2.3.6 Optical figures of merit: absorbance, reflectance and transmittance 26

2.3.7 Quantum efficiency and spectral response 26

2.4 Efficiency Limits 27

2.5 Effect of temperature and loss mechanisms on main figures of merit of a solar cell 30

2.5.1 Effect of temperature 30

2.5.2 Optical losses 32

2.5.3 Open circuit voltage and FF losses 32

2.5.4 Accounting for contact resistances 34
2.6 Light Trapping 37
2.7 Geometrical light trapping 39
2.7.1 Coherent light trapping schemes for thin film solar cells 40
2.8 Antireflection coating layers 43
2.9 Standard crystalline solar cells manufacturing technology 45
2.9.1 Wafer preparation 45
2.9.2 Front contact and emitter design 47
2.9.3 Base and rear surface 49

3 Numerical Simulation of Solar Cells 51
3.1 Introduction to numerical solution of semiconductor device equations . 51
3.1.1 Drift-Diffusion transport equations 52
3.1.2 Electrical Boundary Conditions 53
3.1.3 Effective Intrinsic Carrier Concentration and Band Gap structure 54
3.1.4 Carrier Mobility Models 56
3.1.5 Recombination mechanisms 57
3.1.6 Auger recombination 59
3.2 Numerical methods 60
3.3 Propagation of electromagnetic waves 62
3.3.1 From Maxwell equations to homogeneous Helmholtz equation . . 62
3.3.2 Solution of Helmholtz equations for a normal homogenous medium without sources 65
3.3.3 TE and TM plane waves 66
3.3.4 Geometrical optics and raytracing 68
3.4 Finite Difference Time Domain (FDTD) Method 73

4 Modeling of advanced crystalline silicon solar cells 77
4.1 Selective emitter solar cells 77
4.1.1 Introduction to selective emitter solar cells 77
4.1.2 Selective emitter solar cells: simulation setup and simulated devices 79
4.1.3 Homogeneous emitter solar cell simulation 81
4.1.4 Selective emitter solar cell: impact of LDOP and HDOP profiles on main figures of merit 83

4.1.5 Selective emitter solar cell: loss analysis . . . 85
4.1.6 Selective emitter solar cell: conclusions . . . 86
4.2 Rear point contact solar cells . . . 88
4.2.1 Introduction to rear point contact solar cells . . . 89
4.2.2 Rear Point Contact solar cells: simulation methodology and simulated devices . . . 91
4.2.3 Technological and geometrical options . . . 94
4.2.3.1 Comparison between PERL and PERC solar cells . . . 96
4.2.3.2 Dependence of the main figures of merit of PERL cells on the back-contact diameter . . . 101
4.2.3.3 PERL cells: impact of back-contact pitch on performance 104
4.2.3.4 PERL cells: analysis of the dependence of the main figures of merit on the specific back contact resistivity . 105
4.2.4 Rear Point Contact solar cells: conclusions . . . 107

5 Optical Simulation by Fourier-Modal Methods 111
5.1 Introduction to RCWA . . . 112
5.2 RCWA implementation based on discretization of the Fourier series . . . 114
5.2.0.1 Implementation for TE polarization . . . 115
5.2.0.2 Implementation for TM polarization . . . 120
5.3 RCWA implementation based on auxiliary functions . . . 122
5.3.1 Auxiliary functions and boundary conditions . . . 123
5.3.2 Solving for the auxiliary function . . . 124
5.3.3 Determining the electromagnetic field . . . 126
5.3.4 Solution in homogenous layers . . . 128
5.4 RCWA implementation based on solution of an eigenvalues problem . . 130
5.4.1 Problem definition . . . 130
5.4.2 Expansion of the field in Fourier series . . . 131
5.4.3 Solution within homogenous layer . . . 138
5.4.4 Calculation of the optical generation rate . . . 138
5.5 Validation of RCWA method and accuracy . . . 139
5.5.1 2-D RCWA simulator . . . 139
5.5.2 3-D RCWA simulator . . . 141

5.6 Applications of RCWA tool 143
5.6.1 Application: impact of surface morphology on absorbance 143
5.6.2 Application: nano-rod based solar cell 154

6 Modeling of amorphous silicon thin film solar cells 159
6.1 Thin film solar cells 160
6.2 Continuous distribution of defect density in energy 161
6.3 Optical modeling 164
6.3.1 Optical confinement in thin-film solar cells: modeling by methods based on scalar scattering theory 165
6.4 Application: dependence of main figures of merit of the solar cell on the morphology of the internal interfaces 169
6.4.1 Simulation setup 169
6.4.2 Dependence of figures of merit on ITO/p-type interface roughness level 171

7 Conclusions 181

References 185

List of Figures

2.1 Interface between a dielectric and an absorber material ($z \geq z_0$). The light is propagating from left to right along z-axis. 8

2.2 Dependence of the absorption coefficient α of crystalline silicon on the photon energy at $T = 300K$. 9

2.3 Optical generation rate G_{OPT} calculated at λ=500nm as function of the distance from the front interface in case of a silicon slab featuring infinite thickness. The amplitude E_0 of the incident field is $1Vm^{-1}$. 11

2.4 Optical generation rate G_{OPT} calculated at λ=500nm as function of the distance from the front interface in case of a silicon slab featuring thickness comparable to the wavelength of the radiation. Minima and maxima of G_{OPT} can be observed. The amplitude E_0 of the incident field is $1Vm^{-1}$. 11

2.5 (A) Mono-dimensional (1-D) sketch of an abrupt p-n junction with the associated charge density $\rho(x)$ profile along the x-axis (B). The pint $x = 0$ denotes the metallurgical junction interface. $-X_{D_N}$ and X_{D_P} are the boundaries of the depletion region at the n-type and p-type sides, respectively. N_A and N_D denote the uniform doping concentrations of the p-type and n-type regions, respectively. The electric field plot, the energy bands diagram and the carrier concentration plots are shown in (C), (D) and (E), respectively. In (D) V_0 denotes the built-in potential. 19

2.6 Two-diode circuit model of a solar cell. Diode (A) represents the current due to recombination within the quasi-neutral regions. Diode (B) models the recombination occurring in the depletion region according to eq. 2.64. 24

2.7 I-V characteristic (red solid curve) of a solar cell. The parameters V_{OC} and I_{SC} are the open-circuit voltage and the short-circuit current, respectively. The output power is represented by the black dashed curve, which reaches the maximum value at $V = V_{MPP}$ and $I = I_{MPP}$. 25

2.8 Conventional spectrum AM1.5G ($1000 W m^{-2}$) for direct sun illumination. The plot reports the spectral irradiance. 28

2.9 Dependence of the short-circuit current on the band-gap energy E_g for direct illumination without external reflectance of the top interface calculated assuming the input spectrum AM1.5G ($1000 W m^{-2}$) at T=300K. All photo-generated electron-hole pairs are assumed to be collected by electrodes. 29

2.10 Dependence of the open-circuit voltage V_{OC} on the band-gap energy E_g for direct illumination without external reflectance of the top interface and calculated assuming the spectrum AM1.5G ($1000 W m^{-2}$) at T=300K. The saturation current is in agreement with the lower bound limit proposed by M.A. Green in (1). All photo-generated electron-hole pairs are assumed to be collected by electrodes. 30

2.11 Dependence of the conversion efficiency η on the band-gap energy E_g for direct illumination without external reflectance of the top interface, calculated assuming the spectrum AM1.5G ($1000 W m^{-2}$) at T=300K. The saturation current is chosen in agreement with the lower bound limit proposed by M.A. Green in (1). All photo-generated electron-hole pairs are assumed to be collected by electrodes. 31

2.12 Contact scheme for the front surface of a silicon solar cell. Bus bars and fingers are aimed at delivering current to the external circuit. 32

2.13 Silicon solar cell featuring the front surface textured by pyramids. . . . 33

2.14 Effect of the series parasitic resistance on the I-V characteristic of a solar cell. The current is normalized to the short-circuit current density J_{SC}. 35

2.15 Effect of the shunt parasitic resistance on the I-V characteristic of a solar cell. The current is normalized to the short-circuit current density J_{SC}. 35

2.16 Sketch of a simple solar cell with the lumped-element circuit to model the series parasitic resistances. 36

2.17 Theoretical prediction of the dependence of the absorbance of a crystalline silicon slab featuring a finite thickness on the photon energy in case of single-pass scheme and in case of a light trapping scheme by means of front surface texturing (pathlength equal to $4n^2$ where n is the refractive index of silicon). The one-pass absorption curve of the $200\mu m$-thick silicon layer is comparable to that associated to the textured $20\mu m$-thick layer. 39

2.18 Vertical grooves formed by [111] crystallographic plane orientation. . . . 40

2.19 Cross sections of (A) light trapping scheme proposed by Redfield (2), (B) symmetric vertical grooves and (C) asymmetrical grooves. 41

2.20 Three dimensional upright pyramids: (A) periodic scheme and (B) random pyramids. 42

2.21 Photonic crystals in 2-D scheme (A) and 3-D scheme (B). 43

2.22 Sketch of a simple anti reflection coating layer (ARC) featuring one slab with refractive index n_1. The refractive indices of the superstrate and substrate are n_0 and n_2, respectively. 44

2.23 Examples of ARCs: calculated reflectance. 45

2.24 Refractive indices and extinction coefficients of the crystalline silicon (A) and of SiO_2, TiO_2 and MgF_2 (B) used to calculate the reflectance of Fig. 2.23. 46

2.25 Homogeneous emitter (HE) solar cell. Under the contacted surface and between fingers the same emitter doping profile is adopted. L_{FF}, H_{MET} and W_{MET} denote the front finger length, height and width, respectively. W_{FP} is the distance between front fingers. 48

2.26 Selective emitter (SE) solar cell. A heavily doped emitter doping profile (n^{++}) is present under the contacted surface and a lowly-doped profile (n^{+}) between fingers. L_{FF}, H_{MET} and W_{MET} denote the front finger length, height and width, respectively. W_{FP} is the distance between front fingers. 48

LIST OF FIGURES

3.1 Effective intrinsic carrier density accounting for band-gap narrowing (BGN) as function of the total doping density for different models, including the revised BGN model adopted for numerical simulations in Sentaurus TCAD. 56

3.2 Bulk lifetime versus boron doping concentration for the empirical fitting suggested by Glunz et al. (3) and for the Sentaurus default Scharfetter relation. The bulk lifetime curve provided by the modified relation is also reported. 59

3.3 Single box centered at node i-th for the numerical solution of PDEs. . . 60

3.4 Thin-layer-stack boundary condition used to simulate ARCs with Ray-Tracing in combination with the TMM solver. 71

3.5 Reflection, transmission and refraction of plane waves at a planar interface. 72

3.6 Absorbance for the $2\mu m$-thick (A) and the $1\mu m$-thick (B) slabs of crystalline silicon calculated by raytracer (RT), FDTD and RCWA methods. 74

4.1 (A) Sketch of the cross section of the 2-D simulated selective emitter (SE) solar cell. HDOP and LDOP denote the highly-doped and the lowly-doped emitter profiles, respectively. W is the wafer thickness and $W_{MET} = 100\mu m$ and $W_{SE} = 130\mu m$ are the front-contact finger width and the lateral extension of the HDOP diffusion under the finger, respectively. (B) Emitter doping-profiles adopted for the simulations: the figure shows the doping profile of the homogeneous emitter (HE) solar cell ($39\Omega/sq$), that of the SE under the contact (HDOP) and the emitter profile under the passivated interface between fingers (LDOP) featuring a sheet resistance of $39\Omega/sq$ and $109\Omega/sq$, respectively. 80

4.2 Calculated figures of merit for the SE and the HE ($39\Omega/sq$) cells. The SE are simulated with the profile HDOP featuring $34\Omega/sq$ and LDOP featuring sheet resistance values within the range $47\Omega/sq$-$215\Omega/sq$. Main figures of merit calculated by Sentaurus: (A) Short-circuit current density (J_{SC}), (B) Open-circuit voltage (V_{OC}), (C) Fill Factor (FF) and (D) conversion efficiency. 82

4.3 Comparison of collection efficiency of photo-generated carriers (η_C) between selective emitter SE ($W_{SUB} = 1800\mu m$, HDOP $46\Omega/sq$ and LDOP $109\Omega/sq$) and the reference homogenous emitter solar cell HE ($W_{SUB} = 2100\mu m$, $39\Omega/sq$). Larger η_C within the blue region of the spectrum ($300nm$-$600nm$) is obtained by the SE cell. 86

4.4 2-D Auger recombination rate maps (in $cm^{-3}s^{-1}$) in the passivated emitter region close to the front surface (A) for the homogeneous emitter HE cell ($W_{SUB} = 2100\mu m$, $39\Omega/sq$) and (B) for the optimized selective emitter scheme SE ($W_{SUB} = 1800\mu m$, HDOP $46\Omega/sq$ and LDOP $109\Omega/sq$). In (C) the 1-D Auger recombination rate is reported as function of the distance from the front interface in the region between front-contact fingers. 87

4.5 (A) 3-D sketch of the simulated solar cell with the rear point contact scheme. W_{SUB} and W denote the front contact pitch and the wafer thickness, respectively. The parameter W_M is the width of the front contact finger. The hole pitch is denoted by p. The simulation domain is highlighted in red ($L_x = p/2$, $L_y = W_{SUB}/2$). (B) 2-D cross section of the device with rear surface passivation by silicon nitride (SiN). . . . 90

4.6 Example of 3-D mesh grid adopted for the device numerical simulation. In this case the hole pitch p is $500\mu m$ and the hole diameter s is $50\mu m$. The simulation domain is chosen according to section 4.2.2. Up to 300000 vertices are typically required. 95

4.7 Example of 3-D output maps calculated by the device numerical simulator. In this case the hole pitch p is $500\mu m$ and the hole diameter s is $50\mu m$. The figure shows the 3-D conduction current density map in short-circuit conditions under illumination. 95

4.8 Short circuit current density J_{sc} (left) and open circuit voltage V_{oc} (right) for PERC and PERL solar cells with hole pith $p = 500\mu m$ and substrate resistivity $\rho_s = 0.5\Omega cm$. 98

4.9 Calculated absorbance (A) and reflectance (R) characteristics of a RPC cell featuring $f_0 = 0.2\%$ compared to those of the uniformly contacted cell ($f = 100\%$). 98

4.10 Fill Factor (left) and efficiency (right) for PERC and PERL solar cells with hole pitch $p = 500\mu m$ and substrate resistivity $\rho_s = 0.5\Omega cm$. In case of the PERC two different values of the specific back contact resistivity ρ_{BC} are assumed: $\rho_{BC} = 3m\Omega cm^2$ and $\rho_{BC} = 30m\Omega cm^2$; if the former value of ρ_{BC} is adopted for both PERC and PERL, the curves of the FF are indistinguishable. 99

4.11 Collection efficiency of photo-generated carriers (η_C) from $600nm$ up to $1100nm$ for PERC and PERL solar cells with hole pitch $p = 500\mu m$ and substrate resistivity $\rho_s = 0.5\Omega cm$; η_C is calculated at $f = 100\%$ (uniformly contacted cell) and at the optimum metallization fraction (PERC: $f_0 = 3.14\%$, $s = 100\mu m$; PERL: $f_0 = 7.07\%$, $s = 150\mu m$). . . . 101

4.12 Short circuit current density J_{sc}, open circuit voltage V_{oc}, Fill Factor and conversion efficiency η for PERL solar cells with constant hole pith $p = 500\mu m$ and specific back contact resistivity $\rho_{BC} = 3m\Omega cm^2$, for different substrate resistivity values. 103

4.13 Fill Factor (up) and efficiency (bottom) for PERL solar cells with substrate resistivity $\rho_S = 5\Omega cm$ (left) and $\rho_S = 1\Omega cm$ (right). Specific back contact resistivity $\rho_{BC} = 3m\Omega cm^2$. Hole diameter s as parameter and variable hole pitch. 106

4.14 Conversion efficiency versus hole pitch p for PERL solar cells with substrate resistivity $\rho_S = 5\Omega cm$ (left) and $\rho_S = 1\Omega cm$ (right). Specific back contact resistivity $\rho_{BC} = 3m\Omega cm^2$. Hole diameter s as parameter. . . . 108

4.15 Fill Factor (left) and efficiency (right) for PERL solar cells with hole diameter $s = 50\mu m$, substrate resistivity $\rho_S = 5\Omega cm$ (up) and $\rho_S = 1\Omega cm$ (bottom). Specific back contact resistivity ρ_{BC} as parameter. . . 109

5.1 Sketch of the 2-D simulation domain which includes the superstrate, the substrate and the grating region (left). A typical photovoltaic device is represented by a multi-layer structure (right) in which each layer is homogenous and separated by smooth or rough interfaces. The rough interfaces are treated as grating regions within which the permittivity is not a uniform function of the position. The refractive index of the superstrate is n_I. 117

5.2 Cross section of a homogenous layer with the coefficients of the incident, reflected and transmitted waves. 129

5.3 Schematic of the incidence plane for 3-D optical simulations. The direction of wave propagation vector $\mathbf{k}_1$ is defined by angles θ and ϕ with respect to z-axis and x-axis, respectively. 131

5.4 Sketch of the simulation domain (the top figure reports a 3-D pyramid) split in layers within which the permittivity is approximated by a step function. The bottom figure shows a schematic of a single layer with the Fourier coefficients of the electric field at the boundaries. 134

5.5 Sketch of the 2-D rectangular grating adopted as reference test structure for the validation and the analysis of the accuracy of the RCWA simulator ($a = 25nm$, $b_1 = b_2 = 12.5nm$, $h_1 = 100nm$, $h_2 = 450nm$ and periodicity $p = 50$nm). 140

5.6 Comparison of the absorbance calculated by FDTD and RCWA within the range of wavelengths $380nm - 880nm$ for the grating test structure (Fig. 5.5) in case of TE (A) and TM (B) polarizations. For FDTD simulations performed by Synopsys EMW, 400 cells per wavelength(CPW) have been adopted. RCWA simulations have been carried out by using $N_F = 60$ and $\Delta z = 1nm$. 140

5.7 Accuracy of the relative absorption for 2D-RCWA simulator in case of the test structure (rectangular grating of Fig. 5.5). The accuracy has been calculated for both TE and TM polarizations and for two values of the wavelength of the radiation ($450nm$ and $750nm$). In (A) and (B) the accuracy of relative absorbance is calculated as function of the number of Fourier modes N_F with $\Delta z = 1nm$ and keeping the number of points N_x for the Fourier transform along x-axis constant ($N_x = 1024$). In (C) and (D) the accuracy of relative absorbance is calculated as function of Δz^{-1} adopting $N_F = 201$. The dashed line denotes the minimum value of N_F (Δz^{-1}) above which the accuracy of the relative absorbance is smaller than 10^{-3}. 142

5.8 3-D Photonic Crystal: comparison of the transmission coefficient calculated by 3D-RCWA and that from literature (Fan et al. (4)) versus the periodicity p of the cell normalized to the wavelength of the radiation λ. Thickness and hole diameter are set to $0.5p$ and $0.05p$, respectively. The real part of the permittivity of the dielectric slab is 12. RCWA simulations have been performed by adopting $\theta = 0$, $\phi = 0$ (Fig. 5.3) and $N_{Fx} = 43$, $N_{Fy} = 43$ number of Fourier modes along x-axis and y-axis, respectively. 143

5.9 Sketch of the rectangular 3-D grating adopted as reference test structure for the analysis of the accuracy of RCWA simulator (side length $L = 500nm$ and periodicity $p = 500$nm). 144

5.10 Accuracy of the relative absorption for 3D-RCWA simulator in case of the test structure (3-D rectangular grating of Fig. 5.9) as function of the number of Fourier modes N_{Fx}, N_{Fy} along x-axis and y-axis, respectively. The accuracy has been calculated for $\theta = 0$, $\phi = 0$ (Fig. 5.3). The dashed line denotes the minimum value of N_F above which the accuracy of the relative absorbance is smaller than 10^{-3}. 144

5.11 Sketch of the structures considered for the analysis of the impact of the surface morphology on the absorbance: silicon slab with (A) flat, (B) random rough (Gaussian distribution of heights with root mean square value σ_{RMS}=50nm and correlation length L_c=25nm), (C) triangular (h=500nm), (D) rectangular (h=500nm) and (E) circular (r=400nm) texturing of the front interface. The periodicity p is 1000nm for all structures and the volume of the absorbing material is the same for all slabs. 147

5.12 Absorbance characteristics of the silicon slab with smooth front interface calculated at different angles of incidence θ of the light. The absorbance decreases with increasing θ. 147

5.13 Absorbance characteristics of the silicon slab with Gaussian random roughness at the front interface calculated at different angles of incidence θ of the light. The absorbance decreases with increasing θ similarly to the flat interface case. 148

5.14 Comparison between the absorbance characteristics of the silicon slabs for different kinds of front interface morphology calculated at normal incidence (θ=0), for TE (A) and TM (B) polarization. The absorbance of the slab with smooth interface is remarkably lower than those calculated by considering the texturing. In case of TE polarization, for $\lambda < 750nm$ the maximum absorbance is obtained with the random rough interface while for TM polarization the maximum absorbance is reached by the random rough interface for $\lambda < 600nm$ and by the triangular texturing above. 148

5.15 Monochrome optical generation rate G_{opt} maps per unit volume and time calculated for the slabs featuring smooth (on the left) and random roughness (on the right) interfaces at $\lambda = 600nm$ by assuming normal incidence. On the bottom side the profiles of G_{opt} versus z for the vertical slice at $x = 500nm$ are compared. The optical generation rate G_{opt} in case of random roughness is significantly larger than that of the flat interface throughout the volume of the absorbing layer. 149

5.16 Total absorbance A_w weighted by conventional AM1.5G spectrum of the silicon slabs with different kinds of roughness at the front interface, calculated as function of the angle of incidence θ of the light, for TE (A) and TM polarization (B). For TE polarization A_w decreases with increasing θ for all kinds of surface morphology with the exception of the rectangular case, which features a maximum value of A_w between θ=20 and θ=30 degrees; the random roughness features the maximum value of A_w within the whole considered range of incidence angles. In addition, the figure reports A_w calculated for the periodic triangular surface texture featuring the same root mean square height of the random roughness (H_{RMS}=50nm), at normal incidence and for two different values of the periodicity (p=300nm and p=20nm). In (B), for TM polarization, similar trends are observed with the exception of the rectangular-textured and of the smooth interface, for which A_w increases with increasing θ. . 150

5.17 2-D optical generation rate maps inside the c-Si slab featuring circular, rectangular and triangular texturing (Fig. 5.11) at $\lambda = 450nm$, TE (left) and TM (right) polarization. Simulation performed by RCWA ($N_F = 40$, $\Delta_z = 1nm$). 151

5.18 2-D optical generation rate maps inside the c-Si slab featuring circular, rectangular and triangular texturing (Fig. 5.11) at $\lambda = 750nm$, TE (left) and TM (right) polarization. Simulation performed by RCWA (N_F=40, $\Delta_z = 1nm$). 152

5.19 2-D optical generation rate maps inside the c-Si slab featuring triangular (left) and rectangular (right) texturing (Fig. 5.11) at $\lambda = 750nm$, for different angle of incidence of radiation (in A,D $\theta = 0$ degree, in B,E $\theta = 30$ degree and in C,F $\theta = 60$ degree). Simulation performed by RCWA (N_F=40, $\Delta_z = 1nm$). 153

5.20 Sketch of the 3-D cylindrical nano-rod. Nano-rod diameter D, height H, substrate thickness T_0 and periodicity P are geometrical parameters. . . 155

5.21 Absorbance of the silicon cylindrical nano-rod of Fig. 5.9 calculated by 3D-RCWA from $\lambda = 350nm$ to $\lambda = 950nm$ with $\theta = 0$, $\phi = 0$. Nano-rod diameter D, height H and periodicity P as geometrical parameters. All structures exhibit the same volume of the absorber material. Simulations have been performed adopting $N_{Fx} = 43$, $N_{Fy} = 43$ number of Fourier modes along x-axis and y-axis, respectively. Substrate thickness $10\mu m$ (A) and $100\mu m$ (B). The highest absorbance is obtained by the structure featuring $P = 2120nm$, $D = 1000nm$ and $H = 4000nm$. 155

5.22 Monochromatic optical generation rate of a cylindrical nano-rod featuring $P = 2120nm$, $D = 1000nm$ and $H = 4000nm$ (Fig. 5.20) calculated by the 3D-RCWA simulator at $\lambda = 850nm$ with $\theta = 0$, $\phi = 0$. The 3-D optical generation rate has been mapped and interpolated on the same mesh grid provided as input to the device simulator Sentaurus. The nano-rod features a radial junction with junction depth of $200nm$. Since the illumination is direct, the cylindrical symmetry of the geometry is exploited in order to save computational resources. Therefore only one quarter of the cylinder is considered. 156

6.1 Cross-sectional schematic of a (glass) superstrate single-junction amorphous silicon thin film solar cell, with the transparent conductive oxide (TCO) and the internal rough interfaces. 162

6.2 Density of states distribution in energy (DOS) with exponential band-tail states and Gaussian shaped mid-gap states in amorphous silicon. E_{ACP} and E_{DON} denote the acceptor Gaussian peak energy measured positive from the edge of the valence band E_V and the donor Gaussian peak energy measured positive from the edge of the conduction band E_C, respectively. 164

6.3 Effective media approximation (EMA): the rough interface between two media of refractive index n_1 and n_2 is replaced by a stack of one or more equivalent virtual layers featuring planar interfaces. 166

6.4 Light scattering from rough interface: specular and diffuse reflection (transmission) occur at non-planar interfaces exhibiting roughness featuring size in wave regime. H_R and H_T are the refection and transmission haze parameters, respectively. 166

6.5 Typical haze parameters versus wavelength and angular distribution functions (ADF) for air/glass/ZN:O:Al/air system in thin film solar cells with roughness level σ_{RMS} as paramater. 168

6.6 Optical properties of the media of the simulated single-junction thin film superstrate solar cell: real part (left) and imaginary part (right) of the complex refractive indices. 171

6.7 Accuracy of the relative absorption for 2-D RCWA in case of the simulated superstrate thin film solar cell with one rough interface (ITO/p-region interface with $\sigma_{RMS} = 50nm$). The accuracy has been calculated for both TE and TM polarizations and for two values of the wavelength of the radiation ($\lambda = 450nm$ and $\lambda = 750nm$). In (A) and (B) the accuracy of relative absorbance is calculated as function of Δ_z^{-1} for $N_F = 201$. In (C) and (D) the accuracy of relative absorbance is calculated as function of the number of Fourier modes N_F when $\Delta_z = 1nm$. The dashed line denotes the upper bound limit of the accuracy for the conditions adopted to perform the optical simulation ($N_F = 121$, $\Delta_z = 1nm$). 172

6.8 Calculated electric field (A), optical generation rate map (in $cm^{-3}s^{-1}$) (B), carrier concentrations (C) and recombination rate due to band-tails and mid-gap traps as function of the depth in short-circuit conditions for the p-i-n cell with $\sigma_{RMS} = 0nm$ 173
6.9 Calculated absorbed power within the amorphous silicon layer under direct AM1.5G illumination ($1000Wm^{-2}$) adopting the roughness level σ_{RMS} as parameter. The absorbed power increases with increasing σ_{RMS}.176
6.10 Calculated 2-D full-spectrum optical generation (in $cm^{-3}s^{-1}$) maps within the a-Si layer for $\sigma_{RMS} = 25nm$ and $\sigma_{RMS} = 50nm$. 176
6.11 Collection efficiency η_C of the photo-generated carriers for $\sigma_{RMS} = 0nm$, $\sigma_{RMS} = 25nm$ and $\sigma_{RMS} = 50nm$. At short wavelengths the collection efficiency decreases with increasing roughness level σ_{RMS}. 177
6.12 External quantum efficiency (EQE) of the simulated solar thin film solar cell for $\sigma_{RMS} = 0nm$, $\sigma_{RMS} = 25nm$ and $\sigma_{RMS} = 50nm$. 177
6.13 2-D maps of optical generation rates (per unit time and volume) inside the amorphous silicon absorber layer at wavelength $\lambda = 400nm$ (A) and $\lambda = 750nm$ (B) for all considered values of the roughness σ_{RMS}. Different spatial distributions of the photo-generated electron-hole pairs, depending on σ_{RMS} and on the wavelength of the radiation, are observed.178

1

Introduction

Photovoltaic conversion is the direct production of electrical energy from sun. This conversion does not involve the emission of polluting substances and mechanical movements, therefore it requires minimal maintenance expenses to operate. Although the first basic solar cell has been introduced in 1950s, only in 1960s the photovoltaic technology has been intensively used especially for space applications and starting from mid 1970s the silicon solar technology became attractive for terrestrial use. However, in order to satisfy the continuously increasing demand of energy at constantly growing costs and to be competitive with other energy sources, the photovoltaic technology have to win the challenge of the reduction of costs ensuring at the same time adequate conversion efficiencies. In fact, for decades, many approaches and device architectures aimed at obtaining theoretical enhancements of the conversion efficiency of the solar cells, like those that will be reviewed in the present work, have not being considered as competitive due to the still higher manufacturing costs.

Although that of new materials is one of the most attractive topic of the research community in photovoltaic, silicon is still the most widely used semiconductor for mass production devices and, according to roadmaps, its adoption in solar cell manufacturing, will be competitive for next decades. Recently, an industry-driven reawakening of advanced silicon solar cell architectures has really motivated the interest of researchers in investigating design concepts of 1980s and 1990s with the objective of reducing significantly the cost for volume production. On the other hand, new designs and technologies have been investigated providing the basis for the future generation devices.

1. INTRODUCTION

One promising way to lower the cost of the photovoltaic device is to decrease the volume of material required to convert the light into electric energy.

Second generation of photovoltaic devices, like thin film devices using low-cost substrates and semiconductors, are just aimed at reducing the amount of material at the expense of a significant penalization in terms of performance with respect to the first generation of solar cells. For this class of devices, the material quality -which introduces relatively more electrical losses in comparison with standard silicon technology solar cells of the first generation featuring thick silicon substrates- and the typically limited capability to collect photons from the sun, are the main causes of performance limitation. In order to overcome this limitation by keeping the cost competitive, the most adopted approach is the enhancement of the light trapping or photon management strategy, which allows a more efficient absorption of energy from the external source. This opened the way to third-generation devices which are aimed at saving costs and at improving the conversion efficiency, reaching performance levels comparable or even better than those obtainable by first-generation solar cells. Modeling of photovoltaic devices has become more and more strategic and helpful not only to predict the performance of future generations devices but also to provide new and more specific guidelines to industry in order to reduce costs and time when designing new fabrication lines and new process setups. Prior to last decade, the most effective way to model photovoltaic devices relied mainly on analytical approaches partially supported by the aid of calculators. As the performance of calculators and the availability of computational resources became adequate to provide the support to cpu-intensive numerical simulations, researchers have begun to adopt the numerical device simulator as the most effective tools to perform modeling of semiconductor devices and of solar cells. First numerical simulations were aimed at modeling mono-dimensional (1-D) devices. Many simulators have been specifically introduced to the 1-D numerical simulation of photovoltaic devices and, among them, at least one became a reference in the photovoltaic community; probably the most popular of such tools is PC1-D (5) developed in late 1990s at the University of North South Wales (USNW), Australia. PC1-D has been widely adopted by researchers and designers to predict the efficiency of standard and even advanced solar cells. The main advantage of such easy-to-use tool is the low requirement of computational resources and the quite intuitive user interface. However, an accurate analysis of losses and the prediction of performance of advanced solar cells are often

not possible because of the mono-dimensionality of the simulation domain which can be handled by PC1-D, while non standard device architectures are mostly characterized by two-dimensional (2-D) or even three-dimensional (3-D) geometries. On the other hand, during the last decade, multi-dimensional and general-purpose numerical device simulators (Technology Computer-Aided Design TCAD) have been introduced mostly for the analysis of CMOS devices. However, such simulators are not often easy-to-use; due to this reason, the photovoltaic community has not really accepted their introduction as aid for design and investigation of solar cells.

The simulation of a device under illumination requires the knowledge of the spatial distribution of the amount of photo-generated carriers per time and volume unit within the absorber material. The optical generation rate is coupled to the transport and continuity equations which are part of the semiconductor devices modeling framework. The calculation of the optical generation map can be performed by means of methods based on the geometrical optics constraint like ray tracers, which are widely used also in other fields involving electromagnetic propagation, like the design and the simulation of optical systems including mirrors and lenses. However, the validity of the methods based on the geometrical optics approximation is limited to spatial domains in which the wavelength of the radiation is much larger than the size of the features of the geometry of the structure. This is just the case of first-generation silicon solar cells for which the substrate thickness and the features of the morphology of the surfaces (like the textured front surface) are not comparable to the wavelength of the radiation. In case of thin film devices or nanotextured solar cells like those based on nano-wires (6), nano-clusters (7), nano-rods (8) and diffraction gratings (9), the methods based on the geometrical optics approximation are no longer valid. In thin film solar cells the modeling of the light scattering from rough interfaces (for which the size of the features is comparable to the wavelength) has been treated in literature on the basis of methods derived from the well-known scalar scattering theory, originally developed by Spizzichino and Beckmann in 1960s (10). However, also such methods are limited in the dimensionality of the problem (1-D) and in accuracy, since they are not rigorous solvers of the Maxwell equations. Although these methods have been calibrated in order to be in agreement with experimental data by means of semi-empirical determined coefficients, the scattering from rough interfaces is an open issue unless the optical

simulation is not carried out by rigorous solvers of the Maxwell equations. Among these solvers, the most widespread is the Finite Difference Time Domain (FDTD) for simulation domains of any geometrical dimension. However, the FDTD, especially for 2-D and 3-D problems, is really cpu and memory-intensive. The requirement in terms of processing resources is particularly critical for problems in which the size of the simulation domain is significantly larger than the wavelength of the radiation. Recently, in optical simulation of solar cells, the Fourier Modal Method also known as Rigorous Coupled-Wave Analysis (RCWA), has gained relevance. RCWA may be used for the simulation of a wide range of structures and devices, including image sensors, light emitter diodes (LED) and solar cells.

The objective of this thesis is to provide a contribution to the numerical simulation and modeling of advanced silicon solar cells -including third-generation devices- by exploiting a state-of-the-art TCAD simulator featuring the capability to handle 2-D and 3-D geometries. The thesis describes the work carried out during the three-year period in which a simulation procedure -including the optical part- has been defined. In particular, the focus of the first part of the work is on the device simulation setup. The physical models of interest for the device simulation (like that for the band-gap narrowing occurring when high doping concentration is assumed and that for the carrier lifetime) have been tuned ad-hoc in order to fit data from experiments and from literature. The simulation framework has been successfully applied to the simulation of advanced crystalline silicon cells, like the selective emitter and the rear point contact one, for which the multi-dimensionality of the transport model is required in order to properly account for all physical competing mechanisms occurring in such solar cells. In order to complete the simulation flow, in the second part of the thesis, the optical problem is discussed, as contribution to reach the main objective of the research activity. Two novel and computationally efficient implementations of an electromagnetic simulator for 2-D simulation domains based on Fourier modal expansion of the electromagnetic field have been presented, as result of an intensive collaboration with the Institute of Physics and Technology (FTIAN) of the Russian Academy of Sciences (RAS), Moscow. A third method -still based on Fourier modal approach- has been implemented with the purpose of modeling the light propagation in 3-D structures. The

proposed implementations have been validated in terms of accuracy, numerical convergence, computation time and correctness of results, by means of a comparison with literature data and with those provided by a commercial Finite Difference simulator in case of similar structures. Promising results in terms of computational efficiency have been obtained. The first application of 3-D optical simulation have been presented as basis of future research activities which will involve nanostructured photovoltaic devices.

In the following, the detail of the content of each chapter of the thesis is summarized. After a review of the basic semiconductor transport model in chapter 2, the basis of the simulation of 2-D and 3-D silicon-based solar cells is introduced in chapter 3. In particular the approach adopted to calibrate the physical models of a well-known general purpose device simulator (Sentaurus Device by Synopsys) is shown. The simulation flow and the main standard methods commonly adopted to solve the optical problem in solar cell modeling are described.

Chapter 4 describes two examples of numerical simulation of advanced silicon solar cells: the selective emitter which requires the solution of the transport equations in a 2-D simulation domain and the rear point contact solar cells, which requires true 3-D simulations. The selective emitter and the rear point contact approaches are not mutually exclusive, on the contrary these two designs -which involve different portions of the solar cell- can be adopted simultaneously, enhancing the conversion efficiency towards the record efficiency that has been reached in 1990s by small-area solar cells fabricated in laboratory. The modeling activity of advanced silicon solar cells has been performed in the frame of the collaboration between University of Bologna and Applied Materials, Inc. US, since 2008.

Chapter 5 presents a review of the state-of-the-art Fourier-based algorithms for optical simulation, which are rigorous solvers of the Maxwell equations and lead to an acceptable trade-off between accuracy and computational resources requirement. In addition, chapter 5 describes the details of two novel implementations of RCWA aimed at solving the Maxwell equations in 2-D spatial domains that are not based on the solution of an eigenvalue problem. These methods feature better performance in terms

of cpu simulation time with respect to standard implementations. They have been validated by means of a comparison with a FDTD commercial tool. For 3-D spatial domains an implementation of RCWA based on standard approaches -but more general in terms of validity- has been described. Some applications of the RCWA methods, like the investigations of the impact of different surface morphologies of thin-film devices as well as of the main geometrical parameters of nano-rod based solar cells on the photon absorbance are presented.

Finally chapter 6 outlines the basics of the device physics of thin film amorphous silicon solar cells. Moreover, an application of a 2-D numerical simulation of a single-junction device exhibiting nanorough interfaces, for which the RCWA tool has been successfully adopted to perform the optical simulation, is presented.

2

Solar cell device physics and technology review

In this chapter a review of the semiconductor modeling theory is presented. The main loss mechanisms as well as the absorption process in semiconductor materials are described emphasizing the impact of such phenomena on the conversion of energy from the sun. The main figures of merit of a solar cell are introduced highlighting the theoretical upper bound limit of the conversion efficiency under some simple assumptions. Finally, the main technological options adopted in the design of silicon solar cells, including the most used techniques aimed at enhancing the photons absorption, are presented.

2.1 Absorption of light in semiconductors

If a monochromatic electromagnetic wave characterized by a given intensity and by a wavelength impinges on an interface between a dielectric and an absorber material (Fig. 2.1), part of the incident power is reflected by the interface and the remainder is transmitted into the absorber material. The light passing through the absorber material is attenuated. The entity of the attenuation of the light propagating through an absorbing material depends on the wavelength λ of the radiation and on the material absorption characteristics. It can be demonstrated that, for a simple homogeneous infinite layer of absorber material, the attenuation of the light intensity follows an

exponential decay according to Beer-Lambert Law:

$$I(x,\lambda) = I_0(0,\lambda)e^{-\alpha(\lambda)(x-x_0)} \tag{2.1}$$

where I_0 is the intensity of the light at the interface ($x = x_0$) and α is the absorption coefficient which is related to the extinction coefficient k of the material according to:

$$\alpha(\lambda) = \frac{4\pi k}{\lambda} \tag{2.2}$$

Figure 2.1: Interface between a dielectric and an absorber material ($z \geq z_0$). The light is propagating from left to right along z-axis.

The extinction coefficient k is the imaginary part of the complex refractive index $\tilde{n}$ of the material. An attenuation of the intensity of the light after passing through a distance equal to α^{-1} corresponding to e^{-1} occurs when an electromagnetic wave propagates along the z-direction (electromagnetic propagation basics are described in chapter 3). If n denotes the real part of the refractive index, n and k can be expressed as function of the real and the imaginary part of the permittivity (ε_1 and ε_2 respectively):

$$n = \sqrt{\frac{\sqrt{\varepsilon_1^2 + \varepsilon_2^2} + \varepsilon_1}{2}} \tag{2.3}$$

$$k = \sqrt{\frac{\sqrt{\varepsilon_1^2 + \varepsilon_2^2} - \varepsilon_1}{2}} \tag{2.4}$$

The dependence of the absorption coefficient α of the crystalline silicon at T=300K on the photon energy is shown in Fig. 2.2.

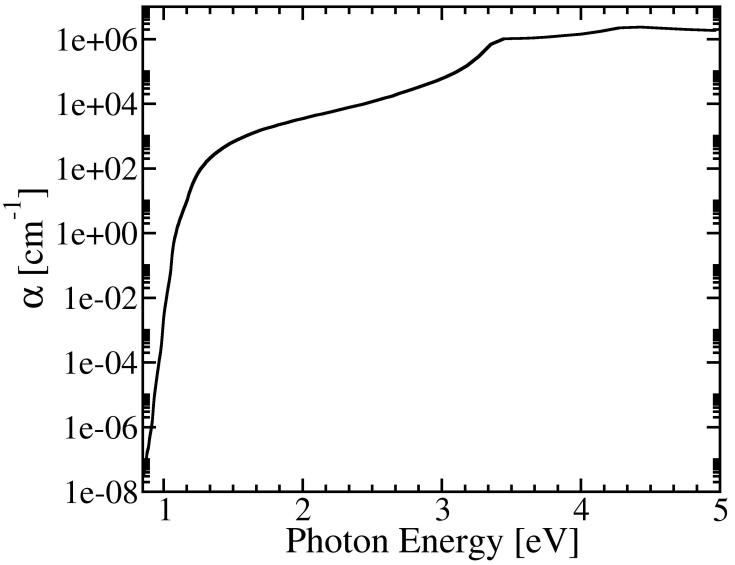

Figure 2.2: Dependence of the absorption coefficient α of crystalline silicon on the photon energy at $T = 300K$.

When a photon is absorbed, an electron of the valence band is excited and leaves a hole by means of a transition to the conduction band. In direct band-gap semiconductors, the crystal momentum is conserved when a transitions to the conduction band occurs because the photon has a smaller momentum compared to that of the crystal. However, the transition is characterized by the following energy balance:

$$E_f - E_i = hf \tag{2.5}$$

in which the difference between the energy that is associated to the final and to the initial states before the transition (E_f and E_i, respectively) must be equal to the photon energy $E_{ph} = hf$, where h is the Planck constant and f is the photon frequency. An approximated theoretical model for the absorption relates the absorption coefficient for direct band-gap material to the photon energy according to:

$$A(hf) \propto \sqrt{E_{ph} - E_g} \tag{2.6}$$

where E_g is the energy band-gap of the semiconductor. A first consequence of this simple model is that, if E_{ph} is much larger than E_g, the probability of photon

absorption is significantly higher in the first few wavelengths distance passing through the semiconductor.

In indirect bad-gap semiconductors like silicon, a photon energy much larger than the forbidden bad-gap is required in order to allow a direct transition of electrons from the valence band to the conduction band. The crystal momentum is not conserved during a transition. The absorption process in an indirect band-gap semiconductor involves a third particle, the phonon, which is characterized by low energy and high momentum. Therefore the probability of light absorption in these semiconductors is significantly lower than that of direct band-gap materials. In order to allow a transition of an electron, the following energy balance must be satisfied:

$$hf = E_g - E_p \tag{2.7}$$

where E_p is the energy of the phonon with a given momentum.

Other absorption processes are possible, like that occurring when the photon energy is so high to allow the excitation across the forbidden bad-gap or the two-step absorption in direct band-gap semiconductors, which involves the emission or the absorption of phonons.

In order to simulate an optoelectronic device such as a solar cell, the calculation of the optical generation rate which gives the amount of photo-generated electron-hole pairs per volume and time unit G_{OPT} inside the absorber material is required. The Beer-Lambert law (eq. 2.1) is valid only for monodimensional structures having linear dimension significantly larger than the absorption length at a given wavelength. When such assumption is not satisfied, effects due to coherent propagation of the light (like interfence) occur and the Beer-Lambert law is not valid. In Fig. 2.3 the optical generation rate per time and volume unit calculated at $\lambda = 500nm$ is reported in case of a silicon slab of infinite thickness. In such case the eq. 2.1 is an acceptable approximation. However, if a thinner slab of silicon is considered (e.g. $100nm$ like that of Fig. 2.4), due to the multiple internal reflections of the light occurring at the front and at back interfaces of the slab, maxima and minima of the light intensity and hence of the optical generation rate can be observed and the eq. 2.1 is not suitable.

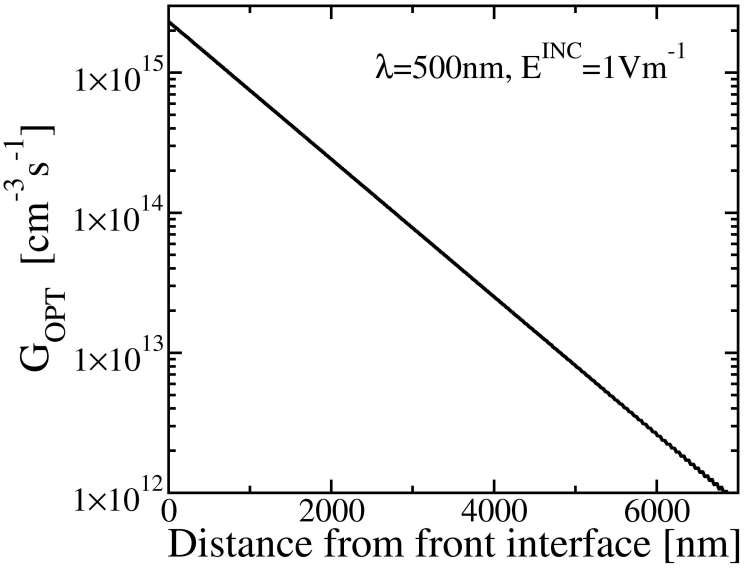

Figure 2.3: Optical generation rate G_{OPT} calculated at λ=500nm as function of the distance from the front interface in case of a silicon slab featuring infinite thickness. The amplitude E_0 of the incident field is $1Vm^{-1}$.

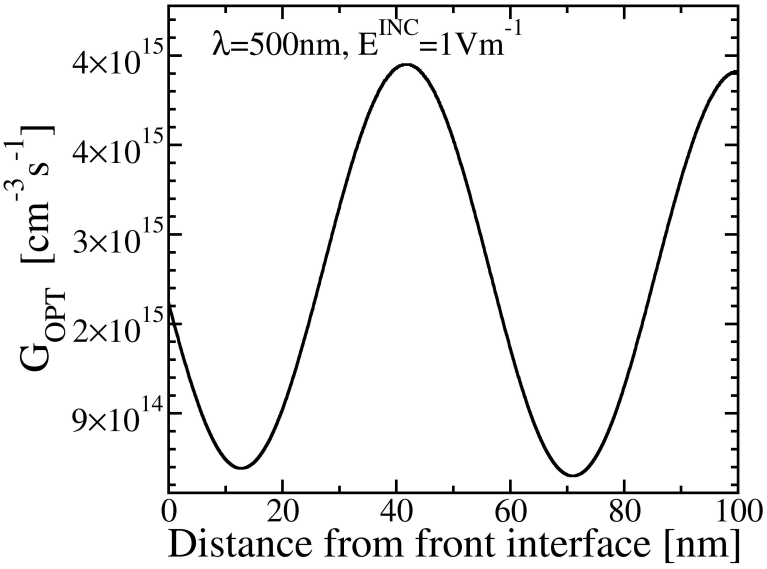

Figure 2.4: Optical generation rate G_{OPT} calculated at λ=500nm as function of the distance from the front interface in case of a silicon slab featuring thickness comparable to the wavelength of the radiation. Minima and maxima of G_{OPT} can be observed. The amplitude E_0 of the incident field is $1Vm^{-1}$.

2.2 Recombination mechanisms

While under illumination conditions the carrier concentration is in excess with respect to their value in equilibrium, in dark the concentration is reduced down to the equilibrium value through the recombination mechanisms which annihilate the electron-hole pairs. In the following, the most common recombination mechanisms -which contribute to the electrical losses in a solar cells- are outlined.

2.2.1 Radiative recombination

The radiative recombination occurs under thermal equilibrium involving a transition from the conduction band down to the valence band; this process leads to the emission of a photon having energy equal to the difference between the energy level before the transition and that after the process. The radiative recombination rate per unit time and volume can be expressed as:

$$R_{rad} = Bnp \tag{2.8}$$

where B is a semiconductor property, n and p are the concentrations of electrons and holes, respectively. The radiative recombination is negligible in indirect band-gap semiconductors since it involves, as the light absorption mechanism, a two-step process with a phonon. Under thermal equilibrium, for which $np = {n_i}^2$, where n_i is the intrinsic carrier density concentration, when the device is in dark conditions and in the absence of an external stimulus, the radiative recombination is balanced by a generation process, therefore the net recombination rate is given by:

$$U_{rad}^{NET} = B(np - n_i^2) \tag{2.9}$$

2.2.2 Auger recombination

The Auger recombination is the reverse process of the impact ionization. When an electron recombines with a hole, its energy is given to a second electron which leads to a phonon emission in order to acquire again its original energy level. The probability of Auger recombination is particularly significant in case of highly doped materials (in particular when doping concentration is above $10^{17} cm^{-3}$) because of the electron excitations in the majority carrier band. Auger recombination is one among the main

loss mechanisms which should be accounted for in designing highly doped regions (like emitters) of solar cells, as it will be shown in chapter 4.

The Auger recombination rate can be expressed as:

$$R_{Aug} = (C_n n - C_p p)(np - n_i^2) \tag{2.10}$$

where C_n and C_p are material-specific parameters.

2.2.3 Trap-assisted recombination

Impurities and defects in semiconductor materials lead to allowed energy levels within the forbidden energy bang-gap. The trap-assisted recombination mechanism occurs when an electron relaxes down to the defect level from the conduction band and then from the defect level to the valence band by exploiting a two-step process. In case of a single level trap (SLT), under the assumption of stationary trapped charge density into the recombination centers, the net recombination can be expressed, according to the Schokley-Read-Hall (SRH) recombination model, as:

$$U_{SRH}^{net} = \frac{(np - n_i^2)}{\tau_{h_{SLT,0}}(n + n_1) + \tau_{e_{SLT,0}}(p + p_1)} \tag{2.11}$$

where

$$n_1 = N_C \exp\left(\frac{E_{TRAP} - E_C}{kT}\right) \qquad p_1 = N_V \exp\left(\frac{E_V - E_{TRAP}}{kT}\right)$$

and E_{TRAP} is the energy level associated to the defect, $\tau_{e_{SLT,0}}$ and $\tau_{h_{SLT,0}}$ are the SRH carrier lifetimes for electrons and holes, respectively. N_C and N_V are the effective density of states in conduction band and in the valence band, respectively. The edges of the conduction and valence bands are denoted by E_C and E_V, respectively. It is worth noting that the peak value of U_{SRH}^{net} occurs when E_{TRAP} is exactly in the mid of the forbidden energy gap, for which the probability of transition is maximum. The single level trap approximation is suitable for crystalline silicon but not for materials like amorphous silicon, for which, an extension of the SRH model accounting for a continuous energy level distribution of defects in energy is typically adopted.

Similarly, it is possible to define a model to take into account the recombination occurring at surfaces where defects act like recombination centers, for which the net recombination rate can be expressed by:

$$U^{net}_{SRH,SURF} = \frac{S_{e_0} S_{h_0} (np - n_i^2)}{S_{e_0} (n + n_1) + S_{h_0} (p + p_1)} \tag{2.12}$$

where S_{e_0}, S_{h_0} are the surface recombination velocities (measured in cm/s). In this case $U^{net}_{SRH,SURF}$ is a net recombination rate for unit time and area.

2.2.4 Effettive carrier lifetime

Independently on the specific recombination mechanism, under the assumption of operating conditions close to equilibrium, for a n-type semiconductor, by using the Taylor approximation, it is possible to reformulate the net recombination function as:

$$U_{net}(n,p) \approxeq U(p_{n_0}, n_{n_0}) + \left(\frac{\partial U}{\partial p}\right)_0 (p - p_{n_0}) + \left(\frac{\partial U}{\partial n}\right)_0 (n - n_{n_0}), \tag{2.13}$$

where p_{n_0} and n_{n_0} denote the equilibrium hole and electron concentrations, respectively. In eq. 2.13 the derivatives are calculated at $p = p_{n_0}, n = n_{n_0}$. Carrier lifetimes are then introduced and defined as:

$$\tau_e = \frac{1}{\left(\frac{\partial U}{\partial n}\right)_0}, \qquad \tau_h = \frac{1}{\left(\frac{\partial U}{\partial p}\right)_0}. \tag{2.14}$$

The terms $p - p_{n_0}$ and $n - n_{n_0}$ represent the excess of carrier concentrations with respect to their equilibrium concentrations. The eq. 2.13 reads:

$$U_{net}(n,p) = \frac{p - p_{n_0}}{\tau_p} + \frac{n - n_{n_0}}{\tau_n}. \tag{2.15}$$

Therefore, an expression of lifetimes for each recombination mechanism can be derived:

$$\tau_{AUG} = \frac{1}{C_n n^2_{n_0}} \tag{2.16}$$

$$\tau_{RAD} = \frac{1}{B n_{n_0}} \tag{2.17}$$

The single-trap level SRH carrier lifetimes of eq. 2.11 can be written as:

$$\tau_{p_{SRH,BULK}} = \frac{1}{\sigma_p v_{TH} N_T} \tag{2.18}$$

where N_T is the concentration of traps, v_{TH} the thermal velocity of carriers and σ_p the capture cross section (which is proportional to the carrier capture probability) of the recombination center. Similary for a p-type doped semiconductor.

The effective lifetime can be defined as:

$$\frac{1}{\tau_{eff}} = \frac{1}{\tau_{SRH,BULK}} + \frac{1}{\tau_{RAD}} + \frac{1}{\tau_{AUG}}. \tag{2.19}$$

2.3 Semiconductor Model Equations

2.3.1 Drift-Diffusion Transport Model

Due to diffusion mechanism, in the absence of any external forces, electrons and holes in semiconductors move from regions of high concentration to regions of low concentration leading to a flux of particles in the direction normal to the surfaces with same concentration. If ϕ_p and ϕ_n denote the flux density of holes and electrons, respectively, the diffusion current densities are given by

$$\begin{cases} \mathbf{J}_p = -qD_p \nabla p \\ \mathbf{J}_n = qD_n \nabla n \end{cases} \tag{2.20}$$

where $n = n(\mathbf{r})$, $p = p(\mathbf{r})$ are the position-dependent electron and holes concentrations and D_p, D_n are the hole and electron diffusion coefficients, respectively.

By applying an electric field $\mathbf{E}$ across a uniformly doped semiconductor, an upward bending of energy bands occurs. As consequence of such electric field, electrons in the conduction band, being negative charges, move in the opposite direction of the applied field. On the contrary, the holes in the valence band. Carriers are therefore accelerated by the electric field. At macroscopic level, carriers appear to move at a constant velocity, the drift velocity v_d, which is directly proportional to the electric field. The drift current densities for holes and electrons can be written as

$$\begin{cases} \mathbf{J}_p = q\mu_p p\mathbf{E}, \\ \mathbf{J}_n = q\mu_n n\mathbf{E}. \end{cases} \tag{2.21}$$

where μ_n and μ_p are the electron mobility and the hole mobility, respectively. In thermal equilibrium the drift and diffusion currents must exactly balance. In nondegenerate materials, the Einstein relations link the diffusion coefficients to the carrier mobilities:

$$D_p = \mu_p \frac{kT}{q}, \qquad D_n = \mu_n \frac{kT}{q}. \tag{2.22}$$

The total current densities, for each carrier, are the superposition of the drift and diffusion contributions:

$$\begin{cases} \mathbf{J}_p = q\mu_p p\mathbf{E} - qD_p \nabla p, \\ \mathbf{J}_n = q\mu_n n\mathbf{E} + qD_n \nabla n. \end{cases} \tag{2.23}$$

The total current is then

$$\mathbf{J} = \mathbf{J}_p + \mathbf{J}_n + \mathbf{J}_D \tag{2.24}$$

where the displacement current density is

$$\mathbf{J}_D = \varepsilon \frac{\partial \mathbf{E}}{\partial t} \tag{2.25}$$

ε denotes the electric permittivity of the semiconductor. The displacement current is typically neglected in solar cells modeling since, in such case, the main figures of merit are static parameters.

2.3.2 Semiconductor equations

Transport equations link the current densities to the carrier concentrations. Since the unknowns of the problem are $n = n(\mathbf{r}, t)$, $p = p(\mathbf{r}, t)$ and $\mathbf{E} = \mathbf{E}(\mathbf{r})$, more equations are required to define the device modeling framework. Two equations, among those required, are the hole and the electron continuity equations ((11)):

$$\begin{cases} \frac{1}{q}\nabla \cdot \mathbf{J}_p = G_{OPT} - R_p - \frac{\partial p}{\partial t}, \\ \frac{1}{q}\nabla \cdot \mathbf{J}_n = R_n - G_{OPT} + \frac{\partial n}{\partial t}. \end{cases} \tag{2.26}$$

where G_{OPT} is the optical generation rate of electron-hole pairs and R_p and R_n include also the thermal generation.

Under quasi-stationary conditions the electrostatic potential $\phi(\mathbf{r}, t)$ is related to the spatial charge density $\rho(\mathbf{r})$ by the Poisson's equation:

$$\nabla^2\phi(\mathbf{r}, t) = -\frac{\rho(\mathbf{r}, t)}{\epsilon} \tag{2.27}$$

and if $N = N_D - N_A$ denotes the total doping concentration (donor and acceptor),

$$\rho = (N_D - N_A + p - n) = (N + p - n). \tag{2.28}$$

Under steady state conditions, in case of a mono-dimensional (1-D) device,

$$\frac{\partial E}{\partial x} = \frac{q}{\epsilon}(p - n + N) \tag{2.29}$$

In case of uniform spatial doping concentration, the mobility and the diffusion coefficients are constant, therefore:

$$\begin{cases} q\mu_p \frac{d}{dx}(p\mathbf{E}) - qD_p \frac{d^2p}{dx^2} = q(G - R), \\ q\mu_n \frac{d}{dx}(n\mathbf{E}) + qD_n \frac{d^2n}{dx^2} = q(R - G). \end{cases} \tag{2.30}$$

2.3.3 1-D single-junction silicon solar cell model

In this subsection, following the approach described in (12), the current-voltage characteristic at electrodes of a 1-D single junction silicon solar cell (Fig. 2.5A) is derived by adopting the semiconductor equations discussed in the previous subsection.

A simple solar cell is formed by a n^+-p junction in which the heavy doped n-type diffusion is the emitter ($-T_N < x < 0$) and the p-type substrate is the base ($0 < x < T_P$) of the solar cell. In thermal equilibrium no net current flows and the Fermi energy does not depend on the position. Due to the gradient of concentration between the two types of semiconductors, holes diffuse from the p-type region into the n-type region. Similarly, electrons from the n-type material diffuse into the p-type region. An electric field is therefore produced limiting the diffusion of carriers. The space-charge region (in Fig. 2.5B for $-X_{D_N} < x < X_{D_P}$) is depleted of both holes and electrons. Under the assumption that the p-type and the n-type regions are thick enough, the regions on either sides of the depletion region (that for $x < -X_{D_N}$ and that for $x > X_{D_P}$) are quasi-neutral. The electrostatic potential difference across the junction is the built-in voltage V_0. The electrostatics of the single-junction system is defined by the Poissons

equation, that, within the depletion region, under the assumption that $p_0, n_0 << |N|$ (where p_0 and n_0 are the equilibrium concentration of holes and electrons, respectively) can be written as:

$$\begin{cases} \frac{d^2\phi}{dx^2} = \frac{q}{\varepsilon}N_A & \text{if} \quad -X_{D_N} < x < 0, \\ \frac{d^2\phi}{dx^2} = -\frac{q}{\varepsilon}N_D & \text{if} \quad 0 < x < X_{D_P}. \end{cases} \tag{2.31}$$

while in the quasi-neutral regions charge neutrality is assumed (depletion approximation):

$$\frac{d^2\phi}{dx^2} = 0. \tag{2.32}$$

As a direct consequence of the definition of V_0,

$$\int_{-X_{D_N}}^{X_{D_P}} E dx = -\int_{-X_{D_N}}^{X_{D_P}} \frac{d\phi}{dx} dx = \phi(-X_{D_N}) - \phi(X_{D_P}) = V_0. \tag{2.33}$$

If conventionally $\phi(X_{D_P}) = 0$, the solution of the previous equations reads:

$$\begin{cases} V_0 & \text{if} \quad x \leq -X_{D_N}, \\ V_0 - \frac{qN_D}{2\epsilon}(x + X_{D_N})^2 & \text{if} \quad -X_{D_N} < x \leq 0, \\ \frac{qN_A}{2\epsilon}(x - X_{D_P})^2 & \text{if} \quad 0 \leq x < X_{D_P}, \\ 0 & \text{if} \quad x \geq X_{D_P}. \end{cases} \tag{2.34}$$

Due to the continuity of the electrostatic potential ϕ and of the electric field at $x = 0$,

$$V_0 - \frac{qN_D}{2\epsilon}x_{D_N}^2 = \frac{qN_A}{2\epsilon}X_{D_P}^2, \qquad x_{D_N}N_D = x_{D_P}N_A. \tag{2.35}$$

Solving the previous equations under equilibrium conditions, the depletion region width can be derived as:

$$W_{DEP} = x_{D_N} + x_{D_P} = \sqrt{\frac{2\epsilon}{q}\left(\frac{N_D + N_A}{N_D N_A}\right)V_0}. \tag{2.36}$$

If an external bias voltage V_A is applied, the previous equation reads:

$$W_{DEP} = x_{D_N} + x_{D_P} = \sqrt{\frac{2\epsilon}{q}\left(\frac{N_D + N_A}{N_D N_A}\right)(V_0 - V_A)}. \tag{2.37}$$

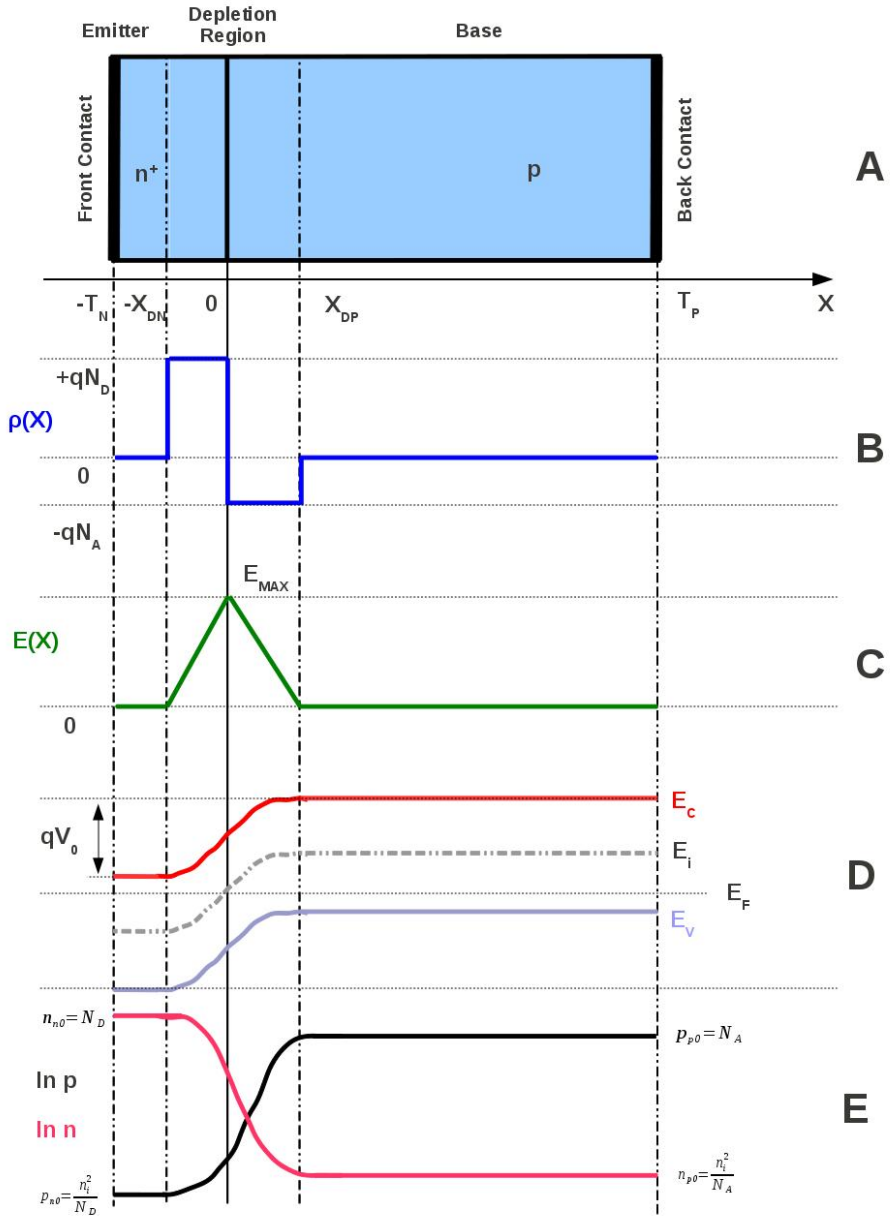

Figure 2.5: (A) Mono-dimensional (1-D) sketch of an abrupt p-n junction with the associated charge density $\rho(x)$ profile along the x-axis (B). The pint $x = 0$ denotes the metallurgical junction interface. $-X_{D_N}$ and X_{D_P} are the boundaries of the depletion region at the n-type and p-type sides, respectively. N_A and N_D denote the uniform doping concentrations of the p-type and n-type regions, respectively. The electric field plot, the energy bands diagram and the carrier concentration plots are shown in (C), (D) and (E), respectively. In (D) V_0 denotes the built-in potential.

Since under thermal equilibrium the net current density of holes and electrons is zero, the expression of the built-in potential can be easily derived:

$$V_0 = \int_{-x_{D_N}}^{x_{D_P}} E dx = \int_{-x_{D_N}}^{x_{D_P}} \frac{kT}{q} \frac{1}{p_0} \frac{dp_0}{dx} dx = \frac{kT}{q} ln \left(\frac{N_D N_A}{n_i^2} \right). \tag{2.38}$$

The charge density, the electric field and the energy bands for the *p*-*n* junction are shown in Fig. 2.5B, Fig. 2.5C and Fig. 2.5D, respectively, while the plots of the carrier concentrations are shown in Fig. 2.5E. It is worth noting that the maximum electric field intensity E_{MAX} is reached at $x = 0$, therefore

$$E_{MAX} = |E(x=0)| = |\frac{d\phi}{dx}|_{x=0} = \sqrt{\frac{2q}{\epsilon}(V_0 - V_A)\left(\frac{1}{N_D} + \frac{1}{N_A} \right)^{-1}}. \tag{2.39}$$

In order to solve the equations of the single-junction solar cell, proper boundary conditions have to be set at the emitter and at the base contacts; if the emitter contact is assumed to be an ideal ohmic contact:

$$\Delta p(-T_N) = 0. \tag{2.40}$$

Modeling the emitter contact with an effective (finite) surface recombination velocity S_F makes the boundary condition more realistic:

$$\frac{d\Delta p}{dx}|_{x=-T_N} = \frac{S_F}{D_p} \Delta p(-T_N). \tag{2.41}$$

It is worth noting that, if $S_F \to \infty$ the previous boundary conditions is reduced to eq. 2.40.

Similarly for the back contact:

$$\frac{d\Delta n}{dx}|_{x=T_P} = \frac{S_B}{D_n} \Delta n(T_P). \tag{2.42}$$

By assuming the semiconductor nondegenerate, under nonequilibrium and low-level injection conditions, it is possible to assume the quasi-Fermi energies constant within the depletion region:

$$qV_A = F_N(x) - F_P(x), \qquad -x_{D_N} \leq x \leq x_{D_P}. \tag{2.43}$$

The boundary conditions at the edges of the depletion region are known as the law of the junction (12):

$$p_N(-x_{D_N}) = \frac{n_i^2}{N_D} e^{\frac{qV_A}{kT}}, \qquad n_P(x_{D_P}) = \frac{n_i^2}{N_A} e^{\frac{qV_A}{kT}}. \tag{2.44}$$

If the solar cell is illuminated, it is possible to express the optical generation rate inside the device by using the Beer-Lambert law (eq. 2.1):

$$G(X) = \int_\lambda \alpha(\lambda) e^{-\lambda(x+T_N)} d\lambda. \tag{2.45}$$

The minority carrier diffusion equations (eq. 2.20) are solved in the quasi-neutral regions; for the p-type side, in case of a monochromatic wave:

$$D_n \frac{d^2 \Delta n_P}{dx^2} - \frac{\Delta n_P}{\tau_n} = -G_\lambda(x), \qquad X_{D_P} \leq x \leq T_P. \tag{2.46}$$

where

$$G_\lambda(x) = I_0 \alpha e^{-\lambda(x+T_N)}. \tag{2.47}$$

and

$$\Delta n_P = n_P - n_{p_0}. \tag{2.48}$$

The eq. 2.46 is a second order differential non-homogeneous equation; its solution is:

$$\Delta p_N(x) = C_{1,P} \quad \sinh\left[\frac{x - X_{D_P}}{L_n}\right] + C_{2,P} \quad \cosh\left[\frac{x - X_{D_P}}{L_n}\right] + G_{\lambda,P}(x). \tag{2.49}$$

where

$$G_{\lambda,P}(x) = \frac{\tau_n}{L_n^2 \alpha(\lambda)^2 - 1} \alpha(\lambda) e^{-\lambda(x+T_N)}. \tag{2.50}$$

and L_n is the diffusion length of electrons defined as $L_n = \sqrt{D_n \tau_n}$. Similarly for n-type side:

$$\Delta p_P(x) = C_{1,N} \sinh\left[\frac{x + X_{D_N}}{L_p}\right] + C_{2,N} \cosh\left[\frac{x + X_{D_N}}{L_p}\right] + G_{\lambda,N}(x). \tag{2.51}$$

where

$$G_{\lambda,N}(x) = \frac{\tau_p}{L_p^2\alpha(\lambda)^2 - 1}\alpha(\lambda)e^{-\lambda(x+T_N)}. \tag{2.52}$$

and L_p is the diffusion length of holes defined as $L_p = \sqrt{D_p\tau_p}$.

The arbitrary constants $C_{j,N}$, $C_{j,P}$ (with $j = 1, 2$) are determined by using the boundary conditions expressed by eq. 2.41, eq. 2.42 and eq. 2.44.

The minority carrier current densities in the quasi-neutral regions are those associated to the diffusion components:

$$\begin{cases} J_{p,N}(x) = -qD_p\frac{d\Delta p_N}{dx}, \\ J_{n,P}(x) = qD_n\frac{d\Delta n_P}{dx}. \end{cases} \tag{2.53}$$

The total current is $J(x) = J_p(x) + J_n(x)$, but the equations 2.53 give the current density in different positions. By integrating the electron continuity equation over the depletion region, it is immediate to link the electron current at the edges of the depletion region:

$$J_n(-X_{D_N}) = J_n(X_{D_P}) + q\int_{-X_{D_N}}^{X_{D_P}} G(X)dx - q\int_{-X_{D_N}}^{X_{D_P}} R_{DEP}dx. \tag{2.54}$$

where

$$R_{DEP} = \frac{n_i\left(e^{\frac{qV_A}{2kT}} - 1\right)}{\tau_{DEP}}. \tag{2.55}$$

is the trap-assisted SLT SRH recombination rate within the depletion region; such recombination rate is assumed constant (12) and calculated at the point $x = x_C$ for which $p(x_C) = n(x_C)$ (Fig. 2.5E). The related (constant) carrier lifetime is τ_{DEP}. Therefore, expanding the previous equation,

$$J_n(-X_{D_N}) = J_n(X_{D_P}) + q\left[e^{-\lambda(T_N - X_{D_N})} - e^{-\lambda(T_N + X_{D_P})}\right] - q\frac{W_{DEP}n_i}{\tau_{DEP}}\left(e^{\frac{qV_A}{2kT}} - 1\right). \tag{2.56}$$

In order to calculate the current density at contacts, the solution to the minority carrier diffusion equations 2.53 is used.

2.3.4 Output characteristic and figures of merit

A common expression for the current voltage characteristic of a single junction solar cell is:

$$J = J_{SC} - J_{0A}\left(e^{\frac{qV_A}{kT}} - 1\right) - J_{0B}\left(e^{\frac{qV_A}{kT}} - 1\right). \tag{2.57}$$

where J_{SC} denotes the short circuit current density, which is the sum of the contributions from the n-type quasi neutral region, the depletion region and the p-type quasi neutral region:

$$J_{SC} = J_{SC_N} + J_{SC_{DEP}} + J_{SC_P}. \tag{2.58}$$

The detailed expressions of these contributions are reported in (12).

The terms J_{0A} and J_{0B} are the dark saturation current densities in the quasi-neutral regions and within the depletion region, respectively.

$$J_{0A} = J_{0A,P} + J_{0A,N}. \tag{2.59}$$

where

$$J_{0A,P} = q\frac{n_i^2}{N_D}\frac{D_p}{L_p}\left[\frac{\frac{D_p}{L_p}\sinh\left(\frac{T_N - X_{D_N}}{L_p}\right) + S_F\cosh\left(\frac{T_N - X_{D_N}}{L_p}\right)}{\frac{D_p}{L_p}\cosh\left(\frac{T_N - X_{D_N}}{L_p}\right) + S_F\sinh\left(\frac{T_N - X_{D_N}}{L_p}\right)}\right]. \tag{2.60}$$

Similarly for $J_{0A,N}$. In case of a long base diode ($L_n \ll T_P$) the expression of $J_{0A,N}$ can be simplified as:

$$J_{0A,N} = q\frac{n_i^2}{N_A}\frac{D_n}{L_n}. \tag{2.61}$$

It is worth noting that there is no influence of the boundary condition (in particular of the back surface recombination velocity S_B) at the back contact on $J_{0A,N}$ under long base approximation. On the contrary, when $L_n \gg T_P$ (short base):

$$J_{0A,N} = q\frac{n_i^2}{N_A}\frac{D_n}{T_P - X_{D_P}}\frac{S_B}{S_B + \frac{D_n}{T_p - X_{D_P}}}. \tag{2.62}$$

In addition, if $S_B \gg 1$ (i.e. no BSF), the following short-base approximation is obtained:

$$J_{0A,N} = q\frac{n_i^2}{N_A}\frac{D_n}{T_P - X_{D_P}}. \tag{2.63}$$

The saturation current density due to recombination in the depletion region is:

$$J_{0B} = q\frac{W_{DEP} n_i}{\tau_{DEP}} \tag{2.64}$$

In J_{0B} the dependence on the applied bias is through W_{DEP}, which is bias-dependent.

Eq. 2.57 suggests the two-diode circuit equivalent model of Fig. 2.6, in which the ideal current generator represents the light polarization and the two diodes in parallel the recombination current terms. It is worth noting that the ideality factor of the two diodes are different: for the recombination in the quasi-neutral regions it is equal to 1 while for the recombination in the depletion regions it is equal to 2. The latter contribution is commonly neglected especially at large bias voltage.

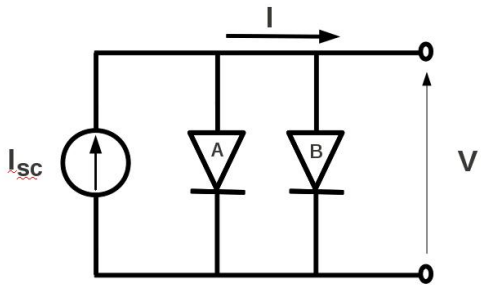

Figure 2.6: Two-diode circuit model of a solar cell. Diode (A) represents the current due to recombination within the quasi-neutral regions. Diode (B) models the recombination occurring in the depletion region according to eq. 2.64.

In Fig. 2.7 the current-voltage $I(V)$ and the output power $P_{OUT}(V)$ characteristics of the cell are shown, where $I = AJ$, $I_{SC} = AJ_{SC}$ and A is the area of the solar cell. In Fig. 2.7 V_{MPP} and I_{MPP} denote the maximum output power voltage and current, respectively. At $V = V_{MPP}, I = I_{MPP}$ the output power reaches the maximum value $P_{OUT}^{MAX} = V_{MPP}I_{MPP}$. The open circuit voltage V_{OC} at which $I(V_{OC}) = 0$ is:

$$V_{OC} \approx \frac{kT}{q}\ln\left(\frac{I_{SC}}{I_{0A}}\right), \qquad I_{SC} \gg I_{0A}, \tag{2.65}$$

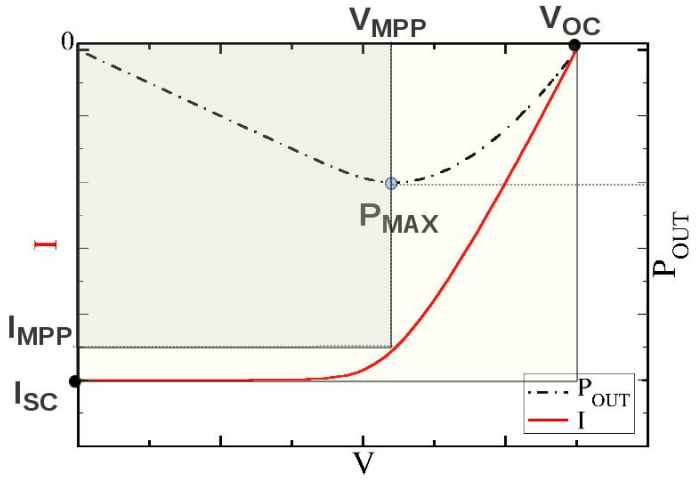

Figure 2.7: I-V characteristic (red solid curve) of a solar cell. The parameters V_{OC} and I_{SC} are the open-circuit voltage and the short-circuit current, respectively. The output power is represented by the black dashed curve, which reaches the maximum value at $V = V_{MPP}$ and $I = I_{MPP}$.

where $I_{0A} = AJ_{0A}$. The ratio of the maximum output power to the theoretical maximum output power is the Fill Factor:

$$FF = \frac{P_{OUT}^{MAX}}{V_{OC} I_{SC}} = \frac{V_{MPP} I_{MPP}}{V_{OC} J_{SC}}. \tag{2.66}$$

Ideally the Fill Factor (FF) is 100. For a silicon solar cell the FF typically ranges between 77.0 and 82.0.

The conversion efficiency η is the most important figure of merit and it is defined as the ratio of the maximum output power to the incident power:

$$EFF = \frac{P_{OUT}^{MAX}}{P_{IN}} = \frac{FF V_{OC} I_{SC}}{P_{IN}}. \tag{2.67}$$

2.3.5 Other figures of merit

Figures of merit like open circuit voltage, Fill Factor and short circuit current are not helpful to understand in detail which are the main loss mechanisms that contribute to

degradation of the efficiency. The short circuit current of a solar cell is limited by recombination mechanisms or by poor light trapping strategy effectiveness. In addition, recombination mechanisms may be dominant within a particular portion of the irradiance spectrum and the photon absorption may be limited by the reflectance properties of the external top interface rather than the absorption properties of the semiconductor. When an analysis of loss mechanisms is performed, some figures of merit are helpful to address the design of the solar cell.

2.3.6 Optical figures of merit: absorbance, reflectance and transmittance

Reflectance $R(\lambda)$ and transmittance $T(\lambda)$ are intuitively defined as

$$R(\lambda) = \frac{P_{REFL}}{P_{INC}}, \qquad T(\lambda) = \frac{P_{TRANS}}{P_{INC}} \tag{2.68}$$

where P_{INC} is the incident power and P_{REFL}, P_{TRANS} are the portion of the incident power which are reflected and transmitted by the solar cell, respectively. If an ideal back reflector is adopted (internal bottom reflectivity equal to 1.0) then $T(\lambda) = 0$. In order to satisfy the optical conservation law,

$$R(\lambda) + T(\lambda) + A(\lambda) = 1. \tag{2.69}$$

$A(\lambda)$ is the absorbance of the solar cell at a given wavelength λ.

2.3.7 Quantum efficiency and spectral response

The external quantum efficiency $EQE(\lambda)$ is defined as the ratio of the number of carriers which contribute to the current at electrodes under short-circuit conditions to the number of incident photons. If $\phi(\lambda)$ denotes the incident power flux (number of photons per time and area unit) and I_0 is the input irradiance (in W/m^2),

$$\phi(\lambda) = \frac{I_0(\lambda)}{E_{ph}(\lambda)} = \frac{I_0(\lambda)}{\frac{hc}{\lambda}}, \tag{2.70}$$

where $E_{ph}(\lambda)$ is the photon energy, h and c are the Planck Constant and the speed of light (in vacuum), respectively.

The number of incident photons N_{INC} per unit time is therefore given by ϕA where A is the area of the solar cell. Therefore,

$$EQE(\lambda) = \frac{J_{sc}(\lambda)}{qN_{INC}(\lambda)} = \frac{J_{sc}(\lambda)}{q\phi(\lambda)} = \frac{J_{sc}(\lambda)}{J_{IN}(\lambda)}. \tag{2.71}$$

The internal quantum efficiency $IQE(\lambda)$ is defined as the number of carriers which contribute to the output current in short-circuit conditions to the total number of photo-generated electron-hole pairs within the volume of the absorber material. Hence $IQE(\lambda)$ can be expressed as (13):

$$IQE(\lambda) = \frac{EQE(\lambda)}{1 - R(\lambda)}. \tag{2.72}$$

The collection efficiency η_C of the photo-generated carriers is defined as:

$$\eta_C(\lambda) = \frac{J_{sc}(\lambda)}{J_{ph}(\lambda)}. \tag{2.73}$$

η_C reports about the property of electrodes to collect the carriers once generated in the absorber material. Carriers recombination leads to reduction of η_C.

Finally, the spectral response $SR(\lambda)$ is defined as the ratio of the current generated by the solar cell to the incident power; if $QE(\lambda)$ denotes the quantum efficiency (either external or internal),

$$SR(\lambda) = \frac{qQE(\lambda)}{E_{ph}(\lambda)}. \tag{2.74}$$

2.4 Efficiency Limits

In this section the theoretical upper bound limits of the main figures of merit of a solar cell are estimated under some simply assumptions described in the following. Under ideal conditions, all photo-generated carriers are collected by electrodes contribute to the short-circuit current density, therefore, if $S(E)$ and $A(E)$ denote the spectral irradiance and the absorbance at a given photon energy E, respectively, the short-circuit current density may be calculated as:

$$J_{SC} = q \int_0^\infty S(E)A(E)dE. \tag{2.75}$$

Ideally all photons having energy higher than the band-gap E_g are absorbed by the semiconductor, hence:

$$J_{SC} = q \int_{E_g}^{\infty} S(E) dE. \tag{2.76}$$

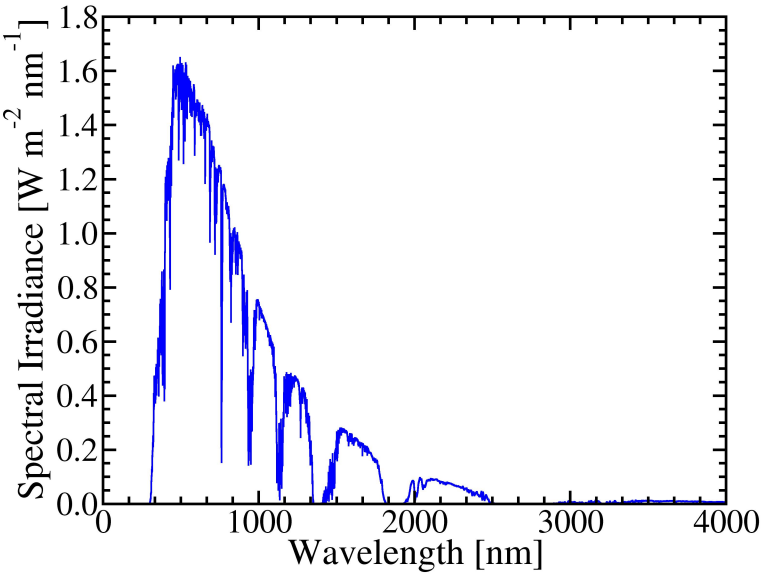

Figure 2.8: Conventional spectrum AM1.5G ($1000 W m^{-2}$) for direct sun illumination. The plot reports the spectral irradiance.

In Fig. 2.9 the dependence of the short-circuit current on the band-gap energy under the assumptions described above is reported. The curve is calculated by adopting direct illumination, neglecting the external reflectance of the top interface and assuming the conventional spectrum AM1.5G ($1000 W m^{-2}$) (14) (Fig. 2.8). It is worth noting that for c-Si ($E_g = 1.12 eV$) the upper bound limit of the J_{SC} is $43.8 mA cm^{-2}$ while for the hydrogenated amorphous silicon (a-Si:H, $E_g = 1.72 eV$) is $21.9 mA cm^{-2}$. Comparing the c-Si limit with the typical short-circuit current density exhibited by the record efficiency cells (laboratory samples), which is about $42 mA cm^{-2}$ (15), the conclusion is that for thick substrates, light-trapping strategies for silicon technology are enough effective to ensure an absorbance close to the maximum achievable. Concerning the a-Si:H, typical J_{SC} values are within the range 12-16$mA cm^{-2}$ (16) while the upper bound limit is above $20 mA cm^{-2}$. These discrepancies are due to light trapping scheme limitations, to the non-zero reflectance of the external front interface, to the finite

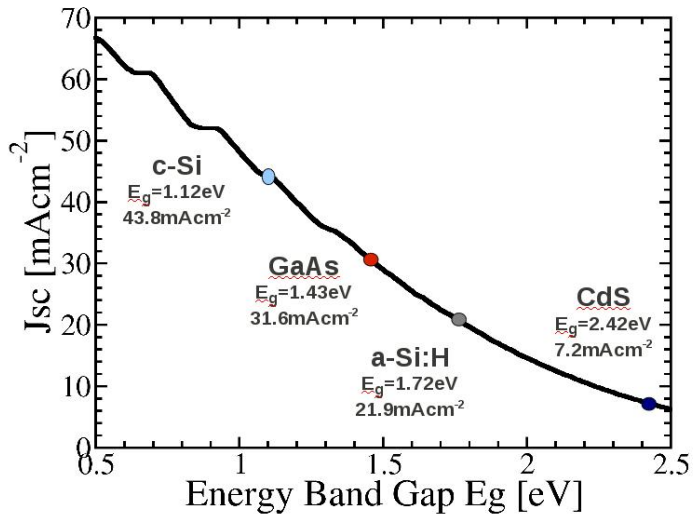

Figure 2.9: Dependence of the short-circuit current on the band-gap energy E_g for direct illumination without external reflectance of the top interface calculated assuming the input spectrum AM1.5G ($1000Wm^{-2}$) at T=300K. All photo-generated electron-hole pairs are assumed to be collected by electrodes.

thickness of the absorbing layer as well as to the recombination losses which reduce the short-circuit current.

M. A. Green in (1) proposed the following estimation of the lower bound limit of the saturation current density:

$$J_0 = 1.5 \times 10^5 \exp\left(-\frac{E_G}{kT}\right) \left[Acm^{-2}\right]. \tag{2.77}$$

This lower bound bang-gap dependent value of the saturation current density is helpful to calculate the open circuit voltage V_{OC} as well as the conversion efficiency η by using the I-V characteristic of eq. 2.57. Results are presented in Fig. 2.10 and in Fig. 2.11. It is possible to observe that for c-Si the maximum expected V_{OC} is about 700mV; depending upon the technology, process conditions and the particular design of the cell, practical devices exhibit V_{OC} within the range 600-670mV.

In case of c-Si, the upper bound limit of the efficiency is 25.9% while for a-Si:H is 25.4%. In order to obtain a value of conversion efficiency close to the peak value, the bang-gap energy should be within the range 1.4-1.6eV. It is worth noting that for

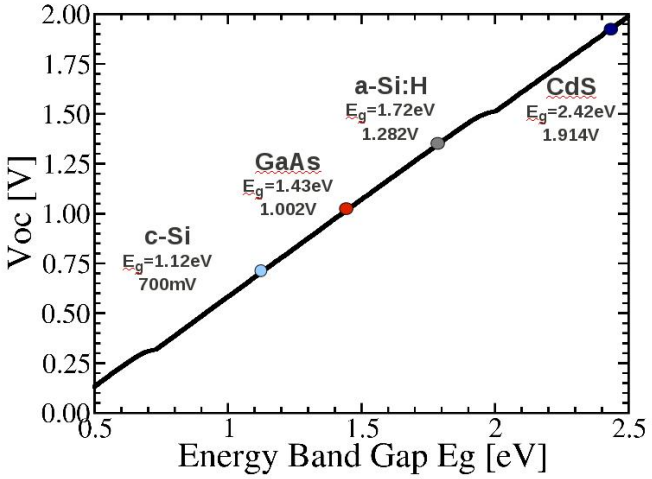

Figure 2.10: Dependence of the open-circuit voltage V_{OC} on the band-gap energy E_g for direct illumination without external reflectance of the top interface and calculated assuming the spectrum AM1.5G ($1000 W m^{-2}$) at T=300K. The saturation current is in agreement with the lower bound limit proposed by M.A. Green in (1). All photo-generated electron-hole pairs are assumed to be collected by electrodes.

GaAs the band-gap is close the optimum value (E_g = 1.43eV, max η = 28%). In addition, small volume laboratory c-Si devices are reported to reach an efficiency closer to the upper bound limit (15); for single junction a-Si:H thin film solar cells, the gap between practical efficiency values (about 9.5%, (16)) and the theoretical upper bound limit (above 25%) is larger, due to the poor material quality and to the limited light trapping scheme effectiveness.

2.5 Effect of temperature and loss mechanisms on main figures of merit of a solar cell

2.5.1 Effect of temperature

The temperature may significantly vary during the operation of a photovoltaic device. Despite the short-circuit current is not significantly affected by change in temperature, it is worth noting that the absorption coefficient is temperature-dependent (17). In addition, the absorption coefficient is doping dependent (18), especially within the

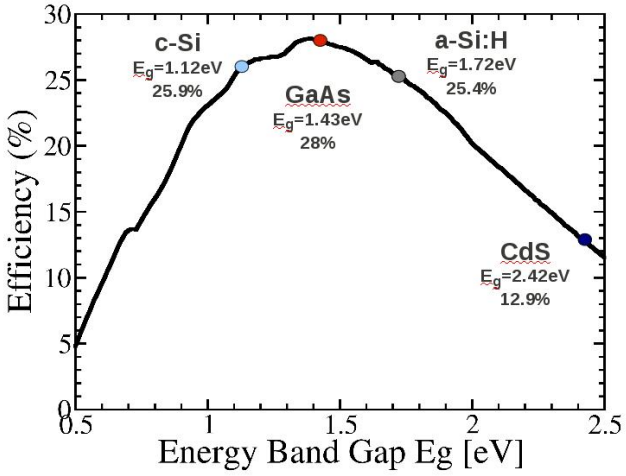

Figure 2.11: Dependence of the conversion efficiency η on the band-gap energy E_g for direct illumination without external reflectance of the top interface, calculated assuming the spectrum AM1.5G ($1000 W m^{-2}$) at T=300K. The saturation current is chosen in agreement with the lower bound limit proposed by M.A. Green in (1). All photo-generated electron-hole pairs are assumed to be collected by electrodes.

infrared region of the spectrum and, in case of a-Si:H, it is strictly dependent on the dilution of silane by hydrogen in plasma deposition (19).

For this reason the short circuit current is expected to increase slightly with increasing temperature. The dependence of the figures of merit on temperature is particularly interesting in concentrator solar cells (CPV)(20), for which, in addition to the change of temperature due to the environmental conditions, large current densities lead to self-heating effects.

However, the impact of temperature on V_{OC} is not negligible. M.A. Green in (1) reports the following approximated expression for the change in open circuit voltage as consequence of a change in temperature:

$$\frac{dV_{OC}}{dT} = -\frac{V_{G_0} - V_{OC} + \gamma\left(\frac{kT}{q}\right)}{T}, \tag{2.78}$$

which predicts a decrease (approximately linear) in V_{OC} with increasing temperature (a typical value of $\frac{dV_{OC}}{dT}$ for c-Si solar cells is about $-2.3 mV/C$). In eq. 2.78 γ is a temperature-dependent parameter.

2.5.2 Optical losses

Main optical losses include the external front reflectance (although the front reflectivity of bare silicon is significantly reduced by texturing and by anti-reflection coating layers as shown in section 2.8), the front contact shadowing (the impact of the solely fingers on the photo-generated current density is typically around 5 percent if realistic front contact pitches -for instance $2mm$- and $100\mu m$-wide fingers are assumed) and the light trapping mechanism limitations. The presence of a bus bar (Fig. 2.12) additionally lowers the photo-generated current -and hence the short circuit current-: state-of-the art commercial c-Si solar cells featuring a side of $156mm$ exhibit three bus bars $2mm$-wide, therefore the ratio of the bus bars total area to the cell area is about 3.8%.

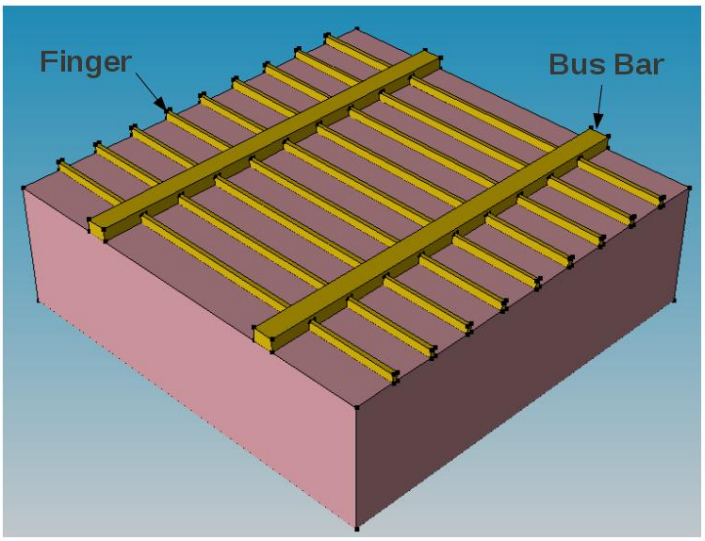

Figure 2.12: Contact scheme for the front surface of a silicon solar cell. Bus bars and fingers are aimed at delivering current to the external circuit.

2.5.3 Open circuit voltage and FF losses

V_{OC} is strongly affected by recombination losses, especially those at interfaces and at bulk level. The back surface field (BSF), by introducing a built-in electric field at the p-p^+ transition, helps to separate carriers photo-generated by large-wavelength photons close to the contacted back-surface and hence leads to an increase of V_{OC}. However,

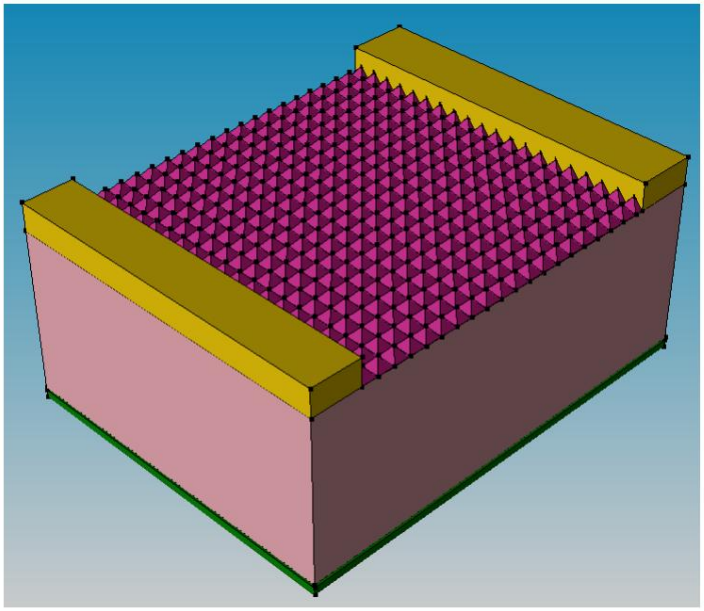

Figure 2.13: Silicon solar cell featuring the front surface textured by pyramids.

due to the large doping concentration of the BSF diffusion, the Auger recombination plays a crucial role in determining the trade-off between the reduced recombination losses at the back surface and the increase of losses at bulk level. The macroscopic effect of the introduction of a BSF is the lower effective back surface recombination velocity with respect to that of the cell without any BSF. But the V_{OC} is also limited by recombination losses in the depletion region (the contribution to the dark saturation current by the second diode in the equivalent circuit of Fig. 2.6). Several techniques, like the passivation of front surfaces and the rear point contact scheme (which will be discussed in chapter 4), are helpful to reduce the recombination losses and hence to enhance the V_{OC}.

Starting form the two-diode circuit model of a solar cell, it is possible to reframe the expression of the I-V characteristic by adopting an effective ideality factor of the diode:

$$J = J_{SC} - J_{0_{EFF}} \left(e^{\frac{qV_A}{n_{EFF}kT}} - 1 \right). \tag{2.79}$$

It is worth noting that the effective ideality factor n_{EFF} varies within the range $1-2$

depending upon the value of the current. The value of n_{EFF} affects the FF; following the approach of M.A. Green (1), for normalized voltages $v_{OC} = q\frac{V_{OC}}{n_{EFF}kT} > 10$,

$$FF = \frac{v_{OC} - \ln(v_{OC} + 0.72)}{v_{OC} + 1}. \tag{2.80}$$

However the main contribution to FF is given by parasitic resistive losses like the series resistance R_S and the shunt resistance R_{SH}. The former contribution is due to the front contact resistance (fingers, bus bars) as well as to the back contact one (in uniformly back contacted solar cells the latter contribution to the series resistance is typically negligible, but it may be significant if the metallization fraction -defined as the ratio of the contacted area to the total area- is significantly smaller than unity, like in case of rear point contact solar cells (21). The shunt resistance (which is ideally infinite) is caused by the current leakage across the p-n junction at the edge of the device, by crystal defects and by precipitates of impurities. In order to quantify the impact of the parasitic resistance on FF, M.A. Green (1) proposed the following models:

$$FF = FF_0\left(1 - \frac{R_S}{R_{CH}}\right). \tag{2.81}$$

and

$$FF = FF_0\left[1 - \frac{(v_{OC} + 0.7)}{v_{OC}}\frac{FF_0}{r_{SH}}\right]. \tag{2.82}$$

where FF_0 denotes the ideal FF (when $R_S = 0$ and $R_{SH} = 0$), $R_{CH} = \frac{V_{OC}}{I_{SC}}$ is a characteristic resistance of the solar cell and $r_{SH} = \frac{R_{SH}}{R_{CH}}$ is the normalized shunt resistance. The previous expressions of the FF are valid under the assumption that $v_{OC} > 10$, $r_S < 0.4$ and $r_{SH} > 2.5$.

The effects of the series resistance and of the shunt resistance on FF are shown in Fig. 2.14 and Fig. 2.15, respectively.

2.5.4 Accounting for contact resistances

The total parasitic resistance of a solar cell is given by the sum of several contributions (Fig. 2.16). The contact resistance of the metal-semiconductor interfaces at rear (R_{bsm}) and at the front surface (R_{fsm}) should be accounted for. That of ohmic contact is an acceptable approximation in case of a metal directly deposited onto a highly-doped

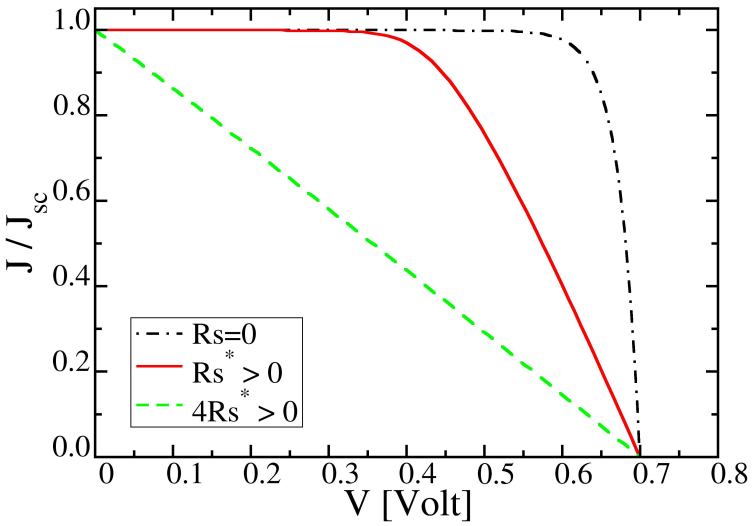

Figure 2.14: Effect of the series parasitic resistance on the I-V characteristic of a solar cell. The current is normalized to the short-circuit current density J_{SC}.

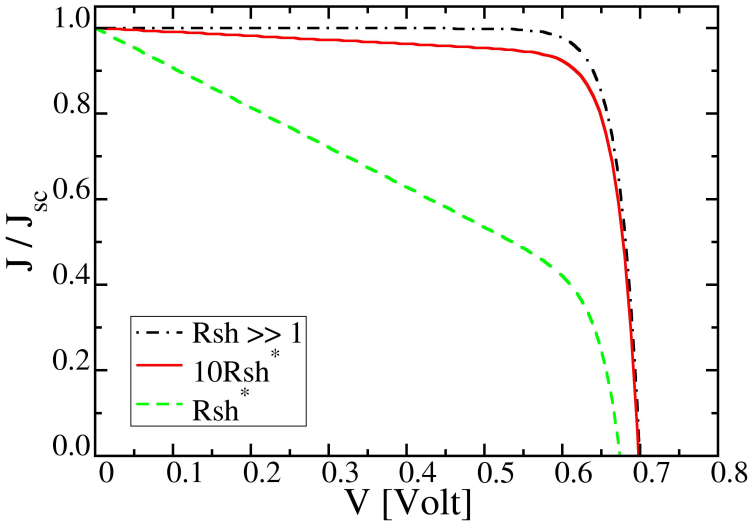

Figure 2.15: Effect of the shunt parasitic resistance on the I-V characteristic of a solar cell. The current is normalized to the short-circuit current density J_{SC}.

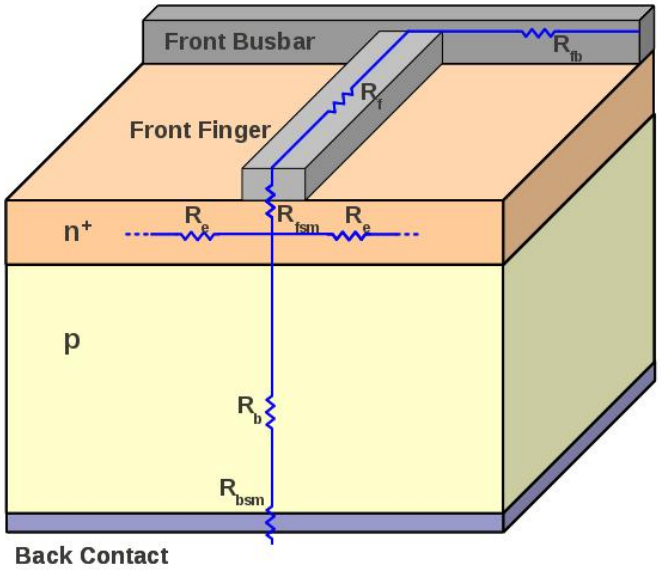

Figure 2.16: Sketch of a simple solar cell with the lumped-element circuit to model the series parasitic resistances.

semiconductor; a narrow space charge region is created and electrons can move through such region by tunnelling. If the metal is deposited onto a lowly-doped semiconductor, the charge transfer occurs by thermionic effect (22). A theoretical relationship between the specific contact resistivity ρ_c and the doping level of the semiconductor at the interface has been proposed in (22). When tunnelling occurs, the contact resistance decreases with increasing doping, while, in case of thermionic effect, the contact resistance is dependent only on the barrier height. In case of a front contact finger, if L_T denotes the transport length and R_{SHT} the sheet resistance of the contacted semiconductor, a general expression for the contact resistance is:

$$R_{fsm} = \frac{\sqrt{R_{SHT}\rho_c}}{L}\coth\left(W\sqrt{\frac{R_{SHT}}{\rho_c}}\right), \tag{2.83}$$

where L and W are the finger length and width, respectively. If $L_T \geq 2W$, then

$$R_{fsm} = \frac{\rho_c}{LL_T} = \frac{\sqrt{\rho_c R_{SHT}}}{L}. \tag{2.84}$$

In case $L_T \leq 2W$, the equation can be approximated by

$$R_{fsm} = \frac{\rho_c}{LW}. \tag{2.85}$$

It is worth noting that, if $L_T \leq 0.5W$ the resistance does not depend on W.

The second contribution to the total series resistance is the contact finger resistance, which can be expressed as (22):

$$R_f = \frac{1}{3}\rho_m \frac{L}{HW}, \tag{2.86}$$

where H is the height of the finger and ρ_m is the resistivity of the metal.

The bus bar resistance, similarly to that of the finger, is expressed by (22):

$$R_{fb} = \frac{1}{6}\frac{L_B}{H_B W_B}\rho_m, \tag{2.87}$$

where L_B, H_B and W_B are the busbar length, height and width, respectively.

2.6 Light Trapping

In crystalline Si (c-Si) and in compound semiconductor photovoltaic technologies, the cost of materials used to fabricate the device is one of the dominant contributions to the total cost of the solar cell. The main challenge in such technologies is the reduction of the cost of the device preserving the performance. The major consequence of the reduction of volume of the semiconductor is the decrease of the amount of absorbed photons from the external source. In case of normal incidence of the light on a simple slab of silicon with finite thickness T, the absence of internal bottom reflection leads to only one passage of the light within the absorber layer, therefore the pathlength is equal to the thickness T. The single-pass absorption scheme is the reference case adopted for the following discussion. In case of a two-pass light trapping scheme, the pathlength is simply twice than that obtainable with only one passage of the radiation. In order to enhance the absorption of photons within the volume of the semiconductor, the probability of photon absorption has to be larger than that resulting when a single passage of the incident photons occurs. A simple light trapping scheme is implemented also in thick-wafer silicon solar cells: the back contact (the aluminum plate) acts like a back reflector (even though its reflectivity is significantly

smaller than that of the ideal reflector (23)) and standard industrial solar cells feature a textured front interface, which, in addition to the anti reflective coating (ARC) layer, contributes to the reduction of the external front reflectivity as well as to the increase of the internal reflectivity (at bottom and at top interfaces). Therefore multiple bounces of light are expected within the absorbing layer, hence enhancing the probability of photon absorption. Two kinds of light trapping schemes are reported in literature: the randomizing or Lambertian light trapping and the geometrical light trapping. The former exploits the features of its surface to randomize the direction of the reflected light; the latter is an attempt to deviate the reflection angle from the normal direction by means of regular geometric patterns on the surface.

In case of a Lambertian reflector, the reflected radiant intensity varies following the rule of $\cos(\theta)$, where θ is the angle of the scattered light (24). It is possible to demonstrate that the pathlength is about $4n^2$ times that of the reference case (single pass) (25), where n is the refractive index of the absorber material. This geometrical limit of the light trapping is referred as the well-known Yablonovitch limit. In case of crystalline silicon, for which n is approximately 3.5, $4n^2$ is 50. The pathlength is a typical figure of merit of a light trapping scheme. The Yablonovitch limit represents the optimum performance that can be obtained by a light trapping scheme in terms of absorbance enhancement in the geometric optics regime for a structure exhibiting an acceptance cone spanning a full hemisphere.

In case of crystalline silicon solar cells, in order to obtain a reasonable value of absorbance, the active layer thickness should be higher than $100\mu m$. A simple calculation shows that the optimal thickness for a crystalline Silicon cell without any light trapping scheme is about $200\mu m$. If a light trapping strategy is adopted, the optimal thickness required can be consequently reduced. In Fig.2.17 it is possible to observe that the one-pass absorption curve of the $200\mu m$-thick silicon layer is comparable to that associated to the textured $20\mu m$-thick one, confirming that texturing enhances the absorption of the silicon layer for a given thickness. However, this approach works for wafers featuring a thickness that is not comparable to the wavelengths of the radiation, because the limit $4n^2$ has been derived under the geometrical optics approximation. Therefore the Yablonovitch limit is not helpful to predict the enhancement of absorption for a thin film solar cell and it is not possible to state which is the best light trapping scheme for such kind of solar cells.

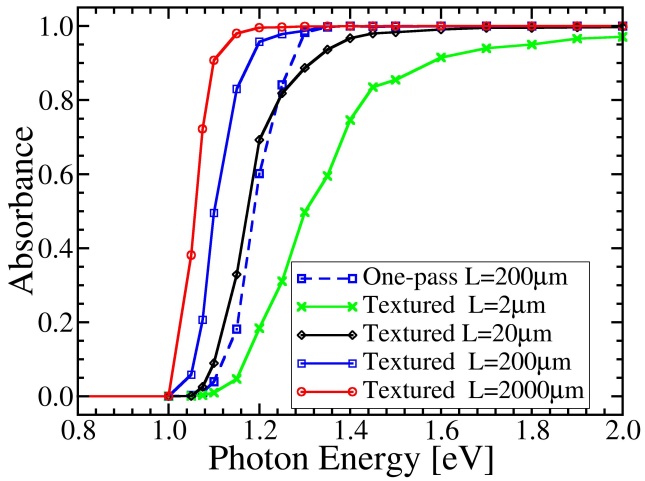

Figure 2.17: Theoretical prediction of the dependence of the absorbance of a crystalline silicon slab featuring a finite thickness on the photon energy in case of single-pass scheme and in case of a light trapping scheme by means of front surface texturing (pathlength equal to $4n^2$ where n is the refractive index of silicon). The one-pass absorption curve of the $200\mu m$-thick silicon layer is comparable to that associated to the textured $20\mu m$-thick layer.

2.7 Geometrical light trapping

In case of geometrical light trapping the direction of the incident sunlight is predictable by analytic formulae. The simpler geometrical light trapping scheme was proposed by Redfield (2); it consists of an oblique rear surface (Fig. 2.19A) with limited slope to take into account for the narrow escape cone from silicon. In addition, the slope of the rear surface must be inverted because the thickness of the cell is supposed to be limited. In the worst case, when the illumination is direct, only four passages of the light within the absorber are expected. Depending upon the position of the reflection on the rear surface, the number of passages may vary.

A more effective scheme has been introduced by grooves formed by (111) crystallographic plane orientation (Fig. 2.18). If the grooves are symmetric (Fig. 2.19B), it can be easily demonstrated that the typical number of passages is two. In case of asymmetry, due to a slight tilt (Fig. 2.19C), the number of passages may increase significantly.

Three dimensional upright pyramids are formed by anisotropically etching (100);

this light trapping scheme is more effective than the two-dimensional groove. In (13) a regular upright 3-D pyramid scheme (Fig. 2.20A) is compared to randomized geometry of upright pyramids (Fig. 2.20B) and to the Lambertian surface. Random pyramids lead to better absorption performance than the case of the regular pyramids. In addition, it is not possible to manufacture regular pyramids in real processes due to the difficulties in controlling the exact geometry. Smith and Roghati (26) demonstrated that an even better performance is obtained by using 3-D inverted pyramids. Other schemes have been proposed providing higher performance for direct illumination and less sensitivity to the angle of incidence (27).

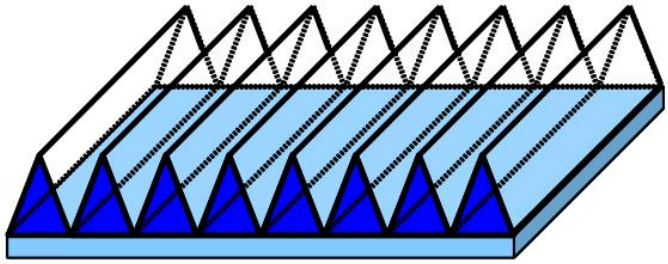

Figure 2.18: Vertical grooves formed by [111] crystallographic plane orientation.

2.7.1 Coherent light trapping schemes for thin film solar cells

Mostly adopted coherent light trapping schemes for thin film solar cells exploit periodic photonic crystals. Structures featuring size in wavelength regime typically cause strong angular and wavelength selective scattering. On the contrary, only when the geometric features of texturing structures are not comparable to the wavelength, a complete randomization of light can be obtained. In thin film solar cells, like hydrogenated amorphous Si (a-Si:H) and micro-crystalline Si (mc-Si) cells -which typically feature textured $SnO_2 : F$ or $ZnO_2 : Al$ coated on glass substrate-, the geometrical approach is less effective than that of thick devices. In addition, in thin film solar cells, the front contact is typically made by transparent conductive oxide (TCO) to ensure an electric contact and to allow the light to pass it through. However, TCO absorbs part of the light. In order to enhance the absorption in solar cells featuring thin substrates, Sheng et al. (28) proposed one (1-D) or two (2-D) dimensional metal

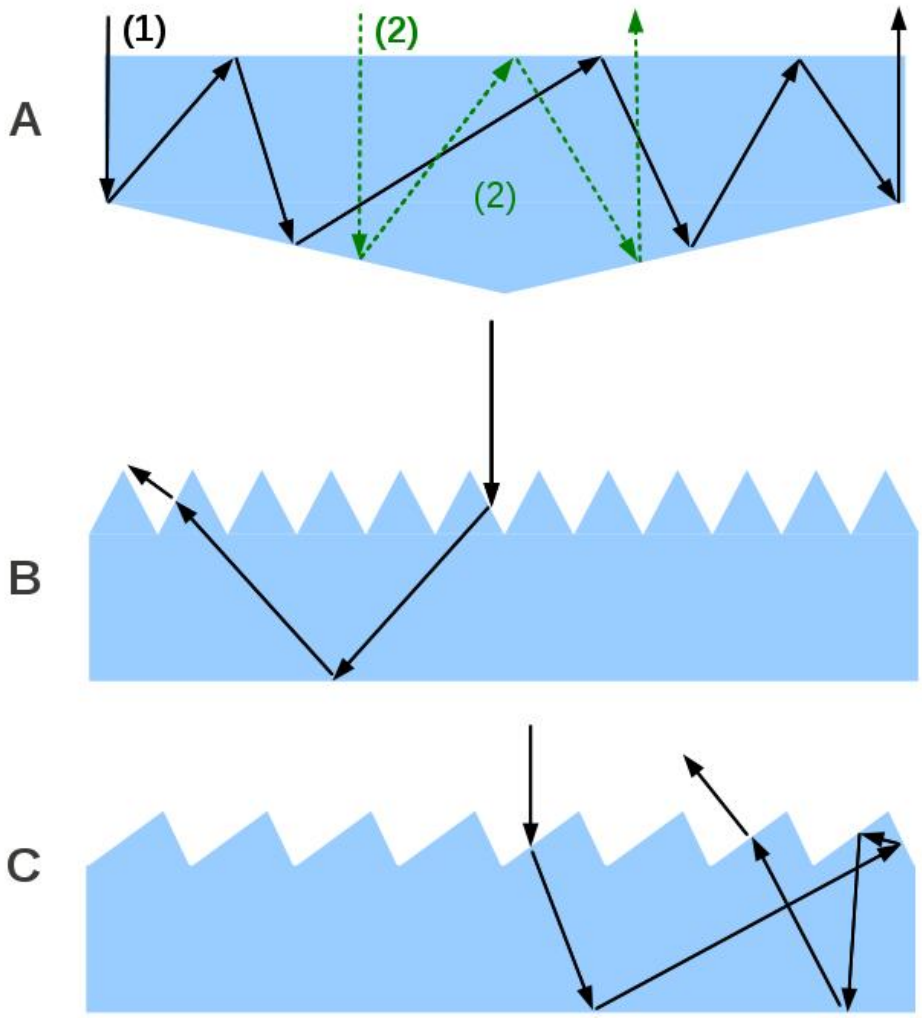

Figure 2.19: Cross sections of (A) light trapping scheme proposed by Redfield (2), (B) symmetric vertical grooves and (C) asymmetrical grooves.

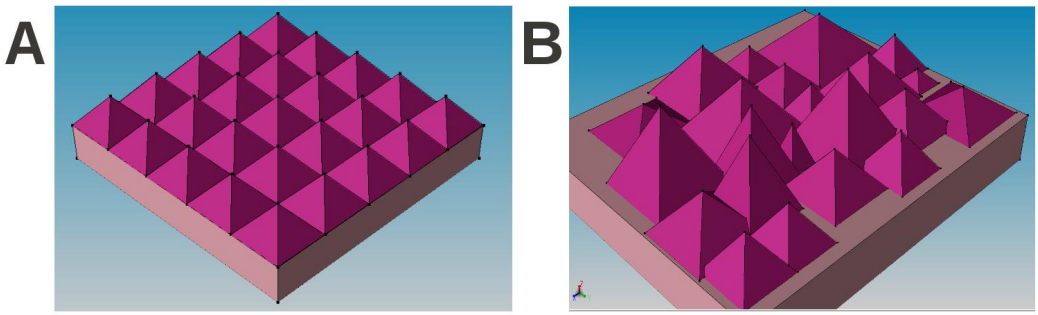

Figure 2.20: Three dimensional upright pyramids: (A) periodic scheme and (B) random pyramids.

gratings as back reflectors for a-Si:H cells. Stiebig et al. (29) have experimentally characterized 1-D rectangular grating structures in $450nm$ thick a-Si:H and $1\mu m$ thick mc-Si:H cells, providing a comparison with the randomly textured substrates; however, they reported an enhancement of absorption that is approximately half of that achieved by random texturing. Feng et al. (30) and Bermel et al. (31) have investigated the adoption of photonic crystals as back reflectors and discussed their optimization. In particular, Bermel and co-authors considered $2\mu m$-thick c-Si cells exhibiting 1-D and 2-D metal gratings, 1-D and 2-D dielectric gratings in combination with distributed Bragg reflectors (32) and photonic crystals; they reported that, cells with 2-D dielectric gratings with Bragg reflectors provide better performance with reference to the photonic crystals (33). In Fig. 2.21, typically adopted photonic crystals in 2-D and 3-D schemes are shown.

Plasmonics is another phenomenon potentially interesting for photovoltaic. When light is incident and scatters from a metal structure featuring nanometric size, a co-operative electron quantized oscillation occurs leading to a coupling of the scattered radiation into the waveguide modes exhibited by such nanometric structures. The absorption can be strongly enhanced by plasmonic effect resulting in a set of wavelengths which, for a given metal nanoparticle, allows light to couple into scattering effect. For instance, for Pd and Au the plasmonic wavelengths are $250nm$ and $525nm$, respectively, but their values is also dependent on substrate, waveguide and medium effects which can shift the value of the plasmonic wavelength. Randomly arranged metal nanoparticles and plasmon crystals (periodic structures) are used to model the electric field

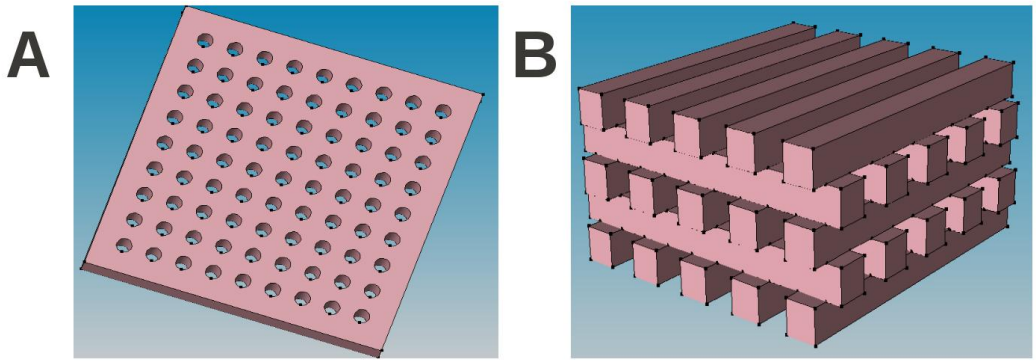

Figure 2.21: Photonic crystals in 2-D scheme (A) and 3-D scheme (B).

intensity inside structures by exploiting the plasmonic effect.

Agrawal (34) theoretically demonstrated that coherent optical schemes are not expected to provide better enhancement of the absorbance with respect to the geometrical optics.

2.8 Antireflection coating layers

As mentioned in the previous section, the reduction of the external reflectance can be achieved by means of a stack of one or more thin layers of different media (Fig. 2.22) (AntiReflection Coating, ARC) or by surface texturing, which, by exploiting multiple reflections and different scattering angles of the light, allows most of the light to be absorbed in the cell. In this section the ARC option is discussed.

An electromagnetic wave exhibits a phase shift of $\lambda/2$ upon entry into an optically denser medium. If the optical path (i.e. the product of refractive index n and layer thickness L) is equal to a quarter of the wavelength ($nL = \frac{\lambda}{4}$), then the destructive interference is achieved, which means that light of such wavelength featuring normal incidence is completely extinguished.

According to Fresnel's formula, the reflection factor is:

$$R = \frac{r_1^2 + r_2^2 + 2r_1 r_2 \cos(2\theta)}{1 + r_1^2 r_2^2 + 2r_1 r_2 \cos(2\theta)}. \tag{2.88}$$

where θ is the incidence angle; if n_0 denotes the refractive index of the uppermost layer (air or glass), n_1 denotes the refractive index of the antireflection layer and n_2

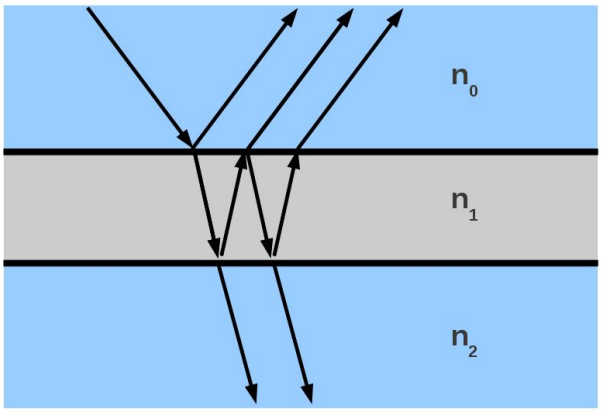

Figure 2.22: Sketch of a simple anti reflection coating layer (ARC) featuring one slab with refractive index n_1. The refractive indices of the superstrate and substrate are n_0 and n_2, respectively.

the refractive index of the silicon,

$$r_1 = \frac{n_0 - n_1}{n_0 + n_1}. \tag{2.89}$$

$$r_2 = \frac{n_1 - n_2}{n_1 + n_2}. \tag{2.90}$$

Finally,

$$\theta = \frac{2\pi n_1 L}{\lambda}. \tag{2.91}$$

In order to minimize the reflection (at $\theta = 0$),

$$R_{MIN} = \left(\frac{n_1^2 - n_0 n_2}{n_1^2 + n_0 n_2} \right)^2. \tag{2.92}$$

The reflection is zero when

$$n_1 = \sqrt{n_0 n_2}. \tag{2.93}$$

In Fig. 2.23 the reflectance of bare crystalline silicon is compared to those of a silicon substrate coated by a single silicon dioxide (SiO_2) $70nm$-thick layer, by a single $70nm$-thick titanium dioxide (TiO_2) layer and by a stack of MgF_2 ($110nm$-thick) and

TiO_2 (70nm-thick) layers. The latter ARC is that minimizes the reflectance within the considered range of wavelength (300-1200nm). The real and the imaginary parts of the refractive index of the silicon and of the other coating materials are shown in Fig. 2.24A and Fig. 2.24B, respectively.

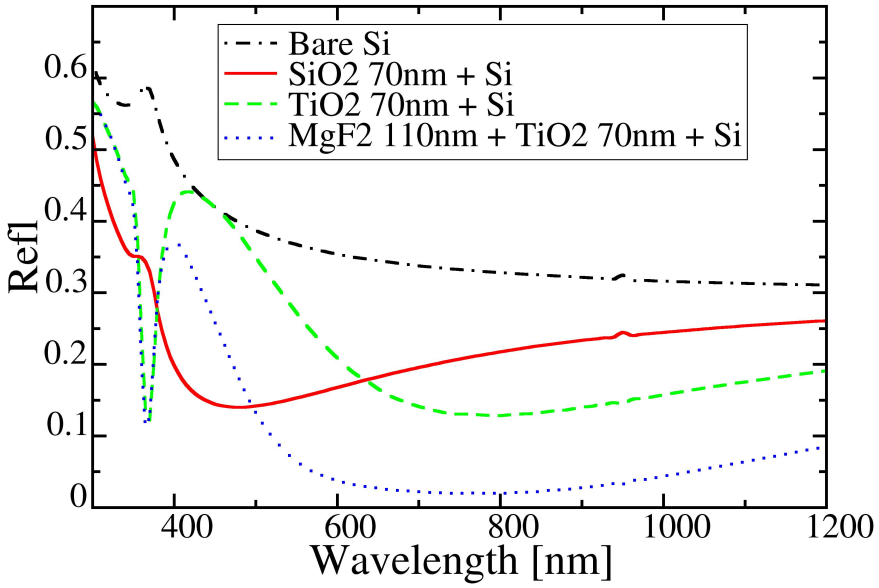

Figure 2.23: Examples of ARCs: calculated reflectance.

In conclusion, by properly designing the ARC, it is possible to enable the destructive interference between reflected and incident light, eliminating reflection at both interfaces; however this technique works only for a single wavelength with direct incidence, so it is not really effective over most of the spectrum. ARCs exhibiting more layers (typically two or three) may be more effective within extended portions of the spectrum, but the ideal coating would have a continuously graded refractive index.

2.9 Standard crystalline solar cells manufacturing technology

2.9.1 Wafer preparation

Despite mono-crystalline float zone (FZ-Si) material allows high crystalline perfection and low contamination level of impurities leading to longest post-processing SRH life-

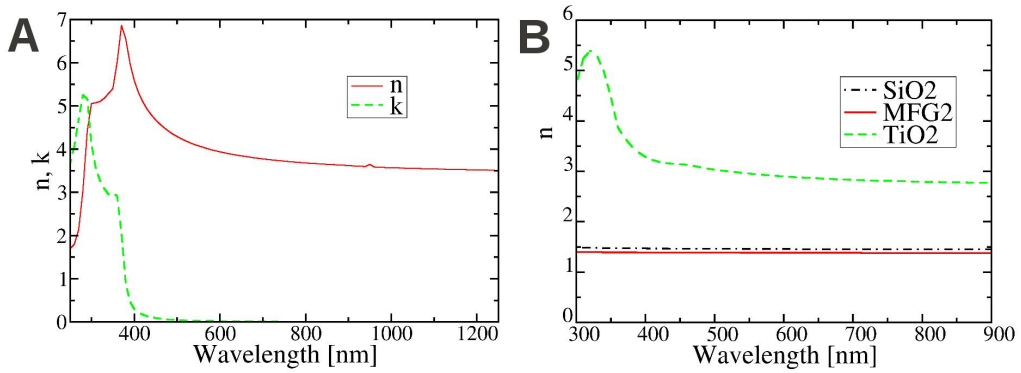

Figure 2.24: Refractive indices and extinction coefficients of the crystalline silicon (A) and of SiO_2, TiO_2 and MgF_2 (B) used to calculate the reflectance of Fig. 2.23.

times (in the millisecond range) and Magnetic Czochralski (MCz) material exhibits a good trade-off between cost and performance (35), industrial solar cells commonly use Czochralski (Cz-Si) wafers because of their availability. The main drawback of Cz-Si wafers is the presence of high concentration of oxygen that limits the carrier lifetime (36). Commercial devices widely use multi-crystalline (mc-Si) substrates which, in addition to crystal defects, such as grain boundaries and dislocations, exhibit higher defect levels of metallic impurities because of lower segregation to the melt during the faster solidification process leading to lower lifetimes. Lifetimes typically change during the cell fabrication process, in fact contamination typically occurs especially during high-temperature steps like furnace cleaning. The integration of gettering steps (37) in the fabrication flow is helpful in order to reduce the contamination leading to final substrate lifetimes of industrial mc-Si cells within the range 1-10μs.

In (38) the gettering obtained with phosphorus and aluminum diffusions for emitter and BSF layers is investigated. Diffusion techniques for p-type doping with $POCl_3$ and PH_3 leave a dead layer of electrically inactive phosphorus near the surface leading to a reduced ultra-violet (UV) response of the cells in case such layer is not etched away (39).

Techniques like sputtering, vacuum evaporation or screen printing allow the aluminum deposition on silicon; the annealing over the eutectic temperature forms a liquid Al-Si layer which is helpful to segregate impurities because of their enhanced solubility

(40) leading to bulk lifetime improvement. Bulk passivation by means of hydrogen is another techniques to improve material quality (41). Industrial cells use boron-doped substrates mainly for practical motivations (42). Intrinsic substrates show effective lifetimes close to those expected in presence of the solely Auger recombination mechanism (the well-known Auger limit), but also large resistivity (as shown in chapter 4, the parasitic series resistance affects the Fill Factor, therefore one way to improve the performance is just to decrease the base resistivity); on the other hand, higher doping concentration leads to larger SRH recombination rates.

Industrial cells are fabricated with substrate doping concentration values within the range $10^{15}cm^{-3}$-$10^{16}cm^{-3}$. The optimum substrate thickness is chosen depending upon optical considerations (light trapping scheme, light absorption properties of the semiconductor) as well as electric parameters, like the carrier lifetimes. As the wafer becomes thinner, the light trapping strategy becomes fundamental in order to maintain acceptable levels of the photo-generated current density. If the diffusion length is longer than the thickness, the most important issue is the surface recombination at the back contact (as shown in chapter 4) which plays a crucial role on the open circuit voltage. The thickness of current standard industrial silicon solar cells is within the range 180-280μm. The diffusion length of Cz-Si, MCz and Fz-Si industrial cells is typically larger than the standard thickness.

2.9.2 Front contact and emitter design

Metal grids are used at the front face to collect the photo-generated carriers. Standard schemes of metal grids for mono-crystalline and mc-Si solar cells include bus bars and fingers as shown in Fig. 2.25. In order to reduce the parasitic series resistance and in particular that associated to the front contact, one way is to increase the contacted emitter surface. The front contact resistance depends also on the emitter doping concentration at interface (43). However, a trade-off between parasitic series resistance and the shadowing effect caused by fingers and busbars (which limits the photo-generated current) is carefully considered in the design of the cell. Laboratory fabricated cells exploit photolithographic techniques and evaporation to form narrow metal fingers (10-20μm-wide) with Ti/Pd/Ag structures to lower the contact resistance. Mass production devices are mostly based on screen printed Ag pastes (44) resulting in 100-200μm-wide fingers.

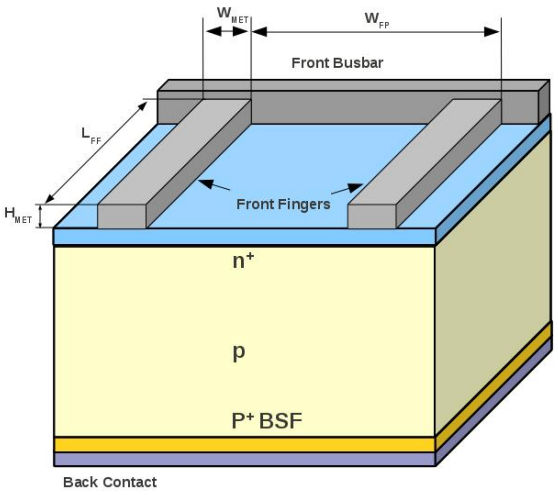

Figure 2.25: Homogeneous emitter (HE) solar cell. Under the contacted surface and between fingers the same emitter doping profile is adopted. L_{FF}, H_{MET} and W_{MET} denote the front finger length, height and width, respectively. W_{FP} is the distance between front fingers.

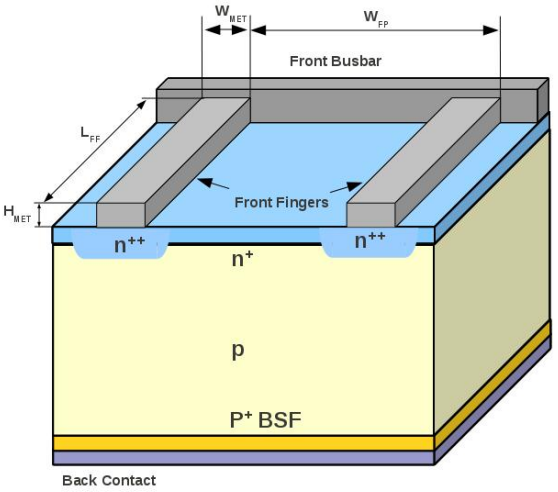

Figure 2.26: Selective emitter (SE) solar cell. A heavily doped emitter doping profile (n^{++}) is present under the contacted surface and a lowly-doped profile (n^{+}) between fingers. L_{FF}, H_{MET} and W_{MET} denote the front finger length, height and width, respectively. W_{FP} is the distance between front fingers.

Under the metal lines, the substrate must be heavily doped to make the contact selective. However, high doping concentration leads to large recombination losses (Auger and trap-assisted) as well as to significant surface recombination losses. On the other hand, lowly doped emitters lead to large emitter resistance and hence to performance degradation. Lowly doped emitter exhibiting a sheet resistance up to 100Ω/square can be contacted (44). Standard industrial emitters feature sheet resistance values within the range 50-70Ω/square. The homogenous emitter (Fig. 2.25) scheme is characterized by the same emitter doping profile between front fingers and under the contacted portion of the front side of the cell. The emitter should be deep enough (0.4-1μm) to reduce the recombination of the photo-generated carriers at front interface and to reduce the emitter resistance. Advanced emitter schemes exhibit a double-diffused emitter (or selective emitter) as described in chapter 4 and as it shown in Fig. 2.26; according to this scheme, a deep and heavily-doped diffusion is adopted under the metal finger to ensure a good ohmic contact. However, very highly-doped regions exhibit a dead layer due to the presence of precipitates resulting in a degraded collection efficiency of short-wavelength light (which leads to photo-generation close to the front surface). Heavy phosphorus diffusions produce very effective gettering. Selective emitters can be fabricated by adopting screen-printing techniques (44).

In literature other advanced solutions concerning metallization schemes featuring combination of pastes aimed at reducing the specific contact resistivity are reported (45); these techniques, in addition to reduce the manufacturing costs, enhance the aspect ratio of the fingers leading to reduced contact shadowing effect and to low metallization fraction with the purpose of reducing the contacted area (the trade-off is between the reduction of recombination losses at the metal-silicon interface and the increase of the contact parasitic resistance).

2.9.3 Base and rear surface

The base contact of industrial solar cells is usually made by printing and subsequent firing of aluminum with Ag-conducting paste. The p+ diffused layer (BSF, back surface field, Fig. 2.25) is helpful in order to reduce the recombination in the base of the device, as previously explained. The BSF is more effective for relatively thin wafer cells for which the carrier diffusion length is comparable to the base thickness. Rear point contact schemes like that of Passivated Emitter and Rear Cell (PERC) (13) with rear

surface passivation, which will be extensively described in chapter 4, are aimed at reducing the effective surface recombination velocity at the back of the solar cell. In addition, the presence of a local $p+$ BSF diffusion may be restricted to point contacts as in Passivated Emitter Rear Locally diffused (PERL) cells (13). However, the main drawback in reducing the metallization fraction of the back contact is the increase of the parasitic series resistance, due to the spreading base resistance and to the back contact resistance. PERC and PERL solar cells allow to reach the record efficiency for silicon solar cells (up to 25%). As general remark, the optimization of the rear section is dependent on the emitter configuration; once the emitter is optimized, a subsequent optimization of the rear is performed.

3

Numerical Simulation of Solar Cells

In the first part of this chapter a review of the simulation methodology by means of numerical Technology Computer-Aided Design (TCAD) is presented. In particular, the approach used to calibrate the physical models adopted in the numerical modeling is described. In the second part, a basic theory of electromagnetic wave propagation is proposed in order to introduce the main approaches to optical simulation of solar cells. In particular, the main limitations and the applicability of the Finite Difference Time Domain (FDTD) and of the raytracing methods are discussed, motivating the need to adopt more computationally efficient tools to solve the optical problem in modeling of advanced solar cells.

3.1 Introduction to numerical solution of semiconductor device equations

In this work numerical simulations have been performed by using the Sentaurs TCAD by Synopsys (46), a general purpose finite element method simulator for semiconductor devices. Solar cells are simulated by adopting the drift-diffusion transport model described in chapter 2. In the following, only isothermal analyses are discussed. The three governing equations for charge transport in semiconductor devices are the Poisson equation (eq. 2.27), the electron and hole continuity equations (eq. 2.26) and the transport equations (eq. 2.23); they provide the general framework for device simulation. The

drift-diffusion model is widely used for the simulation of carrier transport in semiconductors featuring low-power density; it is one of the simplest charge transport models since it does not introduce any independent variable in addition to the electrostatic potential and to the carrier concentrations. The drift-diffusion (D-D) model has been considered adequate for most technologically feasible devices in past decade. However, the D-D approximation becomes less accurate for smaller feature sizes like nano-metric field effect transistors (FET), but in case of solar cells, it can be successfully applied.

3.1.1 Drift-Diffusion transport equations

The current densities can be expressed by means of the quasi-Fermi levels ϕ_n and ϕ_p as:

$$\begin{cases} \mathbf{J}_n = -nq\mu_n \nabla \phi_n, \\ \mathbf{J}_p = -pq\mu_p \nabla \phi_p. \end{cases} \tag{3.1}$$

Under the Boltzmann transport theory approximation:

$$n = n_{i,eff} e^{\left(\frac{q(\psi - \phi_n)}{kT_L}\right)} \tag{3.2}$$

$$n = n_{i,eff} e^{\left(-\frac{q(\psi - \phi_p)}{kT_L}\right)} \tag{3.3}$$

where T_L is the lattice temperature and $n_{i,eff}$ is the effective intrinsic carrier concentration:

$$n_{i,eff} = \sqrt{N_C N_V} e^{-\frac{E_g}{2kT_L}} \tag{3.4}$$

and N_C, N_V are the conduction band and the valence band effective densities of states, respectively.

The quasi-Fermi potential can be therefore rewritten as:

$$\phi_n = \phi - \frac{kT_L}{q} \ln\left(\frac{n}{n_{i,eff}}\right) \tag{3.5}$$

$$\phi_n = \phi + \frac{kT_L}{q} \ln\left(\frac{p}{n_{i,eff}}\right) \tag{3.6}$$

where ϕ is the electrostatic potential. A conventional expression for current densities is:

$$\begin{cases} \mathbf{J}_n = qn\mu_n\mathbf{E}_n + qD_n\nabla n, \\ \mathbf{J}_n = qp\mu_p\mathbf{E}_p - qD_p\nabla p. \end{cases} \tag{3.7}$$

where the effective electric fields $\mathbf{E}_{n,eff}$ and $\mathbf{E}_{p,eff}$ are

$$\mathbf{E}_{n,eff} = -\nabla\left(\phi + \frac{kT_L}{q}\ln(n_{i,eff})\right) \tag{3.8}$$

$$\mathbf{E}_{p,eff} = -\nabla\left(\phi - \frac{kT_L}{q}\ln(n_{i,eff})\right) \tag{3.9}$$

3.1.2 Electrical Boundary Conditions

By default, if no electrodes are specified, on all boundaries of the device the following reflective ideal Neumann boundary conditions are assumed:

$$\mathbf{J}_n \cdot \hat{n} = 0, \qquad \mathbf{J}_p \cdot \hat{n} = 0 \tag{3.10}$$

where $\hat{n}$ denotes the normal to the surface.

At electrodes for which an Ohmic contact is set, charge neutrality and equilibrium are assumed; if n_0 and p_0 denote the equilibrium concentration of carriers,

$$n = n_0, \qquad p = p_0 \tag{3.11}$$

$$n_0 p_0 = n_{i,eff}^2 \tag{3.12}$$

When a finite recombination velocity v_e (v_h) for electrons (holes) is specified, the boundary condition at electrodes becomes:

$$\mathbf{J}_n \cdot \hat{n} = qv_e(n - n_0) \tag{3.13}$$

$$\mathbf{J}_p \cdot \hat{n} = -qv_h(p - p_0) \tag{3.14}$$

3.1.3 Effective Intrinsic Carrier Concentration and Band Gap structure

The intrinsic carrier density n_i is a fundamental quantity in semiconductor physics which plays a significant role in the simulation of silicon solar cells due to the presence of optical excitation. In fact, n_i has a strong impact on the recombination losses which limit the ultimate conversion efficiency of solar cells. Therefore, in order to perform realistic simulations of solar cells, n_i must be accurately determined. Prior to 1990, the most commonly adopted value for crystalline silicon at $T = 300K$ was $n_i = 1.45 \times 10^{10} cm^{-3}$ which was affected by significant deviations from experiments. In 1991 Sproul and Green (47) measured the intrinsic concentration providing the value $n_i = 1 \times 10^{10} cm^{-3}$, which is still the most widely accepted value within the PV community. However, recent theoretical investigations (48) reinterpreted Sproul and Green experiment, demonstrating that their measurements were influenced by the band-gap narrowing (BGN), although at relatively low doping densities. A theoretical study based on the finite-temperature full random-phase approximation model of BGN proposed in (49) revealed that $n_i = 9.65 \times 10^{9} cm^{-3}$ for undoped silicon, consistently with the experiments by Misiakos and Tsamakis (50) performed by capacitance measurements.

The temperature dependent mobility bang gap can be modeled as (51):

$$E_g(T) = E_g(0) - \frac{\alpha T^2}{T + \beta} \tag{3.15}$$

where α and β are material dependent parameters and $E_g(0)$ denotes the band-gap energy at $T = 0K$, which can be expressed as:

$$E_g(0) = E_{g_0} + \Delta E_{g,0} \tag{3.16}$$

where $\Delta E_{g,0}$ and E_{g_0} are determined by the particular band-gap narrowing model used.

At a given temperature T, the effective band-gap is

$$E_{g,eff}(T) = E_g(T) - E_{BGN} \tag{3.17}$$

$$E_{BGN} = \Delta E_g^0 + \Delta E_g^{FERMI} \tag{3.18}$$

The parameter ΔE_g^{FERMI} is a correction factor to account for the adopted carrier statistics (46).

A widely used model to account for band-gap narrowing in n-type silicon is that of del Alamo (52)(53)(54)(55)(56), according which:

$$\Delta E_g^0 = \begin{cases} E_{REF} \quad ln\left(\frac{N_{TOT}}{N_{REF}}\right) & \text{if } N_{TOT} \geq N_{REF}, \\ 0 & \text{if } N_{TOT} < N_{REF}. \end{cases} \tag{3.19}$$

where $N_{REF} = 7 \times 10^{17} cm^{-3}$ and $E_{REF} = 18.7 \times 10^{-3} eV$. In eq. 3.19 N_{TOT} denotes the total doping concentration.

Models like Bennett-Wilson (57), del Alamo, Slotboom (58)(59)(60)(61) and Jain-Roulston (62) are all doping-induced band-gap narrowing models. They do not depend on free carrier concentration. However, high carrier concentration due to optical excitation or high electric field injection may lead to band-gap narrowing effect (plasma-induced band-gap narrowing).

In order to correctly reproduce the increase of n_i occurring at large doping density and to account for large carrier injection due to optical excitation, the value of the parameters of Schenk band-gap narrowing model with Fermi-Dirac statistics can be properly set to obtain the value $n_i = 9.65 \times 10^9 cm^{-3}$ at low doping density.

In Fig. 3.1 the effective intrinsic carrier density accounting for band-gap narrowing is reported as function of the total doping density for different models (Bennett-Wilson, Slotboom, del Alamo, Schenk). The default implementation of Bennett and Schenk models provides at very low doping levels $n_i = 1.075 \times 10^{10} cm^{-3}$, whereas the Slotboom and del Alamo models employ a correction factor, leading to higher values, namely $1.180 \times 10^{10} cm^{-3}$ and $1.412 \times 10^{10} cm^{-3}$, respectively. Fig. 3.1 reports also the values of the effective intrinsic concentration calculated by the revised Schenk bang-gap narrowing model that provides very good agreement with the experimental data reviewed by Altermatt et al. in (48). In Sentaurus it is possible to specify the total doping-dependent band-gap narrowing by using a table, in which the band gap narrowing for acceptors and donors is specified separately; the band-gap narrowing is then calculated as the sum of both contributions. A drawback of this approach to model the band-gap narrowing, is the lack of the dependence on carrier concentration.

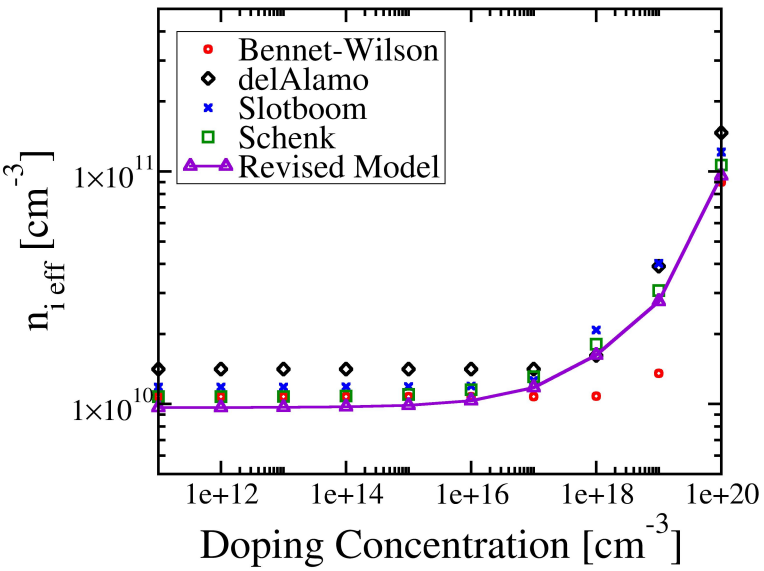

Figure 3.1: Effective intrinsic carrier density accounting for band-gap narrowing (BGN) as function of the total doping density for different models, including the revised BGN model adopted for numerical simulations in Sentaurus TCAD.

3.1.4 Carrier Mobility Models

Electrons and holes are accelerated by electric fields, but their momentum is reduced because of various scattering processes like from phonons, impurity ions, other carriers and surfaces. However, in equations 2.21 all these microscopic effects are accounted by introducing the carrier mobilitiy in the transport equations. The carrier mobility is strongly linked to local electric field, lattice temperature and doping concentration. In presence of low electric fields, carriers are almost in equilibrium with the lattice and the mobility depends on phonon and impurity scattering which leads to mobility degradation. In case of high electric field intensity the carrier mobility is reduced because the carriers -that gain energy- have more probability to take part of more scattering processes. In fact, the mean drift velocity saturates at a constant velocity v_{sat} with increasing field intensity. The saturation velocity is strongly dependent on lattice temperature. Modeling mobility in bulk material involves the knowledge of the low field mobility for a given doping and lattice temperature as well as the dependence of the saturation velocity on the lattice temperature. In addition, surface scattering, carrier-carrier scattering as well as quantum mechanical size quantization effects occur

in inversion layers.

The Philips unified mobility model (63) describes the temperature dependence of the mobility accounting for electron-hole scattering, screening of ionized impurities by charge carriers and clustering of impurities. According to the Philips unified mobility model, a first contribution to the carrier mobility is represented by phonon scattering μ_{PHONON} and by a second contribution μ_{SCATT} (46), which accounts for all other bulk scattering mechanisms like those of free carriers and ionized dopants. Such contributions, for electrons (e) and holes (h), can be accounted for by the following expression:

$$\frac{1}{\mu_{c,eff}} = \frac{1}{\mu_{c,PHONON}} + \frac{1}{\mu_{c,SCATT}}, \qquad c = e, h \tag{3.20}$$

According to Matthiessens rule, for a given temperature T:

$$\mu_{c,PHONON}(T) = \mu_c^{MAX} \left(\frac{T}{300K} \right)^{\theta_c}, \qquad c = e, h \tag{3.21}$$

3.1.5 Recombination mechanisms

As discussed in chapter 2, carrier generation-recombination is the process through which the semiconductor material attempts to return to equilibrium conditions after being disturbed from it (applied bias, device under illumination). The modeling of generation-recombination processes should account for phonon transitions, Auger transitions, surface recombination and impact ionization. Recombination through deep defect levels within the gap is known as Shockley-Read-Hall (SRH) recombination. When Maxwell-Boltzmann statistics is adopted,

$$R_{NET}^{SRH} = \frac{np - n_{i,eff}^2}{\tau_p \left[n + n_{i,eff} e^{\left(\frac{E_T}{kT} \right)} \right] + \tau_n \left[p + n_{i,eff} e^{\left(-\frac{E_T}{kT} \right)} \right]} \tag{3.22}$$

where E_T is the difference between the defect level and intrinsic one ($E_T = 0$ for crystalline silicon).

The doping dependence of the SRH lifetimes is accounted through the Scharfetter relation:

$$\tau_c(N) = \tau_{c,min} + \frac{\tau_{c,max} - \tau_{c,min}}{1 + \left(\frac{N}{N_{REF}} \right)_c^{\gamma}}, \qquad c = e, h \tag{3.23}$$

The temperature dependence is expressed by

$$\tau_c(T) = \tau_{c,0} + \left(\frac{T}{300K}\right)^{\alpha_c}, \qquad c = e, h \tag{3.24}$$

The minority carrier lifetime in standard boron-doped Czochralski silicon (B-Cz-Si) is strongly degraded under illumination or carrier injection due to the metastable Cz-specific defects. Nevertheless, the defect concentration and consequently the lifetime degradation can be significantly reduced by optimized high-temperature annealing steps using conventional or rapid thermal processing as described by Glunz et al. in (3) in which, the measured doping dependence of the bulk lifetime in standard B-Cz-Si is described by a simple empirical fitting. By default, Sentaurus simulator assumes the following values for p-type silicon: $\tau_{min} = 0\mu s$, $\tau_{max} = 10\mu s$, $\gamma = 1$ and $N_{REF} = 10^{16}cm^{-3}$. In order to realistically model the carrier lifetimes in the boron-doped base of silicon solar cell, the parameters in eq. 3.23 have been modified as: $\tau_{min} = 0\mu s$, $\tau_{max} = 134ms$, $\gamma = 1.407$ and $N_{REF} = 10^{14}cm^{-3}$; the empirical fitting of experimental data for standard B-Cz-Si reported in (3) is therefore reproduced. Fig. 3.2 reports the bulk lifetime versus boron doping concentration for the empirical fitting suggested by Glunz et al. (3) and for the Sentaurus default Scharfetter relation. The bulk lifetime curve provided by the modified relation is also reported in Fig. 3.2, showing a good agreement with the fit to experimental data proposed by Glunz.

At interfaces the SRH model is extended by

$$R_{NET}^{SRH,surf} = \frac{np - n_{i,eff}^2}{S_h^{-1}\left[n + n_{i,eff}e^{\left(\frac{E_T}{kT}\right)}\right] + S_e^{-1}\left[p + n_{i,eff}e^{\left(-\frac{E_T}{kT}\right)}\right]} \tag{3.25}$$

The recombination velocities S_e and S_h depend on the concentration of dopants at the surface (64) as well as on process parameters that determine the interface quality. The doping dependence of surface recombination velocities is expressed by:

$$S_c = S_{0,c}\left[1 + S_{REF,c}\left(\frac{N_s}{N_{REF}}\right)^{\gamma_c}\right], \qquad c = e, h \tag{3.26}$$

where N_s denotes the doping concentration at interface, and γ_c, N_{REF} and S_{REF} are tuneable parameters of the model.

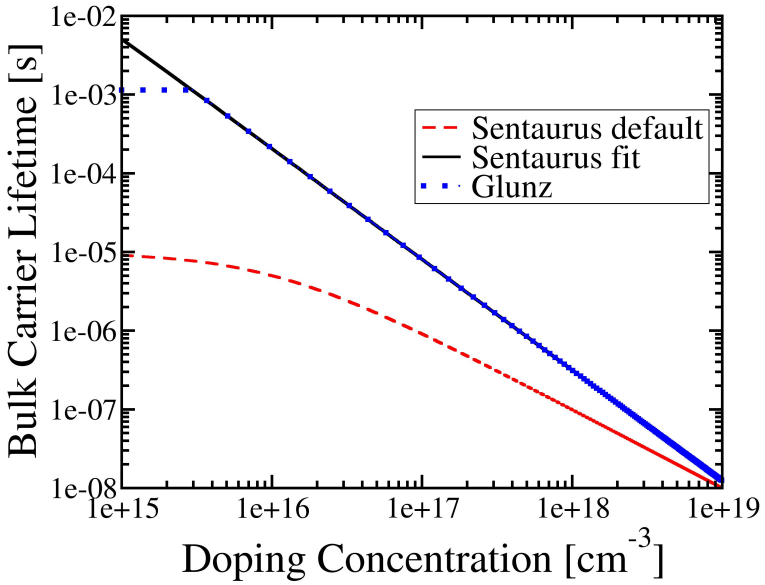

Figure 3.2: Bulk lifetime versus boron doping concentration for the empirical fitting suggested by Glunz et al. (3) and for the Sentaurus default Scharfetter relation. The bulk lifetime curve provided by the modified relation is also reported.

3.1.6 Auger recombination

In Sentaurus, the band-to-band Auger recombination rate is expressed by

$$R_{NET}^{AUG} = \left(np - n_{i,eff}^2\right)\left[C_e(T,n)n + C_p(T,p)p\right] \tag{3.27}$$

where the temperature-dependent Auger coefficients $C_e(T)$ and $C_e(T)$ are given by

$$C_e(T,n) = \left(C_{1,e} + C_{2,e}\left(\frac{T}{T_0}\right) + C_{3,e}\left(\frac{T}{T_0}\right)^2\right) H_e^{INJ}(n) \tag{3.28}$$

$$C_h(T,p) = \left(C_{1,p} + C_{2,p}\left(\frac{T}{T_0}\right) + C_{3,p}\left(\frac{T}{T_0}\right)^2\right) H_p^{INJ}(p) \tag{3.29}$$

Details about the coefficients $H_e^{INJ}(n)$ and $H_p^{INJ}(p)$, which account for effects due to large carrier injection, are reported in (46).

3.2 Numerical methods

The partial differential equations (PDEs) eq. 2.23, eq. 2.27 and eq. 2.26 are discretized by using a numerical grid. A review of the most widely adopted methods of discretization of PDEs for the device simulation is presented in (65). Burgler et al. in (66) discuss the box discretization scheme to solve numerically the Poisson and the continuity equations. A symmetry element of the device is discretized by means of division of the spatial simulation domain in boxes. Rectangular or more effective triangular boxes are typically used for 2-D devices.

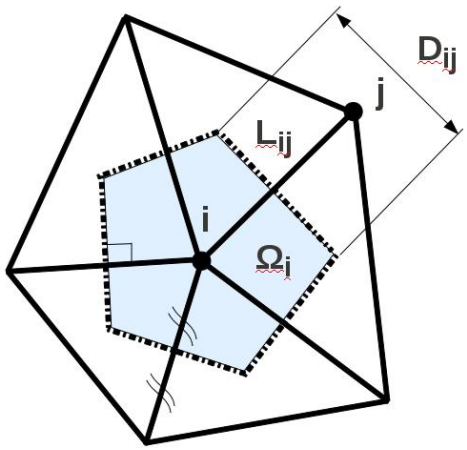

Figure 3.3: Single box centered at node i-th for the numerical solution of PDEs.

For an arbitrary i-th vertex (Fig. 3.3) a single box Ω_i is constructed by choosing box boundaries that are perpendicular bisectors of the lines binding adjacent nodes. In this way it is possible to cover the whole symmetry element. If a PDE is given in the form

$$\nabla \mathbf{\Gamma}(\mathbf{r}) = W(\mathbf{r}), \tag{3.30}$$

where $\mathbf{\Gamma}(P)$ is a vector field and $W(P)$ is a scalar field, such PDE is integrated over the single box volume. In case of the Poisson equation, the electric field is conservative,

therefore it is possible to apply the Gaussian Theorem:

$$\int_{\Omega_i} [\nabla \mathbf{\Gamma}(\mathbf{r}) - W(\mathbf{r})]\, d\tau = \int_{\partial\Omega_i} \nabla \mathbf{\Gamma}(\mathbf{r}) d\hat{n}(\mathbf{r}) - \int_{\Omega_i} W(\mathbf{r}) d\tau = 0 \tag{3.31}$$

where $\hat{n}$ is the normal vector to the box boundary. Therefore the discretized PDE reads:

$$\sum_{j \neq i} \Gamma_{ij} d_{ij} - W_i \tau_i = 0 \tag{3.32}$$

Γ_{ij} is the projection of the vector field $\mathbf{\Gamma}$ onto the edge l_{ij} (3.3) and d_{ij} is the length of the normal bisector between edges j and i. W_i and τ_i denote the value of the scalar field W in node i and the volume of the element Ω_i, respectively. Applying this scheme to the Poisson equation,

$$\sum_{j \neq i} E_{ij} d_{ij} - \rho_i \tau_i = 0 \tag{3.33}$$

or, by expressing the electric field E as a difference of electrostatic potential between nodes i and j along l_{ij}:

$$\sum_{j \neq i} \frac{d_{ij}}{l_{ij}} (\phi_i - \phi_j) - V_i \left(p_i - n_i + N_i\right) = 0 \tag{3.34}$$

Heiser (67) proposed an approach to discretize the continuity equations:

$$\sum_{j \neq i} \frac{d_{ij}}{l_{ij}} \mu_{n_{ij}} \left[n_j B(\phi_j - \phi_i) - n_i B(\phi_i - \phi_j)\right] - V_i \left(r_i - G_i\right) = 0, \tag{3.35}$$

where B denotes the Bernoulli function $B(x) = \frac{x}{e^x - 1}$ and the mobility μ_{ij} is assumed constant on the edge l_{ij}. Similarly for the continuity equation for holes.

The Poisson's, the continuity and the transport equations are discretized in each node of the grid mesh. The unknowns are the carrier concentrations n, p and the electrostatic potential ϕ. The system of PDEs is then solved by the iterative Newton method, which, at each computation step, calculates a new solution until a breaking criterion is reached.

3.3 Propagation of electromagnetic waves

3.3.1 From Maxwell equations to homogeneous Helmholtz equation

A portion of space with a given distribution of current density $\mathbf{J}_i(\mathbf{r},t)$ is considered. The vector $\mathbf{r}$ defines the position and t is the time. The electromagnetic field produced by $J_i(\mathbf{r},t)$ is given by the time and position dependent intensity of electric field $\mathbf{E}(\mathbf{r},t)$ and by the intensity of magnetic field $\mathbf{H}(\mathbf{r},t)$ which satisfy the following system of differential equations:

$$\begin{cases} \nabla \times \mathbf{H}(\mathbf{r},t) = \frac{\partial \mathbf{D}(\mathbf{r},t)}{\partial t} + \mathbf{J}_C(\mathbf{r},t) + \mathbf{J}_i(\mathbf{r},t), \\ \nabla \times \mathbf{E}(\mathbf{r},t) = -\frac{\partial \mathbf{B}(\mathbf{r},t)}{\partial t}. \end{cases} \tag{3.36}$$

which are known as Maxwell equations. $\mathbf{D}(\mathbf{r},t)$ denotes the electric displacement while its partial derivative with respect to the time is the displacement current density. $\mathbf{J}_c(\mathbf{r},t)$ and $\mathbf{B}(\mathbf{r},t)$ are the conduction current density and the magnetic induction, respectively. $\mathbf{J}_c(\mathbf{r},t)$, $\mathbf{B}(\mathbf{r},t)$ and $\mathbf{D}(\mathbf{r},t)$ describe the reaction of the material to the electromagnetic field in terms of free charge transport, magnetic polarization and electric polarization of atoms and molecules, respectively. For a generic material we can write:

$$\mathbf{D}(\mathbf{r},t) = \mathcal{D}\left[\mathbf{E}(\mathbf{r},t), \mathbf{H}(\mathbf{r},t), t\right] \tag{3.37}$$

$$\mathbf{B}(\mathbf{r},t) = \mathcal{B}\left[\mathbf{E}(\mathbf{r},t), \mathbf{H}(\mathbf{r},t), t\right] \tag{3.38}$$

$$\mathbf{J}_C(\mathbf{r},t) = \mathcal{J}\left[\mathbf{E}(\mathbf{r},t), \mathbf{H}(\mathbf{r},t), t\right] \tag{3.39}$$

where $\mathcal{D}$, $\mathcal{B}$ and $\mathcal{J}$ are integral-differential operators which can be non linear, in the most general case. Eq. 3.37, eq. 3.38 and 3.39 are the constitutive relations of the material describing the electrical response of various media to the electromagnetic field. The trivial problem of the solution to the Maxwell equation can be simplified under some assumptions. The first one is the condition of time-invariant medium, which requires that the material does not change its electromagnetic parameters during an arbitrary period of time and that its position never changes with respect to an observer. These assumptions lead to the existence of operators which depends only on the position

r. If the material is nondispersive, time-invariant, linear and anisotropic, equations 3.37, 3.38 and 3.39 read:

$$\mathbf{D}(\mathbf{r},t) = \bar{\varepsilon}(\mathbf{r}) \cdot \mathbf{E}(\mathbf{r},t) \tag{3.40}$$

$$\mathbf{B}(\mathbf{r},t) = \bar{\mu}(\mathbf{r}) \cdot \mathbf{H}(\mathbf{r},t) \tag{3.41}$$

$$\mathbf{J}_C(\mathbf{r},t) = \bar{c}(\mathbf{r}) \cdot \mathbf{E}(\mathbf{r},t) \tag{3.42}$$

where the third equation is the Ohm's Law, $\bar{\varepsilon}(\mathbf{r})$, $\bar{\mu}(\mathbf{r})$ and $\bar{\mathbf{c}}(\mathbf{r})$ are called permittivity, magnetic permeability and conducibility, respectively; for a linear and anisotropic medium they are second-order tensors, therefore, for instance, in case of the permeability,

$$\mathbf{B}(\mathbf{r},t) = \bar{\mu}(\mathbf{r}) \cdot \mathbf{H}(\mathbf{r},t) = \begin{bmatrix} \mu_{11}(\mathbf{r}) & \mu_{12}(\mathbf{r}) & \mu_{13}(\mathbf{r}) \\ \mu_{21}(\mathbf{r}) & \mu_{22}(\mathbf{r}) & \mu_{23}(\mathbf{r}) \\ \mu_{31}(\mathbf{r}) & \mu_{32}(\mathbf{r}) & \mu_{33}(\mathbf{r}) \end{bmatrix} = \begin{bmatrix} H_1(\mathbf{r},t) \\ H_2(\mathbf{r},t) \\ H_3(\mathbf{r},t) \end{bmatrix}. \tag{3.43}$$

where H_1, H_2 and H_3 are the scalar components of the vector field $\mathbf{H}$ and $\mu(\mathbf{r})$ is a 3×3 matrix of elements $\mu_{ij}, i = 1..3, \qquad j = 1..3$. An anisotropic material is a lossless or non-dissipative material if, in every point of the space, $\mu(\mathbf{r})$ and $\varepsilon(\mathbf{r})$ are symmetric tensors and $c(\mathbf{r})$ is antisymmetric, or

$$\bar{\varepsilon}^T(\mathbf{r}) = \bar{\varepsilon}(\mathbf{r}), \qquad \bar{\mu}^T(\mathbf{r}) = \bar{\mu}(\mathbf{r}), \qquad \bar{c}^T(\mathbf{r}) = \bar{c}(\mathbf{r}). \tag{3.44}$$

Finally, the medium is homogenous if the tensors in eq. 3.39, 3.38 and 3.37 are not dependent on the position.

If $\mathbf{H}(\mathbf{r},t)$, $\mathbf{D}(\mathbf{r},t)$, $\mathbf{J}_c(\mathbf{r},t)$, $\mathbf{J}_i(\mathbf{r},t)$, $\mathbf{B}(\mathbf{r},t)$ and $\mathbf{E}(\mathbf{r},t)$ are sinusoidal functions of time with the same angular frequency ω, the following complex vector field

$$\tilde{T}(\mathbf{r},t) = Re\left[\mathbf{T}(\mathbf{r},t)e^{i\omega t}\right] \tag{3.45}$$

can be introduced, in which $\mathbf{T}$ denotes one of the vector fields $\mathbf{H}(\mathbf{r},t)$, $\mathbf{E}(\mathbf{r},t)$, $\mathbf{D}(\mathbf{r},t)$, $\mathbf{J}_C(\mathbf{r},t)$, $\mathbf{J}_i(\mathbf{r},t)$ or $\mathbf{B}(\mathbf{r},t)$. By introducing the complex permittivity $\varepsilon_c(\mathbf{r},\omega)$ defined by

$$\varepsilon_c(\mathbf{r},\omega) = \varepsilon(\mathbf{r},\omega) + \frac{c(\mathbf{r},\omega)}{j\omega}, \tag{3.46}$$

it is possible to reformulate the Maxwell equations as (68):

$$\begin{cases} \nabla \times \mathbf{H}(\mathbf{r},\omega) = i\omega\varepsilon_c(\mathbf{r},\omega)\mathbf{E}(\mathbf{r},\omega) + \mathbf{J}_i(\mathbf{r},\omega) \\ \nabla \times \mathbf{E}(\mathbf{r},\omega) = -i\omega\mu(\mathbf{r},\omega)\mathbf{H}(\mathbf{r},\omega) \end{cases} \tag{3.47}$$

In case of normal and homogenous materials without sources, the Maxwell equations read:

$$\begin{cases} \nabla \times \mathbf{H}(\mathbf{r},\omega) = i\omega\varepsilon_c(\omega)\mathbf{E}(\mathbf{r},\omega) \\ \nabla \times \mathbf{E}(\mathbf{r},\omega) = -i\omega\mu(\omega)\mathbf{H}(\mathbf{r},\omega) \end{cases} \tag{3.48}$$

Since it is possible to derive that for homogeneous materials (68)

$$\nabla \cdot \mathbf{H}(\mathbf{r},\omega) = 0, \tag{3.49}$$

and by defining

$$\sigma^2(\omega) = -\omega^2\mu(\omega)\varepsilon_c(\omega), \tag{3.50}$$

the following equations

$$\begin{cases} \nabla^2\mathbf{E}(\mathbf{r},\omega) - \sigma^2(\omega)\mathbf{E}(\mathbf{r},\omega) = 0 \\ \nabla^2\mathbf{H}(\mathbf{r},\omega) - \sigma^2(\omega)\mathbf{H}(\mathbf{r},\omega) = 0 \end{cases} \tag{3.51}$$

can be derived. Such equations are known as homogenous Helmholtz equations. They are called homogenous since no charges are present in the space. On the contrary, in case of presence of electromagnetic sources, if the medium is homogeneous, similar equations can be derived. The main advantage of the Helmholtz equations with respect to the Maxwell equations is their easier integration in order to calculate the electromagnetic field. However, eq. 3.51 is a 4th-order system of differential equations while eq. 3.48 is a system of 2nd-order differential equations, therefore it is possible to find solutions of eq. 3.51 that are not solutions of eq. 3.48. The eq. 3.51 can be considered a reformulation of the Maxwell equations of the sinusoidal electromagnetic field to describe the propagation of waves in homogeneous media.

3.3.2 Solution of Helmholtz equations for a normal homogenous medium without sources

In the following, a portion of the space which does not include sources and that is occupied by a passive, normal and homogenous medium (for which μ, ε and c are not dependent on the position) is considered. In addition, the sinusoidal electromagnetic field with angular frequency ω is supposed to be dependent only on the y-coordinate. Therefore, from eq. 3.51, for each Cartesian component $g(r)$ of the complex electromagnetic field:

$$\frac{d^2g(r)}{dy^2} - \sigma^2 g(r) = 0, \tag{3.52}$$

where

$$\sigma^2 = -\omega^2\mu\varepsilon + i\omega\mu c. \tag{3.53}$$

For a homogenous medium, $\mu > 0$, $\epsilon > 0$ and $c \geq 0$. For a passive medium, if $\sigma = \alpha + i\beta$ denotes the intrinsic propagation constant of the material, then the general solution of eq. 3.52 is

$$g(r) = G_1 e^{-\sigma y} + G_2 e^{\sigma y} \tag{3.54}$$

where G_1 and G_2 are arbitrary integration constants. Therefore the time-dependent solution is:

$$g(r,t) = G_1 e^{-\alpha y}\cos(\omega t - \beta y) = G_1 e^{-\alpha y}\cos\left[\beta\left(y - v_p t\right)\right] \tag{3.55}$$

that represents a progressive sine wave propagating towards positive y with speed

$$v_p = \frac{\omega}{\beta}. \tag{3.56}$$

Such wave propagates with an attenuation factor $\exp(-\alpha y)$ where α is the absorption coefficient (already defined in chapter 2) or the intrinsic attenuation coefficient of the medium.

The phase of the sinusoidal wave is defined by $\phi = -\beta y$, where β is the phase constant (intrinsic) of the medium. If the surface on which the phase is constant is a plane, eq. 3.55 represents a uniform plane wave.

3.3.3 TE and TM plane waves

A more general solution of the Helmholtz equation

$$\nabla^2 g - \sigma^2 g = \frac{\partial^2 g}{\partial x^2} + \frac{\partial^2 g}{\partial y^2} + \frac{\partial^2 g}{\partial z^2} - \sigma^2 g = 0 \tag{3.57}$$

is a linear combination of solutions of the form (68):

$$g(x, y, z) = g_0 e^{-U_x x} e^{-U_y y} e^{-U_z z}, \tag{3.58}$$

where $U_j, \qquad j = x, y, z$ are arbitrary constants which must satisfy the condition $U_x^2 + U_y^2 + U_z^2 = \sigma^2$ and u_0 is an arbitrary integration constant.

If the position vector is expressed as $\mathbf{r} = x\hat{\mathbf{i}}_x + y\hat{\mathbf{i}}_y + z\hat{\mathbf{i}}_z$, the wave propagation vector is defined as $\mathbf{K} = K_x\hat{\mathbf{i}}_x + K_y\hat{\mathbf{i}}_y + K_z\hat{\mathbf{i}}_z$. The most general solution of the Helmholtz equations for the field intensity are therefore given by superposition of the following vector fields

$$\mathbf{E}(\mathbf{r}) = \mathbf{E}_0 e^{(-\mathbf{K}\cdot\mathbf{r})}, \qquad \mathbf{H}(\mathbf{r}) = \mathbf{H}_0 e^{(-\mathbf{K}\cdot\mathbf{r})}, \tag{3.59}$$

where $\mathbf{H}_0$ and $\mathbf{E}_0$ are constant complex vectors. In addition it is possible to write $\mathbf{K} = \mathbf{K}_1 + i\mathbf{K}_2$ and

$$\mathbf{K}_1 = \|K_1\|\hat{\mathbf{s}}_1, \qquad \mathbf{K}_2 = \|K_2\|\hat{\mathbf{s}}_2 \tag{3.60}$$

If $\hat{\mathbf{s}}_0 = \hat{\mathbf{s}}_1 = \hat{\mathbf{s}}_2$ then $\mathbf{K} = (\alpha + i\beta)\hat{\mathbf{s}}_0 = \sigma\hat{\mathbf{s}}_0$, therefore

$$\mathbf{E}(\mathbf{r}) = \mathbf{E}_0 e^{(-\sigma\hat{\mathbf{s}}_0\cdot\mathbf{r})}, \qquad \mathbf{H}(\mathbf{r}) = \mathbf{H}_0 e^{(-\sigma\hat{\mathbf{s}}_0\cdot\mathbf{r})}, \tag{3.61}$$

and

$$\hat{\mathbf{s}}_0 \cdot \mathbf{E}_0 = 0, \qquad \hat{\mathbf{s}}_0 \cdot \mathbf{H}_0 = 0, \tag{3.62}$$

$$\mathbf{E}_0 = \eta\mathbf{H}_0 \times \hat{\mathbf{s}}_0 \tag{3.63}$$

$$\mathbf{H}_0 = \frac{1}{\eta}\hat{\mathbf{s}}_0 \times \mathbf{E}_0, \tag{3.64}$$

where

$$\eta = \frac{\sigma}{j\omega\varepsilon_c} = \sqrt{\frac{\mu}{\varepsilon_c}} \tag{3.65}$$

is the intrinsic impedance of the homogenous medium.

In particular $\hat{\mathbf{s_0}} \cdot \mathbf{r}$ (the surfaces with same value of the phase -or wavefronts- are planes) is constant and the eq. 3.61 represent plane waves with propagation direction $\hat{\mathbf{s_0}}$. In addition, on the wavefronts the intensity is constant; these waves are called transverse electromagnetic waves or TEM waves. It is possible to demonstrate that these solutions are not physically possible since they carry an infinite power along the propagation direction. Their importance is only theoretical.

If the fields can be expressed as

$$\mathbf{E} = \mathbf{E}_0 \exp(-K_{n_1} \hat{s}_1 \cdot \mathbf{r}) \exp(-iK_{n_2} \hat{s}_2 \cdot \mathbf{r}) \tag{3.66}$$

$$\mathbf{H} = \mathbf{H}_0 \exp(-K_{n_1} \hat{s}_1 \cdot \mathbf{r}) \exp(-iK_{n_2} \hat{s}_2 \cdot \mathbf{r}) \tag{3.67}$$

where $K_{n_q}, q = 1, 2$ are arbitrary constants, the solution is still a plane wave, being the locus of the points with the same phase (wavefront surface) still planes perpendicular to $\hat{\mathbf{s}}_2$. In this case, the intensity of the fields is not constant on the wavefront; however, on surfaces for which $\hat{\mathbf{s}}_1 \cdot \mathbf{r}$ is constant, the vector field norms are constant and such planes are normal to the direction of attenuation of the wave. Therefore these waves are characterized by different direction of propagation and attenuation. In particular if

$$\mathbf{E}_0 = E_0 \hat{s}_1 \times \hat{s}_2 \tag{3.68}$$

then $\hat{\mathbf{s}}_2 \cdot \mathbf{E}_0 = 0$ and $\mathbf{H}$ is elliptically polarized on the plane defined by $\hat{\mathbf{s}}_1$ and $\hat{\mathbf{s}}_2$. In addition, $\mathbf{H}$ exhibits always a component along $\hat{\mathbf{s}}_2$. This waves is called transverse electric (TE). Similarly for a transverse magnetic (TM) wave:

$$\mathbf{H}_0 = H_0 \hat{s}_1 \times \hat{s}_2 \tag{3.69}$$

The most general plane wave is obtained by superposition of TE and of TM waves.

3.3.4 Geometrical optics and raytracing

In the following, a portion of space without sources and featuring a normal medium without losses is considered. Since a non-homogeneous medium is assumed, $\mu = \mu(\mathbf{r})$ and $\varepsilon = \varepsilon(\mathbf{r})$.

In addition, the conditions that allows to obtain solutions of Maxwell equations for which, for every point of the spatial domain, it is possible to define an arbitrary small region with finite volume within which the field intensities satisfies equations similar to eq. 3.61, eq. 3.62, eq. 3.63 and eq. 3.64, are discussed.

The goal is to determine solutions in the form

$$\mathbf{E}(\mathbf{r}) = \mathbf{E}_0(\mathbf{r})\exp\left[-\beta_0 V(\mathbf{r})\right] \tag{3.70}$$

$$\mathbf{H}(\mathbf{r}) = \mathbf{H}_0(\mathbf{r})\exp\left[-\beta_0 V(\mathbf{r})\right] \tag{3.71}$$

where $V(\mathbf{r})$ is called iconal function and $\beta_0 = \omega\sqrt{\mu_0\varepsilon_0}$ is the intrinsic phase constant in vacuum. If the refractive index of the medium is defined as

$$n(\mathbf{r}) = \sqrt{\frac{\mu(\mathbf{r})\varepsilon(\mathbf{r})}{\mu_0\varepsilon_0}}, \tag{3.72}$$

the Maxwell equations can be reframed as:

$$\begin{cases} \frac{n(\mathbf{r})}{\eta(\mathbf{r})}\mathbf{E}_0(\mathbf{r}) - \frac{1}{i\beta_0}\nabla\times\mathbf{H}_0(\mathbf{r}) = \mathbf{H}_0(\mathbf{r})\times\nabla V(\mathbf{r}) \\ n(\mathbf{r})\eta(\mathbf{r})\mathbf{H}_0(\mathbf{r}) + \frac{1}{i\beta_0}\nabla\times\mathbf{E}_0(\mathbf{r}) = \nabla V(\mathbf{r})\times\mathbf{E}_0(\mathbf{r}). \end{cases} \tag{3.73}$$

If

$$\|\lambda_0\eta(\mathbf{r})\nabla\times\mathbf{H}_0(\mathbf{r})\| \ll \|\mathbf{E}_0(\mathbf{r})\| \tag{3.74}$$

$$\|\lambda_0\nabla\times\mathbf{E}_0(\mathbf{r})\| \ll \|\eta(\mathbf{r})\mathbf{H}_0(\mathbf{r})\| \tag{3.75}$$

therefore

$$\begin{cases} \mathbf{E}_0(\mathbf{r}) = \eta(\mathbf{r})\mathbf{H}_0(\mathbf{r})\times\frac{\nabla V(\mathbf{r})}{n(\mathbf{r})} \\ \eta(\mathbf{r})\mathbf{H}_0(\mathbf{r}) = \frac{\nabla V(\mathbf{r})}{n(\mathbf{r})}\times\mathbf{E}_0(\mathbf{r}) \end{cases} \tag{3.76}$$

where $\lambda_0 = \frac{2\pi}{\beta_0}$.

It is possible to demonstrate that the eq. 3.76 represents a local plane wave of TEM type with respect to the direction given by $\nabla V(\mathbf{r})$ (68). In order to make the eq. 3.76 valid, it is necessary to ensure that:

$$|\lambda_0 \nabla \cdot \mathbf{E}_0(\mathbf{r})| \ll \|\mathbf{E}_0(\mathbf{r})\| \tag{3.77}$$

$$|\lambda_0 \nabla \cdot \mathbf{H}_0(\mathbf{r})| \ll \|\mathbf{H}_0(\mathbf{r})\| \tag{3.78}$$

$$|\lambda_0 \nabla \varepsilon(\mathbf{r})| \ll \varepsilon(\mathbf{r}) \tag{3.79}$$

$$|\lambda_0 \nabla \mu(\mathbf{r})| \ll \mu(\mathbf{r}). \tag{3.80}$$

In conclusion, the electromagnetic field can be described in terms of local TEM plane waves when its components and the intrinsic parameters of the medium are not significantly dependent on the position within any spatial variation of coordinates comparable to λ_0: it means that, the approximation introduced by eq. 3.70 and by eq. 3.71, is valid when the size of the structures -that contributes to the definition of the electromagnetic field distribution within the portion of interest of the domain- is significantly larger than the wavelength of the radiation.

By solving for $\mathbf{E}_0(\mathbf{r})$ and $\mathbf{E}_0(\mathbf{r})$:

$$\left[\nabla V(\mathbf{r}) \cdot \nabla V(\mathbf{r}) - n^2(\mathbf{r})\right] \mathbf{E}_0(\mathbf{r}) = 0, \tag{3.81}$$

$$\left[\nabla V(\mathbf{r}) \cdot \nabla V(\mathbf{r}) - n^2(\mathbf{r})\right] \mathbf{H}_0(\mathbf{r}) = 0. \tag{3.82}$$

These equations are not coupled and do not allow non-banal solutions if

$$\nabla V(\mathbf{r}) \cdot \nabla V(\mathbf{r}) = n^2(\mathbf{r}). \tag{3.83}$$

The eq. 3.83 is the fundamental equation of geometrical optics; it is a non-linear partial differential equation which admits an infinite number of possible solutions. Each

particular integral of such equation defines a wave according to the given distribution of the refractive index. The related wavefront is described by the equation

$$V(\mathbf{r}) = C_0 \tag{3.84}$$

where C_0 is an arbitrary real constant.

The normal trajectories to the surfaces defined by eq. 3.84, for any value of the real constant C_0, are called electromagnetic rays. For a given distribution of the refractive index $n(\mathbf{r})$, the optical problem is solved by determining the rays by means of a technique called raytracing.

The geometrical optics approximation is not valid when discontinuities of the medium are assumed. This problem is solved by assuming that each ray, impinging on a surface of discontinuity, acts like a local plane wave which behaves exactly as a uniform wave plane exhibiting the same conditions of incidence in the whole surface. Therefore, rays follow the reflection and transmittance rules defined by the Snell's Law for the plane waves (69).

Since intensity, direction and polarization are the sole information associated to rays, raytracing is not suitable to describe phenomena such as interference and diffraction. The raytracer algorithm uses a recursive method which starts with a source ray and builds a binary tree that tracks the transmission and reflection of the ray at interfaces between media featuring different refractive indices. At interfaces, incident rays split into reflected and transmitted rays: the TE component of the polarization vector maintains the same direction, whereas the TM component changes direction.

Raytrace extensions proposed in commercial simulators like Sentaurus (46) and Silvaco Atlas (70) allow to define special boundary conditions with in order to model interfaces with constant reflectivity/transmittivity, multilayer ARC layers and diffusive reflections. In (70), by default, the diffusive reflection features a Lambertian distribution (exhibiting constant luminance with respect to the angle). Gaussian or Lorenz distributions can be chosen. The raytracer has been successfully adopted to calculate the optical behaviour of a textured silicon wafer in (71).

The Monte Carlo ray trace algorithm (72) is helpful to simulate random textured interfaces like those of thin film solar cells. The light scattering from rough interfaces is determined by using probabilistic estimation through random number generation. Each ray is traced in the direction of propagation until it scatters from an interface;

consequently, reflection and transmission probabilities are estimated by means of standard equations used to calculate transmittance and reflectance. The random number generated by assuming a uniform distribution is compared against the transmission or reflection probability in order to discriminate the sole ray to trace at each scattering event. Interfaces may be described by angular distribution functions (ADFs), which associate a value of intensity of the light to each scattering angle. Arbitrary ADFs can be defined. The modified angle is used to calculate the transmission and reflection probabilities as well as the transmission and reflection angles.

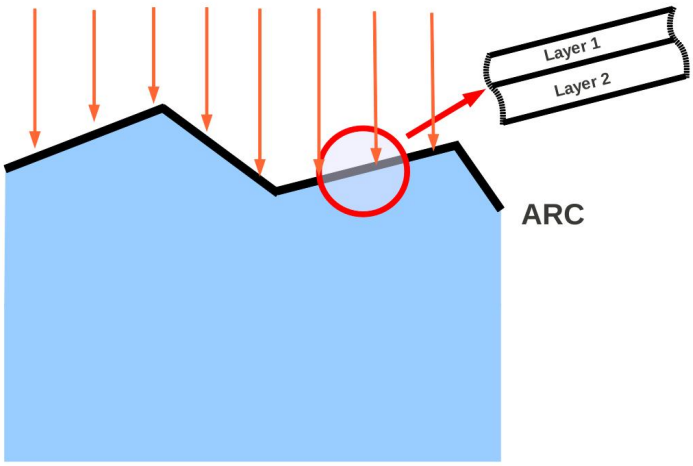

Figure 3.4: Thin-layer-stack boundary condition used to simulate ARCs with RayTracing in combination with the TMM solver.

A thin-layer-stack boundary condition is helpful to simulate ARCs (Fig. 3.4). The angle of incidence of the ray -with respect to the normal to the coating layer surface- is passed as input to the Transfer Matrix Method (TMM) solver (46) which can calculate the reflectance, the transmittance, and the absorbance for thin layers featuring parallel interfaces. The angle of refraction is calculated by the raytracer according to Snell's law in order to ensure the phase matching.

According to Fig. 3.5, which shows the sketch of an infinitely spatially extended planar interface between two lossless media of refractive indices n_1 (for the incident and reflected rays) and n_2 (for transmitted rays), the incident, the reflected and the transmitted angles are denoted by θ_i, θ_r and θ_t, respectively. The scattering of rays

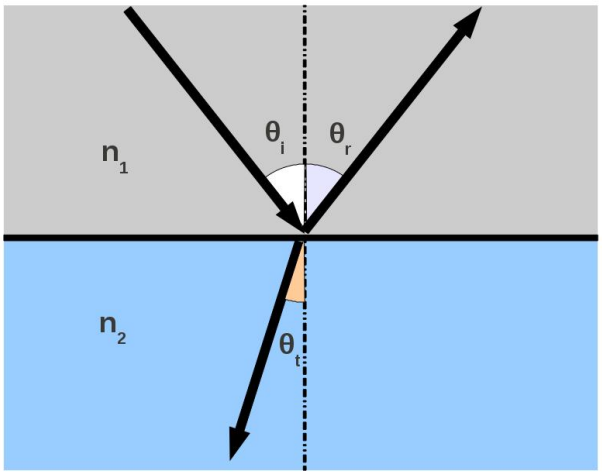

Figure 3.5: Reflection, transmission and refraction of plane waves at a planar interface.

from smooth interfaces is governed by the the Snell's law of the specular reflection. Therefore the transmitted and the reflected angles are linked to that of incidence by the following equations:

$$\theta_r = \theta_i. \tag{3.85}$$

$$n_1 \sin(\theta_i) = n_2 \sin(\theta_t). \tag{3.86}$$

The amplitudes of the electric field for the TE and the TM polarizations are described by

$$E_R^{TE} = \frac{n_2 \cos(\theta_i) - n_1 \cos(\theta_t)}{n_2 \cos(\theta_i) + n_1 \cos(\theta_t)} E_i^{TE}. \tag{3.87}$$

$$E_R^{TE} = \frac{2 n_1 \cos(\theta_i)}{n_2 \cos(\theta_i) + n_1 \cos(\theta_t)} E_i^{TE}. \tag{3.88}$$

$$E_R^{TM} = \frac{n_1 \cos(\theta_i) - n_2 \cos(\theta_t)}{n_1 \cos(\theta_i) + n_2 \cos(\theta_t)} E_i^{TM}. \tag{3.89}$$

$$E_R^{TM} = \frac{2 n_1 \cos(\theta_i)}{n_1 \cos(\theta_i) + n_2 \cos(\theta_t)} E_i^{TM}. \tag{3.90}$$

Thus, the reflectance for the TM case is

$$R^{TM} = \left(\frac{E_r^{TM}}{E_i^{TM}} \right)^2 . \tag{3.91}$$

Since no absorption occurs at interface, by applying the conservation of energy, the transmission is then expressed by

$$R^{TM} = 1 - R^{TM} = \left(\frac{E_t^{TM}}{E_i^{TM}} \right)^2 \frac{n_2}{n_1} \frac{\cos(\theta_t)}{\cos(\theta_i)}. \tag{3.92}$$

3.4 Finite Difference Time Domain (FDTD) Method

FDTD (73) is one of the most popular numeric methods for computational electromagnetics. It is widely applied in many different areas like electromagnetic wave propagation, antennas design and guided wave propagation. In FDTD the electromagnetic quantities are represented in the time domain and the time step is limited by a stability criterion depending upon the size of the smallest cell in the simulation grid, hence limiting the effective applicability of the method for a given frequency range. In fact, small geometric features lead to smaller time steps and hence, a larger amount of time steps are required to simulate a certain number of periods of the wave at a given frequency. Consequently, FDTD results effective with structures featuring size comparable to the wavelength of the radiation. FDTD simulates the continuous electromagnetic waves in spatial region of finite dimension by sampled-data. If the wavelength is much greater than the size, both the spatial sampling factor (or the number of grid-points per wavelength) and the temporal sampling factor (number of time steps per period) are required to be large.

FDTD is based on Maxwell curl equations in derivative form in the time domain which are expressed in a linearized form by means of central finite differences.

The Yee algorithm (74) for Maxwell's curl equations assumes a basic uniform Cartesian grid without using any potential functions. It is based on spatial sampling of the unknown near-field distribution over a period of time. The sampling in space is performed in the Nyquist sense. The sampling in time is selected to ensure numerical stability of the algorithm.

FDTD is based on second-order accurate grid-based algorithms exhibiting concurrent schemes for time-marching the six-vector components of the electromagnetic near

field. The computational burden for the FDTD involves the number of volumetric grid cells N_C -in which the six vector electromagnetic field components must be updated at every time step-, the number of time steps N_S, and the cumulative propagation errors. Overall, a computational burden of order of $N_C N_S$ of about $N_C^{\frac{4}{3}}$ is estimated for FDTD (75).

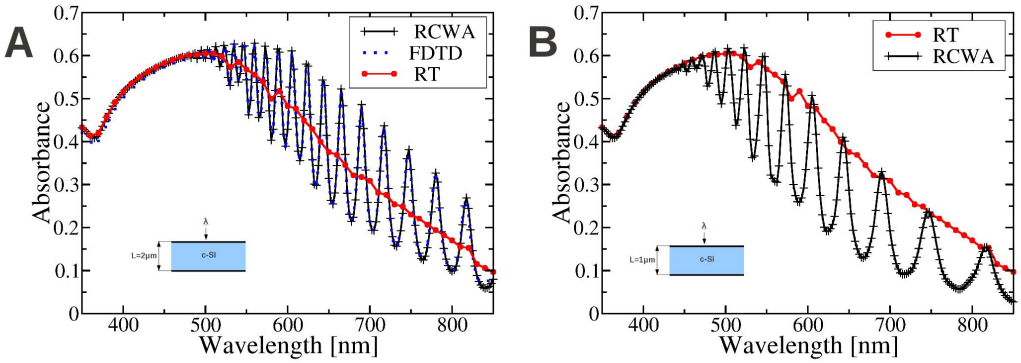

Figure 3.6: Absorbance for the $2\mu m$-thick (A) and the $1\mu m$-thick (B) slabs of crystalline silicon calculated by raytracer (RT), FDTD and RCWA methods.

As examples to put in evidence the limitations of the conventional RT method, a $2\mu m$-thick slab of crystalline silicon featuring ideal smooth interfaces is considered. The absorbance of the silicon slab has been calculated within the range of wavelengths $350nm$-$850nm$. Since the layer thickness is comparable to the wavelength, light diffraction and interference play a crucial role, therefore the optical generation rate inside the silicon layer calculated by raytrace (RT) is affected by significant error. Fig. 3.6A reports the absorbance as calculated by means of RT, RCWA (which will be described in detail in chapter 5) and FDTD simulations. The absorbance calculated by RT differs from those calculated by RCWA and FDTD, as it features an absolute maximum at around $500nm$ and a monotonic trend up to $850nm$. The absorbance curves, calculated by means of methods based on the solution of Maxwell's equations like RCWA and FDTD, are almost coincident. They feature a set of maxima and minima at relatively large wavelengths, due to the finite thickness of the silicon layer. For this particular example, by assuming a standard AM1.5G spectrum, the total absorbed energy integrated over the whole spectrum is essentially the same for all the considered methods. If the silicon thickness of the layer is further reduced (Fig. 3.6B) the absorbed energy

weighted by the AM1.5G spectrum provided by raytrace is significantly overestimated in comparison with that calculated by RCWA (or by other rigorous solvers of the Maxwell's equations).

4

Modeling of advanced crystalline silicon solar cells

This chapter is a contribution towards the 2-D and 3-D electro-optical numerical simulation of advanced crystalline silicon solar cells. Two applications of numerical TCAD simulations are presented. The first application concerns the modeling of a selective emitter solar cell which, due to the adopted scheme of doping profiles in the emitter section of the cell, requires a 2-D simulation. The second application is about a rear point contact solar cell. Rear point contact schemes are used in high-efficiency devices like PERC and PERL solar cells (introduced in chapter 2) and require true 3-D cpu-intensive numerical simulations. In this chapter the simulated devices and the related simulation setups are described in detail. Finally, the simulation results and the conclusions are discussed.

4.1 Selective emitter solar cells

4.1.1 Introduction to selective emitter solar cells

The improvement of the emitter and of the front contact scheme of crystalline solar cells is a challenging goal which requires to account for several trade-offs in the optimization of the device. A paramount requirement of the emitter of high-performance solar cells is the capability to collect photo-generated carriers with high efficiency; this goal may be achieved by designing emitters featuring good transport properties and low recombination losses. An ideal emitter electrode requires high doping levels to be an ohmic

contact; on the other hand, large doping concentration leads to high recombination losses (Auger, trap-assisted as well as surface recombination). Several approaches have been proposed to improve the emitter of solar cells: optimized silver pastes (44)(76) and seed-and-plate approach (77)(78) are promising techniques to allow the contact of high-sheet resistance emitters (above $65\Omega/sq$).

Another approach to boost the solar cell efficiency for low-cost and high-volume productions is the selective emitter design. Selective emitter (SE) (or double-diffused) solar cells, in contrast with standard screen-printed industrial homogeneously diffused emitter (HE) cells are characterized by different doping profiles in the emitter region (Fig. 4.1). A first lowly-doped and shallow diffusion (LDOP), under the passivated uncontacted front-side interface between fingers is followed by a heavy and deep phosphorus diffusion (HDOP) in correspondence of the contacted interface under the metal front fingers (79).

The advantages of the SE cell over the conventional HE cells, are provided by reduced Auger and surface recombination effects in the passivated LDOP surface region and by enhanced spectral response in the blue region (80)(81) because of the reduced doping concentration. However, the adoption of a lowly-doped diffusion between front-contact fingers in the illuminated area, leads to relatively large emitter resistance which contributes to the reduction of the FF, as shown in chapter 2. In SE solar cells a good ohmic contact is ensured by the HDOP diffusion in the non-illuminated region.

Another crucial trade-off in the front-side design of the solar cell is that between the front-contact pitch (or the distance between fingers) and the emitter resistance. Large front contact pitch leads to relatively higher photo-generated current density because of the reduced front contact shadowing. However, the distance between fingers has a strong impact on emitter resistance and hence on FF. Since the emitter resistance, for a given emitter geometry is dependent on the emitter sheet resistance, SE and HE cells designs lead to different optimum values of the front contact pitch.

In previous works the impact of the emitter doping profile has been analyzed by means of analytical models or by 1-D numerical simulations (82)(83).

In this section, 2-D numerical simulations have been successfully used to optimize the emitter design and to investigate the main loss mechanisms which lead to the above described trade-offs. In the following a homogeneous emitter solar cell (optimized in

terms of front contact pitch) is used as reference cell for the SE design, allowing to quantify the predicted enhancement of performance obtainable by the SE. In particular, the dependence of the main figures of merit of the cell on the front metal contact pitch (W_{SUB}) is investigated by using as simulation parameters the doping and geometrical parameters of the HDOP and LDOP diffusions. 2-D simulations are helpful to appreciate the effects of recombination mechanisms which are strongly dependent on the doping concentration as well as to take advantage of the more realistic modeling of the multi-dimensional transport. Indeed, in addition to discriminate regions with different doping concentration (like that between front-contact fingers and that of the non-illuminated regions under the front-contact fingers), a 2-D analysis allows to take into account for the contact shadowing, differently from 1-D simulations. Therefore, for this kind of structures, the lack of 2-D capability of mono-dimensional simulators, like PC-1D (5), which is a well-known and widely used tool in photovoltaic community, may result in inaccurate predictions of expected performance.

4.1.2 Selective emitter solar cells: simulation setup and simulated devices

All the considered cells feature a p-type base region, wafer thickness $D_{SUB} = 180\mu m$, front-contact finger width $W_{MET} = 100\mu m$ and a lateral width of the HDOP diffusion under the finger $W_{SE} = 130\mu m$ (Fig. 4.1A). Doping profiles are chosen as described in the following: the boron-doped base doping concentration is equal to $N_{SUB} = 10^{16} cm^{-3}$ (which corresponds to a substrate resistivity of $1.33\Omega cm$ assuming a constant mobility for holes equal to $470.5 cm^2 V^{-1} s^{-1}$), the boron $p+$ BSF diffusion (common for SE and HE cells) is described by an error function of the depth (starting from the back contact interface) featuring a peak doping concentration $C^{pk}_{BSF} = 10^{20} cm^{-3}$ and junction depth equal to $0.6\mu m$. The HDOP profile is described by an analytical function with parametric junction depth and peak doping in order to obtain different values of the sheet resistance. The LDOP profiles are described by analytical error functions with constant junction depth ($0.27\mu m$) and variable peak doping. Finally, the emitter profile in the HE cell features a sheet resistance of $39\Omega/sq$ resulting from an error function profile characterized by peak doping concentration equal to $C^{pk}_{HE} = 3.7 \times 10^{20} cm^{-3}$ and junction depth of $0.39\mu m$. All sheet resistance values are calculated by using the Arora

model (chapter 2) with Sentaurus' default parameters. The emitter profiles for the SE and the HE solar cells are shown in Fig. 4.1B.

Surface recombination velocity is set to $10^5 cm/s$ (constant) for the metal front and back contacts. The surface recombination velocity at the front passivated interface is assumed to be dependent on the surface doping concentration of the emitter according to the surface SRH model of Sentaurus described in chapter 3, eq. 3.25, with $S_0 = 20cm/s$, $N_{REF} = 10^{16} cm^{-3}$ and $S_{REF} = 10^{-3}$. For instance, if the surface doping concentration is $10^{20} cm^{-3}$, $S = 220cm/s$.

Electrical simulations take into account Auger recombination, doping dependent Shockley-Read-Hall (SRH) bulk and surface recombination, radiative recombination, band-gap narrowing (del Alamo model), doping dependence of carrier mobility (Philips Unified mobility model) and mobility degradation at high fields (Canali Model). The standard Sentaurus' model for intrinsic carrier concentration is adopted (leading to $n_{i,eff} = 1.41164 \times 10^{10} cm^{-3}$ at $T = 300K$ in base). Fermi statistics is adopted in this analysis in order to correct deal with heavy doping concentrations. All the models accounted in the device simulation are discussed in chapter 3.

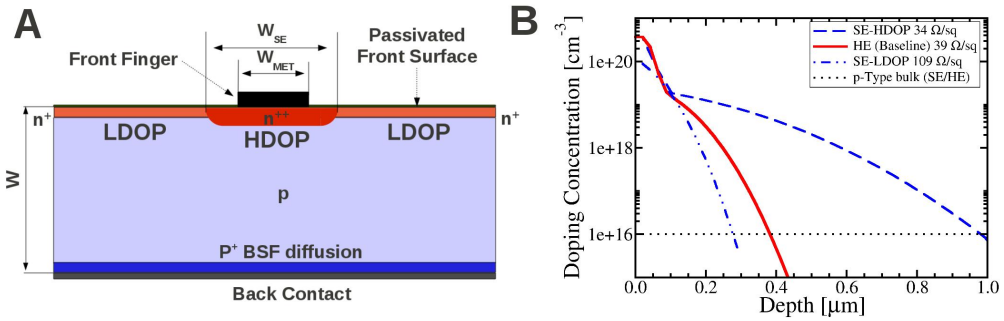

Figure 4.1: (A) Sketch of the cross section of the 2-D simulated selective emitter (SE) solar cell. HDOP and LDOP denote the highly-doped and the lowly-doped emitter profiles, respectively. W is the wafer thickness and $W_{MET} = 100\mu m$ and $W_{SE} = 130\mu m$ are the front-contact finger width and the lateral extension of the HDOP diffusion under the finger, respectively. (B) Emitter doping-profiles adopted for the simulations: the figure shows the doping profile of the homogeneous emitter (HE) solar cell ($39\Omega/sq$), that of the SE under the contact (HDOP) and the emitter profile under the passivated interface between fingers (LDOP) featuring a sheet resistance of $39\Omega/sq$ and $109\Omega/sq$, respectively.

The optical generation resulting from a spectral illumination source (standard AM1.5G

spectrum $1000Wm^{-2}$, direct illumination), is modeled by superimposing the spectrally resolved generation rates. The light at the front surface is assumed to be Lambertian distributed accounting for textured interface coated by 70nm silicon nitride. The external medium is air. The multiple bounces of light inside the device are described analytically in terms of a geometric progression. External reflectivity, internal top and bottom reflectivity coefficients, which are wavelength dependent, are calculated by using the Transfer Matrix Method (TMM) (46). The shadowing under front-contact finger is assumed ideal. The calculated main figures of merit include the short circuit current density (J_{sc}), the open circuit voltage (V_{oc}), the fill factor (FF) and the efficiency (η). The parasitic series resistances are accounted using eq. 2.85 and eq. 2.86, hence the predicted electrical output power of the cell and the FF are affected by resistive losses. In particular the maximum output power is given by:

$$P_M = P_{M_0} - I_{MPP}^2 R, \tag{4.1}$$

where P_{M_0} is the effective maximum output power of the cell without resistive losses and I_{MPP} is the maximum power point current. The total series resistance is denoted by R. The metal-semiconductor-contact resistance and the contact finger resistance are calculated as discussed in chapter 2, assuming as length and thickness of the grid finger $3cm$ and $12\mu m$, respectively. The length of the finger is chosen according to the assumption of considering a cell $12.5x12.5cm^2$ for simulations. For the calculations, the sheet resistivity of the metal and the contact resistivity are set to $6 \times 10^{-6}\Omega cm$ and $10^{-3}\Omega cm^2$, (independently on the emitter doping peak concentration), respectively.

The simulations have been performed by adopting as simulation domain the 2-D symmetry element with lateral size defined by half front contact pitch and height equal to the wafer thickness. Typical numerical grids include 50000 vertices.

4.1.3 Homogeneous emitter solar cell simulation

The HE solar cell has been simulated by varying the front contact pitch W_{SUB} within the range $1400\mu m$-$2600\mu m$ in order to optimize the front contact pattern geometry. As discussed before, for a given front-contact metal finger width, increasing W_{SUB} results in larger J_{SC}. However, large W_{SUB} leads to larger emitter resistance that degrades the FF (Fig. 4.2C). The resulting optimum front contact pitch for the HE cell is approximately $2100\mu m$, for which the calculated efficiency is 16.81% (Fig. 4.2D).

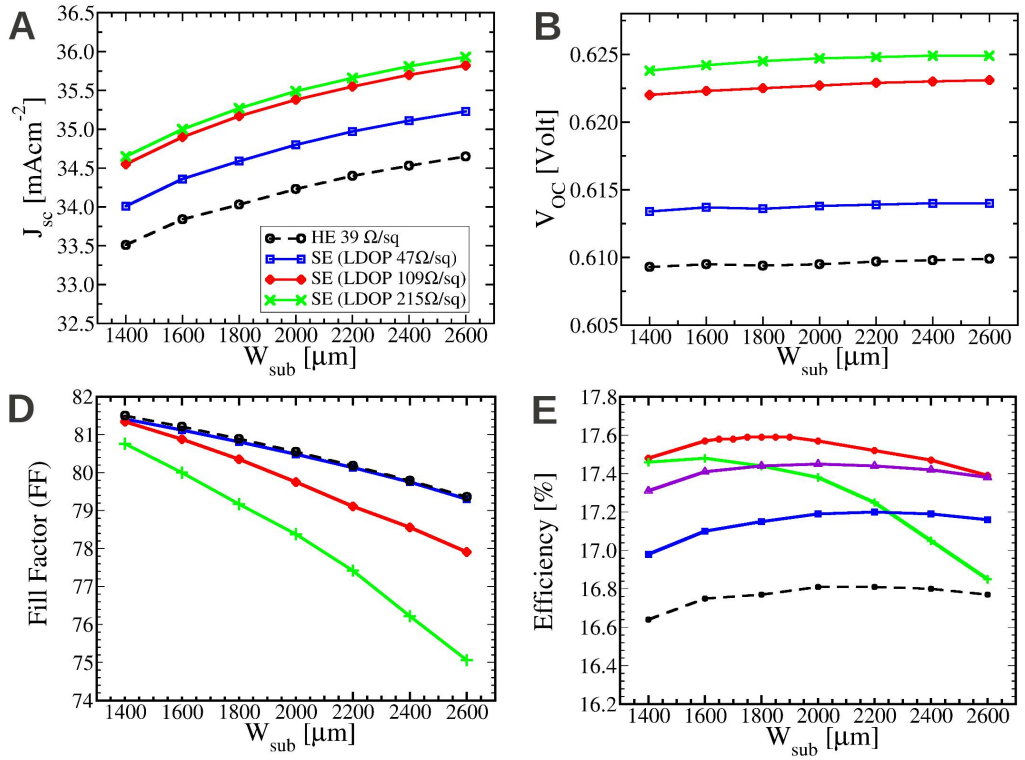

Figure 4.2: Calculated figures of merit for the SE and the HE ($39\Omega/sq$) cells. The SE are simulated with the profile HDOP featuring $34\Omega/sq$ and LDOP featuring sheet resistance values within the range $47\Omega/sq$-$215\Omega/sq$. Main figures of merit calculated by Sentaurus: (A) Short-circuit current density (J_{SC}), (B) Open-circuit voltage (V_{OC}), (C) Fill Factor (FF) and (D) conversion efficiency.

4.1.4 Selective emitter solar cell: impact of LDOP and HDOP profiles on main figures of merit

In order to optimize the LDOP profile for a given HDOP diffusion ($34\Omega/sq$, peak doping concentration $3.7 \times 10^{20} cm^{-3}$, junction depth $0.82\mu m$) the parameters affecting the analytical function which describe the doping profile LDOP are varied, resulting in sheet resistance values within the range $47\Omega/sq$-$215\Omega/sq$ (Tab. 4.1). In particular, since a constant junction depth of $0.27\mu m$ is assumed, only the peak doping of LDOP is changed from $5.0 \times 10^{19} cm^{-3}$ to $3.0 \times 10^{20} cm^{-3}$. The calculated dependence of the figures of merit on the front contact pitch is reported in Fig. 4.2 for the most significant LDOP profiles.

The trend of J_{SC} and V_{OC} are shown in Fig.4.2A and Fig. 4.2B, respectively.

Table 4.1: Peak doping and sheet resistance values of the considered lowly-doped region profiles (LDOP) for the SE solar cell. Simulated LDOP profiles are described by analytical error functions. For all LDOP profiles the junction depth is set to $0.27\mu m$.

Peak Doping $[cm^{-3}]$	Sheet Resistance $[\Omega/sq]$
3.00×10^{20}	47
2.00×10^{20}	68
1.50×10^{20}	87
1.15×10^{20}	109
1.00×10^{20}	123
9.00×10^{19}	136
5.00×10^{19}	215

For a given front contact pitch value, both J_{sc} and V_{oc} of the SE solar cells are larger with respect to those of the HE cell, because the lower doping concentration of LDOP profiles, compared to that of HE cell, results in reduced Auger, trap-assisted and surface recombination losses in the illuminated passivated region between fingers. Hence, the highest values of J_{sc} and V_{oc} are obtained by the SE solar cell featuring the LDOP profile with the lowest doping concentration (sheet resistance $215\Omega/sq$) within the considered range. Moreover, as already observed for the HE solar cell, increasing front contact pitch leads to larger J_{sc} (and consequently higher V_{oc}) due to reduced contact shadowing.

However, increasing sheet resistance of LDOP results in degraded FF due to the strong impact of doping concentration on emitter resistance (Fig. 4.2C). In addition, the increase of the front contact pitch leads to larger emitter resistance and the strongest dependence of FF on W_{SUB} is observed for the largest sheet resistance of the LDOP profile. For a given value of front-contact pitch, the lowest FF is obtained for the LDOP profile with the largest sheet resistance ($215\Omega/sq$). The trade-off between the emitter resistance, the front contact shadowing and the recombination losses in the emitter region are highlighted in Fig. 4.2D. For lower values of W_{SUB}, the efficiency benefits from the increase of both J_{sc} and V_{oc} for increasing W_{SUB}, but for higher W_{SUB}, the emitter resistance losses dominate and hence the efficiency degrades. The above discussed trade-off results in an optimum value of the front contact pitch which strongly depends on the sheet resistance of the LDOP profile. In particular, it is worth noting that the optimum W_{SUB} moves towards lower values of the pitch for higher emitter sheet resistance of LDOP. The maximum predicted efficiency is 17.59%, obtained by the SE cell characterized by LDOP with sheet resistance $109\Omega/sq$. It is worth noting that, as expected, since the resulting emitter resistance is higher than that of the HE cell, a smaller optimum value of W_{SUB} results, in comparison with the homogenous emitter case, as shown in Tab. 4.2, in which an enhancement in terms of conversion efficiency with respect to the HE cell equal to $0.78\%_{Abs}$ is reported. In addition, it can be observed that, although the optimum W_{SUB} is lower in case of the SE with respect to the HE cell, the resulting short-circuit current (and hence the open-circuit voltage) is higher than that of the reference cell.

Table 4.2: Main figures of merit of the simulated solar cells calculated by Sentaurus: short-circuit current density (J_{sc}), open-circuit voltage (V_{oc}), Fill Factor (FF) and efficiency for homogeneous emitter cell ($W_{SUB} = 2100\mu m$, $39\Omega/sq$) and the selective emitter SE cell ($W_{SUB} = 1800\mu m$, HDOP $34\Omega/sq$ and LDOP $109\Omega/sq$).

Cell Type	W_{SUB} $[\mu m]$	J_{SC} $[mAcm^{-2}]$	V_{OC} [mVolt]	FF	Efficiency [%]
HE	2100	34.32	610	80.37	16.81
SE	1800	35.13	623	80.35	17.59

The sheet resistance of the HDOP profiles has been varied from $34\Omega/sq$ to $63\Omega/sq$ (Tab. 4.3), keeping the LDOP profile constant ($109\Omega/sq$) and $W_{SUB} = 1800\mu m$. The simulation results show that there is only a slight dependence of efficiency on HDOP

parameters (peak doping, junction depth). The maximum value of conversion efficiency (17.61%) is obtained by the $46\Omega/sq$ HDOP profile. The emitter resistance is dominated by the diffusion between front-contact fingers (LDOP) and the HDOP profile has only a negligible impact on FF. The conclusion of the analysis of the dependence of the main figures of merit on the features of HDOP is that, under the adopted assumptions, in particular for low values of W_{SE}, the impact of the HDOP profile on the efficiency is weak. On the contrary, when the lateral extension of the HDOP diffusion is significantly larger than that of the front-contact finger, larger recombination losses are expected (in particular due to the Auger mechanism) because of the presence of a heavily-doped region exposed to the illumination. Ideally $W_{SE} = W_{MET}$.

Table 4.3: Peak doping, junction depth and sheet resistance values of the considered HDOP doping profiles.

Peak Doping $[cm^{-3}]$	Junction Depth $[\mu m]$	Sheet Resistance $[\Omega/sq]$
3.5×10^{20}	0.98	34
2.0×10^{20}	0.98	46
1.0×10^{20}	0.98	63
2.0×10^{20}	1.31	41
2.0×10^{20}	0.60	54

4.1.5 Selective emitter solar cell: loss analysis

The SE (featuring the doping profiles HDOP $46\Omega/sq$ and LDOP $109\Omega/sq$) and the HE ($39\Omega/sq$) solar cells are compared in terms of carrier collection efficiency (η_C) defined in chapter 2, by eq. 2.73. The results are reported in Fig. 4.3.

The SE cell features a better collection efficiency in the blue region of the spectrum ($300nm$-$600nm$) resulting in higher short-circuit current ($J_{SC} = 35.17mA/cm^2$ for SE, $J_{SC} = 34.32mA/cm^2$ for the HE cell). As remarked previously, a larger short-circuit current density is reached by the optimized SE cell although its optimum front contact pitch value is smaller than that of the HE cell. The enhancement in terms of collection efficiency is due to the lower doping concentrations in the emitter, which leads to reduced Auger recombination and to a shallow junction in the passivated emitter region, which improves separation for electron-hole pairs generated by photons at lower

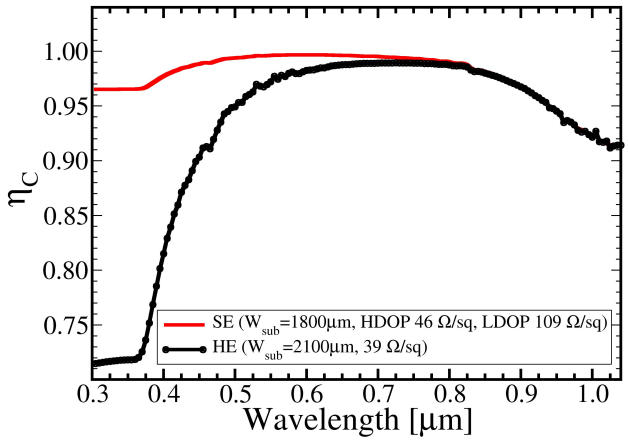

Figure 4.3: Comparison of collection efficiency of photo-generated carriers (η_C) between selective emitter SE ($W_{SUB} = 1800\mu m$, HDOP $46\Omega/sq$ and LDOP $109\Omega/sq$) and the reference homogenous emitter solar cell HE ($W_{SUB} = 2100\mu m$, $39\Omega/sq$). Larger η_C within the blue region of the spectrum ($300nm$-$600nm$) is obtained by the SE cell.

wavelengths that are absorbed close to the front surface. Furthermore, lower doping concentrations lead to reduced surface recombination rates at the front passivated interfaces. Simulations highlight the influence of Auger recombination on efficiency as the major loss mechanism of a homogeneous solar cell with heavy and deep emitter diffusions. By selectively disabling the Auger recombination effect, the SE and HE solar cells increase their efficiencies by an absolute 0.60% and 1.24%, respectively; this means that reduced Auger recombination is the main reason for higher efficiency of the SE cell with respect to the reference HE cell. The 2-D maps of the Auger recombination rates in the region close to the front surface for SE and HE cells are compared in Fig. 4.4A and Fig. 4.4B, respectively. In addition Fig. 4.4C reports the 1-D profile of the Auger recombination rates of the HE and the SE cells between the front-contact fingers, confirming the relatively larger Auger recombination rate for the HE.

4.1.6 Selective emitter solar cell: conclusions

The main figures of merit of a selective emitter solar cell have been investigated as function of the front contact pitch and the emitter doping profiles, providing some guidelines aimed at optimizing the front side of the device. The analysis has been performed by means of 2-D numerical TCAD simulations by using the state-of-the-art

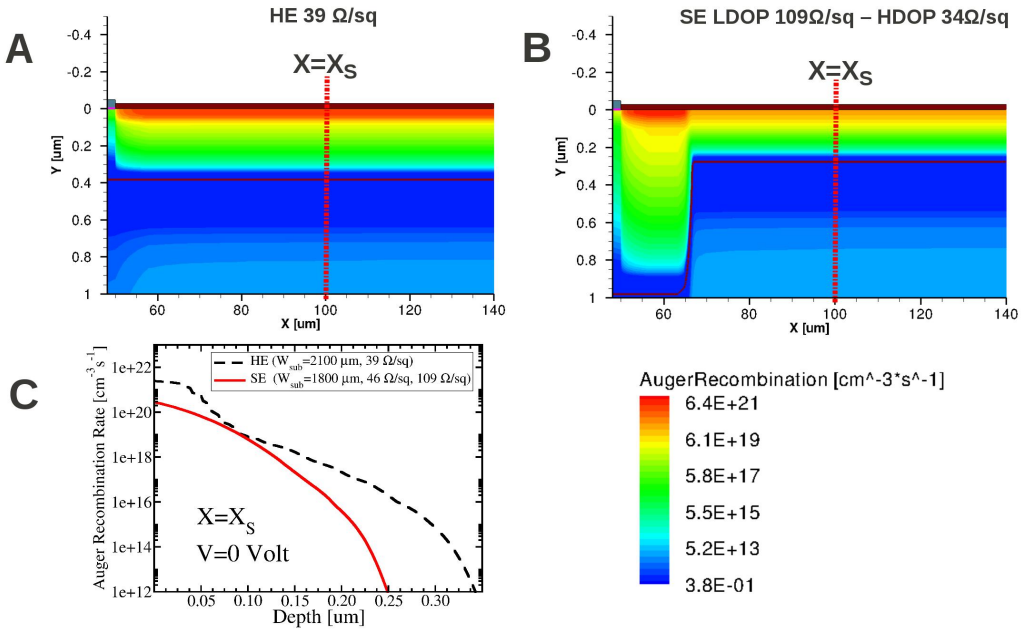

Figure 4.4: 2-D Auger recombination rate maps (in $cm^{-3}s^{-1}$) in the passivated emitter region close to the front surface (A) for the homogeneous emitter HE cell ($W_{SUB} = 2100\mu m$, $39\Omega/sq$) and (B) for the optimized selective emitter scheme SE ($W_{SUB} = 1800\mu m$, HDOP $46\Omega/sq$ and LDOP $109\Omega/sq$). In (C) the 1-D Auger recombination rate is reported as function of the distance from the front interface in the region between front-contact fingers.

models described in chapter 3. According to performed simulations, a selective emitter solar cell may provide an efficiency boost of approximately 0.8% with respect to a standard homogeneous emitter device; such enhancement depends also on the emitter sheet resistance of the considered HE baseline cell (for instance, if a $65\Omega/sq$ emitter cell is assumed as reference, a reduced efficiency boost is expected, approximately 0.5% absolute). The advantages of double-diffused emitters result from the enhancement of the collection efficiency, especially in the blue region of the spectrum, and from reduced Auger recombination due to a lighter emitter doping concentration in the region between fingers. The doping profile under the contacted region should satisfy the requirement of ensuring a good ohmic emitter contact. However, a careful design of the heavy-doped region profile should be considered depending upon the lateral extension of the HDOP diffusion; in presence of a relatively small lateral extension of the HDOP diffusion, a negligible impact of the features of the HDOP profile on the main figures of merit of the cell is observed.

4.2 Rear point contact solar cells

The adoption of Rear Point Contacts (RPCs) schemes at the back surface of high efficiency mono-crystalline silicon solar cells is one of the most promising approaches aimed at reducing the recombination losses at the rear side of the device. However, a drawback of the reduction of the rear contact surface is the increase of series resistance losses which, as described in chapter 2, leads to degradation of the Fill Factor. This section presents an extensive analysis based on 3-D electro-optical numerical device simulations of RPCs in order to highlight the dependence of the figures of merit of the solar cell on the main geometrical and technological parameters of the device, like the hole pitch, the size of the rear point contacts and the substrate resistivity. The TCAD simulator has been successfully adopted in order to accurately solve the transport equations in the semiconductor by taking into account all the loss mechanisms that are crucial in order to address the design of the cell. In subsection 4.2.2 the main issues associated with the numerical simulation of 3-D structures as well as the simulation set-up and the adopted physical models are described. Subsection 4.2.3 reports the results of an extensive analysis of technological options such as local BSF,

substrate resistivity, specific contact resistivity and geometrical features of the back-contact scheme like the contact size and the hole pitch (Fig. 4.5).

4.2.1 Introduction to rear point contact solar cells

An effective approach in c-Si solar cells to improve the conversion efficiency is the adoption of rear point contacts schemes which are adopted in high-efficiency PERC (Passivated Emitter and Rear Cell) and PERL (Passivated Emitter, Rear Locally Diffused) solar cells (13),(1) (reported efficiency values are above 23% (84)).

In standard solar cells exhibiting a uniformly contacted rear surface, significant recombination losses at the back metal-contacted interfaces occur. The main advantage of the RPC scheme derives from the reduction of the effective Back Surface Recombination Velocities ($BSRV_{eff}$) with decreasing metallization fraction (ratio of the contacted to the total back surface area). In addition the rear passivation allows to enhance the effective Internal Bottom Reflectivity (IBR_{eff}) due to the larger reflectivity of c-Si/dielectric/metal stack interface (typically above 0.90, depending upon the dielectric) with respect to the metal/c-Si one (approximately 0.65) (23)(85)(86)(87)(88). Disregarding the increased manufacturing costs, the main drawback of RPCs is the increase of the parasitic series resistances (due to two main contributions: the spreading base resistance and the back contact resistance). In this section only Cz (Czochralski) silicon wafers are considered. Low-cost and high-volume manufacturing processes for RPC solar cells use the Laser Firing Technique (LFC) to form local back-surface-field (BSF) diffusions (89)(90)(91). When LFC techniques are adopted, holes featuring diameters within the range 25-50μm and featuring relatively small specific contact resistivity (0.05-3$m\Omega cm^2$) can be fabricated (91)(92) for a wide substrate resistivity range (0.01-100Ωcm). In rear point contact solar cells (Fig. 4.5), the non-contacted back surface is typically passivated by dielectrics like silicon nitride (SiN) (93) or by silicon dioxide (SiO_2) leading to low surface recombination velocities, within the 1-100cm/s-range, depending on the process parameters and on the substrate resistivity.

Passivation techniques are not limited to those involving the formation of SiN or SiO_2 layers, indeed the future trend toward ultra-thin c-Si solar cells has increased the demand for low-cost rear surface passivation techniques like that by means of amorphous hydrogenated silicon nitride (SiNx) deposited by low-temperature Plasma-Enhanced Chemical Vapour Deposition (PECVD). Very low surface recombination ve-

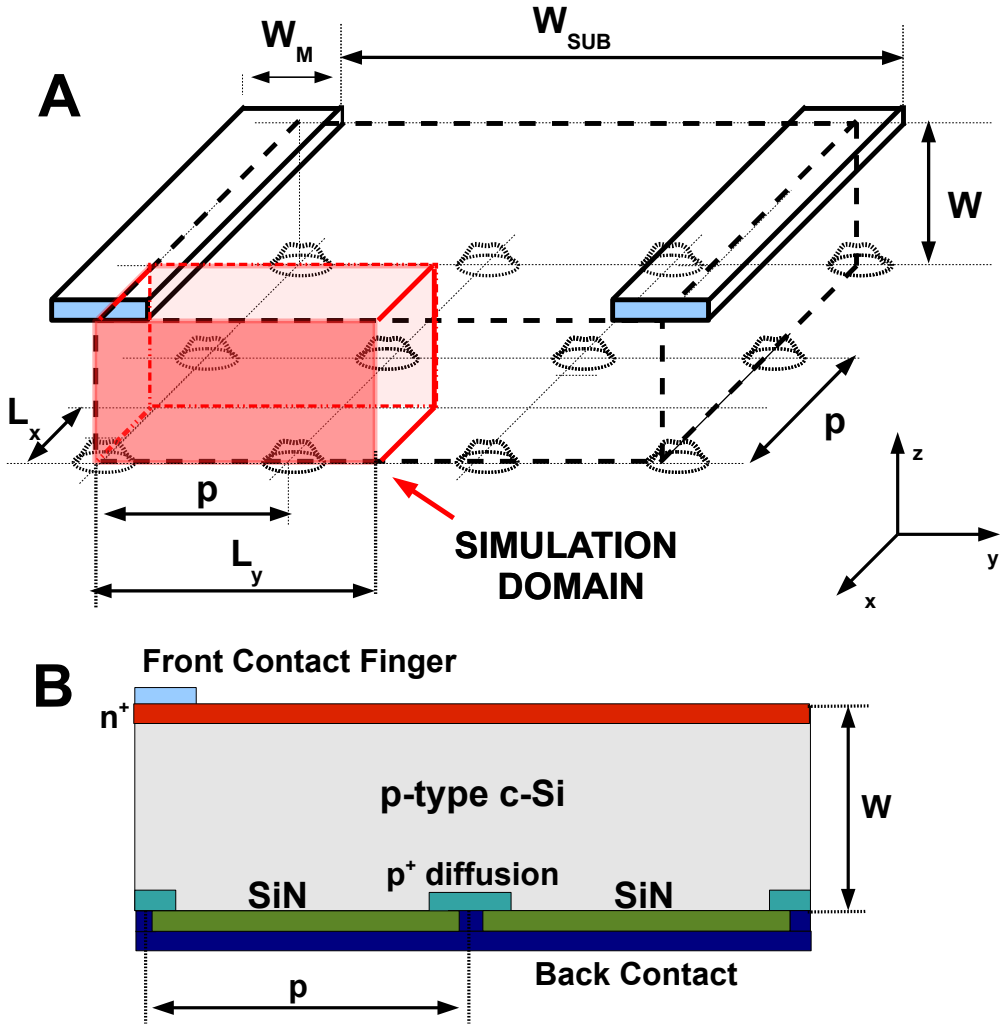

Figure 4.5: (A) 3-D sketch of the simulated solar cell with the rear point contact scheme. W_{SUB} and W denote the front contact pitch and the wafer thickness, respectively. The parameter W_M is the width of the front contact finger. The hole pitch is denoted by p. The simulation domain is highlighted in red ($L_x = p/2$, $L_y = W_{SUB}/2$). (B) 2-D cross section of the device with rear surface passivation by silicon nitride (SiN).

locities (SRVs) have been obtained with SiNx films on low-resistivity p-type silicon wafer (94), (95).

The RPC pattern design requires the optimization of the parameters which define its geometry. Due to the complexity of the structure, modeling by means of TCAD numerical simulation is helpful to analyze the trade-offs between several competing physical mechanisms which have to be accounted for in the optimization of rear point contact solar cells. The rear point contact geometry leads to 3-D conduction paths that are particularly important especially for large substrate resistivity, requiring a rigorous 3-D modelling as already adopted in (96) for the optimization of rear contact geometries and in (97) for the analysis of back contact solar cells (BCSC).

In other works, 1-D numerical simulations have been adopted to approximate the effects of 3-D geometries on electrical trasnport and on recombination losses by means of semi-empirical models to calculate the $BSRV_{eff}$ and the spreading resistance (85) (98) (99). In (100) (101) (102) the analysis has been simplified by considering two-dimensional (2-D) spatial domains leading to potentially misleading and inaccurate predictions, mainly due to incomplete information to calculate correctly the resistive losses and to properly model the 3-D transport. In (103) the optimization of a PERL solar cell has been performed by a simplified 3-D Finite Difference simulation under the following assumptions: low injection conditions and ideal emitter. In (104) a simulation method based on the numerical solution by means of Fast Fourier Transform of the minority and majority carrier transport equations in three dimensions in the base region of the PERC cell has been proposed. In this section, the state-of-the-art TCAD Sentaurus is adopted to perform true 3-D finite element device simulations of RPCs solar cells.

4.2.2 Rear Point Contact solar cells: simulation methodology and simulated devices

The 3-D sketch of the simulated solar cell is shown in Fig. 4.5A. The wafer thickness is $W = 180\mu m$ and the front contact pitch $W_{SUB} = 2mm$. The front contact finger width (W_M) and the height (H_M) are $100\mu m$ and $20\mu m$, respectively. The impact of the rear point contact geometrical parameters on J_{SC}, V_{OC}, Fill-Factor and conversion efficiency (η) is investigated by varying the hole pitch p and the hole diameter s (only circular-shaped back-contact holes are assumed). In the following, f denotes metallization

fraction. In Fig. 4.5A, L_x and L_y denote the width and the length of the simulation domain which are equal to half hole pitch and to half front contact pitch, respectively. The height of the simulation domain is equal to the wafer thickness W. The assumption of choosing the ratio of the front contact pitch to the hole pitch as an integer number is necessary to limit the lateral extension L_y of the simulation domain to $W_{SUB}/2$. The boron-doped wafer resistivity ρ_S is varied within the range 0.5-10Ωcm. The emitter is homogeneously doped and its doping profile is described by a Gaussian function featuring a junction depth equal to 0.4μm and a sheet resistance equal to 75Ω/sq (the emitter peak doping concentration is therefore adjusted depending on the considered substrate resistivity in order to keep the junction depth and emitter sheet resistance constant for each value of wafer doping concentration).

In PERL cells, the $p+$ BSF regions, introduce a built-in electric field at the p-$p+$ transition allowing the separation of carriers photo-generated by large-wavelength photons close to the contacted back-surface; the doping profile of the $p+$ BSF is described by a Gaussian function with a peak doping concentration of $2.5 \times 10^{19} cm^{-3}$ and junction depth in the range 6.7-7.1μm, depending on wafer resistivity. As shown in Fig. 4.5B, the front surface and the uncontacted rear surface are assumed to be passivated by a SiN layer 70nm thick. In order to achieve realistic predictions, the physical models implemented in the TCAD simulator have been calibrated as described in chapter 3. The Schenk band-gap narrowing (BGN) model with Fermi-Dirac statistics is adopted to obtain the value $n_i = 9.65 \times 10^9 cm^{-3}$ at low doping density. The revised BGN model provides good agreement with data reviewed by Altermatt (48) at temperature T=300K as described in section 3.1.3. The considered physical models include the Philips-Unified Mobility Model with carrier drift velocity saturation at high electric fields.

The main recombination losses (trap-assisted SRH, Auger and surface SRH mechanisms) have been accounted for, including their dependence on doping concentration as shown in section 3.1.5. The surface recombination velocities (SRVs) at front and rear passivated interfaces are calibrated according to (64) in which experimental values of SRV between $10 cm/s$ and $100 cm/s$ for bulk doping concentrations within the range $10^{14} cm^{-3}$ to $10^{17} cm^{-3}$ have been reported. The recombination velocity at front contact and at back holes is set to $10^6 cm/s$. Tab. 4.4 summarizes the values of the main physical parameters involved in calculations; as shown in the table, significantly

different situations in terms of bulk carrier lifetimes τ_n and hence of minority carrier diffusion length L_n are considered (for instance for $\rho_S = 0.5\Omega cm$, $\tau_n = 39.75\mu sec$ and $L_n = 303\mu m$; when $\rho_S \geq 5\Omega cm$, $\tau_n = 1136\mu sec$ and $L_n = 1875\mu m$). On the other hand, the back surface recombination velocity modeled according to (64), only slightly depends on the base doping concentrations, ranging from $11cm/s$ to $14cm/s$ for the considered base resistivity range. As in the case of the selective emitter solar cell (4.1), the figures of merit of the solar cell (FF and η), are corrected in order to account for the losses due to the parasitic series resistance associated to contacts and metal fingers. The resistance associated to front contacts and to metal fingers is $0.182\Omega cm^2$. Relatively large specific back contact resistivity ρ_{BC} values within the range $1m\Omega cm^2$-$10m\Omega cm^2$ depending on several LFC processing conditions (like annealing temperature, laser power and passivation material) have been reported in recent experimental works (90), (85). Hence, in the following $\rho_{BC} = 3m\Omega cm^2$ is adopted. The impact of different values of the specific contact resistivity of the back contact is investigated and discussed in subsection 4.2.3.4.

Table 4.4: Physical and electrical parameters adopted for the performed simulations for different type of considered cells and for different substrate resistivity values ρ_S. N_{sub} denotes the substrate doping concentration. τ_n, μ_n and L_n are the bulk minority carrier lifetime, the low-field minority carrier mobility at low doping concentration and the corresponding calculated diffusion length in the base, respectively. The back surface recombination velocity at the passivated rear surface is denoted by $BRSV_{pass}$.

Cell Type	ρ_S	N_{sub}	τ_n	$BRSV_{pass}$	μ_n	L_n
	$[\Omega cm]$	$[cm^{-3}]$	$[\mu sec]$	$[cm/s]$	$[cm^2 s^{-1} V^{-1}]$	$[\mu m]$
PERC	0.5	3.255×10^{16}	39.75	14.58	896	303
PERL	0.5	3.255×10^{16}	39.75	14.58	896	303
PERL	1.0	1.513×10^{16}	115.0	12.66	1027	553
PERL	2.0	7.216×10^{15}	230.0	11.79	1113	814
PERL	5.0	2.781×10^{15}	1136	11.31	1195	1875
PERL	10.0	1.368×10^{15}	1136	11.15	1195	1875

The optical simulation has been performed by a 1-D optical simulator; the calculated optical generation map is then interpolated on the 3-D grid (Fig. 4.6) provided as input for the device simulator. Optical generation rate profiles are calculated on the basis of

the propagation of monochromatic plane waves through layered media. The multiple bounces of light inside the device are described analytically in terms of a geometric progression of plane waves. The internal reflectance (at top and at bottom interfaces) is assumed to be the same for subsequent light bounces. The optical generation rate profiles are calculated assuming direct illumination with a standard AM1.5G spectrum (input irradiance $1000 W/m^2$).

The textured top surfaces coated by a 70nm thick anti-reflection coating layer of SiN is modeled by a measured external reflectivity. In addition, ideal shadowing by front fingers is assumed. The internal bottom reflection coefficient $R_{bi,p}$ of the silicon-dielectric-metal stack interface is set to 0.90 and the internal bottom reflection coefficient of the Al/p-Si interface $R_{bi,m}$ is assumed equal to 0.65 (23). To simplify the optical modeling, the optical simulation is performed in one dimension, therefore the internal bottom reflection coefficient is assumed to be uniform at the rear interface and is set as an average value weighted by the metallization fraction f.

Fig. 4.6 and Fig.4.7 report examples of 3-D mesh grid adopted for the numerical simulation and of a 3-D output map calculated by the device simulator; in particular a 3-D conduction current density map in short-circuit conditions under illumination is shown. The figure allows to observe the 3-D conduction path of the current exhibiting the typical branching in the base and the current crowding occuring close the back contact holes.

4.2.3 Technological and geometrical options

In the following the results of an extensive analysis of the impact of different technological and geometrical parameters of the RPC scheme are discussed. In subsection 4.2.3.1 the PERL and PERC solar cells are compared and the focus of the analysis is the impact of the presence the $p+$ local BSF diffusion on the optimum value of the metallization fraction and on the figures of merit.

In subsection 4.2.3.2 a PERL cell featuring a constant hole pitch p is analyzed and the hole diameter s is adjusted in order to vary the metallization fraction, assuming as simulation parameter the substrate resistivity ρ_S in order to investigate how the parasitic spreading base resistance as well as the doping-dependent bulk recombination losses affect the optimization of the cell.

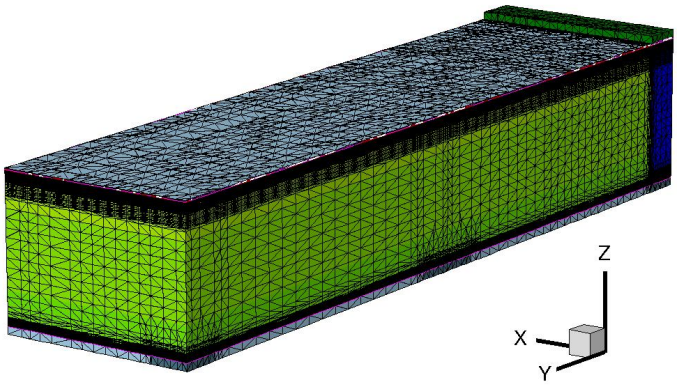

Figure 4.6: Example of 3-D mesh grid adopted for the device numerical simulation. In this case the hole pitch p is $500\mu m$ and the hole diameter s is $50\mu m$. The simulation domain is chosen according to section 4.2.2. Up to 300000 vertices are typically required.

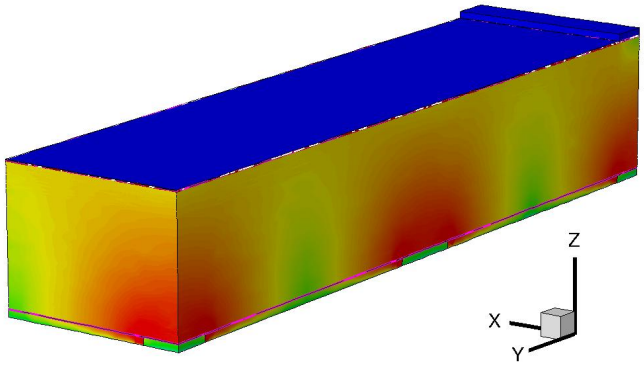

Figure 4.7: Example of 3-D output maps calculated by the device numerical simulator. In this case the hole pitch p is $500\mu m$ and the hole diameter s is $50\mu m$. The figure shows the 3-D conduction current density map in short-circuit conditions under illumination.

In subsection 4.2.3.3 the analysis is performed by varying the hole pitch and by assuming as simulation parameter the hole size for two different values of ρ_S. Finally, in subsection 4.2.3.4 the impact of the back contact specific resistivity on the main figures of merit is investigated.

4.2.3.1 Comparison between PERL and PERC solar cells

PERL and PERC solar cells have been compared in order to investigate the impact of the local $p+$ BSF diffusion on the figures of merit of the solar cell. The characteristics of the doping profile of the BSF diffusion of the PERL cell are described in section 4.2.2. For both PERL and PERC devices $\rho_s = 0.5\Omega cm$ is chosen, since for larger ρ_S values the Al/p-Si interface is rectifying (100). The hole diameter s is varied within the range $25\mu m$-$400\mu m$ (by keeping the hole pitch p constant to $p = 500\mu m$) in order to investigate the dependence of the figures of merit on metallization fraction f. The chosen value of hole pitch is comparable to that reported by other works (105), (106) in which experimental data related to PERC cells are presented. In addition, the choice of $p = 500\mu m$ is motivated by the requirement, previously discussed, to limit the simulation domain to $W_{SUB}/2$. By decreasing the metallization fraction f, a monotonic increase of both V_{oc} and J_{sc} due to the reduced $BSRV_{eff}$ and to the increase of the IBR_eff is observed (Fig. 4.8). In Fig. 4.9 the absorbance and the reflectance characteristics of a RPC cell featuring a significantly low metallization fraction ($f_0 = 0.2\%$) are compared to those of the uniformly contacted cell ($f = 100\%$); in the former case, due to the higher $BSRV_{eff}$ (approximately 0.90) with reference to the baseline ($IBR = 0.65$), the cell exhibits a lower reflectance, in particular at longer wavelengths ($\lambda > 1000nm$), for which the influence of the internal reflection at the bottom interface on the total reflectance is remarkable. Hence, the absorbance of the RPC cell is larger than that of the baseline. Therefore the RPC solar cell exhibits a larger photogenerated current density ($J_{ph} = 39.542mA/cm^2$) than that of the uniformly contacted cell ($J_{ph} = 38.611mA/cm^2$). In addition, due to the smaller losses in the rear side of the device, both V_{oc} and J_{sc} are larger for the PERL cell with reference to the PERC device, indeed, the local BSF in the PERL cell, enhances carrier separation leading to reduced recombination at the highly-defective back metal-semiconductor interfaces thanks to the electric field in the p-$p+$ transition region. However, by reducing the metallization fraction, the impact of the metal-semiconductor interfaces is less dominant

and thus, the difference in terms of V_{oc} and J_{sc} between PERL and PERC cells become smaller (Fig. 4.8). In addition, in case of the PERC, the absence of the local BSF leads to steeper dependence of both V_{oc} and J_{sc} on f, compared to the PERL cell, because of the stronger impact of the $BSRV_{eff}$. The calculated Fill Factor (FF) for the PERL and the PERC cells is reported as a function of f in Fig. 4.10. The base parasitic spreading and the contact series resistances increase with decreasing f, leading to a degradation of the FF. Indeed, the spreading series resistance is associated to the 3-D current branching occurring when the extension of the metallized interface at the back interface is significantly smaller than the total cell area; moreover, the contact series resistance, for a given specific contact resistivity, is inversely proportional to the area of the contacted surface. Since the hole pitch p is assumed to be constant, lower f leads to larger distance between the metallized surfaces due to reduced diameter of the holes. Moreover, lower f means larger back contact resistance due to a lower contacted area. Since, due to a lower peak doping concentration at the metal-silicon interface, a larger ρ_{BC} in case of the PERC is expected, simulations of the PERC cell have been performed by assuming as specific back contact resistivity $\rho_{BC} = 3m\Omega cm^2$ (value common to both PERL and PERC to allow a direct comparison without introducing the influence of the specific back contact resistivity) and $\rho_{BC} = 30m\Omega cm^2$ (the specific back contact resistivity of the PERC cell is expected to be significantly larger than that of the PERL device due to the absence of the BSF diffusion). It is worth noting that, when PERC and PERL are compared by assuming the same value of specific back contact resistivity, the FF curves are indistinguishable; however, in case of PERC cell, if $\rho_{BC} = 30m\Omega cm^2$ is assumed, the FF is strongly degraded with reference to the PERL cell because of the significant parasitic series resistance introduced by the rear point contact pattern; in addition its dependence on f is steeper.

Concerning the curves of conversion efficiency (Fig. 4.10), a typical bell-shape is obtained due to a trade-off between two competing mechanisms: when f decreases, V_{oc} and J_{sc} enhance, on the contrary the FF degrades significantly leading to an optimum value of metallization fraction f_0 for which the efficiency reaches its maximum value. Moreover f_0 is different for the PERC and PERL: the maximum efficiency for the PERL cell is 19.68% (at $f_0 = 7.07\%$), while in case of the PERC, the calculated values of maximum efficiency are 19.31% ($f_0 = 3.14\%$) and 18.74% ($f_0 = 9.62\%$) for $\rho_{BC} = 3m\Omega cm^2$ and $\rho_{BC} = 30m\Omega cm^2$, respectively. The optimum RPC configuration,

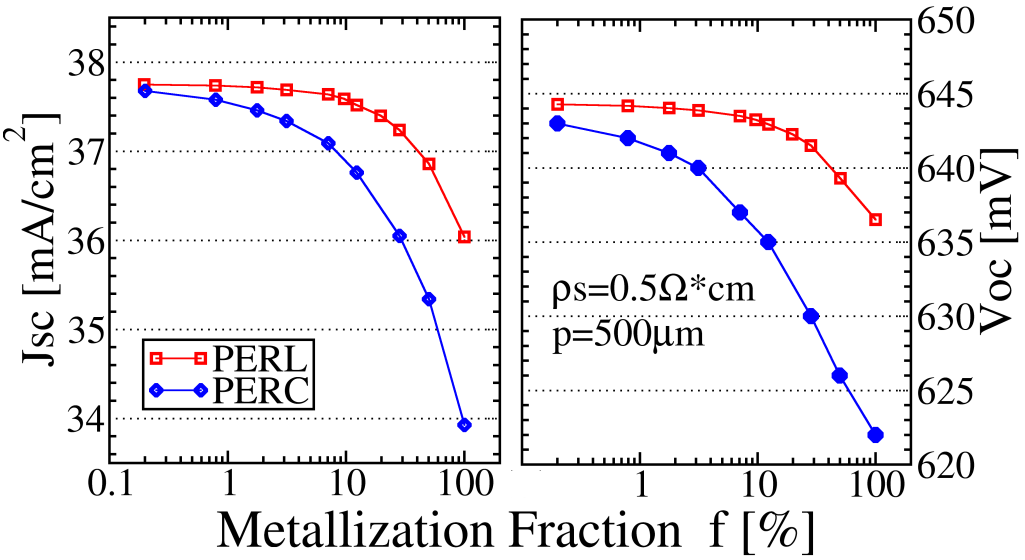

Figure 4.8: Short circuit current density J_{sc} (left) and open circuit voltage V_{oc} (right) for PERC and PERL solar cells with hole pith $p = 500\mu m$ and substrate resistivity $\rho_s = 0.5\Omega cm$.

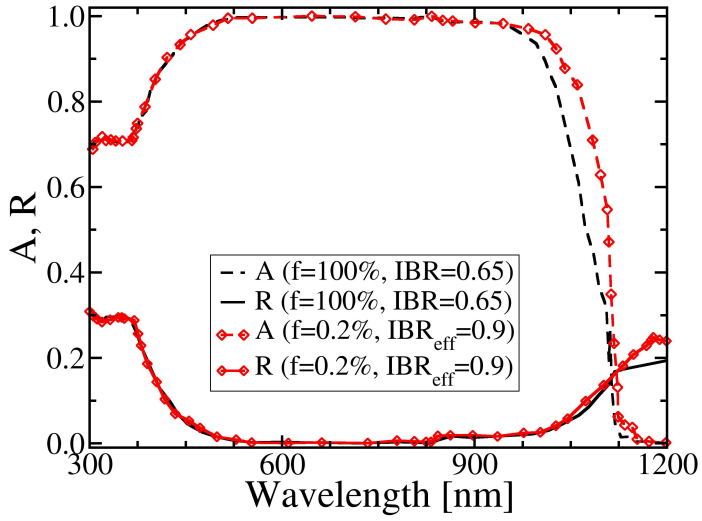

Figure 4.9: Calculated absorbance (A) and reflectance (R) characteristics of a RPC cell featuring $f_0 = 0.2\%$ compared to those of the uniformly contacted cell ($f = 100\%$).

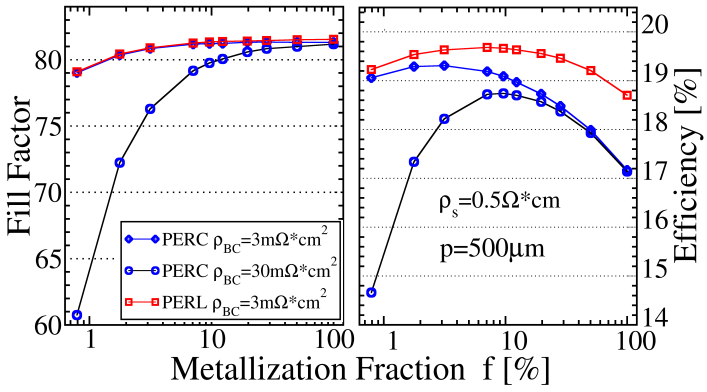

Figure 4.10: Fill Factor (left) and efficiency (right) for PERC and PERL solar cells with hole pitch $p = 500\mu m$ and substrate resistivity $\rho_s = 0.5\Omega cm$. In case of the PERC two different values of the specific back contact resistivity ρ_{BC} are assumed: $\rho_{BC} = 3m\Omega cm^2$ and $\rho_{BC} = 30m\Omega cm^2$; if the former value of ρ_{BC} is adopted for both PERC and PERL, the curves of the FF are indistinguishable.

with reference to the case of the uniformly back contacted solar cell ($f = 100\%$), allows an enhancement in terms of efficiency of $0.88\%_{abs}$ and $2.14\%_{abs}$ ($\rho_{BC} = 3m\Omega cm^2$) for the PERL and the PERC cells, respectively. The larger enhancement in case of the PERC cell is due to the significant reduction of the losses in the base region thanks to the low metallization fraction. However, the reduction of the losses in the base region is not so remarkable for the PERL cell, indeed the BSF mitigates the dependence of the figures of merit on the boundary conditions at the back interface almost for all values of f, even for the case of the uniformly contacted solar cell. In particular, as shown in Fig. 4.10, a weak dependence of the efficiency on f within the range 0.8-12% is observed in the case of the PERL cell, consistently with the small dependence of V_{oc} and J_{sc} on f. Hence, the performance of PERL cells is expected to be less sensitive to the uncertainties affecting geometrical parameters.

In the considered solar cells the values of the obtainable short-circuit current density and hence of the calculated values of conversion efficiency are lower than those reported in (1) and (84) (J_{sc} significantly above $40mA/cm^2$ and efficiencies above 23%). The main reason of these discrepancies relies on the absence in the device simulated in this work of photo-lithographic techniques for texturing (for instance inverted pyramids) and for contact definition, that allow the reduction of the front reflectance and of the front

contact shadowing effect, respectively. On the contrary, photo-lithographic techniques are adopted in the cited works. In addition, in the mentioned high-performance solar cells, FZ wafers are adopted; as observed in chapter 2.9.1, such high-quality substrates allow to reach longer minority carrier lifetimes, even in millisecond range.

The calculated main figures of merit for the simulated PERC and PERL cells are summarized in Tab. 4.5.

Table 4.5: Results of the simulations for PERL and PERC solar cells with $p = 500\mu m$ and substrate resistivity $\rho_s = 0.5\Omega cm$. The PERC solar cell has been simulated with back contact specific resistivities $\rho_{BC} = 3m\Omega cm^2$ and $\rho_{BC} = 30m\Omega cm^2$. The parameter s denotes the hole diameter. The table reports only the main figures of merit of the uniformly contacted cell and those of the RPC solar cell calculated at the optimum metallization fraction f_0. The related efficiency boost $\Delta\eta$ (with respect to the baseline) is reported in the last column.

Cell Type	ρ_{BC}	f	f_0	J_{sc}	V_{oc}	FF	η	$\Delta\eta$
	$[m\Omega cm^2]$	$[\mu m]$	[%]	$[mAcm^{-2}]$	$[mVolt]$		[%]	$[\%_{abs}]$
PERL	3	150	7.07	37.64	643	81.26	19.68	0.88
PERL	3	-	100	36.04	637	81.54	18.70	
PERC	3	100	3.14	37.34	640	80.84	19.31	2.14
PERC	3	-	100	33.93	622	81.31	17.17	
PERC	30	175	9.62	36.93	636	79.76	18.74	1.60
PERC	30	-	100	33.93	622	81.18	17.14	

In order to perform a more detailed analysis about the different impact of loss mechanisms on PERC and PERL solar cells, the collection efficiency η_C of the photo-generated electron-hole pairs (defined in section 2.3.7) has been calculated within the range of wavelength $600nm$-$1100nm$ (below $600nm$ the collection efficiency is not affected by the RPC scheme since high-energy photons are absorbed in the emitter region). In Fig. 4.11 the collection efficiency has been calculated in correspondence of the optimum metallization fraction f_0 value and for $f = 100\%$ (uniformly contacted solar cell). For long wavelengths, for which photons are mostly absorbed in the base region close to the rear surface, η_C is significantly larger with reference to the uniformly contacted counterpart in case of low metallization fraction because of the remarkable reduction of the $BSRV_{eff}$ obtained by the RPC scheme. In addition, the collection

efficiency of the optimized RPC with respect to the baseline cell is larger for the PERC, because, in PERL solar cells, the presence of the BSF, as already discussed, leads to reduced losses in the base region also in case of uniformly contacted devices.

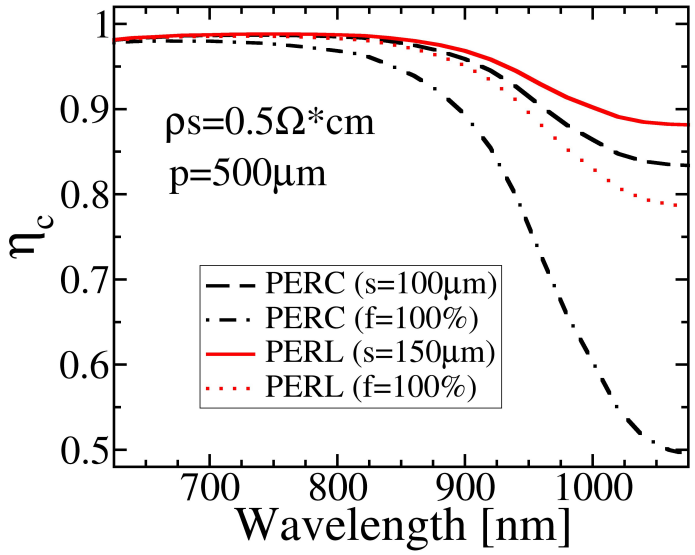

Figure 4.11: Collection efficiency of photo-generated carriers (η_C) from $600nm$ up to $1100nm$ for PERC and PERL solar cells with hole pitch $p = 500\mu m$ and substrate resistivity $\rho_s = 0.5\Omega cm$; η_C is calculated at $f = 100\%$ (uniformly contacted cell) and at the optimum metallization fraction (PERC: $f_0 = 3.14\%$, $s = 100\mu m$; PERL: $f_0 = 7.07\%$, $s = 150\mu m$).

4.2.3.2 Dependence of the main figures of merit of PERL cells on the back-contact diameter

In this section the dependence of the figures of merit of the PERL cell on the metallization fraction -by assuming as simulation parameter the substrate resistivity ρ_S- are investigated. The substrate resistivity has a strong impact on both the spreading resistance and the recombination losses. In this analysis, the peak doping concentration of the local BSF diffusion at the metallized interface is assumed to be independent on ρ_S. The following values of ρ_S are assumed: 0.5, 1, 2, 5 and $10\Omega cm$. The metallization factor varies as consequence of a change in hole diameter s within the range $25\mu m$-$400\mu m$. On the contrary, the hole pitch is assumed to be constant ($p = 500\mu m$). The curves showing the dependence of the figures of merit on the metallization fraction f of the analyzed cells are shown in Fig. 4.12. Both V_{oc} and J_{sc} are strongly affected

by the substrate resistivity; indeed, smaller substrate resistivity values corresponds to larger bulk recombination losses as shown in Tab. 4.4 where, for each considered substrate resistivity value, the doping dependent carrier lifetime is reported. However, the bulk doping concentration weakly affects also the surface recombination velocity at the passivated interfaces. In addition, in case of higher substrate doping concentration, the local $p+$ diffusion depth decreases, leading to larger $BSRV_{eff}$. Therefore, increasing ρ_S leads to larger V_{oc} and J_{sc}. For $\rho_S > 5\Omega cm$ such dependence is weaker because the carrier lifetime saturates for a Cz wafer (Tab. 4.4). In addition a slight dependence of V_{oc} on f is observed for low ρ_s values. Indeed, the lower is ρ_s, the lower is the carrier lifetime, therefore the minority carrier diffusion length degrades and the impact of the boundary conditions at rear interface is less dominant.

A remarkable degradation of the FF is observed with decreasing f, in particular for large ρ_s values. Indeed, larger substrate resistivity values lead to enhanced spreading base resistance, hence to a more significant impact of the metallization fraction on FF. An approximate calculation of the spreading resistance as function of the metallization fraction and of the base resistivity by using the model proposed by Cox and Strack (107) shows that, at lower metallization fraction (around 1%), for relatively low values of ρ_s, the effect of the back contact resistance on the FF is almost of the same magnitude of that of the spreading resistance; however, the relative contribution of the base parasitic series resistance is significantly higher, (even above 80%) for larger ρ_s (for instance $10\Omega cm$); this represents one of the main drawbacks occurring when the substrate doping concentration in RPC designs is decreased. As a consequence of two competing mechanisms -reduced losses at large ρ_s and increased base resistance at low ρ_s- a strong dependence of the optimum metallization fraction f_0 and of the maximum efficiency value on ρ_s is observed. The calculated maximum efficiency is obtained for $\rho_S = 5\Omega cm$ ($f_0 = 12.32\%$, $s = 200\mu m$). For $\rho_S = 10\Omega cm$ the maximum achievable efficiency is 20.00% at $f_0 = 7.07\%$. It is worth noting that for $\rho_S = 10\Omega cm$ the efficiency gain between the optimum rear point contact geometry and the uniformly contacted counterpart is $0.59\%_{abs}$; however, for $\rho_S = 1\Omega cm$ the enhancement in terms of efficiency is even higher: $1.03\%_{abs}$. The calculated main figures of merit of the simulated PERL cells for different values of ρ_S are reported in Tab. 4.6.

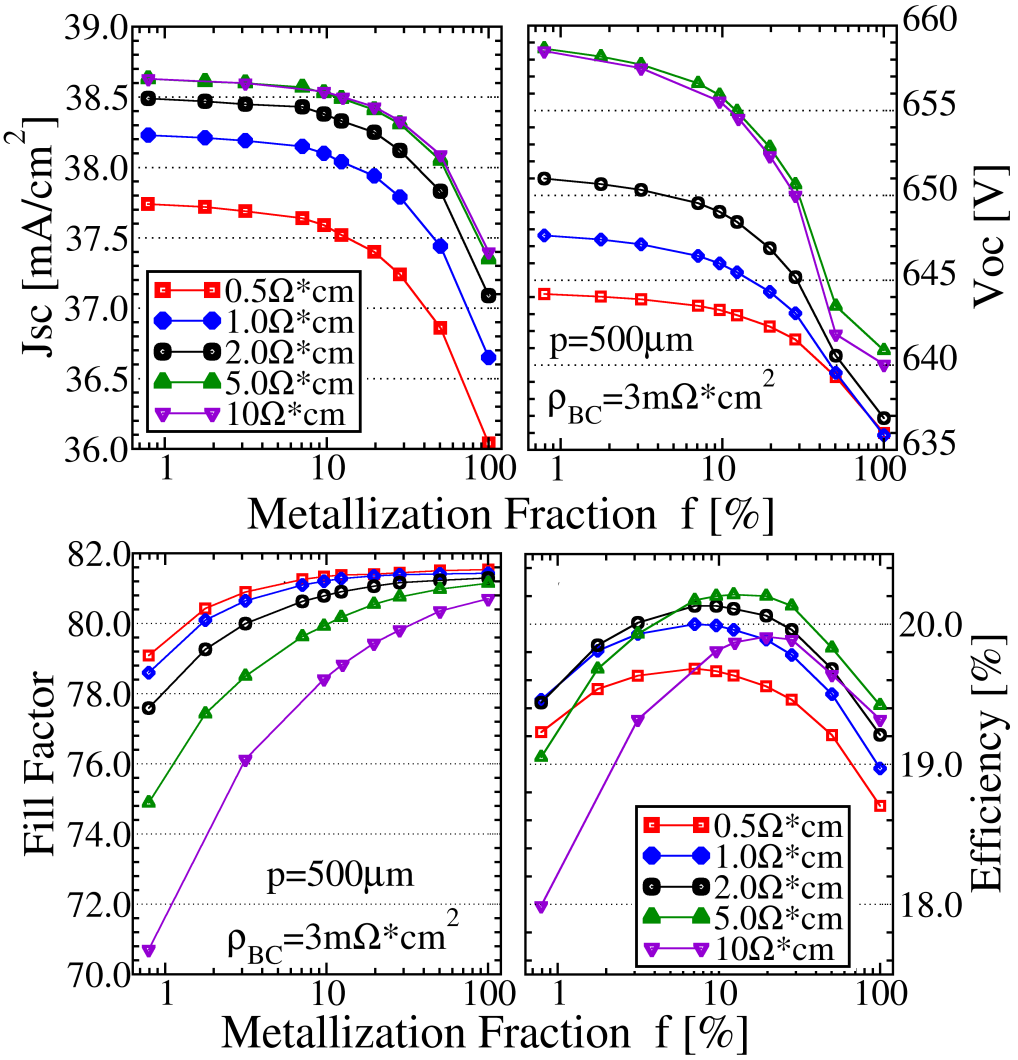

Figure 4.12: Short circuit current density J_{sc}, open circuit voltage V_{oc}, Fill Factor and conversion efficiency η for PERL solar cells with constant hole pith $p = 500\mu m$ and specific back contact resistivity $\rho_{BC} = 3m\Omega cm^2$, for different substrate resistivity values.

Table 4.6: Results of the simulations for PERL solar cells with $p = 500\mu m$, specific back contact resistivity $\rho_{BC} = 3m\Omega cm^2$ and substrate resistivity as parameter. The parameter s denotes the hole diameter. The table reports only the main figures of merit of the uniformly contacted cell and those of the RPC solar cell calculated at the optimum metallization fraction f_0. The related efficiency boost $\Delta\eta$ (with respect to the baseline) is reported in the last column.

ρ_S	s	f_0	J_{sc}	V_{oc}	FF	η	$\Delta\eta$
$[m\Omega cm]$	$[\mu m]$	[%]	$[mAcm^{-2}]$	$[mVolt]$		[%]	$[\%_{abs}]$
10	250	19.63	38.43	652	79.44	19.91	0.59
10	-	100	37.39	640	80.71	19.32	
5	200	12.32	38.49	655	80.18	20.21	0.79
5	-	100	37.35	641	81.15	19.42	
2	175	9.62	38.38	649	80.79	20.13	0.92
2	-	100	27.09	637	81.30	19.21	
1	150	7.07	38.15	646	81.10	20.00	1.03
1	-	100	36.65	636	81.43	18.97	
0.5	150	7.07	37.64	643	81.26	19.68	0.98
0.5	-	100	36.04	636	81.53	18.70	

4.2.3.3 PERL cells: impact of back-contact pitch on performance

In this section the dependence of the efficiency of a PERL solar cell on the contact pitch p is analysed for two values of the substrate resistivity: $\rho_S = 1\Omega cm$ and $\rho_S = 5\Omega cm$. The adopted simulation paramater is the hole diameter s; three values of s are considered: 50, 100 and $175\mu m$. The hole pitch p, differently from the previous analyses, is varied in order to control the metallization fraction f. V_{oc} and J_{sc} are only weakly dependent on the hole diameter s. Indeed, the dependence of V_{oc} and J_{sc} on f is mainly due to the back-surface recombination losses, hence to the area of the contacted back-surface. The calculated trend of the FF is shown in Fig. 4.13; it is worth noting that a steep degradation of the FF occurs at large s and for low metallization fractions ($f \leq 10\%$). The reason of such dependence is that, for a given f, larger hole diameter means larger distance between the adjacent rear contacts, consequently leading to larger spreading resistance. A first conclusion is that, in order to achieve high values of efficiency, small hole diameter values are required, as shown in Tab. 4.7

and Fig. 4.13.

In case of $\rho_S = 5\Omega cm$, the maximum calculated efficiency (20.34%) is achieved for $s = 50\mu m$. The efficiency boost (with respect to the uniformly contacted counterpart) which derives by the RPC featuring substrate resistivity $\rho_S = 5\Omega cm$ is $0.92\%_{abs}$ ($s = 50\mu m$). However, the lower bound limit of the hole size is determined by technological limitations in opening small laser fired holes and by the increase of back contact resistance.

Qualitatively similar results have been obtained in the case $\rho_S = 1\Omega cm$. The maximum efficiency for the optimized RPC geometry ($p = 181.12\mu m$, $f = 5.94\%$, Fig. 4.14) is lower than that obtained assuming $\rho_S = 5\Omega cm$. The efficiency gain of the cell featuring substrate resistivity $\rho_S = 1\Omega cm$ with respect to the conventional cell is $1.05\%_{abs}$ for $s = 50\mu m$.

Finally, it is worth noting that, on the basis of the predicted trend of the efficiency on the metallization fraction, if realistic uncertainties in terms of hole pitch and hole size for a standard laser opening process are accounted for (85), in case of an optimized PERL cell design with $\rho_S = 1\Omega cm$, the resulting metallization fraction may vary from 4% to 9% (the calculated metallization fraction for the optimized RPC pattern is 5.94%), thus the efficiency may be affected by uncertainty up to $0.02\%_{abs}$. In case of $\rho_S = 5\Omega cm$ the expected uncertainty affecting the efficiency is slightly higher ($0.04\%_{abs}$).

4.2.3.4 PERL cells: analysis of the dependence of the main figures of merit on the specific back contact resistivity

In previous analyses the adopted value of specific back contact resistivity ρ_{BC} is $3m\Omega cm^2$. However, as mentioned in subsection 4.2.2, experimental works report a relatively extended range of values of specific back contact resistivity. In this section a PERL cell featuring a hole diameter $s = 50\mu m$ and substrate resistivity $\rho_S = 1\Omega cm$ and $\rho_S = 5\Omega cm$ has been simulated adopting as simulation parameter ρ_{BC}. The simulated values of ρ_{BC} are: $\rho_{BC} = 0$ (ideal case), 0.6, 3, 6, 9 and $15m\Omega cm^2$. The simulation results are reported in Fig. 4.15 . As expected, for a given metallization fraction, the degradation of the FF is steeper with increasing ρ_{BC}, while both V_{oc} and J_{sc} are almost independent on ρ_{BC}. Therefore the optimum metallization fraction f_0 moves towards higher values with increasing ρ_{BC}. For $\rho_S = 1\Omega cm$ and $\rho_{BC} = 0m\Omega cm^2$ the maximum calculated efficiency 20.11% is achieved at $f_0 = 2.41\%$ ($FF = 81.32$) while

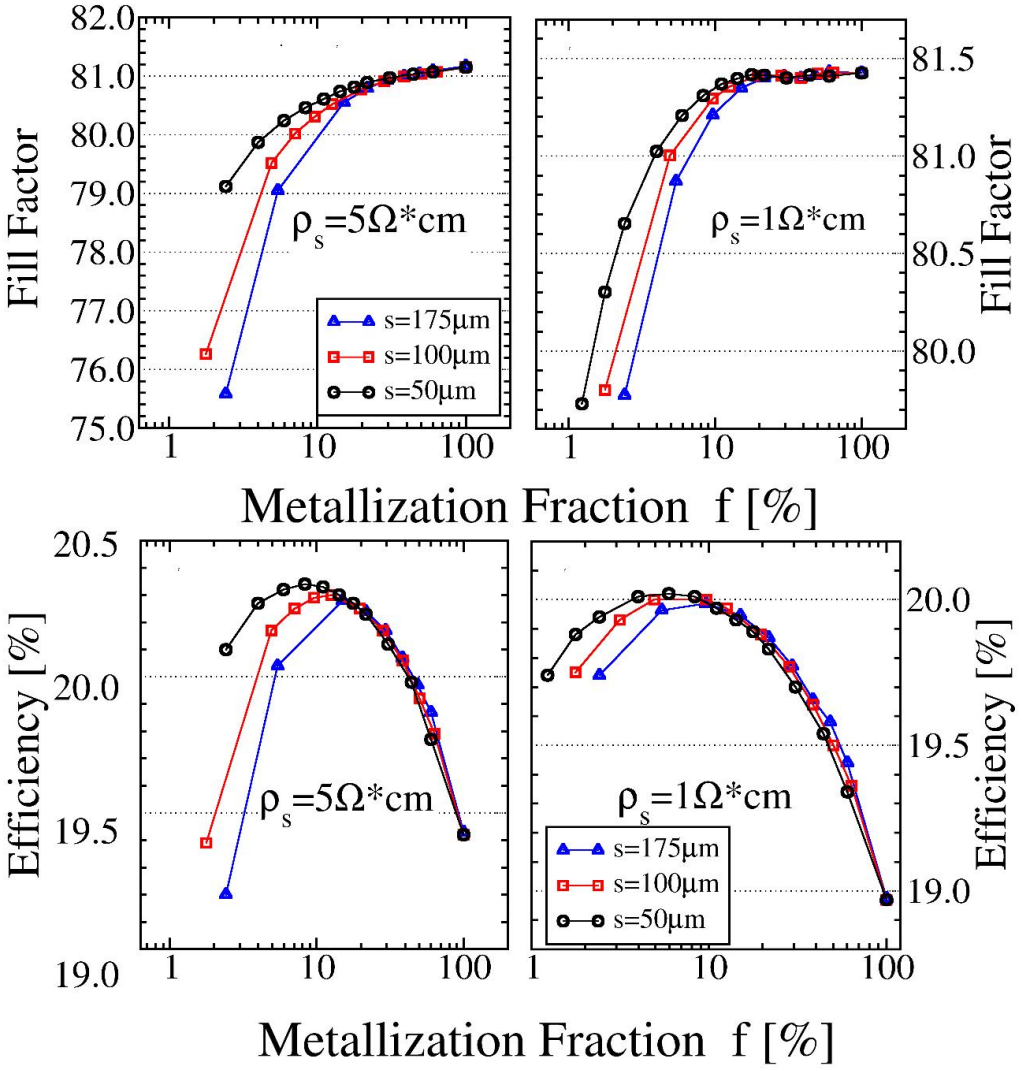

Figure 4.13: Fill Factor (up) and efficiency (bottom) for PERL solar cells with substrate resistivity $\rho_S = 5\Omega cm$ (left) and $\rho_S = 1\Omega cm$ (right). Specific back contact resistivity $\rho_{BC} = 3m\Omega cm^2$. Hole diameter s as parameter and variable hole pitch.

Table 4.7: Simulations results for PERL solar cells with hole diameter s as parameter, specific back contact resistivity $\rho_{BC} = 3m\Omega cm^2$, substrate resistivity $\rho_S = 1\Omega cm$ and $\rho_S = 5\Omega cm$. The parameter p denotes the hole pitch of the rear point contact pattern. The table reports only the main figures of merit of the uniformly contacted cell and those of the RPC solar cell calculated at the optimum metallization fraction f_0.

ρ_S	s	p	f_0	J_{sc}	V_{oc}	FF	η
$[m\Omega cm]$	$[\mu m]$	$[\mu m]$	[%]	$[mAcm^{-2}]$	$[mVolt]$		[%]
5	50	154	8.30	38.54	656	80.46	20.34
	100	250	12.6	38.49	655	80.52	20.30
	175	400	15.0	38.47	654	80.44	20.25
			100	37.35	641	81.15	19.42
1	50	181	5.94	38.13	646	81.21	20.02
	100	286	9.62	38.08	646	81.30	20.00
	175	500	9.62	38.10	646	81.20	19.99
			100	36.65	636	81.43	18.97

for $\rho_{BC} = 15m\Omega cm^2$ the maximum efficiency (19.83%) is obtained at $f_0 = 11.04\%$ ($FF = 80.79$). For $\rho_S = 5\Omega cm$, the impact of back contact resistance is lower, with respect to the case of $\rho_S = 1\Omega cm$, due to the larger contribution of the base spreading resistance. The calculated boost of efficiency with reference to the uniformly back-contacted solar cell is remarkably significant also for the largest specific back contact resistivity within the considered range.

4.2.4 Rear Point Contact solar cells: conclusions

In this section the dependence of the main figures of merit of rear point contact solar cells on the geometrical parameters of the rear contact pattern configuration, on the back specific contact resistance and on the substrate resistivity ρ_S, has been investigated. The performed analyses confirmed the effectiveness of the local BSF diffusion of the PERL cell. In addition, the dependence of the efficiency on the metallization fraction at constant hole pitch, variable contact-hole diameter and substrate resistivity as simulation parameter has been analyzed. Simulations highlighted that the metallization fraction is a crucial parameter in the design of a rear point contact cell. For relatively small values of metallization fraction, the contribution of the series back con-

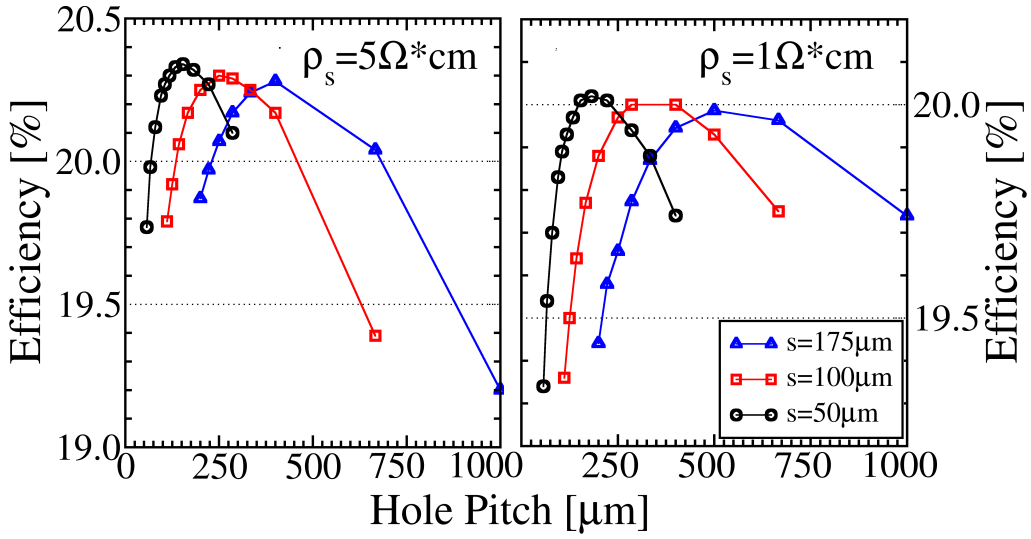

Figure 4.14: Conversion efficiency versus hole pitch p for PERL solar cells with substrate resistivity $\rho_S = 5\Omega cm$ (left) and $\rho_S = 1\Omega cm$ (right). Specific back contact resistivity $\rho_{BC} = 3m\Omega cm^2$. Hole diameter s as parameter.

tact resistance and of the base parasitic spreading resistance to the significant reduction of FF is remarkable. On the other hand, large values of metallization fraction lead to dominant recombination losses as well as lower effective internal bottom reflectivity. Therefore, the value of the metallization fraction which optimizes the RPC design is strongly dependent on the presence of the BSF local diffusion, on the specific back contact resistivity, on the base doping concentration as well as on the contact size. In a rear point contact design the goal of enhancing the efficiency can be achieved by reducing both the specific back contact resistivity and the hole size. However, it is worth noting that the specific back contact resistivity is the most sensitive to the optimization of the RPC cell. Once the specific back contact resistivity and of the hole size are minimized, the substrate resistivity still plays a remarkable role in determining the maximum obtainable efficiency. Moreover, the performed simulations reported that the optimum design of a RPC cell is only weakly sensitive to the uncertainties of the main geometrical parameters which lead to the optimized configuration, such as the hole size and the hole pitch.

For the best considered configuration (PERL cell, $\rho_S = 5\Omega cm$), the maximum

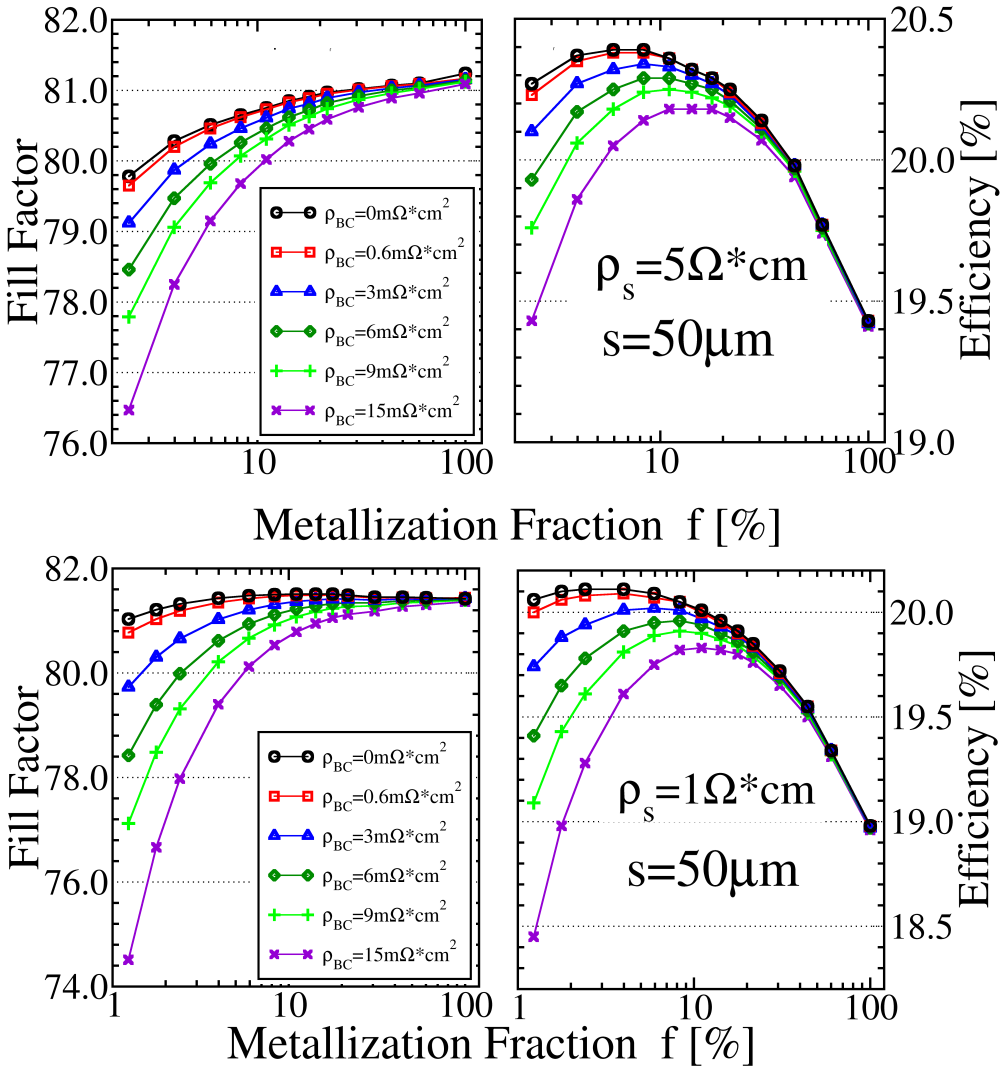

Figure 4.15: Fill Factor (left) and efficiency (right) for PERL solar cells with hole diameter $s = 50\mu m$, substrate resistivity $\rho_S = 5\Omega cm$ (up) and $\rho_S = 1\Omega cm$ (bottom). Specific back contact resistivity ρ_{BC} as parameter.

achievable calculated efficiency is $\eta = 20.34\%$ and the associated optimum metallization fraction is $f_0 = 8.30\%$; the improvements in terms of efficiency is $0.92\%_{abs}$ with respect to the uniformly contacted counterpart.

5

Optical Simulation by Fourier-Modal Methods

Modeling of optoelectronic devices and in particular of solar cells, requires an accurate prediction of the optical generation rate per volume and time unit inside the semiconductor. An effective way to improve the performance of photovoltaic devices is the photon management strategy, which is aimed at increasing the absorbance of the device within the largest possible portion of the solar spectrum. Nano-metric structures and nano-rough interfaces are commonly adopted in advanced photovoltaic devices. As discussed in chapter 3, the ray tracer tool, which is commonly adopted in modeling of crystalline silicon solar cell exhibiting thick wafers, is not suitable for modeling of nano-structured devices and thin film solar cells. In addition, as it will be discussed in chapter 6, the solution to the optical problem in multi-layer devices featuring nano-rough interfaces (like amorphous silicon thin film solar cells) can be supported by methods based on the scalar scattering theory (10), which exhibit several theoretical limitations, due to the approximations which these methods rely on. Practically, methods based on scalar scattering theory can be applied only when the wavelength of the radiation is significantly larger than the size of the roughness. However, such methods are commonly adopted in commercial 1-D tools specifically aimed at simulating thin film solar cells in which the scattering parameters are calibrated by empirical data in order to fit experiments.

Rigorous numerical solvers of the Maxwell equations are required to treat the near field optical problem. The most common approaches to the solution of the Maxwell

equations are the Finite Difference Time Domain method (FDTD) (73), the Finite Element Method (108), the Beam Propagation Method (BPM) (109) and the Fourier Modal Method (FMM), also known as Rigorous Coupled-Wave Analysis (RCWA) (110). RCWA is a general and accurate method based on a Fourier expansion in terms of the spatial harmonics of the electromagnetic field and the permittivity, that can be applied to a wide variety of optical problems. RCWA leads to a good trade-off between computational resources requirement and accuracy, which depends on the number of Fourier modes included in the calculations.

5.1 Introduction to RCWA

Many implementations of the RCWA method have been presented in the literature; the first formulation for planar dielectric gratings was proposed by Moharam and Gaylor (111); subsequently the original implementation was extended to metallic and dielectric surface relief gratings (112)(113). The electromagnetic field in the external media (substrate and superstrate), expressed in terms of a Rayleigh expansion (34), was required to match the in-plane space harmonics of the field within the grating region by means of phase-matching conditions. The problem of determining out-of-plane variations in terms of amplitudes of the space harmonics within the diffraction grating and the subsequent matching in order to find the amplitude of the Rayleigh terms of the field in the external media, has been solved by using the space-state method (111) in combination to a transmittance matrix formulation (T-Matrix). When T-Matrix formulation is adopted, however, the numerical stability is critical, as discussed in section 5.2, in which a new implementation of RCWA based on T-Matrix is presented.

Recently, RCWA has been used to study near field optical problems in corrugated waveguides (114), nanostructured light emitting diodes (115), arbitrary aperiodic geometries (116) and to model the light propagation in solar cells (117). A detailed review of the state-of-the-art implementations of RCWA is reported in (34), where the author proposes a computationally efficient formulation of RCWA based on the solution of an eigenvalue problem associated to a second order coupled-wave equation system which reframes the Maxwells equations. In (118), a more general solution still based on eigenvalues calculation is proposed, employing Jordan factorization. However, as

discussed in (118), the computational effort is a serious open issue for methods based on eigenvalue calculation.

In this work three implementations of the RCWA method are presented. Section 5.2 and section 5.3 describe two approaches adopted for the solution of the electromagnetic problem in 2-D simulation domains previously proposed for the solution of the Schrödinger equation. The proposed implementations are more computationally efficient with respect to standard solvers based on eigenvalue problems, since they do not require the calculation of matrix exponentials and square roots. The first implementation, in particular, is computationally efficient for structures exhibiting thin layers (with respect to the wavelength of the radiation) and rough surfaces. The second method is more efficient for structures featuring thick grating regions, within which the permittivity is not a uniform function of the position, although it requires more memory than the first method. Both proposed implementations are not restricted to periodic structures, but they can be applied to arbitrary geometries.

In section 5.4, an implementation of the RCWA aimed at solving the Maxwell equations in 3-D simulation domains based on a more standard eigenvalue problem, is presented. In such implementation the problem of finding the Fourier coefficients associated to the electromagnetic field is formulated as a second order differential equations system. The proposed implementation is more general than that presented in (34), in which the authors assume that the eigenvectors associated to the second order differential equations problem are not linearly independent; this assumption -which is however reasonable for most practical applications- limits the applicability of the tool to materials (or to range of the wavelength of the radiation) for which the imaginary part of the dielectric constant is zero (or significantly smaller with respect to the real part).

In the last section of this chapter, a validation by means of a comparison with a commercial FDTD simulator as well as a discussion on accuracy and convergence properties of the tools are presented. In addition, some applications of the proposed implementations are described.

5.2 RCWA implementation based on discretization of the Fourier series

In this section, a new and numerically stable RCWA implementation based on finite difference approximation of the wave equations, in which the electromagnetic field and the permittivity are expanded by means of truncated Fourier series, is presented. The proposed T-Matrix formulation of the problem, which has been previously used to numerically solve the Schrödinger equation in (119), has been successfully applied to accurately model the light propagation in devices featuring particular kinds of front surface texturing like grooves, rectangular texturing and non-periodic geometries like random rough interfaces. The proposed method, unlike standard implementations proposed in literature, that are based on the solution of an eigenvalue problem, does not involve the calculation of matrix exponentials or square roots; it simply requires fast matrix multiplications; therefore, it is computationally efficient especially in case of near field optical problems involving thin film layers with rough interfaces.

However, when the T-Matrix approach is adopted, an instability problem occurs because of the presence of both growing and evanescent modes in the general solution of the problem, that leads to a loss of significant digits when a large quantity is to be summed to a significantly smaller one. This situation is particularly critical for deep grating structures (34). To remove the instability problem, Moharam and other authors proposed an improved T-Matrix method (110) that, however, features convergence problems when transverse magnetic polarization is assumed. In this work the problem of the numerical instability is solved by using an arbitrary number of digits (multi-precision arithmetic) with ad-hoc libraries for the implementations of critical calculations.

The method is described in detail for the solution of the Maxwell equations in 2-D simulation domains. However it can be straightforwardly extended to 3-D problems. In order to describe the general solution of the electromagnetic problem, both the Transverse Electric (TE) and the Transverse Magnetic (TM) polarizations are considered. The simulation domain is represented by a superstrate and a substrate regions where the permittivity ε is constant and by a grating region where ε depends on position (Fig. 5.1).

5.2.0.1 Implementation for TE polarization

In the TE case, the electric field $\mathbf{E} = \mathbf{E}(0, E_y, 0)$ is parallel to the y-axis and $\mathbf{H}$ lies in the x-z plane. For the TM polarization, $\mathbf{H}$ is parallel to the y-axis and $\mathbf{E}$ lies in the x-z plane. We start the description of the method from the Maxwell's equations for a linear isotropic and magnetically homogenous material without free charges.

In case of TE polarization, under the assumptions previously mentioned, the Maxwell's equations for the single nonzero components E_y of the electric field can be reformulated by the following wave equation:

$$\Delta E_y = -k_0^2 \varepsilon(x, z) E_y, \quad E_x = E_z = 0, \tag{5.1}$$

where $\varepsilon(x, y)$ is the relative permittivity, $k_0^2 = \varepsilon_0 \mu_0 \omega^2 = \omega^2 c^{-2} = (2\pi)^2 \lambda^{-2}$, c is the speed of light in vacuum, ω is the angular frequency, ε_0 and μ_0 are the permittivity and the permeability of free space, respectively.

We consider a plane wave propagating in the superstrate region (Fig. 5.1). The incident wave exhibiting a propagation direction forming an angle θ with the normal to the device surface is described by

$$E_y^{inc} = e^{ik_0 n_I (x \sin(\theta) + z \cos(\theta))}, \tag{5.2}$$

where n_I is the refractive index of the superstrate. We assume that the grating region features a periodicity p; therefore, lateral translation from the coordinate x to $x + p$ leads to multiplication of the incident wave by an exponential phase factor, as expressed by the Floquet boundary condition (118):

$$E_y(x + p, z) = e^{ik_0 n_I p \sin(\theta)} E_y(x, z), \tag{5.3}$$

Therefore, if $C(x, z)$ is a periodic function of the spatial coordinate x with periodicity p, by using the Fourier expansion of the electric field we obtain:

$$\begin{aligned} &E_y(x, z) = \\ &\quad = e^{ik_0 n_I x \sin(\theta)} C(x, z) = e^{ik_0 n_I x \sin(\theta)} \sum_{s=-\infty}^{+\infty} c_s(z) e^{is(2\pi \frac{x}{p})} = \sum_{s=-\infty}^{+\infty} c_s(z) e^{ik_{xs} x}, \end{aligned} \tag{5.4}$$

where $k_{xs} = k_0 n_I \sin(\theta) + s\frac{2\pi}{p} = k_0\left(n_I \sin(\theta) + s\left(\frac{\lambda}{p}\right)\right)$ and $c_s(z)$ are the Fourier coefficients independent of x.

Therefore:

$$\left(-\frac{d^2}{dz^2} + k_{xs}^2\right) c_s(z) = k_1^2 c_s(z). \tag{5.5}$$

In addition, according to the spatial Fourier expansion of the permittivity along x:

$$\varepsilon(x,z) = \sum_{h=-\infty}^{+\infty} \varepsilon_h(z) e^{ih\left(\frac{2\pi x}{p}\right)}. \tag{5.6}$$

By applying the finite version of Laurent's rule (120), adopting the simultaneous truncation approximation in order to handle the product of the two Fourier expansions:

$$\left(-\frac{d^2}{dz^2} - \frac{d^2}{dx^2}\right) e^{ik_0 n_I x \sin(\theta)} C(x,z) = k_0^2 \varepsilon(x,z) e^{ik_0 n_I x \sin(\theta)} C(x,z), \tag{5.7}$$

$$\left(-\frac{d^2}{dz^2} - \frac{d^2}{dx^2}\right) \sum_{s=-M_x}^{M_x} c_s(z) e^{ik_{xs}x} = k_0^2 \varepsilon(x,z) \sum_{s=-M_x}^{M_x} c_s(z) e^{ik_{xs}x}, \tag{5.8}$$

$$\left(-\frac{d^2}{dz^2} + k_{xs}^2\right) c_s(z) = k_0^2 \sum_{s=-M_x}^{M_x} \varepsilon_{s,h}(z) c_h(z). \tag{5.9}$$

Equating the corresponding terms on the left and right-hand side for $s = -M_x \ldots M_x$:

$$\frac{d^2 c_s(z)}{dz^2} = \sum_{h=-M_x}^{+M_x} A_{s,h}(z) c_h(z). \tag{5.10}$$

where $A_{s,h}(z)$ are linear combinations of the Fourier coefficients of the permittivity. Differently from previous implementations of the RCWA, this system of ordinary differential equations is solved for the unknown coefficients $c_h(z)$ through discretization on a uniform mesh with nodes in z_k, $k = 1 \ldots N$, and step Δz. The finite difference approximation leads to:

$$c_s(z_{k-1}) = -c_s(z_{k+1}) + 2c_s(z_k) + \Delta z^2 \sum_j A_{s,j}(z_k) c_j(z_k) \tag{5.11}$$

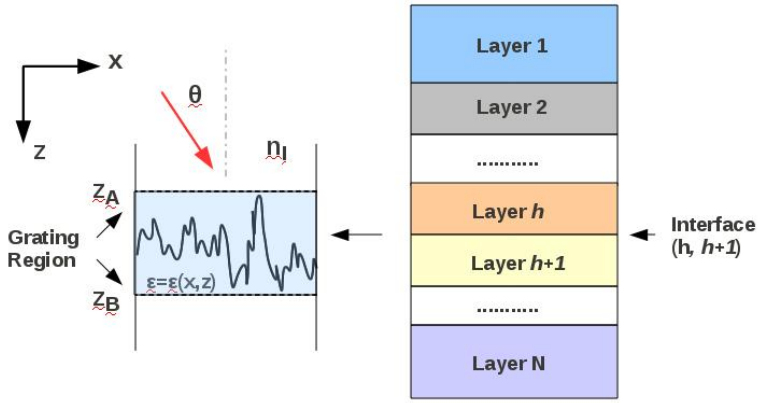

Figure 5.1: Sketch of the 2-D simulation domain which includes the superstrate, the substrate and the grating region (left). A typical photovoltaic device is represented by a multi-layer structure (right) in which each layer is homogenous and separated by smooth or rough interfaces. The rough interfaces are treated as grating regions within which the permittivity is not a uniform function of the position. The refractive index of the superstrate is n_I.

By adopting the vector notation:

$$\mathbf{c}(z_{k-1}) = -\mathbf{c}(z_{k+1}) + 2\mathbf{c}(z_k) + \Delta z^2 \mathbf{A}(z_k)\mathbf{c}(z_k) = -\mathbf{c}(z_{k+1}) + \tilde{\mathbf{A}}(z_k)\mathbf{c}(z_k) \tag{5.12}$$

where $\mathbf{c}$ denotes the vector of the $2M_x + 1$ coefficients in eq. 5.5. Therefore

$$\begin{bmatrix} \mathbf{c}(z_{k-1}) \\ \mathbf{c}(z_k) \end{bmatrix} = \begin{bmatrix} \tilde{\mathbf{A}}(z_k) & -\mathbf{I} \\ \mathbf{I} & 0 \end{bmatrix} \begin{bmatrix} \mathbf{c}(z_k) \\ \mathbf{c}(z_{k+1}) \end{bmatrix} = \mathbf{T}(z_k) \begin{bmatrix} \mathbf{c}(z_k) \\ \mathbf{c}(z_{k+1}) \end{bmatrix} \tag{5.13}$$

where $\mathbf{I}$ is a unity matrix. By applying the previous equation to all nodes z_k we obtain the following expression for the set of coefficients $\mathbf{c}$ at the top boundary of the grating region:

$$\begin{bmatrix} \mathbf{c}(z_{-1}) \\ \mathbf{c}(z_0) \end{bmatrix} = \prod_{k=0}^{N} T(z_k) \begin{bmatrix} \mathbf{c}(z_N) \\ \mathbf{c}(z_{N+1}) \end{bmatrix} = \mathbf{T} \begin{bmatrix} \mathbf{c}(z_N) \\ \mathbf{c}(z_{N+1}) \end{bmatrix} \tag{5.14}$$

This equation relates the coefficients $\mathbf{c}$ at the top boundary with those at the bottom one through the total transfer-matrix $\mathbf{T}$ which is obtained by multiplying the transfer-matrices $\mathbf{T}(z_k)$ calculated at each node z_k. This leads to a particularly computationally

efficient algorithm that does not involve to solve an eigenvalue problem, therefore, differently from (34) and (118), it does not require the calculation of matrix exponentials and roots, but only the multiplications of matrices. In fact, it is worth noting that the matrices $\mathbf{T}(z_k)$ are simply calculated as linear combination of the Fourier coefficients of the permittivity expansion.

In order to properly set the boundary conditions we express the coefficients c_s in terms of amplitudes of ingoing and outgoing waves:

$$c_s(z) = c_s^+(z) + c_s^-(z) \tag{5.15}$$

In the substrate and superstrate, where the relative permittivity $\varepsilon = \varepsilon_l$ with l=1,2 is constant:

$$c_{s,l}(z+\Delta z) = c_{s,l}^+(z)e^{+i\sqrt{k_0^2\varepsilon_l - k_{xs}^2}\Delta z} + c_{s,l}^-(z)e^{-i\sqrt{k_0^2\varepsilon_l - k_{xs}^2}\Delta z} \tag{5.16}$$

where $l = 1$ denotes the superstrate and $l = 2$ the substrate. In addition,

$$c_{s,l}^+(z) = b_{11}^{s,l}c_{s,l}(z) + b_{12}^{s,l}c_{s,l}(z+\Delta z) \tag{5.17}$$

$$c_{s,l}^-(z) = b_{21}^{s,l}c_{s,l}(z) + b_{22}^{s,l}c_{s,l}(z+\Delta z) \tag{5.18}$$

where

$$b_{11}^{s,l} = \frac{1}{1 - e^{2i\sqrt{k_0^2\varepsilon_l - k_{xs}^2}\Delta z}}, \qquad b_{12}^{s,l} = \frac{1}{e^{i\sqrt{k_0^2\varepsilon_l - k_{xs}^2}\Delta z} - e^{-i\sqrt{k_0^2\varepsilon_l - k_{xs}^2}\Delta z}},$$

$$b_{11}^{s,l} = \frac{1}{1 - e^{-2i\sqrt{k_0^2\varepsilon_l - k_{xs}^2}\Delta z}}, \qquad b_{22}^{s,l} = \frac{1}{e^{-i\sqrt{k_0^2\varepsilon_l - k_{xs}^2}\Delta z} - e^{+i\sqrt{k_0^2\varepsilon_l - k_{xs}^2}\Delta z}} = -b_{12}^{s,l},$$

Moreover

$$c_{s,l}(z) = \tilde{b}_{11}^{s,l}c_{s,l}^+(z) + \tilde{b}_{12}^{s,l}c_{s,l}^-(z) \tag{5.19}$$

$$c_{s,l}(z+\Delta z) = \tilde{b}_{21}^{s,l}c_{s,l}^+(z) + \tilde{b}_{22}^{s,l}c_{s,l}^-(z) \tag{5.20}$$

where

$$\tilde{b}_{11}^{s,l} = 1, \qquad \tilde{b}_{12}^{s,l} = 1,$$

$$\tilde{b}_{21}^{s,l} = e^{+i\sqrt{k_0^2\varepsilon_l - k_{xs}^2}\Delta z}, \qquad \tilde{b}_{22}^{s,l} = e^{-i\sqrt{k_0^2\varepsilon_l - k_{xs}^2}\Delta z},$$

The eq. 5.13 can be reformulated as:

$$\begin{bmatrix} \mathbf{c}(z_{-3}) \\ \mathbf{c}(z_{-2}) \end{bmatrix} = \mathbf{T}(z_{-2}) \begin{bmatrix} \mathbf{c}(z_{-2}) \\ \mathbf{c}(z_{-1}) \end{bmatrix} = \mathbf{T}(z_{-2}) \left[\mathbf{T}(z_{-1}) \begin{bmatrix} \mathbf{c}(z_{-1}) \\ \mathbf{c}(z_{-0}) \end{bmatrix} \right] =$$

$$= \mathbf{T}(z_{-2}) \left[\mathbf{T}(z_{-1}) \left[\mathbf{T}(z_0) \begin{bmatrix} \mathbf{c}(z_0) \\ \mathbf{c}(z_1) \end{bmatrix} \right] \right] = \mathbf{T}(z_{-2})\mathbf{T}(z_{-1})\mathbf{T}(z_0) \begin{bmatrix} \mathbf{c}(z_0) \\ \mathbf{c}(z_1) \end{bmatrix} = ... =$$

$$= \prod_{k=-2}^{N+2} \mathbf{T}(z_k) \begin{bmatrix} \mathbf{c}(z_{N+2}) \\ \mathbf{c}(z_{N+3}) \end{bmatrix} = \mathbf{T} \begin{bmatrix} \mathbf{c}(z_{N+2}) \\ \mathbf{c}(z_{N+3}) \end{bmatrix} \tag{5.21}$$

By applying the eq. 5.19, the eq. 5.20 and using the eq. 5.21,

$$\begin{bmatrix} \mathbf{c}^+(z_{-3}) \\ \mathbf{c}^-(z_{-3}) \end{bmatrix} = \mathbf{B} \begin{bmatrix} \mathbf{c}(z_{-3}) \\ \mathbf{c}(z_{-2}) \end{bmatrix} = \mathbf{B} \cdot \mathbf{T} \begin{bmatrix} \mathbf{c}(z_{N+2}) \\ \mathbf{c}(z_{N+3}) \end{bmatrix} =$$

$$= \mathbf{B} \cdot \mathbf{T} \cdot \tilde{\mathbf{B}} \begin{bmatrix} \mathbf{c}^+(z_{N+2}) \\ \mathbf{c}^-(z_{N+2}) \end{bmatrix} = \tilde{\mathbf{T}} \begin{bmatrix} \mathbf{c}^+(z_{N+2}) \\ \mathbf{c}^-(z_{N+2}) \end{bmatrix} \tag{5.22}$$

where $\tilde{\mathbf{B}}$ is a $(4M_x + 2)$-order square matrix:

$$\tilde{\mathbf{B}} = \begin{bmatrix} b_{11}^{-M_x} & 0 & 0 & b_{12}^{-M_x} & 0 & 0 \\ 0 & ... & 0 & 0 & ... & 0 \\ 0 & 0 & b_{11}^{M_x} & 0 & 0 & b_{12}^{M_x} \\ b_{12}^{-M_x} & 0 & 0 & b_{22}^{-M_x} & 0 & 0 \\ 0 & ... & 0 & 0 & ... & 0 \\ 0 & 0 & b_{21}^{M_x} & 0 & 0 & b_{22}^{M_x} \end{bmatrix}. \tag{5.23}$$

At the top and at the bottom of the grating region, for $z = z_{-3}$ and $z = z_{N+2}$, respectively, the following boundary conditions are adopted:

$$\mathbf{c}^+(z_{-3}) = \begin{bmatrix} 0 \\ ... \\ 0 \\ e^{ik_0 n_I z_{-3} cos(\theta)} \\ 0 \\ ... \\ 0 \end{bmatrix}, \qquad \mathbf{c}^-(z_{N+2}) = \mathbf{0}, \tag{5.24}$$

which allow to obtain:

$$\begin{bmatrix} \mathbf{c}^+(z_{-3}) \\ 0 \end{bmatrix} = \begin{bmatrix} \mathbf{T}_{11} & \mathbf{0} \\ \mathbf{T}_{21} & -\mathbf{I} \end{bmatrix} = \mathbf{B} \cdot \mathbf{T} \begin{bmatrix} \mathbf{c}^+(z_{N+2}) \\ \mathbf{c}^-(z_{-3}) \end{bmatrix} \tag{5.25}$$

where $\mathbf{c}^-(z_{-3})$, $\mathbf{c}^+(z_{N+2})$ are reflection and transmission coefficients, respectively. The coefficients $\mathbf{c}^+(z_{-3})$, which are defined by the eq. 5.24, represent the incident wave. To solve the well known numerical stability issues of the T-matrix method, multi-precision arithmetic is adopted by dynamically adjusting the amount of digits in numbers with multi-precision representation. However, the use of the arbitrary multi-precision is limited to some critical calculations (for instance to accumulate the resulting transfer matrix in eq. 5.14) and double precision is adopted otherwise to save computational time. The proposed method may work with complicated and arbitrary geometrical configurations of the grating regions.

5.2.0.2 Implementation for TM polarization

In case of TM polarization, the Maxwell's equations for the single nonzero components H_y of the electric field leads to the following equation:

$$\Delta\mathbf{H} = -\varepsilon\mu\omega^2\mathbf{H} - \frac{1}{\varepsilon}\nabla(\varepsilon) \times \nabla \times \mathbf{H}, \tag{5.26}$$

that can be expressed as

$$\frac{\partial}{\partial z}\left(\frac{1}{\varepsilon(x,z)}\frac{\partial H_y}{\partial z}\right) = -\frac{\partial}{\partial x}\left(\frac{1}{\varepsilon(x,z)}\frac{\partial H_y}{\partial x}\right) - k_0^2 H_y, \quad H_x = H_z = 0, \tag{5.27}$$

The incident wave, similarly to the TE polarization is

$$H_y^{inc} = e^{ik_0 n_I (x\sin(\theta) + z\cos(\theta))}. \tag{5.28}$$

The component $H_y(x,z)$ can be expressed as a truncated Fourier expansion by means of coefficients $c_s(z)$:

$$H_y(x,z) = e^{ik_0 n_I x \sin(\theta)} \sum_{s=-M_x}^{+M_x} c_s(z) e^{is(2\pi\frac{x}{p})} = \sum_{s=-M_x}^{+M_x} c_s(z) e^{ik_{xs}x}, \tag{5.29}$$

In 5.27 the functions $(x,z) \to \frac{1}{\varepsilon(x,z)}$ and $(x,z) \to \frac{\partial H_y}{\partial x}$ are only piecewise continuous, however the function $(x,z) \to \frac{1}{\varepsilon(x,z)}\frac{\partial H_y}{\partial x}$ is continuous (118), therefore the following Fourier expansion can be defined:

$$e^{-ik_0 n_I x \sin(\theta)} \frac{1}{\varepsilon(x,z)} \frac{\partial H_y}{\partial x} = \sum_{s=-M_x}^{+M_x} c_{1,s}(z) e^{is(2\pi \frac{x}{p})}, \tag{5.30}$$

where the coefficients $\mathbf{c}_1$ are given by

$$\mathbf{c}_1(z) = i \left[\varepsilon(z)\right]^{-1} \mathbf{K}\mathbf{c}(z), \tag{5.31}$$

and $\mathbf{K}$ is the diagonal matrix with k_{xs} elements.
Following the approach proposed in (120),

$$\frac{i}{\varepsilon(x,z)} \frac{\partial H_y}{\partial x} = \sum_{s=-M_x}^{+M_x} c_{1s}(z) e^{ik_{xs}x}, \tag{5.32}$$

$$\frac{\partial}{\partial x}\left(\frac{1}{\varepsilon(x,z)}\frac{\partial H_y}{\partial x}\right) + k_0^2 H_y = \sum_{s=-M_x}^{+M_x} \left(ic_{1s}(z)k_{xs} + k_0^2 c_s(z)\right) e^{ik_{xs}x}. \tag{5.33}$$

From eq. 5.27 and eq. 5.33,

$$\frac{\partial}{\partial z}\left(\frac{1}{\varepsilon(x,z)} \sum_{s=-M_x}^{+M_x} \frac{dc_s(z)}{dz} e^{ik_{xs}x}\right) = -\sum_{s=-M_x}^{+M_x} \left(ic_{1s}(z)k_{xs} + k_0^2 c_s(z)\right) e^{ik_{xs}x}. \tag{5.34}$$

The finite difference approximation of eq. 5.34, for each k-th node is:

$$\begin{aligned} &\sum_{s=-M_x}^{+M_x} \left(\frac{c_s(z_{k+1}) - c_s(z_k)}{\varepsilon(x, z_{k+\frac{1}{2}})} - \frac{c_s(z_k) - c_s(z_{k-1})}{\varepsilon(x, z_{k-\frac{1}{2}})}\right) e^{ik_{xs}x} = \\ &= -\Delta z^2 \textstyle\sum_{s=-M_x}^{+M_x} \left(ic_{1s}(z)k_{xs} + k_0^2 c_s(z)\right) e^{ik_{xs}x}, \end{aligned} \tag{5.35}$$

that can be expressed in matrix notation as:

$$\left[\frac{1}{\varepsilon(z_{k+\frac{1}{2}})}\right] \left(\mathbf{c}(z_{k+1} - \mathbf{c}(z_k)\right) - \left[\frac{1}{\varepsilon(z_{k-\frac{1}{2}})}\right] \Big(\mathbf{c}(z_k - \mathbf{c}(z_{k-1})\Big) = \mathbf{A}_1 \mathbf{c}(z_k), \tag{5.36}$$

where

$$\mathbf{A}_1 = \Delta z^2 \left(\mathbf{K} \left[\varepsilon(z_k) \right]^{-1} \mathbf{K} - k_0^2 \mathbf{I} \right). \tag{5.37}$$

By rearranging all terms, similarly to the TE case,

$$\begin{bmatrix} \mathbf{c}(z_{k-1}) \\ \mathbf{c}(z_k) \end{bmatrix} = \begin{bmatrix} \mathbf{T}_{1,1} & \mathbf{T}_{1,2} \\ \mathbf{I} & 0 \end{bmatrix} \begin{bmatrix} \mathbf{c}(z_k) \\ \mathbf{c}(z_{k+1}) \end{bmatrix} = \mathbf{T}(z_k) \begin{bmatrix} \mathbf{c}(z_k) \\ \mathbf{c}(z_{k+1}) \end{bmatrix} \tag{5.38}$$

$$\mathbf{T}_{1,1} = \left[\frac{1}{\varepsilon(z_{k-\frac{1}{2}})} \right]^{-1} \left(\left[\frac{1}{\varepsilon(z_{k+\frac{1}{2}})} \right] + \mathbf{A}_1 \right) + \mathbf{I},$$

$$\mathbf{T}_{1,2} = - \left[\frac{1}{\varepsilon(z_{k-\frac{1}{2}})} \right]^{-1} \left[\frac{1}{\varepsilon(z_{k+\frac{1}{2}})} \right]. \tag{5.39}$$

5.3 RCWA implementation based on auxiliary functions

In this section the electromagnetic field within the grating region is expressed by means of an expansion through auxiliary functions which are determined by using a numerical discretization technique. The amplitude of the harmonics within the grating region are then matched with those of the field in the external region by using Dirichlet boundary conditions on the auxiliary functions as well as on the amplitude and on the first spatial derivative of the field amplitude with respect to the propagation direction. The adoption of the auxiliary functions is reported also in (121) for the solution of the Schrödinger equations; in the mentioned work, however, the auxiliary functions are determined analytically since they are applied in regions featuring simple and known geometries, like rectangular-shaped domains. This approach allows to limit the extension of the discretization grid only within the grating region, differently from the method presented in section 5.2, for which, in order to numerically solve the approximated wave functions, the discretization is adopted throughout the simulation domain. An advantage of this approach, in comparison with the first implementation, is the enhanced computational efficiency for structures exhibiting grating regions in combination to relatively thick (with reference to the wavelength of the radiation) homogenous layers, within which, in order to save simulation time, the solution can be calculated by using an analytical approach.

5.3.1 Auxiliary functions and boundary conditions

In the following a common approach to the solution of the electromagnetic problem for TE and TM polarization is described. The function $\phi(x,z)$ denotes either the component $E_y(x,z)$ or the component $H_y(x,z)$ of the filed depending upon the particular polarization, TE or TM, respectively. The function $\phi(x,z)$ can be therefore expressed as:

$$\phi(x,z) = \begin{cases} \sum_{s=-N}^{N} \left(c_{1,s}^{+} e^{i\sqrt{k_1^2 - k_{xs}^2}(z-z_1)} + c_{1,s}^{-} e^{-i\sqrt{k_1^2 - k_{xs}^2}(z-z_1)} \right) e^{ik_{xs}x}, & z \le z_1 \\ \sum_{s=-N}^{N} \left(d_{1,s}\chi_{1,s}(x,z) + d_{2,s}\chi_{2,s}(x,z) \right), & z_1 \le z \le z_2 \\ \sum_{s=-N}^{N} \left(c_{2,s}^{+} e^{i\sqrt{k_2^2 - k_{xs}^2}(z-z_2)} + c_{2,s}^{-} e^{-i\sqrt{k_2^2 - k_{xs}^2}(z-z_1)} \right) e^{ik_{xs}x}, & z \ge z_2 \end{cases} \tag{5.40}$$

where $k_l = k_0\sqrt{\varepsilon_l}$, $l = 1,2$ (ε_1 and ε_2 are the values of permittivity of the superstrate and of the substrate, respectively. According to eq. 5.40, the function $\phi(x,z)$ is expanded into $2N+1$ terms within the grating region ($z_1 \le z \le z_2$) by means of the auxiliary functions $\chi_{j,s}$, $j = 1,2$, $s = -N..+N$. The following Dirichlet boundary conditions are applied at the boundaries of the grating regions ($z = z_1$, $z = z_2$) for $s = -N..+N$:

$$\chi_{1,s}|_{z=z_1} = e^{ik_{xs}x}, \quad \chi_{1,s}|_{z=z_2} = 0, \quad \chi_{2,s}|_{z=z_1} = 0 \quad \chi_{2,s}|_{z=z_2} = e^{ik_{xs}x}. \tag{5.41}$$

In addition, the following periodic Floquet boundary condition is applied along the x-axis:

$$\chi_{j,s}(x+p,z) = e^{ik_0 N_I psin(\theta)} \chi_{j,s}(x,z), \qquad j = 1,2, \qquad s = -N..+N. \tag{5.42}$$

In case of TE polarization, at each boundary of the grating region, the continuity of the electric field and of its first derivative with respect to z have to be satisfied:

$$E_y|_{z=z_{i-0}} = E_y|_{z=z_{i+0}}, \qquad \frac{\partial E_y}{\partial z}|_{z=z_{i-0}} = \frac{\partial E_y}{\partial z}|_{z=z_{i+0}}, \tag{5.43}$$

where $i = 1$ for the top boundary ($z = z_1$) and $i = 2$ for the bottom boundary ($z = z_2$) of the grating region. Similarly for the TM polarization:

$$H_y|_{z=z_{i-0}} = H_y|_{z=z_{i+0}}, \qquad \frac{1}{\varepsilon(x,z)}\frac{\partial H_y}{\partial z}|_{z=z_{i-0}} = \frac{1}{\varepsilon(x,z)}\frac{\partial H_y}{\partial z}|_{z=z_{i+0}}, \tag{5.44}$$

5.3.2 Solving for the auxiliary function

In the following the algorithm used to solve the eq. 5.40 for the auxiliary function is described. The auxiliary functions $\chi_{s,j}$ with $s = -N..N, \qquad j = 1, 2$ are required to be solution of the Helmholtz equation 5.1 (for TE polarization) or of the eq. 5.26 (for TM polarization). The proposed method to solve the Helmholtz equations relies on the Fourier expansion of the auxiliary functions along x-axis, by using, in order to simplify the algorithm, the same truncation order N adopted in eq. 5.40. Therefore, if a uniform discretization grid of N_z points is adopted along the propagation direction z, for each node z_k with $k = 0, 1, ..., N_z - 1$:

$$\chi_{s,j}(x, z_k) = \sum_{h=-N}^{N} = \hat{\chi}(z_k) e^{ik_{xh}x}, \tag{5.45}$$

where $\hat{\chi}(z_k)$ denote the Fourier coefficient of the auxiliary function expansion. The Helmholtz equations are then discretized on the uniform mesh along z; for each node z_k:

$$\sum_{h=-N}^{N} \frac{\hat{\chi}_h(z_{k-1}) - 2\hat{\chi}_h(z_k) + \hat{\chi}_h(z_{k+1})}{(\Delta z)^2} e^{ik_{xh}x} + \sum_{h=-N}^{N} -K_{xh}^2 \hat{\chi}_h(z_k) e^{ik_{xh}x} = \\ = k_0^2 \varepsilon(x, z_k) \sum_{h=-N}^{N} \hat{\chi}_h(z_k) e^{ik_{xh}x}. \tag{5.46}$$

Both terms of eq. 5.46 are multiplied by $e^{-ik_{xj}x}, \qquad i, j = 1..N$ and integrated over the x-axis from $x = 0$ to $x = p$, where p is the periodicity of the grating region. Therefore:

$$\int_0^p e^{i(k_{xh} - k_{xj})x} dx = \delta(h, j) = \begin{cases} 1 & if \qquad h = j, \\ 0 & if \qquad h \neq j. \end{cases} \tag{5.47}$$

Eq. 5.46 can be then reformulated as:

$$\frac{\hat{\chi}_j(z_{k-1}) - 2\hat{\chi}_j(z_k) + \hat{\chi}_j(z_{k+1})}{(\Delta z)^2} - K_{xj}^2 \hat{\chi}_j(z_k) = k_0^2 \sum_{h=-N}^{N} \varepsilon_{h,j}(z_k) \hat{\chi}_h(z_k), \tag{5.48}$$

where

$$\varepsilon_{h,j}(z_k) = \int_0^p \varepsilon(x, z_k) e^{i(k_{xh} - k_{xj})x} dx. \tag{5.49}$$

If $k = 0$ (top boundary), by applying the boundary conditions expressed by eq. 5.41,

$$\chi_{1,s}(x, z_0) = e^{ik_{xs}x} = \sum_{h=-N}^{N} \hat{\chi}_h(z_k) e^{ik_{xh}x} \tag{5.50}$$

which requires that $\chi_{h=s}(z_0) = 1, \qquad \chi_{h\neq s}(z_0) = 0$. Similarly for the bottom boundary of the grating region ($z = z_{N_z-1}$).

For $k = 1, 2, ..., N_z - 2$, multiplying by Δz^2 and rearranging eq. 5.48,

$$-\hat{\chi}_j(z_{k-1}) + \sum_{i=-N}^{+N} \left[\left(2 - \Delta z^2 k_{xj}^2\right) \delta_{hj} - \Delta_z^2 k_0^2 \varepsilon_{h,j}(z_k) \right] \hat{\chi}_j(z_k) - \hat{\chi}_j(z_{k+1}) = 0 \tag{5.51}$$

Similarly, for $k = 0$, using eq. 5.50, eq. 5.48 reads

$$\sum_{h=-N}^{+N} \left[\left(2 - \Delta z^2 k_{xj}^2\right) \delta_{hj} - \Delta_z^2 k_0^2 \varepsilon_{h,j}(z_0) \right] \hat{\chi}_j(z_0) - \hat{\chi}_j(z_1) = \delta_{s,h} \tag{5.52}$$

Finally, if $k = N_z - 1$,

$$\sum_{h=-N}^{+N} \left[\left(2 - \Delta z^2 k_{xj}^2\right) \delta_{hj} - \Delta_z^2 k_0^2 \varepsilon_{h,j}(z_{N_z-1}) \right] \hat{\chi}_j(z_{N_z-1}) - \hat{\chi}_j(z_{N_z-3}) = 0. \tag{5.53}$$

In vector notation, equations from 5.51 to 5.53 can be written as:

$$\tilde{\mathbf{A}} \cdot \hat{\chi} = \mathbf{B} \tag{5.54}$$

where $\tilde{\mathbf{A}}$ is the tridiagonal block matrix of elements $[a_{i,j}], \qquad i, j = 1 \cdots N_{z-1}$:

$$\mathbf{A} = \begin{bmatrix} [a_{1,1}] & [a_{1,2}] & 0 & \cdots & 0 & 0 & 0 & 0 \\ [a_{2,1}] & [a_{2,2}] & [a_{2,3}] & 0 & \cdots & 0 & 0 & 0 \\ 0 & [a_{3,2}] & [a_{3,3}] & [a_{3,4}] & 0 & \cdots & 0 & 0 \\ 0 & 0 & \cdots & \cdots & \cdots & 0 & \cdots & 0 \\ \cdots & \cdots & \cdots & \cdots & \cdots & \cdots & \cdots & \cdots \\ 0 & 0 & 0 & 0 & 0 & [a_{N_z-4,N_z-4}] & [a_{N_z-3,N_z-3}] & [a_{N_z-2,N_z-2}] \end{bmatrix}.$$

$$
\begin{aligned}
[a_{n,n-1}] &= -\left[K_{jx}^2\right] \\
[a_{n,n}] &= \left[\left(2-\Delta z^2 k_{xj}^2\right)\delta_{ij} - \Delta_z^2 k_0^2 \varepsilon_{i,j}(z_{N_z-1})\right] \\
[a_{n,n+1}] &= -\left[K_{jx}^2\right]
\end{aligned}
$$

$$
\mathbf{B} = \begin{bmatrix}
\left[K_{-N,x}^2\right] & 0 & 0 & 0 & 0 & 0 \\
0 & \left[K_{-N+1,x}^2\right] & 0 & 0 & 0 & 0 \\
\cdots & \cdots & \cdots & \cdots & \cdots & \cdots \\
0 & 0 & 0 & \cdots & 0 & \left[K_{N,x}^2\right]
\end{bmatrix}.
$$

$$
\hat{\chi} = \begin{bmatrix}
[\hat{\chi}_{s=-N}(z_1)] & [\hat{\chi}_{s=-N+1}(z_1)] & \cdots & [\hat{\chi}_{s=+N}(z_1)] \\
[\hat{\chi}_{s=-N}(z_2)] & [\hat{\chi}_{s=-N+1}(z_2)] & \cdots & [\hat{\chi}_{s=+N}(z_2)] \\
\cdots & \cdots & \cdots & \cdots \\
[\hat{\chi}_{s=-N}(z_{N_z-2})] & [\hat{\chi}_{s=-N+1}(z_{N_z-2})] & \cdots & [\hat{\chi}_{s=+N}(z_{N_z-2})]
\end{bmatrix}.
$$

The system of linear equations 5.54 is solved by means of standard algorithms in order to determine the Fourier coefficients $\hat{\chi}_i$ and subsequently the auxiliary functions $\chi_{s,j}$.

5.3.3 Determining the electromagnetic field

Once determined the auxiliary function as described in the previous subsection, the problem of finding the coefficients $c_{j,s}$ and $d_{j,s}$ (with $j = 1, 2$ and $s = -N \cdots + N$) of the system of equations 5.40 can be solved by applying the matching conditions 5.43 or 5.44, depending upon the polarization; for TE polarization, by applying the first of the eq.5.43 :

$$
\sum_{s=-N}^{+N} \left(c_{1,s}^{+} + c_{1,s}^{-}\right) e^{ik_{xs}x} = \sum_{s=-N}^{N} \left(d_{1,s}\chi_{1,s}(x,z_1) + d_{2,s}\chi_{2,s}(x,z_1)\right), \tag{5.55}
$$

$$
\sum_{s=-N}^{+N} \left(c_{2,s}^{+} + c_{2,s}^{-}\right) e^{ik_{xs}x} = \sum_{-N}^{N} \left(d_{1,s}\chi_{1,s}(x,z_2) + d_{2,s}\chi_{2,s}(x,z_2)\right). \tag{5.56}
$$

By applying the second of the eq. 5.43,

$$\sum_{s=-N}^{+N} i\sqrt{k_1^2 - k_{xs}^2}\left(c_{1,s}^{+} - c_{1,s}^{-}\right) e^{ik_{xs}x} =$$
$$= \sum_{-N}^{N}\left(d_{1,s}\frac{\partial\chi_{1,s}(x,z)}{\partial z}|_{z=z_1} + d_{2,s}\frac{\partial\chi_{2,s}(x,z)}{\partial z}|_{z=z_1}\right), \tag{5.57}$$

$$\sum_{s=-N}^{+N} i\sqrt{k_2^2 - k_{xs}^2}\left(c_{2,s}^{+} - c_{2,s}^{-}\right) e^{ik_{xs}x} =$$
$$= \sum_{s=-N}^{N}\left(d_{1,s}\frac{\partial\chi_{1,s}(x,z)}{\partial z}|_{z=z_2} + d_{2,s}\frac{\partial\chi_{2,s}(x,z)}{\partial z}|_{z=z_2}\right). \tag{5.58}$$

By multiplying by $e^{ik_{xs_1}x}$ and integrating the eq. from 5.55 to 5.58 over x-axis from $x = 0$ to $x = p$,

$$c_{1,s_1}^{+} + c_{1,s_1}^{-} = d_{1,s_1}, \tag{5.59}$$

$$c_{2,s_1}^{+} + c_{2,s_1}^{-} = d_{2,s_1}, \tag{5.60}$$

$$i\sqrt{k_1^2 - k_{xs_1}^2}\left(c_{1,s_1}^{+} - c_{1,s_1}^{-}\right) =$$
$$= \sum_{s=-N}^{N} d_{1,s}\frac{1}{p}\int_0^p e^{-ik_{xs_1}x}\frac{\partial\chi_{1,s}(x,z)}{\partial z}|_{z=z_1}dx +$$
$$d_{2,s}\frac{1}{p}\int_0^p e^{-ik_{xs_1}x}\frac{\partial\chi_{2,s}(x,z)}{\partial z}|_{z=z_1}dx, \tag{5.61}$$

$$i\sqrt{k_2^2 - k_{xs_1}^2}\left(c_{2,s_1}^{+} - c_{2,s_1}^{-}\right) =$$
$$= \sum_{s=-N}^{N} d_{1,s}\frac{1}{p}\int_0^p e^{-ik_{xs_1}x}\frac{\partial\chi_{1,s}(x,z)}{\partial z}|_{z=z_2}dx +$$
$$d_{2,s}\frac{1}{p}\int_0^p e^{-ik_{xs_1}x}\frac{\partial\chi_{2,s}(x,z)}{\partial z}|_{z=z_2}dx, \tag{5.62}$$

which can be expressed in vector-matrix notation as:

$$\begin{cases} \mathbf{c}_1^+ + \mathbf{c}_1^- = \mathbf{d}_1 \\ \mathbf{c}_2^+ + \mathbf{c}_2^- = \mathbf{d}_2 \\ \mathbf{F}_1 \left(\mathbf{c}_1^+ - \mathbf{c}_1^-\right) = \mathbf{A}_{1,1}\mathbf{d}_1 + \mathbf{A}_{1,2}\mathbf{d}_2 \\ \mathbf{F}_2 \left(\mathbf{c}_1^+ - \mathbf{c}_1^-\right) = \mathbf{A}_{2,1}\mathbf{d}_1 + \mathbf{A}_{2,2}\mathbf{d}_2 \end{cases} \tag{5.63}$$

or

$$\begin{cases} \mathbf{F}_1 \left(\mathbf{c}_1^+ - \mathbf{c}_1^-\right) = \mathbf{A}_{1,1} \left(\mathbf{c}_1^+ + \mathbf{c}_1^-\right) + \mathbf{A}_{1,2} \left(\mathbf{c}_2^+ + \mathbf{c}_2^-\right) \\ \mathbf{F}_2 \left(\mathbf{c}_1^+ - \mathbf{c}_1^-\right) = \mathbf{A}_{2,1} \left(\mathbf{c}_1^+ + \mathbf{c}_1^-\right) + \mathbf{A}_{2,2} \left(\mathbf{c}_2^+ + \mathbf{c}_2^-\right) \end{cases} \tag{5.64}$$

In S-matrix formulation:

$$\begin{bmatrix} \mathbf{c}_2^+ \\ \mathbf{c}_1^- \end{bmatrix} = \mathbf{S} \begin{bmatrix} \mathbf{c}_1^+ \\ \mathbf{c}_2^- \end{bmatrix}. \tag{5.65}$$

where

$$\mathbf{S} = \begin{bmatrix} \mathbf{A}_{1,2} & \mathbf{A}_{1,1} + \mathbf{F}_1 \\ \mathbf{A}_{2,2} - \mathbf{F}_2 & \mathbf{A}_{2,1} \end{bmatrix}^{-1} \begin{bmatrix} \mathbf{F}_1 - \mathbf{A}_{1,1} & -\mathbf{A}_{1,2} \\ -\mathbf{A}_{2,1} & -\mathbf{A}_{2,2} - \mathbf{F}_2 \end{bmatrix}. \tag{5.66}$$

In T-matrix formulation:

$$\begin{bmatrix} \mathbf{c}_2^+ \\ \mathbf{c}_2^- \end{bmatrix} = \mathbf{T} \begin{bmatrix} \mathbf{c}_1^+ \\ \mathbf{c}_1^- \end{bmatrix}. \tag{5.67}$$

where $\mathbf{T}$, in block matrix representation, is:

$$\mathbf{T} = \begin{bmatrix} \mathbf{T}_{1,1} & \mathbf{T}_{1,2} \\ \mathbf{T}_{2,1} & \mathbf{T}_{2,2} \end{bmatrix}. \tag{5.68}$$

and

$$\mathbf{S} = \begin{bmatrix} \mathbf{T}_{1,1} - \mathbf{T}_{1,2}\mathbf{T}_{2,2}^{-1}\mathbf{T}_{2,1} & \mathbf{T}_{1,2}\mathbf{T}_{2,2}^{-1} \\ -\mathbf{T}_{2,2}^{-1}\mathbf{T}_{2,1} & \mathbf{T}_{2,2}^{-1} \end{bmatrix}. \tag{5.69}$$

5.3.4 Solution in homogenous layers

Within homogenous layers, in which the permittivity ε is uniform, the matrix $\mathbf{S}$ can be calculated by using an analytical formula, leading to reduced computation time. For a homogenous layer of thickness Δz (Fig. 5.2),

$$\begin{bmatrix} \mathbf{c}^+(z+\Delta z) \\ \mathbf{c}^-(z) \end{bmatrix} = \mathbf{S} \begin{bmatrix} \mathbf{c}^+(z) \\ \mathbf{c}^-(z+\Delta z) \end{bmatrix} =$$
$$= \begin{bmatrix} e^{+i\sqrt{k_l^2-k_{xs}^2}\Delta z} & 0 \\ 0 & e^{+i\sqrt{k_l^2-k_{xs}^2}\Delta z} \end{bmatrix} \begin{bmatrix} \mathbf{c}^+(z) \\ \mathbf{c}^-(z+\Delta z) \end{bmatrix}. \tag{5.70}$$

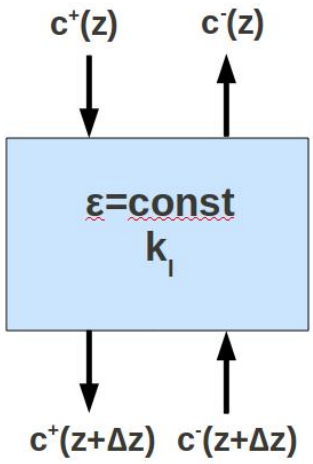

Figure 5.2: Cross section of a homogenous layer with the coefficients of the incident, reflected and transmitted waves.

If the scattering matrices of two layers are known ($\mathbf{S}^{(1)}$ and $\mathbf{S}^{(2)}$, respectively), the total scattering matrix $\mathbf{S}^{(12)}$is

$$\mathbf{S}^{(12)} = \mathbf{S}^{(1)} \bigotimes \mathbf{S}^{(2)} = \begin{bmatrix} \mathbf{S}_{1,1}^{(12)} & \mathbf{S}_{1,2}^{(12)} \\ \mathbf{S}_{2,1}^{(12)} & \mathbf{S}_{2,2}^{(12)}. \end{bmatrix}. \tag{5.71}$$

where

$$\mathbf{S}_{1,1}^{(12)} = \mathbf{S}_{1,1}^{(2)} \left(1 - \mathbf{S}_{1,2}^{(1)}\mathbf{S}_{2,1}^{(2)}\right)^{-1} \mathbf{S}_{1,1}^{(1)},$$

$$\mathbf{S}_{1,2}^{(12)} = \mathbf{S}_{1,2}^{(2)} + \mathbf{S}_{1,1}^{(2)} \left(1 - \mathbf{S}_{1,2}^{(1)}\mathbf{S}_{2,1}^{(2)}\right)^{-1} \mathbf{S}_{1,2}^{(1)}\mathbf{S}_{2,2}^{(2)},$$

$$\mathbf{S}_{2,1}^{(12)} = \mathbf{S}_{2,1}^{(1)} + \mathbf{S}_{2,2}^{(1)}\mathbf{S}_{2,1}^{(2)} \left(1 - \mathbf{S}_{1,2}^{(1)}\mathbf{S}_{2,1}^{(2)}\right)^{-1} \mathbf{S}_{1,1}^{(1)},$$

$$\mathbf{S}_{2,2}^{(12)} = \mathbf{S}_{2,2}^{(1)} \left(\mathbf{S}_{2,1}^{(2)} \left(1 - \mathbf{S}_{1,2}^{(1)} \mathbf{S}_{2,1}^{(2)} \right)^{-1} \mathbf{S}_{1,2}^{(1)} + 1 \right) \mathbf{S}_{2,2}^{(2)}.$$

Finally, if $\mathbf{S}$ denotes the total scattering matrix of the entire structure, it is possible to relate the coefficients of the incident ($\mathbf{c}_{IN}$), reflected ($\mathbf{c}_{RL}$) waves to those of the transmitted wave ($\mathbf{c}_{TR}$):

$$\begin{bmatrix} \mathbf{c}_{TR} \\ \mathbf{c}_{RL} \end{bmatrix} = \mathbf{S} \begin{bmatrix} \mathbf{c}_{IN} \\ \mathbf{0} \end{bmatrix}. \tag{5.72}$$

where the amplitude of the incident wave from the substrate is supposed to be zero.

5.4 RCWA implementation based on solution of an eigenvalues problem

In this section, a RCWA implementation based on a more standard eigenvalues calculation problem for 3-D structures is described. The method follows the same approach proposed in (34), by removing some assumptions that potentially limit its applicability to a restricted range of structures.

5.4.1 Problem definition

The following incident plane wave is considered according to Fig. 5.3:

$$\mathbf{E}_{INC}(\mathbf{r}) = \mathbf{E}_0 e^{i\mathbf{k}_1\mathbf{r}} = \mathbf{E}_0 e^{ik_0 n_I (xsin(\theta)cos(\phi) + ysin(\theta)cos(\phi) + zcos(\theta))}, \tag{5.73}$$

where $k_0^2 = \varepsilon_0\mu_0\omega^2 = (2\pi\lambda^{-1})^2$ and n_I is the refractive index of superstrate. The grating region is supposed to be $\mathbf{p}$-periodic, where $\mathbf{p} = p_x\hat{\mathbf{i}}_x + p_y\hat{\mathbf{i}}_y$ is a vector of the xy-plane. According to the Floquet's theorem for diffraction gratings,

$$\mathbf{E}(\mathbf{r}) = e^{i\mathbf{k}_0 n_I \left(x\hat{\mathbf{i}}_x + y\hat{\mathbf{i}}_y\right)} \mathbf{S}(\mathbf{r}) = e^{i\mathbf{k}_1 \left(x\hat{\mathbf{i}}_x + y\hat{\mathbf{i}}_y\right)} \mathbf{S}(\mathbf{r}) = e^{i\mathbf{k}_1\mathbf{p}} \mathbf{S}(\mathbf{r}), \tag{5.74}$$

where $\mathbf{S}(\mathbf{r})$ is a $\mathbf{p}$-periodic function of the position. Similarly for the magnetic field:

$$\mathbf{H}(\mathbf{r}) = -i \left(\frac{\varepsilon_0}{\mu_0} \right)^{\frac{1}{2}} e^{i\mathbf{k}_1\mathbf{p}} \mathbf{U}(\mathbf{r}). \tag{5.75}$$

Finally, the Maxwell equations, in case of time-harmonic fields, assuming $\mu = 1$ and $\sigma = 0$, read (eq. 3.48):

$$\begin{cases} \nabla \times \mathbf{E}(\mathbf{r}) = j\omega\mu_0 \mathbf{H}(\mathbf{r}) \\ \nabla \times \mathbf{H}(\mathbf{r}) = -j\omega\varepsilon(\mathbf{r})\varepsilon_0 \mathbf{E}(\mathbf{r}) \end{cases} \tag{5.76}$$

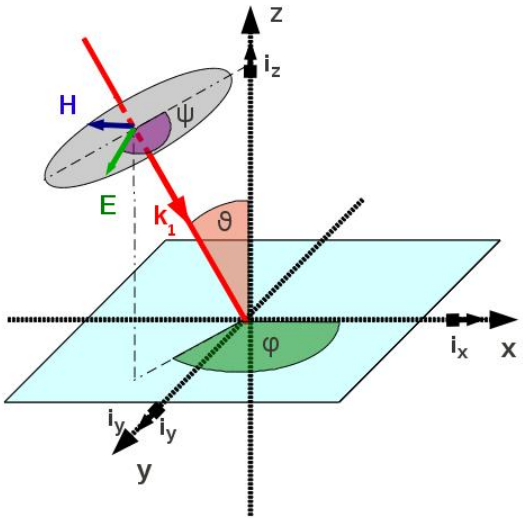

Figure 5.3: Schematic of the incidence plane for 3-D optical simulations. The direction of wave propagation vector $\mathbf{k}_1$ is defined by angles θ and ϕ with respect to z-axis and x-axis, respectively.

5.4.2 Expansion of the field in Fourier series

The fields $\mathbf{S}(\mathbf{r})$ and $\mathbf{U}(\mathbf{r})$ defined in the previous section are expanded according to Fourier sums, therefore the expressions of the electromagnetic field read:

$$\mathbf{E}(\mathbf{r}) = e^{i\mathbf{k}_1\mathbf{p}}\mathbf{S}(\mathbf{r}) = \sum_{i_x=-\infty}^{\infty} \sum_{i_y=-\infty}^{\infty} S_{i_x,i_y}(z) e^{i\left(k_{x,i_x}x + k_{y,i_y}y\right)}, \tag{5.77}$$

$$\mathbf{H}(\mathbf{r}) = -i\left(\frac{\varepsilon_0}{\mu_0}\right)^{\frac{1}{2}} e^{i\mathbf{k}_1\mathbf{p}}\mathbf{U}(\mathbf{r}) =$$

$$= -i\left(\frac{\varepsilon_0}{\mu_0}\right)^{\frac{1}{2}} \sum_{i_x=-\infty}^{\infty} \sum_{i_y=-\infty}^{\infty} U_{i_x,i_y}(z) e^{i\left(k_{x,i_x}x + k_{y,i_y}y\right)}, \tag{5.78}$$

where S_{i_x,i_y} and U_{i_x,i_y} denote the Fourier coefficients, $k_{x,i_x} = k_0\left(n_I sin(\theta)cos(\phi) + i_x\left(\frac{\lambda}{p_x}\right)\right)$ and $k_{y,i_y} = k_0\left(n_I sin(\theta)cos(\phi) + i_y\left(\frac{\lambda}{p_y}\right)\right)$. The expansions of eq. 5.77 and eq. 5.78 are truncated to a finite order, M_x and M_y for the x-axis and the y-axis, respectively.

Therefore, by replacing the eq. 5.77 and 5.78 into eq. 5.76, the following scalar equations are obtained:

$$ik_{y,i_y}S_{z,i_x,i_y}(z) - \frac{\partial S_{y,i_x,i_y}(z)}{\partial z} = k_0 U_{x,i_x,i_y} \tag{5.79}$$

$$-ik_{x,i_x}S_{z,i_x,i_y}(z) + \frac{\partial S_{x,i_x,i_y}(z)}{\partial z} = k_0 U_{y,i_x,i_y} \tag{5.80}$$

$$ik_{x,i_y}S_{y,i_x,i_y}(z) - ik_{y,i_y}S_{x,i_x,i_y}(z) = k_0 U_{z,i_x,i_y} \tag{5.81}$$

$$k_{y,i_y}U_{z,i_x,i_y}(z) + i\frac{\partial U_{y,i_x,i_y}(z)}{\partial z} = -ik_0 \sum_{j_x,j_y} S_{x,j_x,j_y}\mathbf{A}_{1,i_x,i_y,j_x,j_y} \tag{5.82}$$

$$-k_{x,i_x}U_{z,i_x,i_y}(z) - i\frac{\partial U_{x,i_x,i_y}(z)}{\partial z} = -ik_0 \sum_{j_x,j_y} S_{y,j_x,j_y}\mathbf{A}_{2,i_x,i_y,j_x,j_y} \tag{5.83}$$

$$k_{x,i_x}U_{y,i_x,i_y}(z) - ik_{y,i_y}U_{x,i_x,i_y}(z) = -ik_0 \sum_{j_x,j_y} S_{z,j_x,j_y}\mathbf{A}_{3,i_x,i_y,j_x,j_y} \tag{5.84}$$

The matrix $\mathbf{A}$ is a Lifeng Li's permittivity matrix (122).

The tangential components of the electric field are continuous because of the absence of surface current density, therefore the component E_x of the electric field is a continuous function of y and z; similarly, E_z is continuous along x and y. In addition, the normal components of the electric displacement are continuous due to the absence of surface charge density and consequently the product εE_x is continuous along x-axis, εE_y is continuous along y-axis and εE_z is continuous along z-axis. Since the permittivity $\varepsilon(\mathbf{r})$ may exhibit a discontinuity, the Fourier transform of $\frac{1}{\varepsilon(\mathbf{r})}$ is calculated along the x-axis, where also the electric field is discontinuous. Then the permittivity matrix coefficients have the form $A_{n,i_x,j_x,i_y,j_y} = \left[\left[\frac{1}{\varepsilon(\mathbf{r})}\right]^{-1}_{i_x,j_x}\right]_{i_y,j_y}$ for $n = 1$. In order to obtain the coefficients A_{n,i_x,j_x,i_y,j_y}, $n = 2$, the Fourier series associated to $\frac{1}{\varepsilon(\mathbf{r})}$ along y-axis is calculated. Subsequently, for each value of x, the inverse matrix is calculated, therefore $A_{2,i_x,j_x,i_y,j_y} = \left[\left[\frac{1}{\varepsilon(\mathbf{r})}\right]^{-1}_{i_y,j_y}\right]_{i_x,j_x}$. Since E_z is continuous along x and y, simply $A_{3,i_x,j_x,i_y,j_y} = \left[[\varepsilon(\mathbf{r})]_{i_y,j_y}\right]_{i_x,j_x}$.

Eq. 5.79 and 5.82 in matrix notation are:

$$\frac{\partial \mathbf{s}_y(z)}{k_0 \partial z} = i\mathbf{k}_y \mathbf{s}_z(z) - \mathbf{u}_x, \tag{5.85}$$
$$\frac{\partial \mathbf{s}_x(z)}{k_0 \partial z} = i\mathbf{k}_x \mathbf{s}_z(z) + \mathbf{u}_y, \tag{5.86}$$
$$\mathbf{u}_z = i\mathbf{k}_x \mathbf{s}_y(z) - i\mathbf{k}_y \mathbf{s}_x(z), \tag{5.87}$$

$$\frac{\partial \mathbf{u}_y(z)}{k_0 \partial z} = -\mathbf{A}_1 \mathbf{s}_x(z) + i\mathbf{k}_y \mathbf{u}_z(z), \tag{5.88}$$
$$\frac{\partial \mathbf{u}_x(z)}{k_0 \partial z} = \mathbf{A}_2 \mathbf{s}_y(z) + i\mathbf{k}_x \mathbf{u}_z(z), \tag{5.89}$$
$$\mathbf{s}_z(z) = i\mathbf{A}_3^{-1} \left(\mathbf{k}_x \mathbf{u}_y(z) - \mathbf{k}_y \mathbf{u}_x(z) \right), \tag{5.90}$$

where $\mathbf{k}_x = \frac{1}{k_0} \left[k_{x,i_x} \right]$ and $\mathbf{k}_y = \frac{1}{k_0} \left[k_{y,i_y} \right]$ are diagonal matrices. By removing the z-component from eq. 5.85 and 5.88,

$$\begin{aligned}
\frac{\partial \mathbf{s}_x(z)}{k_0 \partial z} &= \mathbf{k}_x \mathbf{A}_3^{-1} \mathbf{k}_y \mathbf{u}_x(z) - \left(\mathbf{k}_x \mathbf{A}_3^{-1} \mathbf{k}_x - \mathbf{I} \right) \mathbf{u}_y(z) \\
\frac{\partial \mathbf{s}_y(z)}{k_0 \partial z} &= \left(\mathbf{k}_y \mathbf{A}_3^{-1} \mathbf{k}_y - \mathbf{I} \right) \mathbf{u}_x(z) - \mathbf{k}_y \mathbf{A}_3^{-1} \mathbf{k}_x \mathbf{u}_y(z) \\
\frac{\partial \mathbf{u}_x(z)}{k_0 \partial z} &= \mathbf{k}_x \mathbf{k}_y \mathbf{s}_x(z) + \left(\mathbf{A}_2 - \mathbf{k}_x^2 \right) \mathbf{s}_y(z) \\
\frac{\partial \mathbf{u}_y(z)}{k_0 \partial z} &= -\left(\mathbf{A}_1 - \mathbf{k}_y^2 \right) \mathbf{s}_x(z) - \mathbf{k}_y \mathbf{k}_x \mathbf{s}_y(z)
\end{aligned} \tag{5.91}$$

or, in more compact notation,

$$\begin{aligned}
\frac{\partial \mathbf{s}(z)}{k_0 \partial z} &= \mathbf{Q}\mathbf{u}(z) \\
\frac{\partial \mathbf{u}(z)}{k_0 \partial z} &= \mathbf{F}\mathbf{s}(z).
\end{aligned} \tag{5.92}$$

Each system of equations in 5.92 is a set of $2M_xM_y$ equations.

As shown in Fig. 5.4, the simulation domain is split in N layers with interfaces parallel to the xy-plane. Within each layer, the permittivity $\varepsilon(\mathbf{r})$ is replaced by a step function for which the permittivity is constant along z-axis. This approximation allows

to treat an arbitrary surface profile as a set of 2-D rectangular grating regions. The thickness $\Delta z_q, \qquad q = 1..N$ of each layer must be carefully chosen, with regarding to the spatial variation of the surface and the wavelength of the radiation. In order to reduce by a factor 2 the number of equations, the first two systems of equations in 5.91 are differentiated with respect of the variable z, then the derivatives of the magnetic field coefficients are replaced into the third and the fourth equation. In addition, due to the approximation, within each layer, the spatial derivative of the permittivity matrix is zero. Therefore:

$$\begin{bmatrix} \frac{\partial^2 \mathbf{s}_x(z)}{\partial \tilde{z}^2} \\ \frac{\partial^2 \mathbf{s}_y(z)}{\partial \tilde{z}^2} \end{bmatrix} = \begin{bmatrix} \left(\mathbf{k}_x \mathbf{A}_3^{-1} \mathbf{k}_x - \mathbf{I}\right) \mathbf{A}_1 + \mathbf{k}_y^2 & \mathbf{k}_x \left(\mathbf{A}_3^{-1} \mathbf{k}_y \mathbf{A}_2 - \mathbf{k}_y\right) \\ \mathbf{k}_y \left(\mathbf{A}_3^{-1} \mathbf{k}_x \mathbf{A}_1 - \mathbf{k}_x\right) & \left(\mathbf{k}_y \mathbf{A}_3^{-1} \mathbf{k}_y - \mathbf{I}\right) \mathbf{A}_2 + \mathbf{k}_x^2 \end{bmatrix} \begin{bmatrix} \mathbf{s}_x(z) \\ \mathbf{s}_y(z) \end{bmatrix},$$

or

$$\frac{\partial^2 \mathbf{s}(z)}{\partial \tilde{z}^2} = -\mathbf{K}\mathbf{s}(z) \tag{5.93}$$

where $\tilde{z} = k_0 z$.

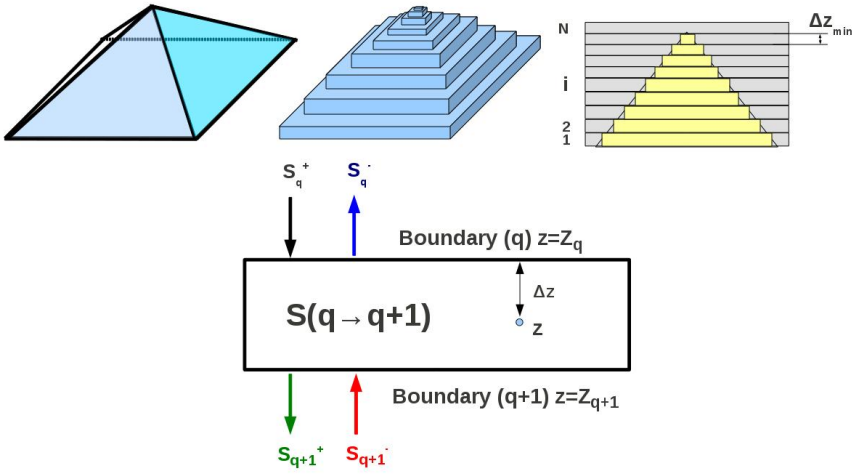

Figure 5.4: Sketch of the simulation domain (the top figure reports a 3-D pyramid) split in layers within which the permittivity is approximated by a step function. The bottom figure shows a schematic of a single layer with the Fourier coefficients of the electric field at the boundaries.

The solution in terms of spatial harmonics of the electric field of the problem of eq. 5.93 within each homogenous layer ($z_q \leq z \leq z_{q+1} = z_q + \Delta z_q$), calculated at the generic point ($z_q + \Delta z$) is (Fig. 5.4):

$$\mathbf{s}(z_q + \Delta z) = e^{ik_0\sqrt{\mathbf{K}}\Delta z}\mathbf{s}^+(z) + e^{-ik_0\sqrt{\mathbf{K}}\Delta z}\mathbf{s}^-(z) \tag{5.94}$$

As in the standard implementation of the RCWA method, the coupled-wave equations of eq. 5.93 are solved by finding the eigenvalues and eigenvectors of $\mathbf{K}$ defined in eq. 5.93, which is a matrix of rank $2M_xM_y$. It is worth noting that, the matrix $\mathbf{K}$, in the most general case, is not an Hermitian matrix, as assumed in (34), therefore it is not possible to write $\mathbf{K}$ as a diagonal matrix, in which, the diagonal elements are the positive square roots of the eigenvalues of the matrix. By removing this assumption, which requires that the eigenvectors associated to the matrix $\mathbf{K}$ are not linearly independent, the implementation proposed in this work, is the most general possible; the assumption of considering $\mathbf{K}$ a Hermitian matrix -which is however reasonable for most practical applications- limits the applicability of the tool to materials (or to range of the wavelength of the radiation) for which the imaginary part of the dielectric constant is zero (or significantly smaller with respect to the real part).

At the boundaries of each layer the continuity of the tangential components of the electric and magnetic fields must be ensured, as expressed by:

$$E_x|_{z-0} = E_x|_{z+0}, \qquad E_y|_{z-0} = E_y|_{z+0}, \tag{5.95}$$

$$H_x|_{z-0} = H_x|_{z+0}, \qquad H_y|_{z-0} = H_y|_{z+0}, \tag{5.96}$$

which lead to the following condition on the Fourier coefficients of the tangential components of the field:

$$\begin{aligned} S_{x,i_x,i_y}|_{z-0} &= S_{x,i_x,i_y}|_{z+0}, \qquad S_{y,i_x,i_y}|_{z-0} = S_{y,i_x,i_y}|_{z+0}, \\ U_{x,i_x,i_y}|_{z-0} &= U_{x,i_x,i_y}|_{z+0}, \qquad U_{y,i_x,i_y}|_{z-0} = U_{y,i_x,i_y}|_{z+0}, \end{aligned} \tag{5.97}$$

or in vector form:

$$\mathbf{s}|_{z-0} = \mathbf{s}|_{z+0}, \qquad \mathbf{u}|_{z-0} = \mathbf{u}|_{z+0}, \tag{5.98}$$

In order to calculate the coefficients $\mathbf{s}$ and $\mathbf{u}$ at the bottom boundary of the q-th layer ($z_q \leq z \leq z_q + \Delta_q$, Fig. 5.4), from eq. 5.92 and 5.94, by applying the boundary conditions of eq. 5.97:

$$\begin{aligned}\mathbf{s}(z_q + \Delta z_q - 0) = e^{ik_0\sqrt{\mathbf{K}_q}\Delta z_q}\mathbf{s}_q^+(z) + e^{-ik_0\sqrt{\mathbf{K}_q}\Delta z_q}\mathbf{s}_q^-(z) = \\ = \mathbf{s}_{q+1}^+ + \mathbf{s}_{q+1}^- = \mathbf{s}(z_q + \Delta z_q + 0),\end{aligned} \tag{5.99}$$

$$\begin{aligned}\mathbf{u}(z_q + \Delta z_q - 0) = \mathbf{Q}_q^{-1}\frac{\partial \mathbf{s}}{k_0 \partial z}|_{z_q+\Delta z_q-0} = \\ = i\mathbf{Q}_q^{-1}\sqrt{\mathbf{K}_q}\left(e^{ik_0\sqrt{\mathbf{K}_q}\Delta z_q}\mathbf{s}_q^+(z) - e^{-ik_0\sqrt{\mathbf{K}_q}\Delta z_q}\mathbf{s}_q^-(z)\right) = \\ = i\mathbf{Q}_{q+1}^{-1}\sqrt{\mathbf{K}_{q+1}}\left(\mathbf{s}_{q+1}^+(z) - \mathbf{s}_{q+1}^-(z)\right) = \\ = \mathbf{Q}_{q+1}^{-1}\frac{\partial \mathbf{s}}{k_0 \partial z}|_{z_q+\Delta z_q+0} = \mathbf{u}|_{z_q+\Delta z_q+0}\end{aligned} \tag{5.100}$$

or

$$\begin{aligned}\mathbf{P}_q\mathbf{s}_q^+ + \mathbf{P}_q^{-1}\mathbf{s}_q^- = \mathbf{s}_{q+1}^+ + \mathbf{s}_{q+1}^- \\ \mathbf{W}_q\left(\mathbf{P}_q\mathbf{s}_q^+ - \mathbf{P}_q^{-1}\mathbf{s}_q^-\right) = \mathbf{W}_{q+1}\left(\mathbf{s}_{q+1}^+ - \mathbf{s}_{q+1}^-\right),\end{aligned} \tag{5.101}$$

where

$$\mathbf{P}_q = e^{ik_0\sqrt{\mathbf{K}_q}\Delta_z}, \qquad \mathbf{W}_q = \mathbf{Q}_q^{-1}\sqrt{\mathbf{K}_q}, \qquad \mathbf{W}_{q+1} = \mathbf{Q}_{q+1}^{-1}\sqrt{\mathbf{K}_{q+1}}. \tag{5.102}$$

The Fourier coefficients of the electric field at the boundaries of the q-th layer can be linked by the scattering matrix $\mathbf{S}^{(q\to q+1)}$:

$$\begin{bmatrix} \mathbf{s}_{q+1}^+ \\ \mathbf{s}_q^- \end{bmatrix} = \mathbf{S}^{(q\to q+1)} \begin{bmatrix} \mathbf{s}_q^+ \\ \mathbf{s}_{q+1}^- \end{bmatrix}. \tag{5.103}$$

where

$$\mathbf{S}^{(q\to q+1)} = \begin{bmatrix} \mathbf{S}_{1,1}^{(q\to q+1)} & \mathbf{S}_{1,2}^{(q\to q+1)} \\ \mathbf{S}_{2,1}^{(q\to q+1)} & \mathbf{S}_{2,2}^{(q\to q+1)} \end{bmatrix}. \tag{5.104}$$

$$\mathbf{S}_{1,1}^{(q\to q+1)} = 2\left(\mathbf{W}_q + \mathbf{W}_{q+1}\right)^{-1}\mathbf{W}_q\mathbf{P}_q,$$

$$\mathbf{S}_{1,2}^{(q\to q+1)} = -\left(\mathbf{W}_q + \mathbf{W}_{q+1}\right)^{-1}\left(\mathbf{W}_q - \mathbf{W}_{q+1}\right),$$

$$\mathbf{S}_{2,1}^{(q\to q+1)} = \mathbf{P}_q\left(\mathbf{W}_q + \mathbf{W}_{q+1}\right)^{-1}\left(\mathbf{W}_q - \mathbf{W}_{q+1}\right)\mathbf{P}_q,$$

$$\mathbf{S}_{2,2}^{(q\to q+1)} = 2\mathbf{P}_q\left(\mathbf{W}_q + \mathbf{W}_{q+1}\right)^{-1}\mathbf{W}_{q+1}.$$

When all layers are accounted ($n = 1\cdots N$),

$$\begin{bmatrix} \mathbf{s}_N^+ \\ \mathbf{s}_1^- \end{bmatrix} = \mathbf{S}^{(1\to N)}\begin{bmatrix} \mathbf{s}_1^+ \\ \mathbf{s}_N^- \end{bmatrix}. \tag{5.105}$$

where the scattering matrix $\mathbf{S}^{(1\to N)}$ is calculated similarly to that of eq. 5.71. Finally, the coefficients of the incident field ($\mathbf{s}^I$) are linked to those of the reflected and transmitted fields ($\mathbf{s}^R$ and $\mathbf{s}^T$, respectively) by the following equation:

$$\begin{bmatrix} \mathbf{s}^T \\ \mathbf{s}^R \end{bmatrix} = \mathbf{S}^{B,z=0}\bigotimes\mathbf{S}^{(1\to N)}\begin{bmatrix} \mathbf{s}^I \\ 0 \end{bmatrix}. \tag{5.106}$$

where the matrix $\mathbf{S}^{B,z=0}$ is given by:

$$\mathbf{S}^{B,z=0} = \begin{bmatrix} \mathbf{S}_{1,1}^{B,z=0} & \mathbf{S}_{1,2}^{B,z=0} \\ \mathbf{S}_{2,1}^{B,z=0} & \mathbf{S}_{2,2}^{B,z=0} \end{bmatrix}. \tag{5.107}$$

$$\mathbf{S}_{1,1}^{B,z=0} = 1 + \left(\mathbf{W}_q + \mathbf{W}_{q+1}\right)^{-1}\left(\mathbf{W}_q - \mathbf{W}_{q+1}\right),$$

$$\mathbf{S}_{1,2}^{B,z=0} = 2\left(\mathbf{W}_q + \mathbf{W}_{q+1}\right)^{-1}\mathbf{W}_{q+1} - 1,$$

$$\mathbf{S}_{2,1}^{B,z=0} = \left(\mathbf{W}_q + \mathbf{W}_{q+1}\right)^{-1}\left(\mathbf{W}_q - \mathbf{W}_{q+1}\right),$$

$$\mathbf{S}_{2,2}^{B,z=0}2\left(\mathbf{W}_q + \mathbf{W}_{q+1}\right)^{-1}\mathbf{W}_{q+1},$$

and the symbol $\bigotimes$ denotes the matrix operator already defined in eq. 5.71.

5.4.3 Solution within homogenous layer

Within homogenous layers with parallel front and bottom interfaces, the solution can be significantly simplified. Indeed, the coefficient of the magnetic and electric fields are not coupled, therefore eq. 5.91 represents in this case a system of independent equations. The permittivity matrix can be replaced by the (constant) permittivity ε_l of the layer, hence:

$$\begin{bmatrix} \frac{\partial^2 s_{x,i_x,i_y}(z)}{\partial \tilde{z}^2} \\ \frac{\partial^2 s_{y,i_x,i_y}(z)}{\partial \tilde{z}^2} \end{bmatrix} = \frac{1}{k_0^2} \begin{bmatrix} k_{x,i_x}^2 + k_{y,i_y}^2 - k_l^2 & 0 \\ 0 & k_{x,i_x}^2 + k_{y,i_y}^2 - k_l^2 \end{bmatrix} \begin{bmatrix} s_{x,i_x,i_y}(z) \\ s_{y,i_x,i_y}(z) \end{bmatrix}, \quad (5.108)$$

where $\tilde{z} = k_0 z$ and $k_l^2 = k_0^2 \varepsilon_l$. Matrices $\mathbf{Q}$, $\mathbf{K}$ and $\mathbf{P}$ are in the form:

$$\mathbf{Q}_{l,i_x,i_y} = \frac{1}{k_l^2} \begin{bmatrix} k_{x,i_x} k_{y,i_y} & -k_{x,i_x}^2 + k_l^2 \\ k_{y,i_y}^2 - k_l^2 & -k_{x,i_x} k_{y,i_y} \end{bmatrix}, \quad (5.109)$$

$$\mathbf{K}_{l,i_x,i_y} = \frac{k_l^2 - \left(k_{x,i_x}^2 + k_{y,i_y}^2\right)}{k_0^2} \mathbf{I}, \quad (5.110)$$

$$\mathbf{P}_{l,i_x,i_y} = e^{i\sqrt{k_0^2 \varepsilon_l - \left(k_{x,i_x}^2 + k_{y,i_y}^2\right)} \Delta z} \mathbf{I}. \quad (5.111)$$

where $\mathbf{I}$ denotes the unity matrix of size 2. Therefore matrix $\mathbf{W}$ can be written as:

$$\mathbf{W}_{l,i_x,i_y} = \mathbf{Q}_l^{-1} \sqrt{\mathbf{K}_l} = \frac{1}{k_0^2 \sqrt{k_l^2 - \left(k_{x,i_x}^2 + k_{y,i_y}^2\right)}} \begin{bmatrix} -k_{x,i_x} k_{y,i_y} & -k_l^2 + k_{x,i_x}^2 \\ k_l^2 - k_{y,i_y}^2 & k_{x,i_x} k_{y,i_y} \end{bmatrix}. \quad (5.112)$$

5.4.4 Calculation of the optical generation rate

The flux of energy through a plane perpendicular to z-axis (Fig. 5.3) is:

$$S_z = \frac{1}{2} Re\left(E_x H_y^* - H_x^* E_y\right) \quad (5.113)$$

where S_z is the z-component of the Poynting vector, defined as:

$$\mathbf{S} = \frac{1}{2} Re\left[\mathbf{E} \times \mathbf{H}^*\right]. \quad (5.114)$$

Integrating with respect of x, y:

$$\int_0^{px}\int_0^{py} S_z(x,y,z)dxdy =$$

$$= \frac{1}{2}\sqrt{\frac{\varepsilon_0}{\mu_0}}p_x p_y Im\left(\sum_{i_x,i_y=-\infty}^{\infty}\left[s_{y,i_x,i_y}(z)u^*_{x,i_x,i_y}(z) - s_{x,i_x,i_y}(z)u^*_{y,i_x,i_y}(z)\right]\right). \quad (5.115)$$

In order to calculate the energy absorption per unit time and volume, the divergence of the Poynting vector must be calculated:

$$\mathbf{S} = \frac{1}{2}Re\left(\nabla,[\mathbf{E},\mathbf{H}^*]\right) = \frac{1}{2\mu_0\omega}Im\left(\mathbf{E},\nabla\times\nabla\times\mathbf{E}^*\right) \quad (5.116)$$

Since, from Maxwell equations (Eq. 3.36) $\nabla x\nabla x\mathbf{E}^*(\mathbf{r}) = \omega^2\mu_0\varepsilon_0\varepsilon(\mathbf{r})\mathbf{E}(\mathbf{r})$, and being the optical generation rate equal to the absorbed energy to the photon energy,

$$G_{opt}(\omega) = -\frac{2\pi div\mathbf{S}}{h\omega} = \frac{21pi\varepsilon_0 Im(\varepsilon)|\mathbf{E}|^2}{2h}, \quad (5.117)$$

where h is the Planck constant.

5.5 Validation of RCWA method and accuracy

5.5.1 2-D RCWA simulator

The proposed RCWA simulators have been checked by means of a comparison with a commercial FDTD tool in terms of calculated absorbance (Sentaurus Device Electromagnetic Wave Solver EMW by Synopsys, (123)) with a similar 2-D test structure (crystalline silicon grating surrounded by air shown in Fig. 5.5, with $a = 25nm$, $b_1 = b_2 = 12.5nm$, $h_1 = 100nm$, $h_2 = 450nm$ and period $p = 50nm$) within the range of wavelength 380nm-880nm. A good agreement has been observed for both TE and TM polarizations (Fig. 5.6). The maximum accuracy of the relative absorbance is comparable to that obtained by the commercial simulator on the basis of the expertise on FDTD simulations with EMW. For the FDTD calculations, 400 cells per wavelength (CPW) have been adopted. The size of the tensor grid cell used by the FDTD simulator is determined by the ratio of the wavelength of the radiation to CPW.

The accuracy of the RCWA simulator versus the number of Fourier modes (N_F) and versus the discretization step Δ_z along the propagation direction (Fig. 5.7) within

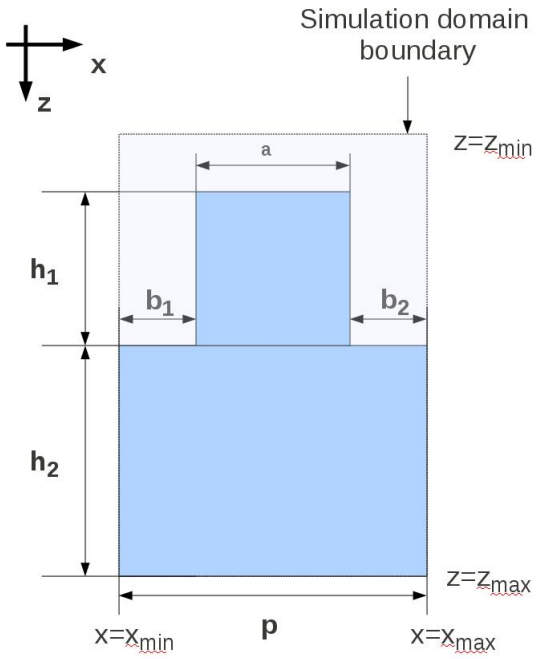

Figure 5.5: Sketch of the 2-D rectangular grating adopted as reference test structure for the validation and the analysis of the accuracy of the RCWA simulator ($a = 25nm$, $b_1 = b_2 = 12.5nm$, $h_1 = 100nm$, $h_2 = 450nm$ and periodicity $p = 50$nm).

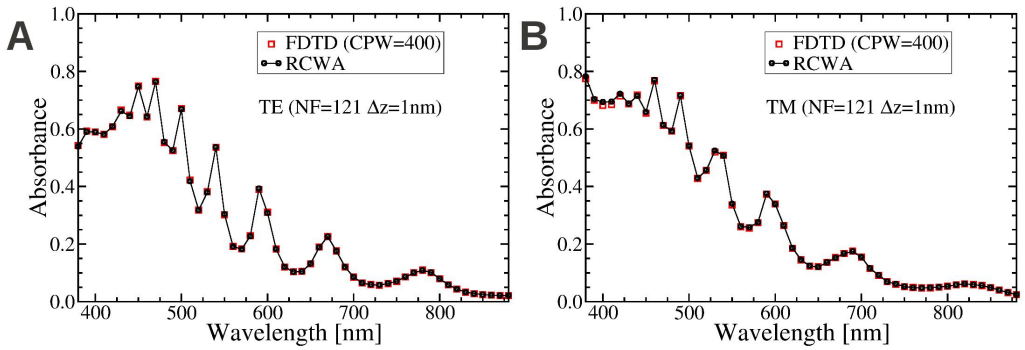

Figure 5.6: Comparison of the absorbance calculated by FDTD and RCWA within the range of wavelengths $380nm - 880nm$ for the grating test structure (Fig. 5.5) in case of TE (A) and TM (B) polarizations. For FDTD simulations performed by Synopsys EMW, 400 cells per wavelength(CPW) have been adopted. RCWA simulations have been carried out by using $N_F = 60$ and $\Delta z = 1nm$.

the grating region has been investigated for two different values of the wavelengths of the radiation ($\lambda = 450nm$ and $\lambda = 750nm$) in case of the grating test structure (Fig. 5.5).

The accuracy of relative absorbance for both TE and TM polarizations (the absorbance calculated adopting $N_F = 301$ is used as reference) has been plotted as function of the number of modes in Fig. 5.7A and 5.7B at wavelengths of the radiation equal to $450nm$ and $750nm$, respectively, by adopting $\Delta_z = 1nm$. For the considered structure the accuracy of the relative absorbance is below 0.001 for $N_F > 10$.

The accuracy of relative absorbance for both TE and TM polarizations (the absorbance calculated adopting $\Delta_z = 0.1nm$ is used as reference) has been plotted as function of Δ_z^{-1} in Fig. 5.7C and 5.7D at wavelengths of the radiation $450nm$ and $750nm$, respectively, by adopting $N_F = 201$. The relative absorbance is below 0.001 for $\Delta_z \leq 1nm$ for the considered rectangular grating.

The simulation time of the RCWA implementation presented in section 5.3 has been compared to that of FDTD for the 2-D test grating (Fig. 5.5). The calculation of the absorbance by FDTD requires about 30 times more time then RCWA algorithm to achieve the same accuracy (for RCWA $N_F = 121$ and $\Delta_z = 1nm$ have been adopted while for FDTD, $CPW = 200$). For the multi-layer structures with rough interfaces the method is almost 10 times faster then the classical RCWA (eigenvalue calculations) with the same number of modes and the same accuracy.

5.5.2 3-D RCWA simulator

The 3D RCWA simulator results have been compared to those provided by Fan et al. (4). The test structure is a 3-D photonic crystal exhibiting a single slab (permittivity $\varepsilon = 12$) with circular air holes arranged in a square lattice with periodicity $p = 200nm$ (Fig. 5.8). The thickness of the slab and the radius of holes are equal to $0.5p$ and $0.05p$, respectively. The slab is lossless (extinction coefficient of the material equal to zero). The transmission coefficient calculated by RCWA shows a good agreement to data reported by Fan et al. (4), as shown in Fig. 5.8.

Fig. 5.10 reports the accuracy of relative absorbance for the test structure of Fig. 5.9 (cuboid of silicon with lateral side equal to $500nm$ surrounded by air) versus the number of Fourier modes along x-axis and y-axis, denoted by N_{Fx} and N_{Fy}, respectively. The reference absorbance is calculated by adopting $N_{Fx} = 89$, $N_{Fy} = 161$ and $\theta = 0$, $\phi = 0$

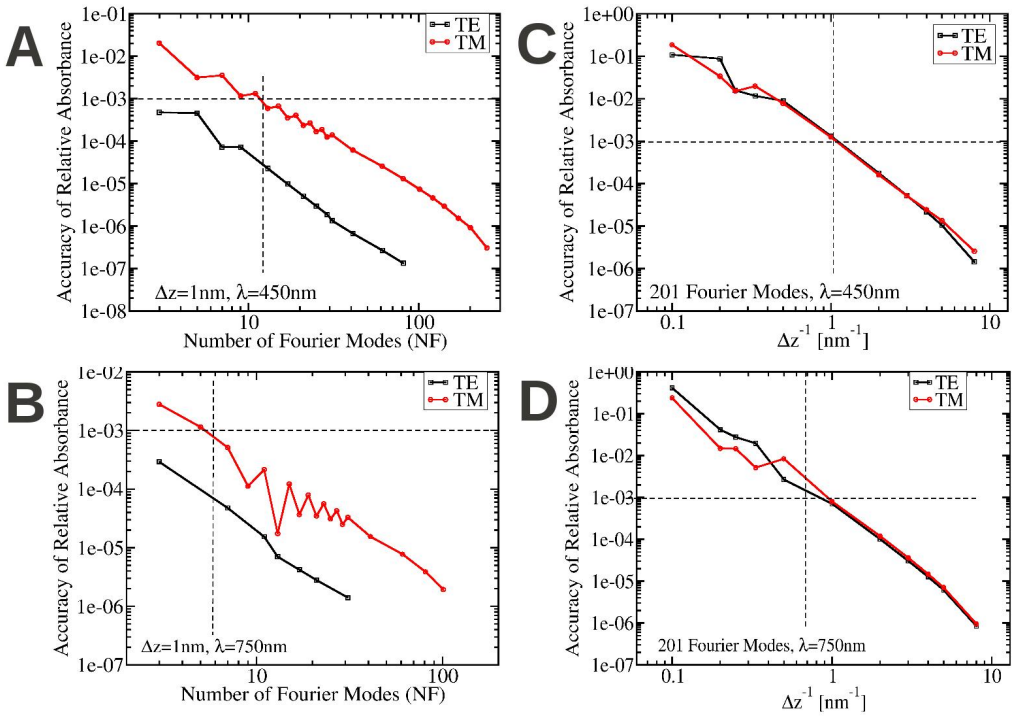

Figure 5.7: Accuracy of the relative absorption for 2D-RCWA simulator in case of the test structure (rectangular grating of Fig. 5.5). The accuracy has been calculated for both TE and TM polarizations and for two values of the wavelength of the radiation ($450nm$ and $750nm$). In (A) and (B) the accuracy of relative absorbance is calculated as function of the number of Fourier modes N_F with $\Delta z = 1nm$ and keeping the number of points N_x for the Fourier transform along x-axis constant ($N_x = 1024$). In (C) and (D) the accuracy of relative absorbance is calculated as function of Δz^{-1} adopting $N_F = 201$. The dashed line denotes the minimum value of N_F (Δz^{-1}) above which the accuracy of the relative absorbance is smaller than 10^{-3}.

(Fig. 5.3) at $\lambda = 350nm$. It is worth noting that, for the reference structure and for the given wavelength of the radiation, in order to obtain a relative accuracy below 10^{-3}, more than 90 Fourier modes are required.

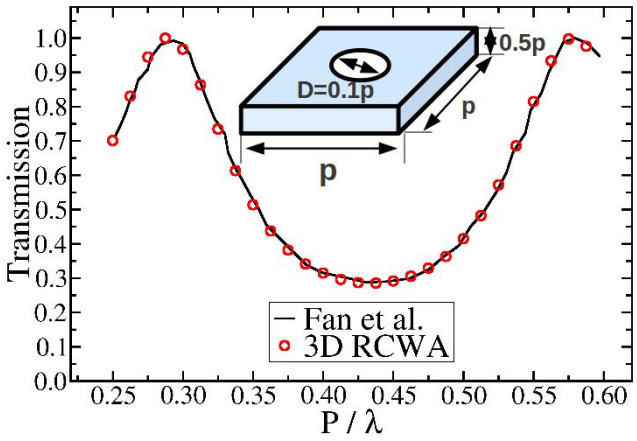

Figure 5.8: 3-D Photonic Crystal: comparison of the transmission coefficient calculated by 3D-RCWA and that from literature (Fan et al. (4)) versus the periodicity p of the cell normalized to the wavelength of the radiation λ. Thickness and hole diameter are set to $0.5p$ and $0.05p$, respectively. The real part of the permittivity of the dielectric slab is 12. RCWA simulations have been performed by adopting $\theta = 0$, $\phi = 0$ (Fig. 5.3) and $N_{Fx} = 43$, $N_{Fy} = 43$ number of Fourier modes along x-axis and y-axis, respectively.

5.6 Applications of RCWA tool

5.6.1 Application: impact of surface morphology on absorbance

The 2-D RCWA simulator has been applied to model the light propagation in crystalline silicon layers with different kinds of front texturing exhibiting micrometric and nanometric features, such as the triangular, rectangular, circular texturing and the Gaussian random roughness (Fig. 5.11). For each considered kind of texturing the absorbance of the structure -featuring a nominal thickness of the silicon slab equal to $10.25\mu m$- has been calculated for different angles of incidence θ of the radiation (Fig. 5.1). Simulations have been performed for both TE and TM polarizations by adopting as numerical parameters $N_F = 121$ and $\Delta z = 1nm$. Absorbance characteristics have

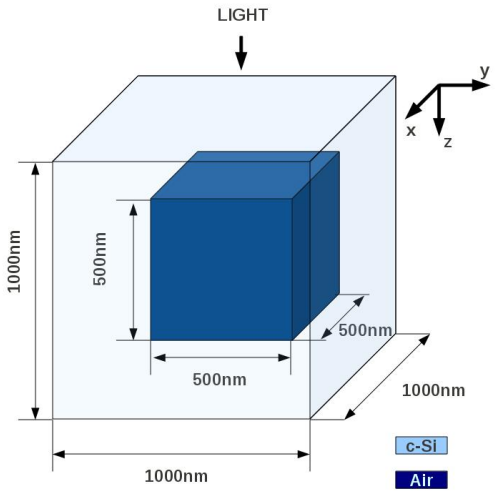

Figure 5.9: Sketch of the rectangular 3-D grating adopted as reference test structure for the analysis of the accuracy of RCWA simulator (side length $L = 500nm$ and periodicity $p = 500$nm).

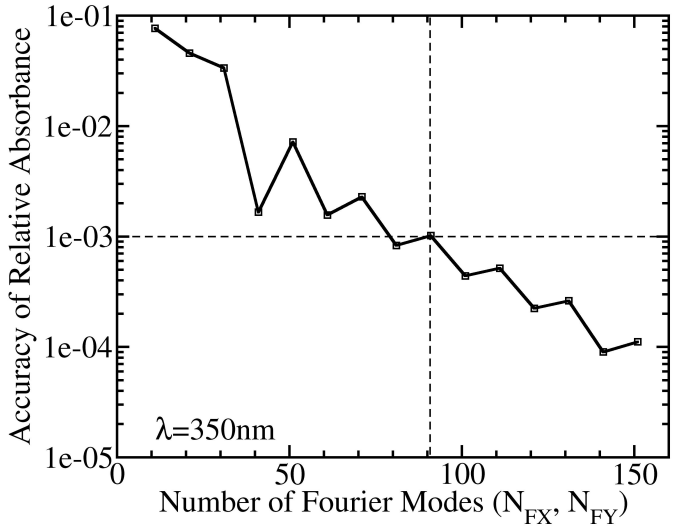

Figure 5.10: Accuracy of the relative absorption for 3D-RCWA simulator in case of the test structure (3-D rectangular grating of Fig. 5.9) as function of the number of Fourier modes N_{Fx}, N_{Fy} along x-axis and y-axis, respectively. The accuracy has been calculated for $\theta = 0$, $\phi = 0$ (Fig. 5.3). The dashed line denotes the minimum value of N_F above which the accuracy of the relative absorbance is smaller than 10^{-3}.

been calculated within the spectral range 350nm-950nm. The absorbance characteristics calculated for the flat surface and the Gaussian-random one are reported in Fig. 5.12 and Fig. 5.13, in case of TE polarization; as expected, the absorbance decreases with increasing θ; similar results have been obtained for all other considered kinds of surface morphology. In Fig. 5.14 the absorbance characteristics of the silicon slabs for different types of surface texturing are reported, assuming normal incidence ($\theta = 0$ degree) and TE polarization of the light. It is worth noting that the surface texturing increases the absorbance of the silicon slab and that the best curve of absorbance is obtained with the Gaussian random rough roughness.
Fig. 5.15 reports the optical generation rate per volume and time unit calculated at $\lambda = 600nm$ for the slabs featuring flat and random rough interfaces under normal light incidence, TE polarization. It is possible to observe that, in case of random roughness, the optical generation rate G_{opt} is significantly larger than that of the flat interface throughout the volume of the absorbing layer. The enhancement in terms of absorption due to the random roughness with nanometric features is exploited in thin film solar cells, for which, typical interfaces between amorphous silicon and transparent conductive oxide exhibit nano-roughness with root mean square height within the range 10-100nm (124).

In order to compare the different structures, in order to introduce a more realistic figure of merit from the point of view of view of practical applications, the following performance parameter is defined as the total absorption weighted by the Air Mass 1.5 Global spectrum (AM1.5G) and normalized by the total input irradiance:

$$A_w = \frac{\sum_{\lambda_i} S(\lambda_i) A(\lambda_i) \Delta\lambda_i}{\sum_{\lambda_i} S(\lambda_i) \Delta\lambda_i} \tag{5.118}$$

where $A(\lambda_i)$ and $S(\lambda_i)$ are the calculated absorbance and the spectral irradiance for a given wavelength λ_i, respectively. A_w is equals unity when the absorbance is maximum within the entire spectrum. In Fig. 5.16 and Tab. 5.1 the calculated A_w for different kids of front surface morphology and different angles of incidence θ of the light are reported, for both TE and TM polarizations. It is worth noting that, in case of TE polarization (Fig. 5.16A), A_w decreases with increasing θ for all the considered surface geometries, with the exception of the rectangular case, which features a maximum value

of A_w between $\theta = 20$ and $\theta = 30$ degrees; the random roughness reaches the maximum value of A_w within the whole considered range for θ. In addition, if a periodic triangular surface texturing featuring the same root mean square height of the random roughness ($H_{RMS} = 50nm$) is considered, by reducing the periodicity p down to a value close to that of the random roughness (average spatial periodicity approximately $20nm$), the value of the parameter A_w reaches values closer to that of the random roughness as shown in Fig. 5.16A, where, in addition, the values of A_w calculated for periodicity $p = 300nm$ and $p = 20nm$ at normal incidence are reported (black symbols). For TM polarization (Fig. 5.16B), similar trends are observed with the exception of the rectangular textured and the smooth interfaces, for which A_w increases with increasing θ.

Examples of optical generation maps calculated by RCWA are shown in Fig. 5.17 and Fig. 5.18, in which triangular, rectangular and circular surface texturing of Fig. 5.11 are considered. Monochromatic maps of G_{opt} are reported for both TE and TM polarizations. The effect of the angle of incidence of the radiation θ is considered in Fig. 5.19, in which the G_{opt} maps are reported for $\theta = 0$ (direct illumination), $\theta = 30$ degrees and $\theta = 69$ degrees.

Table 5.1: Total normalized absorbance A_w (defined in eq. 5.118) weighted by conventional AM1.5G spectrum for the considered kinds of morphology of the front interface calculated at different values of θ.

Polarization	θ	Flat	Random	Triangular	Rectangular	Circular
TE	0	0.5354	0.7972	0.6763	0.6179	0.6664
TE	15	0.5255	0.7927	0.6731	0.6472	0.6648
TE	30	0.4956	0.7748	0.6481	0.6442	0.6336
TE	45	0.4395	0.7335	0.6161	0.5954	0.5775
TE	60	0.3490	0.6462	0.5468	0.4892	0.4638
TM	0	0.5354	0.8156	0.8448	0.6321	0.7082
TM	30	0.5767	0.8022	0.8104	0.7290	0.7567
TM	60	0.7258	0.6986	0.6883	0.7589	0.7702

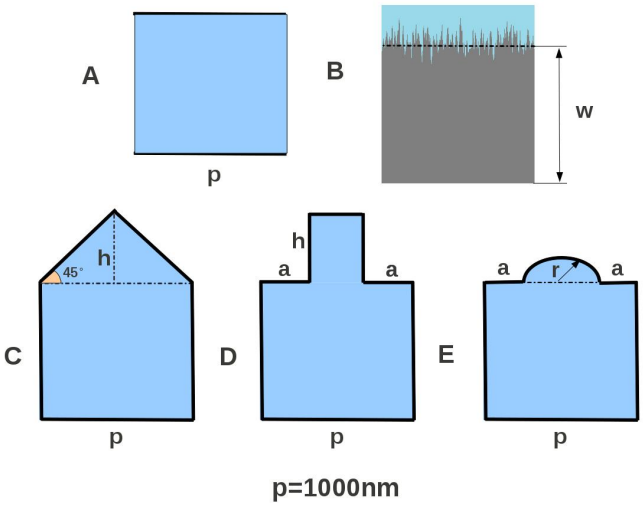

Figure 5.11: Sketch of the structures considered for the analysis of the impact of the surface morphology on the absorbance: silicon slab with (A) flat, (B) random rough (Gaussian distribution of heights with root mean square value σ_{RMS}=50nm and correlation length L_c=25nm), (C) triangular (h=500nm), (D) rectangular (h=500nm) and (E) circular (r=400nm) texturing of the front interface. The periodicity p is 1000nm for all structures and the volume of the absorbing material is the same for all slabs.

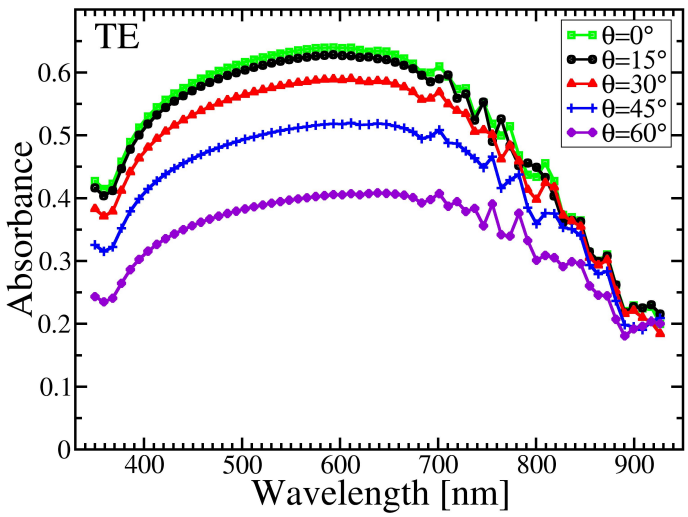

Figure 5.12: Absorbance characteristics of the silicon slab with smooth front interface calculated at different angles of incidence θ of the light. The absorbance decreases with increasing θ.

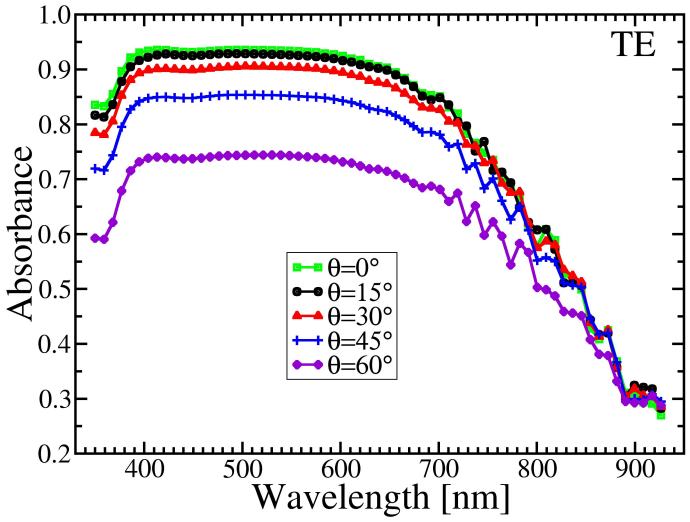

Figure 5.13: Absorbance characteristics of the silicon slab with Gaussian random roughness at the front interface calculated at different angles of incidence θ of the light. The absorbance decreases with increasing θ similarly to the flat interface case.

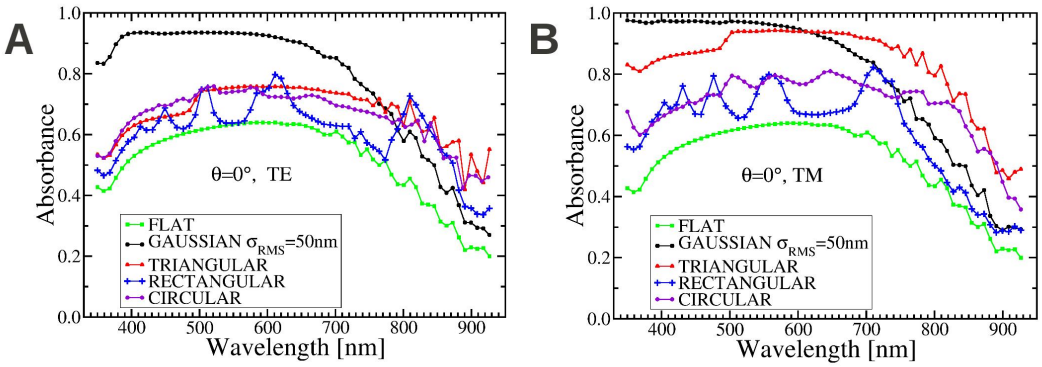

Figure 5.14: Comparison between the absorbance characteristics of the silicon slabs for different kinds of front interface morphology calculated at normal incidence (θ=0), for TE (A) and TM (B) polarization. The absorbance of the slab with smooth interface is remarkably lower than those calculated by considering the texturing. In case of TE polarization, for $\lambda < 750nm$ the maximum absorbance is obtained with the random rough interface while for TM polarization the maximum absorbance is reached by the random rough interface for $\lambda < 600nm$ and by the triangular texturing above.

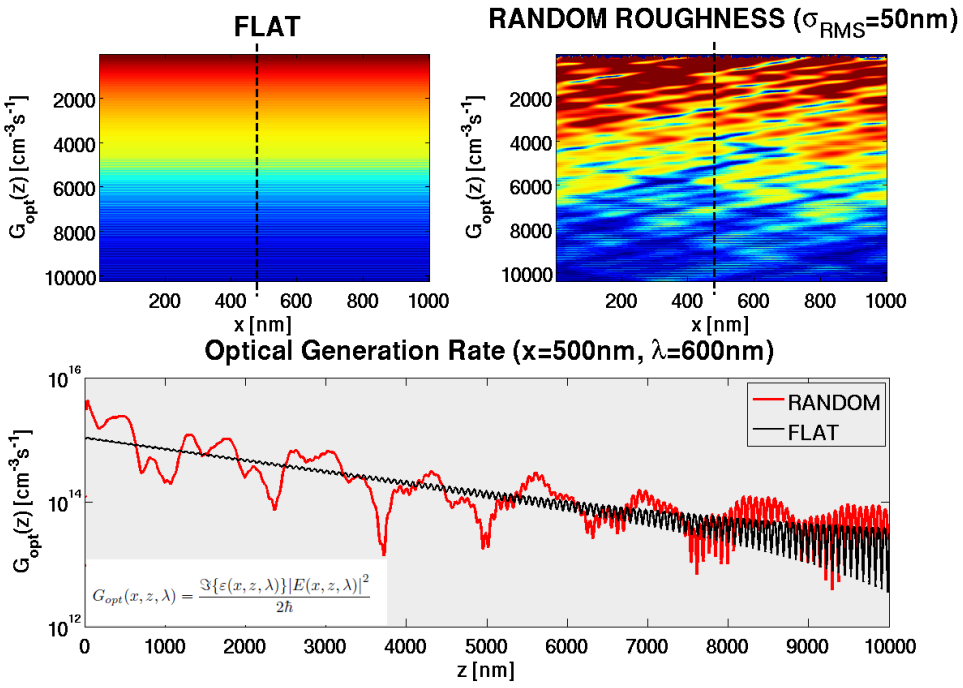

Figure 5.15: Monochrome optical generation rate G_{opt} maps per unit volume and time calculated for the slabs featuring smooth (on the left) and random roughness (on the right) interfaces at $\lambda = 600nm$ by assuming normal incidence. On the bottom side the profiles of G_{opt} versus z for the vertical slice at $x = 500nm$ are compared. The optical generation rate G_{opt} in case of random roughness is significantly larger than that of the flat interface throughout the volume of the absorbing layer.

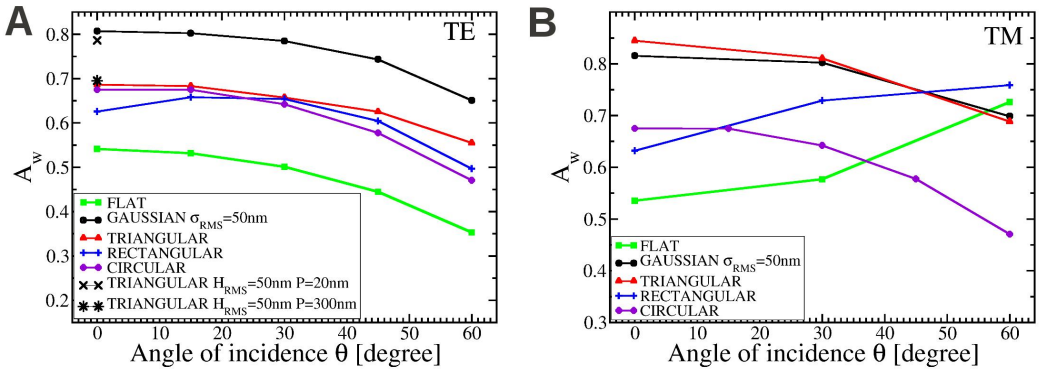

Figure 5.16: Total absorbance A_w weighted by conventional AM1.5G spectrum of the silicon slabs with different kinds of roughness at the front interface, calculated as function of the angle of incidence θ of the light, for TE (A) and TM polarization (B). For TE polarization A_w decreases with increasing θ for all kinds of surface morphology with the exception of the rectangular case, which features a maximum value of A_w between θ=20 and θ=30 degrees; the random roughness features the maximum value of A_w within the whole considered range of incidence angles. In addition, the figure reports A_w calculated for the periodic triangular surface texture featuring the same root mean square height of the random roughness (H_{RMS}=50nm), at normal incidence and for two different values of the periodicity (p=300nm and p=20nm). In (B), for TM polarization, similar trends are observed with the exception of the rectangular-textured and of the smooth interface, for which A_w increases with increasing θ.

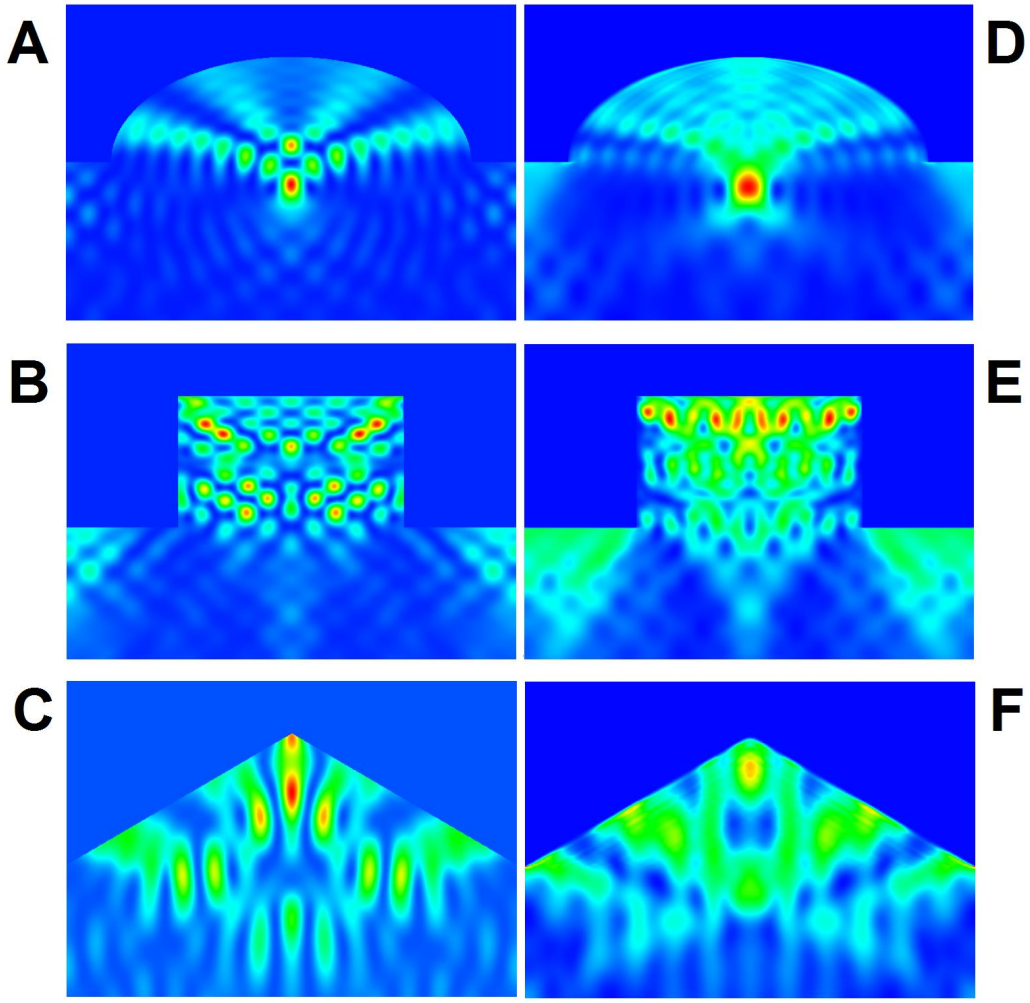

Figure 5.17: 2-D optical generation rate maps inside the c-Si slab featuring circular, rectangular and triangular texturing (Fig. 5.11) at $\lambda = 450nm$, TE (left) and TM (right) polarization. Simulation performed by RCWA ($N_F = 40$, $\Delta_z = 1nm$).

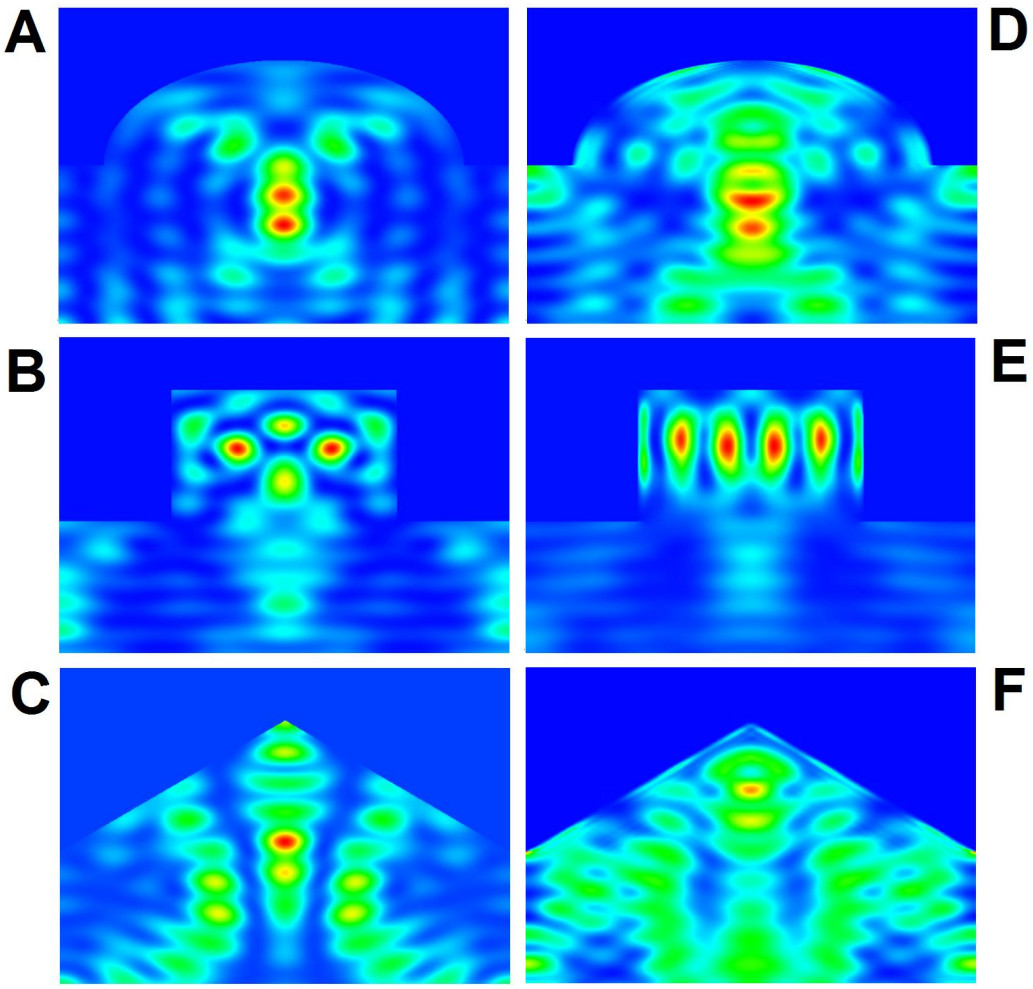

Figure 5.18: 2-D optical generation rate maps inside the c-Si slab featuring circular, rectangular and triangular texturing (Fig. 5.11) at $\lambda = 750nm$, TE (left) and TM (right) polarization. Simulation performed by RCWA (N_F=40, $\Delta_z = 1nm$).

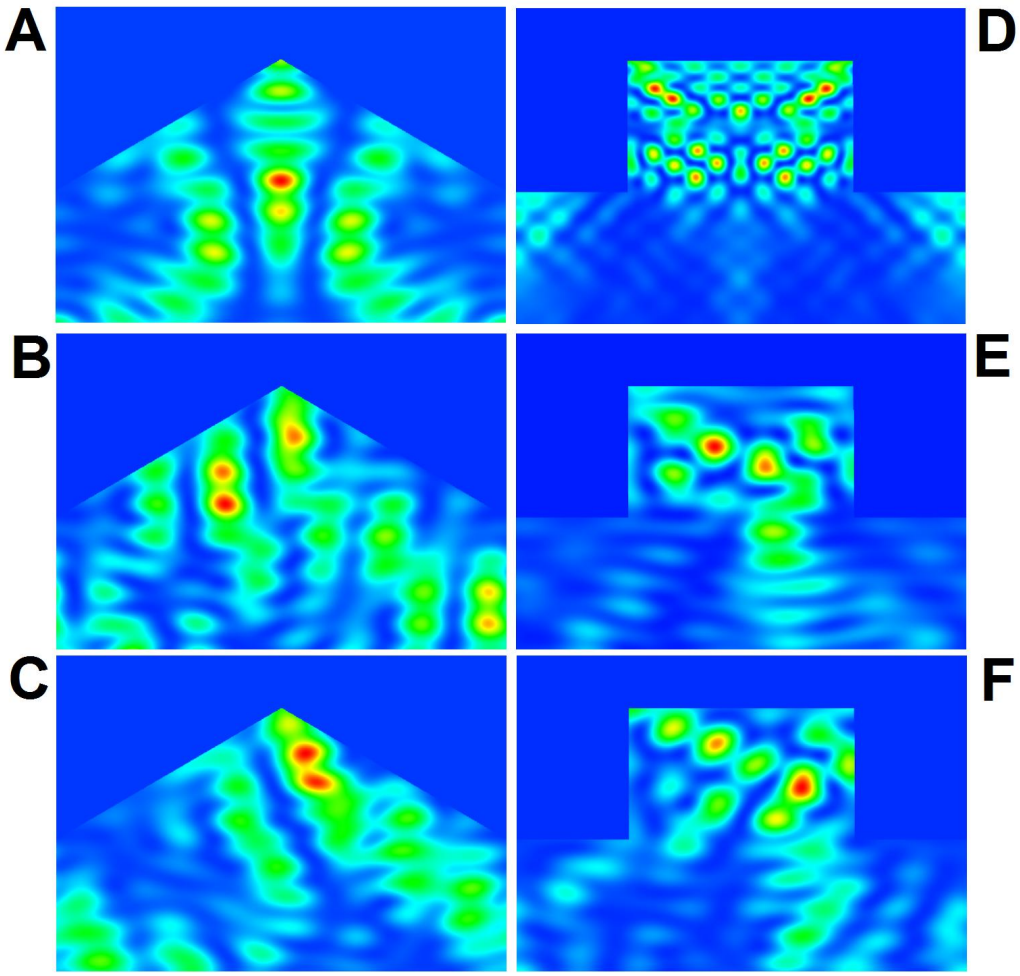

Figure 5.19: 2-D optical generation rate maps inside the c-Si slab featuring triangular (left) and rectangular (right) texturing (Fig. 5.11) at $\lambda = 750nm$, for different angle of incidence of radiation (in A,D $\theta = 0$ degree, in B,E $\theta = 30$ degree and in C,F $\theta = 60$ degree). Simulation performed by RCWA (N_F=40, $\Delta_z = 1nm$).

5.6.2 Application: nano-rod based solar cell

3D-RCWA simulator has been adopted to calculate the absorbance characteristic of cylindrical silicon nano-rods (Fig. 5.20) in order to determine the best optimum configuration (by varying geometrical parameters like periodicity, diameter and height) in terms of optical performance. In this work, due to the relatively high computation cost of the simulation of the absorbance characteristics, only few geometries have been investigated: in particular only two values of the diameter ($1000nm$ and $2000nm$) and two values of height ($4\mu m$ and $8\mu m$) are accounted for. The periodicity P has been chosen in order to maintain the volume of the absorber material constant independently on the value of the geometrical parameters. Two different thicknesses of the silicon substrate have been accounted for: $10\mu m$ and $100\mu m$; the related absorbance characteristics have been reported in Fig. 5.21A and Fig. 5.21B, respectively. The absorbance has been compared to that of the smooth substrate featuring the same volume of silicon. Simulations have been performed adopting $\theta = 0$ degree, $\psi = 0$ degree (Fig. 5.3) and $N_{Fx} = 53$, $N_{Fy} = 53$ number of Fourier modes along x-axis and y-axis, respectively. For both considered values of substrate thickness, the highest absorbance is obtained by the structure featuring $P = 2120nm$, $D = 1000nm$ and $H = 4000nm$, within the range of wavelength $350nm$-$950nm$.

Fig. 5.22 report an example of calculated monochromatic optical generation map for a cylindrical nano-rod featuring $P = 2120nm$, $D = 1000nm$ and $H = 4000nm$ calculated by the 3D-RCWA simulator at $\lambda = 850nm$ ($\theta = 0$, $\phi = 0$). The 3-D optical generation rate has been mapped and interpolated on the same mesh grid provided as input to Sentaurus TCAD. The nano-rod features a radial junction with depth of $200nm$ and peak doping concentration at the external surface of the cylinder equal to $10^{19}cm^{-3}$; the doping concentration of the core of the cylinder is $10^{18}cm^{-3}$. Since the illumination is direct, the cylindrical symmetry of the geometry is exploited in order to save computational resources. Therefore only one quarter of the cylinder is considered. The numerical mesh grid exhibits about a million vertices.

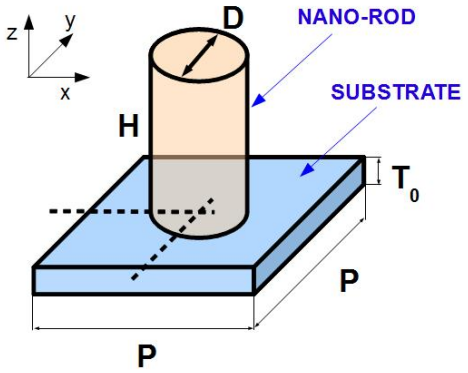

Figure 5.20: Sketch of the 3-D cylindrical nano-rod. Nano-rod diameter D, height H, substrate thickness T_0 and periodicity P are geometrical parameters.

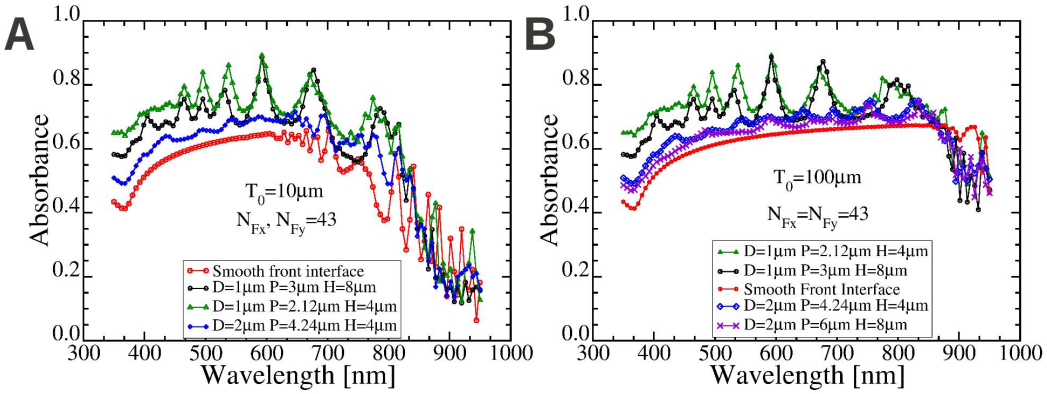

Figure 5.21: Absorbance of the silicon cylindrical nano-rod of Fig. 5.9 calculated by 3D-RCWA from $\lambda = 350nm$ to $\lambda = 950nm$ with $\theta = 0$, $\phi = 0$. Nano-rod diameter D, height H and periodicity P as geometrical parameters. All structures exhibit the same volume of the absorber material. Simulations have been performed adopting $N_{Fx} = 43$, $N_{Fy} = 43$ number of Fourier modes along x-axis and y-axis, respectively. Substrate thickness $10\mu m$ (A) and $100\mu m$ (B). The highest absorbance is obtained by the structure featuring $P = 2120nm$, $D = 1000nm$ and $H = 4000nm$.

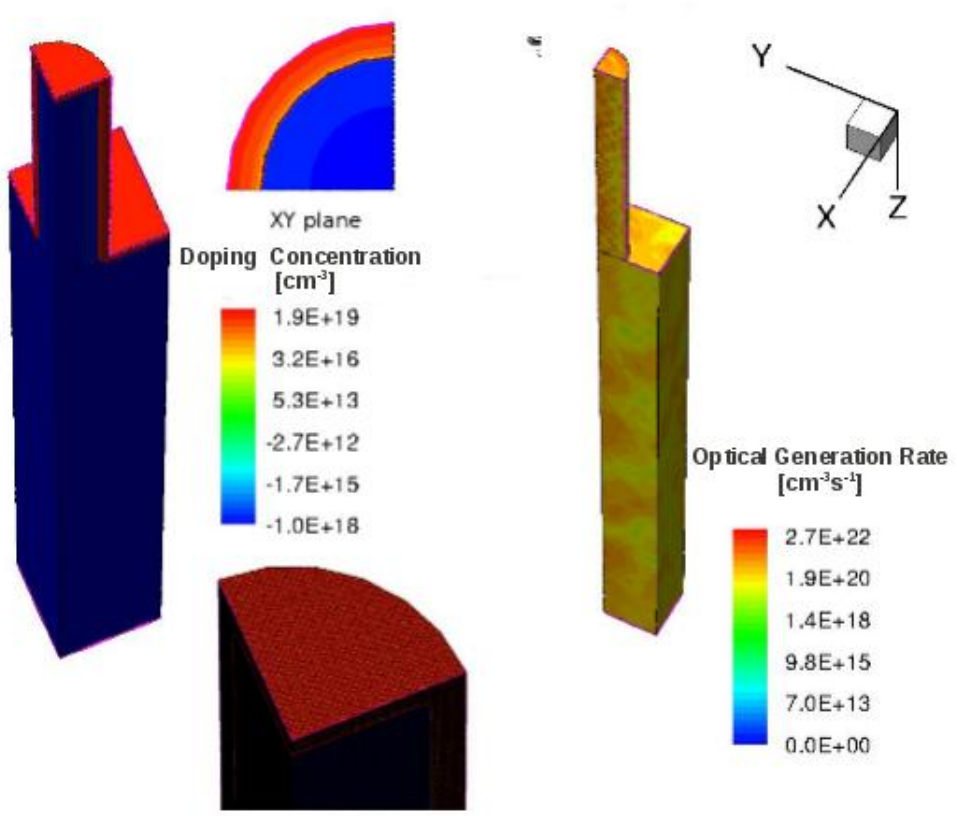

Figure 5.22: Monochromatic optical generation rate of a cylindrical nano-rod featuring $P = 2120nm$, $D = 1000nm$ and $H = 4000nm$ (Fig. 5.20) calculated by the 3D-RCWA simulator at $\lambda = 850nm$ with $\theta = 0$, $\phi = 0$. The 3-D optical generation rate has been mapped and interpolated on the same mesh grid provided as input to the device simulator Sentaurus. The nano-rod features a radial junction with junction depth of $200nm$. Since the illumination is direct, the cylindrical symmetry of the geometry is exploited in order to save computational resources. Therefore only one quarter of the cylinder is considered.

6

Modeling of amorphous silicon thin film solar cells

As discussed in chapter 2, an effective method to reduce the cost of photovoltaic devices is the adoption of thin semiconductor films instead of high-purity materials. Several materials have been considered for thin film solar cells, like copper indium gallium diselenide (CIGS) (125), dye-sensitized nanocrystalline titanium dioxide $nc-TiO_2$ (126), amorphous silicon (a-Si) (127) and cadmium telluride (CdTe) (128). Amorphous silicon is the most mature and widely used thin film for commercial panels. However several trade-offs have to be accounted for in designing thin film devices. Aside from considerations of material stability and relatively large recombination losses with reference to crystalline materials, light confinement is one of the most challenging issues in thin film solar cells. Although the absorption length of the radiation is remarkably higher for a-Si, the thickness of thin film devices cannot be increased arbitrarily because of the large defect density; indeed, the relative thicker absorber layer leads to reduced collection efficiency. In order to take into account the several competing physical mechanisms occurring in thin film solar cells, TCAD simulators can be helpfully adopted to realistically predict trends and performance of such devices. State-of-the-art simulators -specifically developed for the numerical simulation of thin film devices- are mostly 1-D tools (ASA (129), SUNSHINE (130), AMPS-1D (131)); this means that, not only the optical problem is solved in one dimension, but also the transport is mono-dimensional. In addition, simulators like ASA, which can be considered as the most mature simulator in thin film solar cells field, adopt an optical simulation method based on the scalar

scattering approach which, being a non rigorous solver of the Maxwell equations, is not theoretically suitable to solve the near field optical problem in presence of nanostructured features like those exhibited by typical interfaces between layers of a thin film solar cell (132); however, for most practical devices an acceptable agreement with experiments is obtained by means of calibration of the light scattering coefficients from rough interfaces.

This chapter outlines the basics of thin film devices with specific reference to amorphous silicon solar cells. In addition, the physical models commonly adopted for device simulation are described and a review of the approaches to optical modeling adopted by state-of-the-art 1-D simulators for thin film devices is presented. The chapter focus is on the application and the calibration of Sentaurus TCAD simulator for 2-D a-Si solar cells modeling as well as on the optical simulation performed by the implemented RCWA simulator described in detail in chapter 5. The presented application concerns the investigation of the impact of internal surface morphology on performance of a single junction a-Si thin film solar cell. Transport and light propagation are modeled in two dimensions as in (133), where only smooth interfaces are accounted for. Finally, an investigation of the loss mechanisms by device simulation is presented.

6.1 Thin film solar cells

Commonly, in superstrate solar cells (Fig.6.1) a p-doped/intrinsic/n-doped (p-i-n) junction is deposited on a thick glass substrate coated with transparent conductive oxide (TCO). The front electrode material is typically Sn-doped In_2O_3 (ITO), boron or aluminum doped ZnO or F-doped SnO_2 (127)(134). Amorphous silicon is deposited by plasma enhanced chemical vapour deposition (PEVCD) in the temperature range $150-250°C$. The typical thickness of the intrinsic region is within the range $200-750nm$ (135)(136) and that of the doped layers is in the range $10-30nm$ in order to reduce the impact of high defective semiconductor on device performance; indeed, large doping concentration leads to remarkable low electric mobility in a-Si. The intrinsic layer absorbs photons from the sun and allows the transport of the photo-generated carriers due to the relatively higher mobility with respect to the doped layers. The spectral response of a-Si is determined by the optical band-gap E_{Go} which is typically in the range $1.55eV$-$1.75eV$ (137) for optimized devices, like those containing bonded

hydrogen concentration. High-quality amorphous silicon solar cells use hydrogenated materials (a-Si:H) (138). Since the diffusion length in a-Si:H is typically within the range $100nm$-$200nm$, the dominant transport mechanism is drift. Differently from crystalline materials, amorphous silicon exhibits a continuous distribution of states in energy throughout the band-gap, which is defined, for this materials, as the difference between the energy levels which bounds the localized and the non-localized transport (conventionally called conduction and valence band edges) (139). The concentration of defect states increases towards the boundaries of the intrinsic layer leading to relatively high space charge regions at the p/i and i/n interfaces. Therefore, the highest field intensity is reached in the portions of the device close to the electrodes. Hence, if the intrinsic layer is too thick, in the middle part of such region the field intensity may be too low to sustain the drift, therefore in such case only diffusion ensure transport; however, due to the upper bound value of the carrier mobility in a-Si, thick i-layers lead to degraded collection efficiency. Due to well-known Staebler-Wronski effect (140), the presence of strained bonds (weak bonds between silicon atoms) leads to high probability of bond breaking with consequent creation of metastable defects because of the release of energy due to electron-hole recombination events boosted by illumination. The increase of dangling bonds concentration reduces the electric field intensity and enhances the recombination losses leading to conversion efficiency degradation. However, this effect is self-limiting, therefore the performance of the cell typically reach stabilized values (approximately 20-30% lower than the initial value) within the first year of life of the module (141).

6.2 Continuous distribution of defect density in energy

In amorphous materials only the short-range crystallographic order can be assumed to be the same of crystalline counterparts. Since lattice periodicity cannot be defined in such materials, the wave vector is not helpful to describe the allowed electronic states. The singularities in the density of states distribution at the boundaries of the bands are replaced by gradually decreasing distributions called band-tails, which extension is a measure of the entity of the disorder in the atomic structure. Because the lack of periodicity, these states are localized. In amorphous silicon the model of traps assumes the presence of donor-like states (charged for electrons) and of acceptor-like states

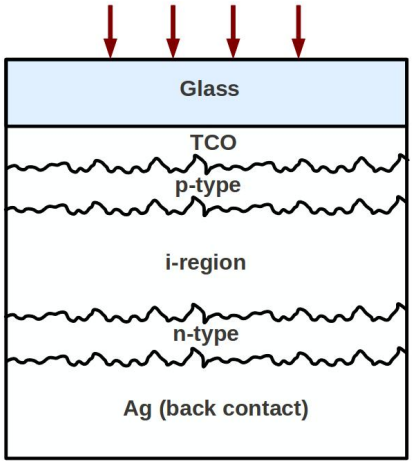

Figure 6.1: Cross-sectional schematic of a (glass) superstrate single-junction amorphous silicon thin film solar cell, with the transparent conductive oxide (TCO) and the internal rough interfaces.

(charged for holes). The density of states in energy (DOS) consists of two exponential distributions of tail states ($g^{BT}_{A,D}(E)$) in superposition with Gaussian-distributed mid-gap states ($g^{MG}_{A,D}(E)$) accounting for dangling bonds (Fig. 6.2). Therefore the total DOS can be defined as superposition of four distributions of states (142):

$$g(E) = g^{BT}_{D}(E) + g^{BT}_{A}(E) + g^{MG}_{D}(E) + g^{MG}_{A}(E), \tag{6.1}$$

where

$$g^{BT}_{D}(E) = \frac{G_{D,BT}}{2} exp\left[-\frac{E - E_{0,D}}{E_D}\right], \qquad g^{BT}_{A}(E) = \frac{G_{A,BT}}{2} exp\left[\frac{E - E_{0,A}}{E_A}\right], \tag{6.2}$$

and

$$g^{MG}_{D}(E) = \frac{N_{D,MG}}{\sigma_D} exp\left[-\frac{(E - E_{D,MG})^2}{2\sigma_D}\right], \tag{6.3}$$

$$g^{BT}_{A}(E) = \frac{N_{A,MG}}{\sigma_A} exp\left[-\frac{(E - E_{A,MG})^2}{2\sigma_A}\right], \tag{6.4}$$

where $E_{A,MG}$, $E_{D,MG}$ are the energy positions for the Gaussian peaks, $N_{A,MG}$, $N_{D,MG}$ are the total number of states of the Gaussian distributions and $\sigma_{D,A}$ their

standard deviations. For acceptor-like states the probability of occupation is defined by the following function:

$$f_A(E) = \frac{n + C_A N_V exp\left[\frac{E_V - E}{kT}\right]}{n + C_A p + N_C exp\left[\frac{E - E_C}{kT}\right] + C_A N_V exp\left[\frac{E_V - E}{kT}\right]}, \tag{6.5}$$

where E_C and E_V are the edges of the conduction and valence bands, N_C and N_V the density of states in conduction and valence bands, $C_A = \frac{\sigma_{A,p}}{\sigma_{A,n}}$ and $\sigma_{A,p}$, $\sigma_{A,n}$ the sections of charged traps (holes for acceptor-like states) and neutral ones (electron for acceptor-like states); similarly for the donor-like states:

$$f_D(E) = \frac{nC_D + N_V exp\left[\frac{E_V - E}{kT}\right]}{C_D n + p + C_D N_C exp\left[\frac{E - E_C}{kT}\right] + N_V exp\left[\frac{E_V - E}{kT}\right]}, \tag{6.6}$$

In case of amorphous materials, in order to extend the SRH model for single-level traps (described in section 2.11) to a continuous distribution of energy levels with arbitrary shapes, the Taylor-Simmons statistics is applied (143). Therefore the concentrations of trapped electrons and holes are given by:

$$n_T(n,p) = \int_{E_V}^{E_C} f_A(E) g_A(E) dE, \qquad p_T(n,p) = \int_{E_V}^{E_C} \left[1 - f_D(E)\right] g_D(E) dE. \tag{6.7}$$

Hence, the extended SRH model, under steady state conditions, can be formulated as:

$$R_p(n,p) = R_n(n,p) =$$

$$= C v_{th} \sigma_n \left(np - n_i^2\right) \int_{E_V}^{E_C} \frac{g_D(E)}{C_D n + p + N_V exp\left[\frac{E_V - E}{kT}\right] + C_D N_C exp\left[\frac{E - E_C}{kT}\right]} + \frac{g_A(E)}{n + C_A p + C_A N_V exp\left[\frac{E_V - E}{kT}\right] + N_C exp\left[\frac{E - E_C}{kT}\right]} dE, \tag{6.8}$$

where C is the ratio of the section of charged traps to neutral ones and v_{th} is the thermal velocity of carriers.

The expression of the net recombination rate due to traps in Sentaurus is different from that of eq. 6.8, which is adopted by AMPS-1D. Indeed, in Sentaurus device,

instead of N_C and N_V, the effective carrier concentration $n_{i,eff}$ is used; this difference has to be considered in order to calibrate the model for trap definition in Sentaurus with that implemented in AMPS-1D (144).

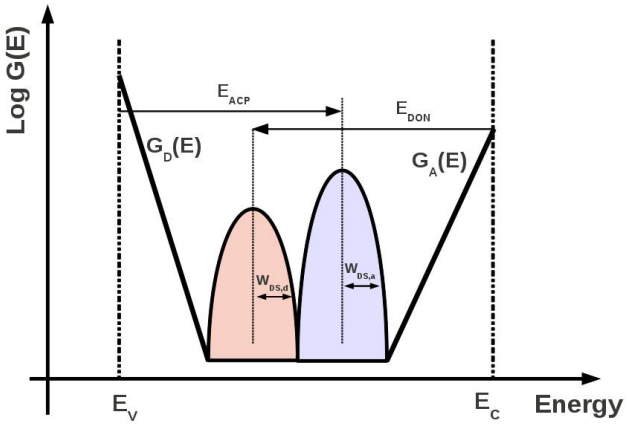

Figure 6.2: Density of states distribution in energy (DOS) with exponential band-tail states and Gaussian shaped mid-gap states in amorphous silicon. E_{ACP} and E_{DON} denote the acceptor Gaussian peak energy measured positive from the edge of the valence band E_V and the donor Gaussian peak energy measured positive from the edge of the conduction band E_C, respectively.

6.3 Optical modeling

In this section the main issues related to the optical confinement in thin film solar cells are outlined. The focus of the section is on state-of-the-art optical modeling techniques adopted in commercial tools for thin film devices. Among these 1-D approximated techniques, the Bruggeman's effective media approximation (EMA) (145) and the Monte Carlo ray-tracing (described in chapter 3) are commonly used. According to EMA approach, the region of the simulation domain interested by the roughness (or discontinuity of the permittivity) is replaced by virtual homogenous layers with smooth interfaces and refractive indices calculated as average of the refractive indices of the materials separated by the interface and weighted by the spatial dependence of the surface heights (Fig. 6.3). However, the most adopted approach to optical simulation of

thin film solar cells is that based on the scalar scattering theory or on its modifications with respect to the original formulation (10). This method, adopted by well-known simulators like ASA and SUNSHINE, is described in the next section.

6.3.1 Optical confinement in thin-film solar cells: modeling by methods based on scalar scattering theory

One effective way to enhance light confinement in thin film solar cell is the introduction of rough and nanotextured interfaces in the multi-layer structure; this results in an enhanced average optical path in the layers due to light scattering from rough interfaces which introduces higher angular dependent reflectance than those occurring in case of normal incidence or scattering from smooth interfaces. Rough interfaces are introduced in the multi-layer structure by using substrates with textured surface. For supestrate solar cells, a stack of relatively thick glass (with thickness in the millimeter range) and textured TCO film (for instance magnetron sputtered ZnO:Al film (146)) is used to form the front contact; different surface roughness levels and morphologies can be obtained by wet chemical etching in diluted hydrochloric acid (HCl). The deposition of thin a-Si:H films helps to transfer the roughness to all internal surfaces. As result of the stack of different materials and rough interfaces, a multiple light reflection mechanism exhibiting interference effects occurs inside the structure. Practical surface morphologies exhibit random roughness featuring height root mean square values (σ_{RMS}) within the range $20nm$-$100nm$ (147) and which can be adequately described by Gaussian spatial distributions of heights. The height root mean square value is defined by:

$$\sigma_{RMS} = \sqrt{\frac{1}{N}\sum_{i=1}^{N}(z_i - \tilde{z})^2}, \tag{6.9}$$

where N is the number of samples of the surface heights, z_i is the data point and $\tilde{z}$ is the average surface level.

A critical issue in optical modeling of these structures is the description of the scattering parameters of light from random rough interfaces depending on the morphology. In (148)(147) two types of descriptive scattering parameters are introduced: the haze parameter (H_T and H_R for transmission and reflection, respectively) and the angular distribution function (ADF). The haze parameter describes which is the portion of the

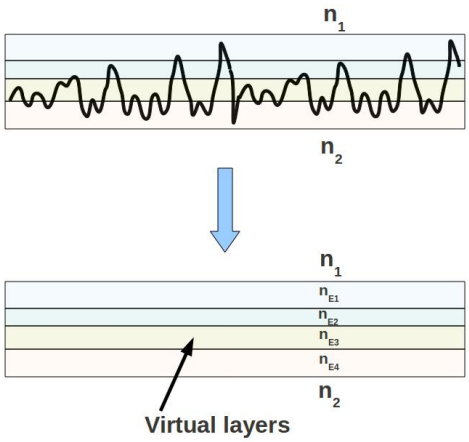

Figure 6.3: Effective media approximation (EMA): the rough interface between two media of refractive index n_1 and n_2 is replaced by a stack of one or more equivalent virtual layers featuring planar interfaces.

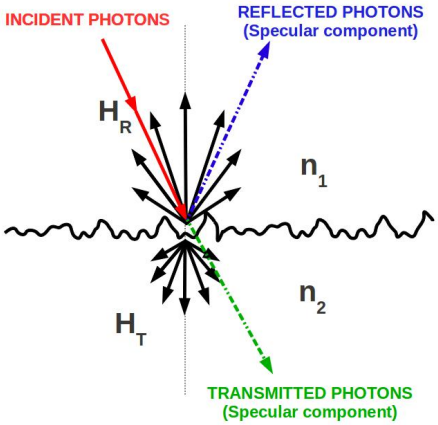

Figure 6.4: Light scattering from rough interface: specular and diffuse reflection (transmission) occur at non-planar interfaces exhibiting roughness featuring size in wave regime. H_R and H_T are the refection and transmission haze parameters, respectively.

light intensity that is diffused to the total incident intensity at the interface (Fig. 6.4). The ADF relates the intensity distribution of the scattered light to the scattering angle. Typically, these parameters are experimentally determined. Approaches aimed at modifying and at measuring the ADFs and the haze parameters of internal interfaces are also described in (147). Applying different etching times it is possible to control the roughness level of ZnO:Al films. Characterization and analysis of surfaces are performed by atomic force microscopy (AFM) and scanning electron microscopy (SEM). The latter technique allows to determine statistical parameters of the random rough interfaces like height distribution and correlation length. Total integrating scattering (TIS) technique allows the measurement of the total and diffused transmittance (reflectance) of an interface, T_{tot} (R_{tot}) and T_{diff} (R_{diff}), respectively, therefore the haze parameters can be calculated as $H_T = \frac{T_{diff}}{T_{tot}}$ and $H_R = \frac{R_{diff}}{R_{tot}}$. In order to measure ADFs, the angular resolved scattering (ARS) technique is commonly used. Typical examples of normalized haze parameters and ADFs are shown in Fig. 6.5A and Fig. 6.5B, respectively. In (147), the trend of normalized haze parameters for glass/ZnO:Al interfaces are reported to increase with increasing σ_{RMS} and to decrease with increasing wavelength λ of the radiation, indicating that the scattering from such interfaces is more effective for short wavelength and large roughness level. In addition, ADFs are reported to decrease with increasing σ_{RMS}, therefore for relatively large roughness levels, the scattering into smaller angles is more remarkable; on the contrary, when σ_{RMS} is lower, the light scattering is more effective into shallow angles. However, direct measurement of scattering parameters is difficult. The scalar scattering theory (10) allows to define a link between optical properties of bulk materials, haze parameters and morphology of the interface. The approach described in (147) assumes that the total intensity of transmitted and reflected light does not depend on the roughness level. If ϕ_1 and ϕ_2 denote the incident and the outgoing angle of the specular beam, respectively, and n_1 and n_2 are the real part of the complex refractive indices of the materials separated by the interface, the haze parameters are given by:

$$H_R = 1 - exp\left[-\left(\frac{4\pi\sigma_{RMS}C_R\left(\lambda,\sigma_{RMS}\right)n_1 cos(\phi_1)}{\lambda}\right)^2\right], \tag{6.10}$$

$$H_T = 1 - exp\left[-\left(\frac{4\pi\sigma_{RMS}C_T\left(\lambda,\sigma_{RMS}\right)|n_1 cos(\phi_1) - n_2 cos(\phi_2)|}{\lambda}\right)^a\right], \tag{6.11}$$

where $C_T(\lambda, \sigma_{RMS})$ and $C_R(\lambda, \sigma_{RMS})$ are correction wavelength and morphology-dependent parameters which are introduced into the original scalar scattering theory in order to fit experimental data and a is a power factor for H_T (typically within the range 2-3). Haze parameters and ADFs can be used to reformulate the Fresnel coefficients in presence of rough interfaces extending the well-know theory valid for planar interfaces between homogeneous media (149).

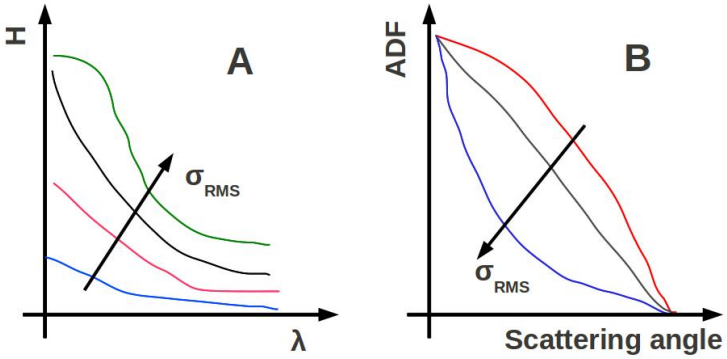

Figure 6.5: Typical haze parameters versus wavelength and angular distribution functions (ADF) for air/glass/ZN:O:Al/air system in thin film solar cells with roughness level σ_{RMS} as paramater.

Original scalar scattering theory is assumed to be an acceptable approximation of the haze parameters only for a restricted range of wavelength of the radiation and not for any arbitrary surface morphology (147). Indeed, the scalar scattering theory is a good approximation if the distribution of the surface heights is completely random and the correlation length of the interface morphology is much larger than the wavelength (in order to neglect shadowing and multiple scattering effects at the rough interface). Typically, these assumptions are not satisfied by practical interfaces. Therefore rigorous solvers of the Maxwell equations like the RCWA method described in chapter 5 can be successfully adopted to perform the optical simulation of thin film solar cells.

6.4 Application: dependence of main figures of merit of the solar cell on the morphology of the internal interfaces

In the following the dependence of the main figures of merit of a thin film a-Si superstrate solar cell (Fig. 6.1) on the morphology of the rough TCO/a-Si interface is investigated by means of 2-D electro-optical simulations. In subsection 6.4.1 the simulation methodology adopted by using Sentaurus Device as TCAD numerical tool is described; a simple solar cell with 1-D symmetry is simulated in order to validate the simulation setup by means of a comparison with the simulation results obtained by AMPS-1D (144), when similar devices and physical parameters are adopted. The remainder of the section is the discussion of the results from Sentaurus 2-D simulations of the cell exhibiting the rough internal interface as well the analysis of the loss mechanisms occurring with increasing roughness level. The optical simulations of the devices featuring rough interfaces have been carried out by the 2-D RCWA tool.

6.4.1 Simulation setup

The simulated device is a superstrate thin film solar cell featuring a $500nm$-thick a-Si layer deposited on a stack of $1mm$-thick SiO_2 substrate and $200nm$-thick transparent conductive oxide (TCO). The back contact is made of silver (Ag). All internal interfaces are smooth (layers with parallel interfaces) with the exception of the TCO/a-Si interface for which heights are described by a spatial Gaussian distribution with correlation length equal to $25nm$. Three root mean square (RMS) values of roughness height have been considered in this work: $\sigma_{RMS} = 0$ (smooth interface), $\sigma_{RMS} = 25$ and $\sigma_{RMS} = 50nm$. The a-Si layer forms a p-doped/intrinsic/n-doped p-i-n junction with uniformly doped regions ($N_A = 3 \times 10^{19} cm^{-3}$, $N_D = 1 \times 10^{19} cm^{-3}$); the thickness of the p-doped and n-doped regions are $8nm$ and $15nm$, respectively. Doping parameters are comparable to those presented in (133)(139)(150). The stack of layers ITO/p-type/intrinsic region is a conformal structure, while the interface between the intrinsic and the p-type regions is flat.

The mobility band-gap is $1.72eV$ (independent on doping concentration). Optical properties of the materials are shown in Fig. 6.6. For the 2-D optical simulation carried out by RCWA, 121 Fourier modes (N_F) and a discretization step $\Delta_z = 1nm$ have been

adopted (section 5.3); with this set of numerical parameters, the accuracy of the relative absorption of the a-Si layer, in case of the multi-layer structure with one rough interface ($\sigma_{RMS} = 50nm$) for both TE and TM polarizations at $\lambda = 450nm$ and at $\lambda = 750nm$, is below 10^{-3}, as shown in Fig. 6.7A and Fig. 6.7B -in which the accuracy is plotted as function of Δ_z^{-1} (adopting $N_F = 201$)- and in Fig. 6.7C and Fig. 6.7D, where the relative accuracy is reported as function of the number of Fourier modes (assuming $\Delta_z = 1nm$). It is worth noting that a relatively higher number of Fourier modes are required -with respect to the rectangular grating considered in chapter 5- in order to attain the same relative accuracy, due to the more complicated geometry of the surface profile.

The optical generation maps are calculated by assuming normal incidence, TE polarization and the AM1.5G spectrum ($1000Wm^{-2}$). The results from the optical simulator have been imported into a 2-D drift-diffusion device simulator by means of interpolation over the numerical grid of Sentaurus.

The density of states as function of energy in the amorphous silicon is described by continuous exponential and Gaussian distributions of trap levels (section 6.2). The parameters of the defect energy levels distribution, which are comparable to those proposed in (142)(139), are reported in Tab. 6.1. Recombination at electrodes (bottom and ITO/p-region interfaces) is accounted by setting a recombination velocity for minority carriers equal to $10^7 cms^{-1}$. The carrier mobility is constant and equal to $20cmV^{-1}s^{-1}$ and $2cmV^{-1}s^{-1}$ for electrons and holes, respectively. Since the work function difference between TCO and a-Si p-layer causes band bending and builds a potential barrier in the p-layer resulting in an imperfect ohmic contact (151), front electrode is modeled by a Schottky contact with barrier set to 1.54eV. Non ideality of the back contact is accounted for by assuming a barrier of 0.2eV. The figures of merit calculated by means of the electro-optical TCAD simulations of the cell with smooth ITO/p-region interface are reported in Tab. 6.2 ($\sigma_{RMS} = 0nm$). The simulation of such simple device featuring 1-D symmetry has been carried out in order to validate the simulation setup and the physical models adopted in Sentaurus by means of a comparison of the main figures of merit as well as of the internal maps of electrostatic potential, electric field, recombination rates, generations rates and free carrier concentrations with those calculated by AMPS-1D. In order to calibrate the physical models in Sentaurus, since AMPS-1D adopts a different model to calculate the net trap recombination rate of eq.

6.8 as discussed in section 6.2, the peak concentration of the mid-gap Gaussian defects (for donors and acceptors) has been set to $5 \times 10^{16} cm^{-3}$ in AMPS-1D, differently to the value adopted in Sentaurus shown in Tab. 6.1. Under these conditions, a good agreement between the two simulators has been obtained. Fig. 6.8 shows the electric field, the optical generation rate, the carrier concentrations and the trap recombination rates in short-circuit conditions calculated by Sentaurus for the cell featuring $\sigma_{RMS} = 0nm$.

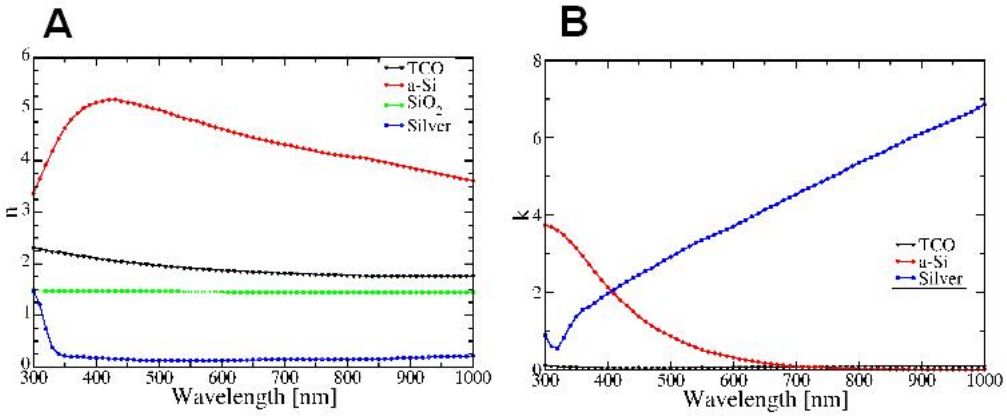

Figure 6.6: Optical properties of the media of the simulated single-junction thin film superstrate solar cell: real part (left) and imaginary part (right) of the complex refractive indices.

6.4.2 Dependence of figures of merit on ITO/p-type interface roughness level

Tab. 6.2 reports the main figures of merit of the simulated cell for different values of roughness level of the ITO/p-region interface. The photo-generated current density J_{ph} increases with the roughness level (Tab. 6.2) which leads to reduced reflectance; this trend is consequence of that of the absorbed power within the a-Si layer, which is reported in Fig. 6.9, where the roughness level is a simulation parameter. Fig. 6.10 reports the 2-D calculated full-spectrum optical generation rate maps inside the a-Si layer for $\sigma_{RMS} = 25nm$ and $\sigma_{RMS} = 50nm$.

In Tab. 6.2 it is worth noting that the maximum short-circuit current density J_{sc} and the maximum conversion efficiency η, are obtained for $\sigma_{RMS} = 25nm$ while, for $\sigma_{RMS} = 50nm$, the J_{sc} and the conversion efficiency are smaller than those for $\sigma_{RMS} = 25nm$. In order to explain this trend Tab. 6.3, Fig. 6.11 and Fig. 6.12, which

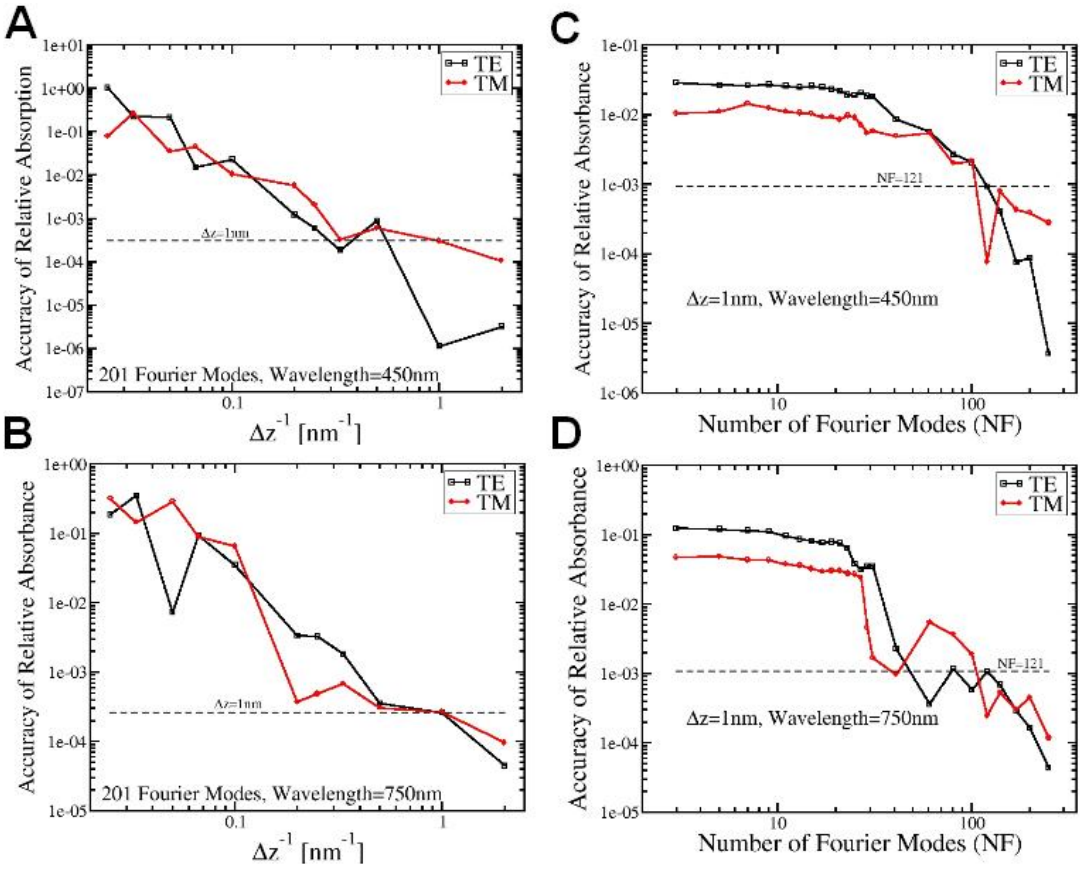

Figure 6.7: Accuracy of the relative absorption for 2-D RCWA in case of the simulated superstrate thin film solar cell with one rough interface (ITO/p-region interface with $\sigma_{RMS} = 50nm$). The accuracy has been calculated for both TE and TM polarizations and for two values of the wavelength of the radiation ($\lambda = 450nm$ and $\lambda = 750nm$). In (A) and (B) the accuracy of relative absorbance is calculated as function of Δ_z^{-1} for $N_F = 201$. In (C) and (D) the accuracy of relative absorbance is calculated as function of the number of Fourier modes N_F when $\Delta_z = 1nm$. The dashed line denotes the upper bound limit of the accuracy for the conditions adopted to perform the optical simulation ($N_F = 121$, $\Delta_z = 1nm$).

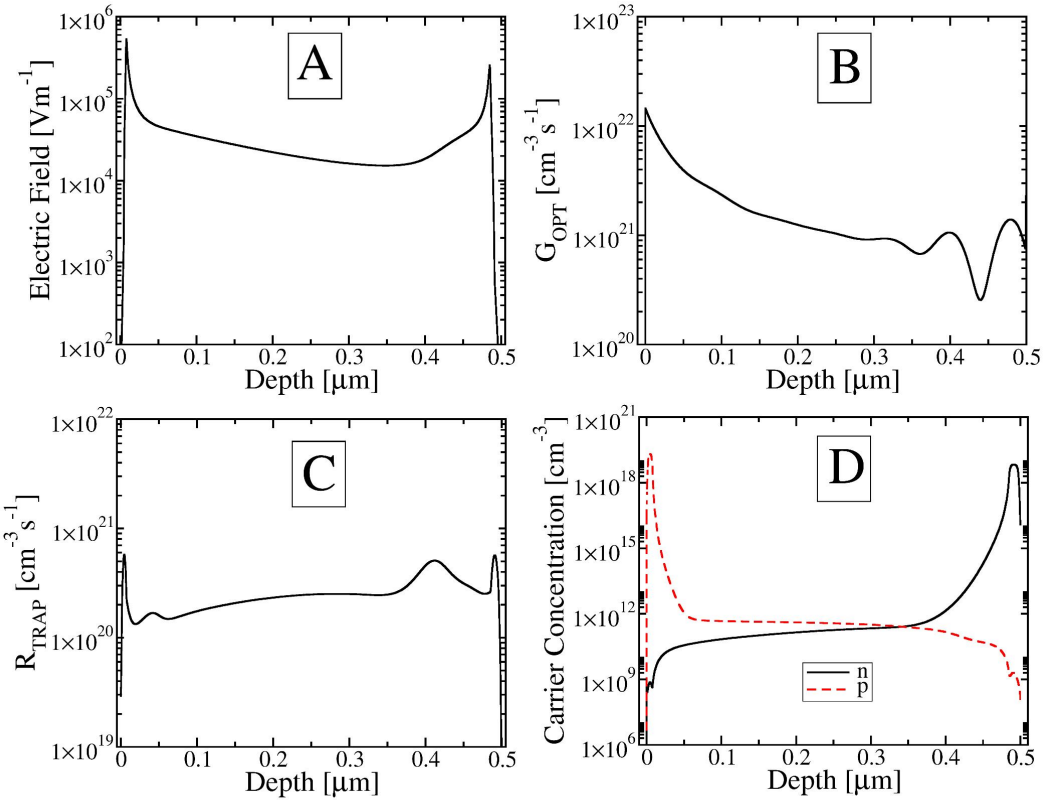

Figure 6.8: Calculated electric field (A), optical generation rate map (in $cm^{-3}s^{-1}$) (B), carrier concentrations (C) and recombination rate due to band-tails and mid-gap traps as function of the depth in short-circuit conditions for the p-i-n cell with $\sigma_{RMS} = 0nm$.

Table 6.1: Density of states in energy for Gaussian shaped and exponential states for the simulated thin film solar cell.

Symbol	Unit	p-region	i-region	n-region
$G_{D,BT}$	cm^{-3}	10^{21}	10^{21}	10^{21}
$E_{0,D}$	eV	0	0	0
E_D	eV	0.05	0.05	0.05
$G_{A,BT}$	cm^{-3}	10^{21}	10^{21}	10^{21}
$E_{0,A}$	eV	0	0	0
E_A	eV	0.03	0.03	0.03
$N_{D,MG}$	cm^{-3}	5×10^{19}	7×10^{16}	10^{19}
$E_{D,MG}$	eV	1.24	1.12	1.12
σ_D	eV	0.15	0.15	0.15
$N_{D,MG}$	cm^{-3}	5×10^{18}	7×10^{16}	10^{19}
$E_{D,MG}$	eV	1.14	1.02	1.02
σ_D	eV	0.15	0.15	0.15
$\sigma_{n,A}^{BT}$	cm^2	10^{-17}	10^{-17}	10^{-17}
$\sigma_{p,A}^{BT}$	cm^2	10^{-15}	10^{-15}	10^{-15}
$\sigma_{n,A}^{MG}$	cm^2	10^{-15}	10^{-15}	10^{-15}
$\sigma_{p,A}^{MG}$	cm^2	10^{-14}	10^{-14}	10^{-14}
$\sigma_{n,D}^{BT}$	cm^2	10^{-15}	10^{-15}	10^{-15}
$\sigma_{p,D}^{BT}$	cm^2	10^{-17}	10^{-17}	10^{-17}
$\sigma_{n,D}^{MG}$	cm^2	10^{-14}	10^{-14}	10^{-14}
$\sigma_{p,D}^{MG}$	cm^2	10^{-15}	10^{-15}	10^{-15}

show the collection efficiency and the external quantum efficiency (EQE) characteristics for different roughness levels, respectively, can be successfully considered. It is possible to observe that the contribution of the lowest portion ($300nm$-$600nm$) and of that from $600nm$ up to $1000nm$ of the AM15G spectrum to the photo-generated current density J_{ph} is of the same magnitude for all simulated roughness levels. In addition, the collection efficiency calculated within the range $300nm$-$600nm$ is clearly degraded for $\sigma_{RMS} = 50nm$ with respect to that for $\sigma_{RMS} = 25nm$ and to that for the smooth interface (Fig. 6.11).

At short wavelengths (Fig. 6.13A, $\lambda = 450nm$) the optical generated electron-hole pairs are clearly spatially concentrated close to the front side of the absorber layer

Table 6.2: Calculated figures of merit (photo-generated current density J_{ph}, short-circuit current density J_{sc}, open-circuit voltage V_{oc}, Fill Factor and efficiency η) of the simulated thin film solar cell for different roughness levels σ_{RMS} of the internal ITO/p-region interface.

σ_{RMS}	J_{ph}	J_{sc}	V_{oc}	FF	η
$[nm]$	$[mAcm^{-2}]$	$[mAcm^{-2}]$	$[Volt]$		[%]
0	15.34	12.16	0.897	56.50	6.16
25	17.40	13.58	0.902	56.78	6.95
50	17.84	12.82	0.897	57.84	6.62

due to the wavelength-dependent absorption profile of a-Si, while at longer wavelength (Fig. 6.13B, $\lambda = 750nm$), the optical generation is spatially distributed over the entire absorber layer; the morphology of the interface featuring $\sigma_{RMS} = 50nm$ further enhances the amount of photo-generated carriers in the p-layer. As consequence of the different spatial distribution of the photo-generated electron-hole pairs, at lower wavelengths the recombination at the front electrode is significantly larger than that occurring at longer wavelengths and its magnitude increases with increasing roughness leading to a decreasing trend of the collection efficiency η_C versus the roughness level. At longer wavelengths, the contribution of the recombination at the front electrode to the total losses is negligible, while the main contribution to electrical losses is provided by defects at bulk level, which increases with increasing σ_{RMS} similarly to the case of shorter wavelengths. However, at longer wavelengths η_C is enhanced by the roughness level since the increase of photo-generated current is far larger than that of the recombination current because of defects.

Moreover, simulations reveal that, for each value of σ_{RMS}, both loss mechanisms (bulk defects and recombination at top electrode) play a paramount role in determining the collection of carriers at electrodes and that increasing σ_{RMS} leads to different relative contribution of recombination mechanisms to the total recombination current.

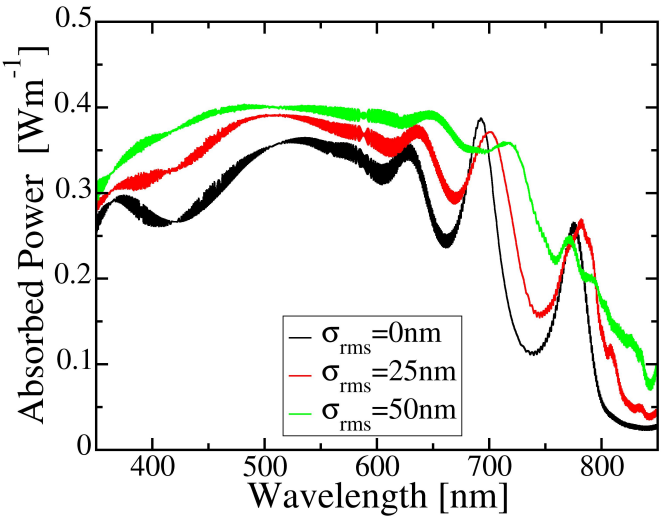

Figure 6.9: Calculated absorbed power within the amorphous silicon layer under direct AM1.5G illumination ($1000 W m^{-2}$) adopting the roughness level σ_{RMS} as parameter. The absorbed power increases with increasing σ_{RMS}.

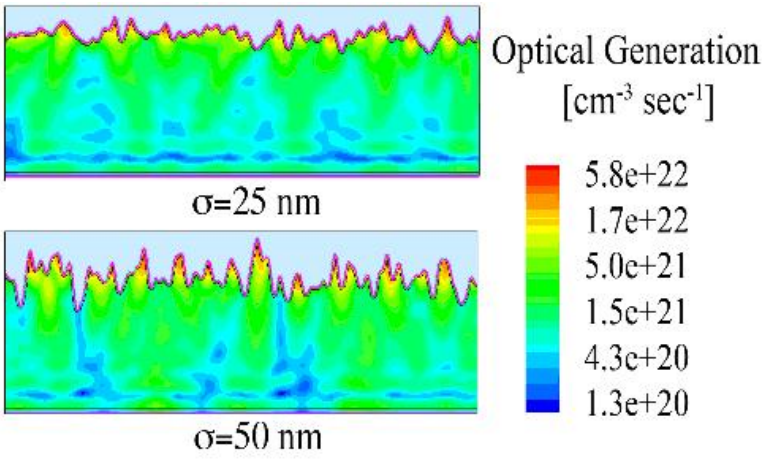

Figure 6.10: Calculated 2-D full-spectrum optical generation (in $cm^{-3}s^{-1}$) maps within the a-Si layer for $\sigma_{RMS} = 25nm$ and $\sigma_{RMS} = 50nm$.

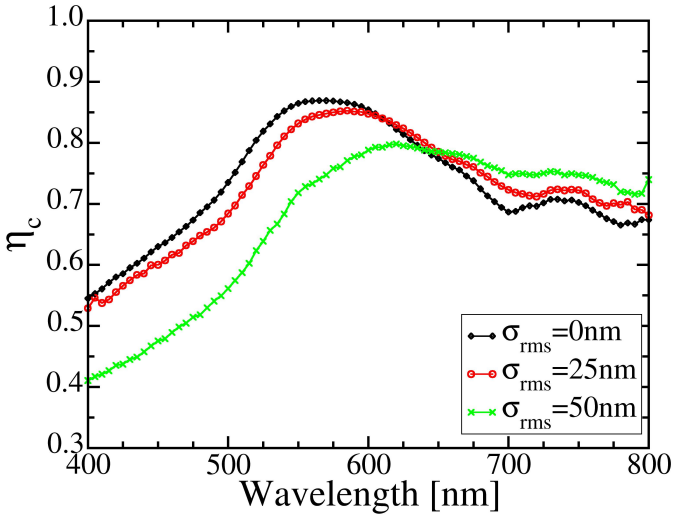

Figure 6.11: Collection efficiency η_C of the photo-generated carriers for $\sigma_{RMS} = 0nm$, $\sigma_{RMS} = 25nm$ and $\sigma_{RMS} = 50nm$. At short wavelengths the collection efficiency decreases with increasing roughness level σ_{RMS}.

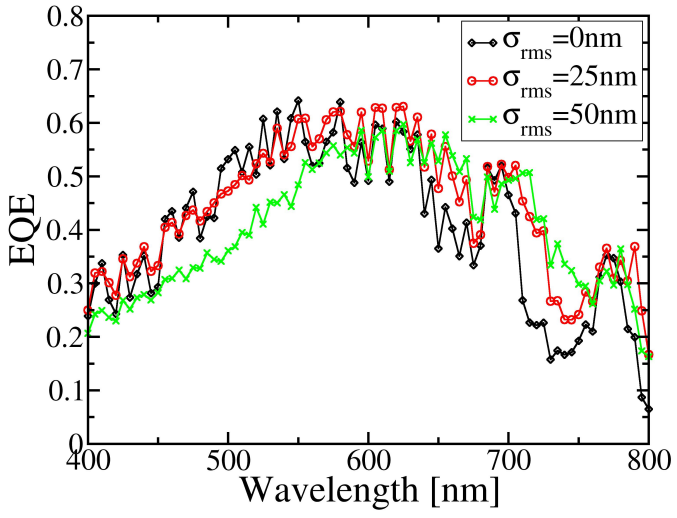

Figure 6.12: External quantum efficiency (EQE) of the simulated solar thin film solar cell for $\sigma_{RMS} = 0nm$, $\sigma_{RMS} = 25nm$ and $\sigma_{RMS} = 50nm$.

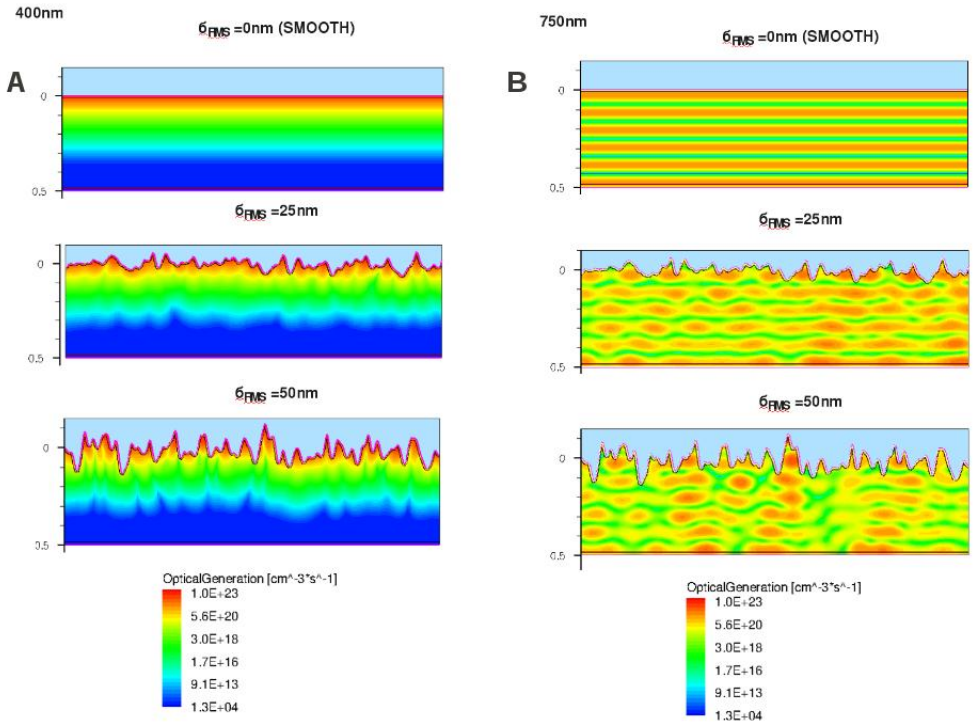

Figure 6.13: 2-D maps of optical generation rates (per unit time and volume) inside the amorphous silicon absorber layer at wavelength $\lambda = 400nm$ (A) and $\lambda = 750nm$ (B) for all considered values of the roughness σ_{RMS}. Different spatial distributions of the photo-generated electron-hole pairs, depending on σ_{RMS} and on the wavelength of the radiation, are observed.

Table 6.3: Contributions of the lower part (300nm-600nm) and of the highest portion (600nm-1000nm) of the spectrum to the total photo-generated current density (J_{ph}^{TOT}) calculated within the range of wavelengths from 300nm up to 1000nm for different values of σ_{RMS}.

σ_{RMS}	$J_{ph}^{300-600}/J_{ph}^{TOT}$	$J_{ph}^{600-1000}/J_{ph}^{TOT}$
$[nm]$	$[\%]$	$[\%]$
0	53.4	46.6
25	49.5	50.5
50	48.0	52.0

7

Conclusions

One of the most challenging goal in photovoltaic industry and research is the manufacturing of low-cost, high-efficiency and reliable solar cells. The PV market is, so far, largely dominated by crystalline silicon devices, and recently a reawakening of advanced solar cell architectures has driven the research towards process and design optimizations in order to enhance the conversion efficiency. On the other hand, thin film solar cells are the most effective way towards low-cost photovoltaic, but the main drawbacks associated to these second-generation devices are the poor material quality -which leads to higher losses- and the significantly limited optical absorption. In this thesis, after an outline of the main physical mechanisms which limit the ultimate conversion efficiency, the basis of the numerical modeling of solar cells -including both device and optical simulation- has been discussed with the emphasis on the main issues and limitations of the state-of-the-art tools - mostly 1-D or 2-D- aimed at simulating photovoltaic devices.

In the first part of the thesis, as a main contribute towards the goals of this work, the physical models adopted as well as the methodology used to perform the tuning of the models from experimental data in order to set up a simulation framework by means of the state-of-the-art TCAD Sentaurus by Synopsys have been discussed. In particular, a simulation procedure for 2-D and 3-D spatial domains has been introduced and two solar cell architectures of interest have been investigated. The first considered scheme is a double-diffused emitter solar cell which has been investigated and optimized by means of 2-D electro-optical simulations. The second application concerns the optimization of the rear point contact scheme which has been carried out by true

3-D numerical simulations. In this work, the numerical simulation has not been limited to the optimization of the device in terms of doping and geometrical parameters, which results from trade-offs between competing physical mechanisms, but it has been successfully exploited to investigate the main loss mechanisms which limit the conversion efficiency of solar cells. With respect to 1-D simulators, the adoption of 2-D and 3-D tools in combination to ad-hoc tuned physical models, allows to predict realistic results and trends highlighting the effectiveness of each parameter involved in the device design as well as the sensitiveness of the main figures of merit to such parameters. The numerical modeling activity of advanced crystalline solar cells has been carried out in the framework of the collaboration between University of Bologna and Applied Materials, Inc.

The second part of the thesis is on the optical simulation. After a review of the main approaches to optical modeling of optoelectronic devices (FDTD, Raytracing, effective media approximation and scalar scattering approach) with particular reference to solar cells, for which the theoretical limitations of non-rigorous methods to model the light propagation in practical devices featuring nanostructured geometries have been highlighted, two novel implementations of Fourier modal (or RCWA) solvers of the Maxwell equations aimed at simulating 2-D structures have been presented. Besides featuring new algorithms, the proposed approaches are computationally efficient with respect to the state-of-the-art implementations of RCWAs, especially when processing devices involving multi-layers structures with nanorough interfaces. Finally a third method aimed at solving the near field optical problem in 3-D simulation domains, based on a standard -but more general in terms of validity- approach has been implemented. All the proposed methods, developed with the strategic collaboration with the Institute of Physics and Technology of RAS, Moscow, which provided support to the implementation of the code as well as to the solution of trivial numerical problems, have been validated by means of comparison with either commercial finite difference tools and literature data. In addition, the RCWA method has been applied to the optical simulation of thin film amorphous silicon solar cells featuring nanorough interfaces as well as nano-rods.

The adoption of proposed simulation techniques as well as of the implemented tools for the optical problem will be the basis for several future activities which will involve

the analysis and the optimization of advanced photovoltaic devices of second and third generations.

References

[1] M. A. Green. *Solar Cells: Operating Principles Technology (The Red Book).* UNSW Photovoltaics., 1996. xx, 29, 30, 31, 34, 89, 99

[2] D. Redfield. **Multiple-pass thin-film silicon solar cell.** *Appl. Phys. Lett.*, **25**:647 – 649, 1974. xxi, 39, 41

[3] S. W. Glunz, S. Rein, J. Y. Lee, and W. Warta. **Minority carrier lifetime degradation in boron-doped Czochralski silicon**. *J. Appl. Phys.*, **90**:2397 – 2404, 2001. xxii, 58, 59

[4] S. Fan and J. D. Joannopoulos. **Analysis of guided resonances in photonic crystal slabs**. *Phys. Rev. B*, **65**(23):235112, 2002. xxvi, 141, 143

[5] D. A. Clugston and P. A. Basore. **PC1D version 5: 32-bit solar cell modeling on personal computers**. *Conference Record of the 26th IEEE Photovoltaic Specialists Conference, 1997*, pages 207 – 210, 1997. 2, 79

[6] E. C Garnett, M. L. Brongersma, Y. Cui, and M. D. McGehee. **Nanowire Solar Cells**. *Annual Review of Materials Research*, **41**:269 –295, 2011. 3

[7] M. Westphalen, U. Kreibig, J. Rostalski, H. Luth, and D. Meissn. **Metal cluster enhanced organic solar cells**. *Solar Energy Materials and Solar Cells*, **61**(1):97 – 105, 2000. 3

[8] B. M. Kayes, C. E. Richardson, N. S. Lewis, and H. A. Atwater. **Radial pn junction nanorod solar cells: device physics principles and routes to fabrication in silicon.** *Conference Record of the 31st IEEE Photovoltaic Specialists Conference*, pages 55 – 68, 2005. 3

[9] S. H. Zaidi, J. M. Gee, and D. S. Ruby. **Diffraction grating structures in solar cells.** *Conference Record of the 28th IEEE Photovoltaic Specialists Conference.*, pages 395 – 398, 2000. 3

[10] P. Beckmann and A. Spizzichino. *The scattering of electromagnetic waves from rough surfaces.* International series of monographs on electromagnetic waves. Pergamon Press, New York, 1963. 3, 111, 165, 167

[11] S. M. Sze and K. Ng Kwok. *Physics of Semiconductor Devices.* John Wiley EEE Sons, Inc., 2007. 16

[12] A. Luque and S. Hegedus. *Handbook of Photovoltaic Science and Engineering.* John Wiley EEE Sons, Inc., 2003. 17, 21, 22, 23

[13] M. A. Green. *Silicon Solar Cells: Advanced Principles and Practice (The Green Book).* UNSW Photovoltaics, 1995. 27, 40, 49, 50, 89

[14] *ASTM G173 - 03(2008) Standard Tables for Reference Solar Spectral Irradiances: Direct Normal and Hemispherical on 37° Tilted Surface.* ASTM International, West Conshohocken, PA, 2003, 2008. 28

[15] M. A. Green, K. Emery, Y. Hishikawa, and W. Warta. **Solar Cell Efficiency Tables (Version 33).** *Prog. Photovolt: Res. Appl.*, **17**:85 94, 2009. 28, 30

[16] J. Meier, J. Sitznagel, U. Kroll, C. Bucher, S. Fay, T. Moriarty, and A. Shah. **Potential of amorphous and microcrystalline silicon solar cells.** *Thin Solid Films*, **17**:518 – 524, 2004. 28, 30

[17] K. Bucher, J. Bruns, and H. G. Wagemann. **Absorption coefficient of silicon: An assessment of measurements and the simulation of temperature variation.** *J. Appl. Phys.*, **75**:1127 – 1133, 1994. 30

[18] J. C. Sturm and C. M. Reaves. **Fundamental mechanisms and doping effects in silicon infrared absorption for temperature measurement by infrared transmission.** *Proc. SPIE Conf. on Rapid Thermal Processing*, (1393):309 – 315, 1990. 30

[19] S. T. Hama, H. Okamoto, Y. Hamakawa, and T. Matsubara. **Hydrogen content dependence of the optical energy gap in a-Si:H.** *J. Non-Cryst. Solids*, **59-60**:333 – 336, 1983. 31

[20] A. Luque and V. Andreev. *Concentrator Photovoltaics.* Springer Series in Optical Sciences, Vol. 130, 2007. 31

[21] A. G. Aberle. *Crystalline Silicon Solar Cells: Advanced Surface Passivation and Analysis.* The University of New South Wales, Sydney, Australia, 1999. 34

[22] A. Goetzberger, J. Knobloch, and B. Voβ. *Crystalline Silicon Solar Cells.* John Wiley EEE Sons, 1998. 36, 37

[23] S. W. Glunz. **High-Efficiency Crystalline Silicon Solar Cells.** *Adv. in OptoElec.*, **2007**, 2007. 38, 89, 94

[24] A. Goetzberger. **Optical confinement in thin Si-solar cells by diffuse back reflectors.** *Conference Record of the 15th IEEE Photovoltaic Specialists Conference*, pages 867 – 870, 1981. 38

[25] E. Yablonovitch and G. D. Cody. **Intensity enhancement in textured optical sheets for solar cells**. *IEEE Trans. Electron Devices*, **29**(2):300 – 305, 1982. 38

[26] A. W. Smith and A. Rohatgi. **Ray tracing analysis of the inverted pyramid texturing geometry for high efficiency silicon solar cells.** *Solar Energy Materials and Solar Cells*, **29**(1):37 – 49, 1993. 40

[27] P. Campbell and M. A. Green. **Light trapping properties of pyramidally textured surfaces.** *J. Appl. Phys.*, **62**:243 – 250, 1987. 40

[28] P. Sheng, A. N. Bloch, and R. S. Stepleman. **Wavelength-selective absorption enhancement in thin-film solar cells**. *Appl. Phys. Lett.*, **43**(2):579 – 581, 1983. 40

REFERENCES

[29] H. Stiebig, N. Senoussaoui, C. Zahren, C. Haase, and J. Muller. **Silicon thin-film solar cells with rectangular-shaped grating couplers**. *Progress in Photovoltaics: Research and Applications.*, **14**(2):13 – 24, 2006. 42

[30] N. Feng, J. Michel, L. Zeng, J. Liu, C. Y. Hong, L. C. Kimerling, and X. Duan. **Design of Highly Efficient Light-Trapping Structures for Thin-Film Crystalline Silicon Solar Cells**. *IEEE Trans. Electron Devices*, **54**(8):1926 – 1933, 2007. 42

[31] P. Bermel, C. Luo, L. Zeng, L. C. Kimerling, and J. D. Joannopoulos. **Design of Highly Efficient Light-Trapping Structures for Thin-Film Crystalline Silicon Solar Cells**. *Opt. Express.*, **15**(25):16986 – 17000, 2007. 42

[32] J. Prazmowska, R. Paszkiewicz, M. Wosko, and M. Tlacz. **Solar cells conversion efficiency enhancement techniques.** *Optica Applicata 2007*, **37**(1-2):93 – 99, 2007. 42

[33] R. H. Lipson and C. Lu. **Photonic crystals: a unique partnership between light and matter.** *Eur. J. Phys.*, **30**:33 – 48, 2009. 42

[34] M. Agrawal. *Photonic Design for Efficient Solid State Energy Conversion, PhD Thesis / Dissertation.* Stanford University, Stanford, CA, Dec 2008., 2008. 43, 112, 113, 114, 118, 130, 135

[35] T. F. Ciszek and T. H. Wang. **Silicon Float-Zone Crystal Growth as a Tool for the Study of Defects and Impurities.** *Electrochemical Society-Fall Conference, Phoenix, Arizona, October 22-27, 2000*, 2000. 46

[36] D. K. Schroder. **Carrier Lifetimes in Silicon.** *IEEE Trans. Electron Devices*, **44**(1):160 – 170, 1997. 46

[37] Seibt M. Myers, S. M. and and W. Schroter. **Mechanisms of transition-metal gettering in silicon.** *J. Appl. Phys.*, **88**:3795 – 3820, 2000. 46

[38] S. A. McHugo, H. Hieslmair, and E. R. Weber. **Gettering of metallic impurities in photovoltaic silicon.** *Applied Physics A: Materials Science and Processing*, **64**(2):127 – 137, 1997. 46

[39] S. R. Wenham and M. A. Green. **Silicon solar cells.** *Silicon solar cells. Progress in Photovoltaics: Research and Applications*, **4**(1):3 –33, 1996. 46

[40] S. Joshi, U. Gosele, and T. Tan. **Improvement of minority carrier diffusion length in Si by Al gettering.** *J. Appl. Phys.*, **77**:3858 – 3863, 1995. 47

[41] B. L. Sopori, X. Deng, J. P. Benner, J.P. Bennera, A. Rohatgi, P. Sanab, S.K. Estreicherc, Y.K. Parkc, and M.A. Roberson. **Hydrogen in silicon: a discussion of diffusion and passivation mechanisms.** *Solar Energy Materials and Solar Cells*, **41 - 42**:159 – 169, 1996. 47

[42] M. A. Green. **Silicon solar cells: at the crossroads.** *Progress in Photovoltaics: Research and Applications*, **8**:443 – 450, 2000. 47

[43] D. K. Schroder and D. L. Meier. **Solar Cell Contact Resistance-A Review**. *IEEE Trans. Electron Devices*, **31**(5):637 – 647, 1984. 47

[44] M. M. Hilali, A. Rohatgi, and S. Asher. **Development of screen-printed silicon solar cells with high fill factors on 100 Ω/sq emitters**. *IEEE Trans. Electron Devices*, **51**(6):948 – 955, 2004. 47, 49, 78

[45] M. Galiazzo, V. Furin, D. Tonini, G. Cellere, and A. Baccini. **Double printing of front contact Ag in c-Si solar cells**. *Proc. of 25th EUPVSEC Valencia 2010*, 2010. 49

[46] *Sentaurus Device User Guide, Version C-2009.06.* Synopsys. Inc., 2009. 51, 55, 57, 59, 70, 71, 81

[47] A. B. Sproul and M. A. Green. **Improved value for the silicon intrinsic carrier concentration from 275 to 375 K**. *J. Appl. Phys.*, **70**:846 – 854, 1991. 54

[48] P. P Altermatt, A. Schenk, F. Geelhaar, and G. Heiser. **Reassessment of the intrinsic carrier density in crystalline silicon in view of band-gap narrowing**. *J. Appl. Phys.*, **93**:1598 – 1604, 1991. 54, 55, 92

[49] A. Schenk. **Finite-temperature full random-phase approximation model of band gap narrowing for silicon device simulation**. *J. Appl. Phys.*, **84**:3684 – 3695, 1998. 54

[50] K. Misiakos and D. Tsamakis. **Accurate measurements of the silicon intrinsic carrier density from 78 to 340 K**. *J. Appl. Phys.*, **74**:3293 – 3297, 1993. 54

[51] W. Bludau, A. Onton, and W. Heinke. **Temperature dependence of the band gap in silicon**. *J. Appl. Phys.*, **45**(4):1846 – 1848, 1974. 54

[52] J. del Alamo, S. Swirhun, and R. M. Swanson. **Hole Mobility and Bandgap Narrowing in Heavily Doped n-Type Silicon**. *IEDM Technical Digest, Washington, DC, USA*, **31**:290 – 293, 1985. 55

[53] J. del Alamo, S. Swirhun, and R. M. Swanson. **Measuring and Modeling Minority Carrier Transport in Heavily Doped Silicon**. *Solid-State Electronics*, **28**(1 - 2):47 – 54, 1985. 55

[54] S. E. Swirhun, Y.-H. Kwark, and R. M. Swanson. **Measurement of Electron Lifetime, Electron Mobility and Band-Gap Narrowing in Heavily Doped p-Type Silicon**. *IEDM Technical Digest, Los Angeles, CA, USA*, **32**:24 – 27, 1986. 55

[55] S. E. Swirhun, J. A. del Alamo, and R. M. Swanson. **Measurement of Hole Mobility in Heavily Doped n-Type Silicon**. *IEEE Electron Device Letters*, **32**:168 – 171, 1986. 55

[56] J. A. del Alamo and R. M. Swanson. **Measurement of Steady-State Minority-Carrier Transport Parameters in Heavily Doped n-Type Silicon**. *IEEE Trans. Electron Devices*, **34**(7):1580 – 1589, 1987. 55

[57] H. S. Bennett and C. L. Wilson. **Statistical comparisons of data on band-gap narrowing in heavily doped silicon: Electrical and optical measurements**. *J. Appl. Phys.*, **55**(2):3582 – 3587, 1944. 55

[58] J. W. Slotboom and H. C. de Graaff. **Measurements of Bandgap Narrowing in Si Bipolar Transistors**. *Solid-State Electronics*, **19**(10):857 – 862, 1976. 55

[59] J. W. Slotboom and H. C. de Graaff. **Bandgap Narrowing in Silicon Bipolar Transistors**. *IEEE Trans. Electron Devices*, **24**(8):1123 – 1125, 1977. 55

[60] J. W. Slotboom. **The pn-Product in Silicon**. *Solid-State Electronics*, **20**(4):279 – 283, 1977. 55

[61] D. B. M. Klaassen, J. W. Slotboom, and H. C. de Graaff. **Unified Apparent Bandgap Narrowing in n- and p-Type Silicon**. *Solid-State Electronics*, **35**(2):125 – 129, 1992. 55

[62] S. C. Jain and D. J. Roulston. **Simple Expression for Band Gap Narrowing (BGN) in Heavily Doped Si, Ge, GaAs and GexSi1-x Strained Layers**. *Solid-State Electronics*, **34**(5):453 – 465, 1991. 55

[63] D. B. M. Klaassen. **A unified mobility model for device simulation I. Model equations and concentration dependence**. *Solid-State Electronics*, **35**(7):953 959, 1992. 57

[64] A. Cuevas, M. J. Kerr, and J. Schmidt. **Passivation of crystalline silicon using silicon nitride**. *Proc. of 3rd World Conference on Photovoltaic Energy Conversion*, pages 913 – 918, 2003. 58, 92, 93

[65] R. E. Bank, D. J. Rose, and W. Fichtner. **Numerical methods for semiconductor device simulation**. *IEEE Trans. Electron Devices*, **30**(9):1031 – 1041, 1983. 60

[66] J. F. Burgler, W. M. Jr. Coughran, and W. Fichtner. **Passivation of crystalline silicon using silicon nitride**. *IEEE Transactions on Computer-Aided Design of Integrated Circuits and Systems*, **10**(10):1251 – 1258, 1991. 60

[67] G. Heiser, C. Pommerell, J. Weis, and W. Fichtner. **Passivation of crystalline silicon using silicon nitride**. *IEEE Transactions on Computer-Aided Design of Integrated Circuits and Systems*, **10**(10):1218 – 1230, 1991. 61

[68] Rizzoli V. *Lezioni di campi elettromagnetici*. Soc. Editrice Esculapio, Bologna, Italy, 1995. 64, 66, 69

[69] K. K. Sharma. *OPTICS: Principles and Applications*. Academic Press, Elsevier, 2006. 70

[70] *Silvaco Atlas Manual*. Silvaco. Inc., 2012. 70

[71] V. Moroz, J. Huang, K. Wijekoon, and D. Tanner. **Experimental and theoretical analysis of the optical behavior of textured silicon wafers**. *Conference Record of the Thirty-seventh IEEE Photovoltaic Specialists Conference 2011*, 2011. 70

[72] Th. Bierhoff, E. Griese, and G. Mrozynski. **An Efficient Monte Carlo Based Ray Tracing Technique for the Characterization of Highly Multimode Dielectric Waveguides with Rough Surfaces**. *Proc. of 30th European Microwave Conference, 2000.*, pages 1 – 4, 2000. 70

[73] K. S. Kunz and R. J. Luebbers. *The Finite Dierence Time Domain Method for Electromagnetics*. CRC Press, 1993. 73, 112

[74] A. Taflove and M. E. Brodwin. **Numerical solution of steady-state electromagnetic scattering problems using the time-dependent Maxwell's equations**. *IEEE Transactions on Microwave Theory and Techniques*, **23**(8):623 – 630, 1975. 73

[75] A. Taflove. *Computational Electrodynamics. The Finite-Dierence Time-Domain Method*. Artech House Boston, 1995. 74

[76] M. M. Hilali and M. M. Al-Jassim. **Understanding the Formation and Temperature Dependence of Thick-Film Ag Contacts on High-Sheet-Resistance Si Emitters for Solar Cells**. *J. Electrochem. Soc.*, **152**(10):52G742 – G749, 2005. 78

[77] A. Ebong, B. Rounsaville, I. B. Cooper, K. Tate, A. Rohatgi, S. Glunz, M. Horteis, A. Mette, M. Gundermann, and X. Xjet. **High efficiency silicon solar cells with ink jetted seed and plated grid on high sheet resistance emitter**. *Conference record of 35th IEEE Photovoltaic Specialists Conference (PVSC), 2010*, pages 1363 – 1367, 2010. 78

[78] M. Horteis and S. W. Glunz. **Fine Line Printed Silicon Solar Cells Exceeding 20% Efficiency**. *Prog. Photovolt: Res. Appl.*, **16**(3 pages=555 - 560, doi=10.1002/pip.850,), 2008. 78

[79] G. Hahn. **Status of Selective Emitter Technology**. *Proc. of 25th European Photovoltaic Solar Energy Conference and Exhibition / 5th World Conference on Photovoltaic Energy Conversion, 6-10 September 2010, Valencia, Spain*, pages 1091 – 1096, 2010. 78

[80] T. Roder, P. Grabitz, S. Eisele, C. Wagner, J. R. Kohler, and J. H. Werner. **0.4% absolute efficiency gain of industrial solar cells by laser doped selective emitter**. *Conference record of 34th IEEE Photovoltaic Specialists Conference (PVSC), 2009*, pages 871 – 873, 2009. 78

[81] T. U. Jager, S. Mack, A. Kimmerle, A. Wolf, and R. Preu. **Influence of doping profile of highly doped regions for selective emitter solar cells**. *Conference record of 35th IEEE Photovoltaic Specialists Conference (PVSC), 2010*, pages 3185 – 3189, 2010. 78

[82] N. Stem and N. Cid. **Physical limitations for homogeneous and highly doped n-type emitter monocrystalline silicon solar cells**. *Solid-State Electronics*, **48**(2):197 – 205, 2004. 78

[83] A. Cuevas and D. A. Russell. **Co-optimisation of the emitter region and the metal grid of silicon solar cells**. *Prog. Photovolt: Res. Appl.*, **8**(6):603 – 616, 2001. 78

[84] A. Wang, J. Zhao, and M. A. Green. **4% efficient silicon solar cells**. *Applied Physics Letters*, **57**(6):602 – 604, 1990. 89, 99

[85] C. Mader, J. Musller, S. Gatz, T. Dullweber, and R. Brendel. **Rear-side point-contacts by inline thermal evaporation of aluminum**. *Conference Record of the 35th IEEE Photovoltaic Specialists Conference (PVSC), 2010*, pages 1446 – 1449, 2010. 89, 91, 93, 105

REFERENCES

[86] A. Ristow, A. Ebong, M. Hilali, and A. Rohatgi. **Rear-side point-contacts by inline thermal evaporation of aluminum**. *Proc. of the 17th European Photovoltaic Solar Energy Conference and Exhibition, Munich, Germany, October 22-26, 2001.*, pages 1335 – 1338, 2010. 89

[87] T. Dullweber, S. Gatz, H. Hannebauer, T. Falcon, R. Hesse, J. Schmidt, and R. Brendell. **Towards 20% efficient large-area screen-printed rear-passivated silicon solar cells**. *Progress in Photovoltaics: Research and Applications*, 2011. 89

[88] J.-H. Lai, A. Upadhyaya, S. Ramanathan, A. Das, K. Tate, V. Upadhyaya, A. Kapoor, Chia-Wei Chen, and A. Rohatgi. **Towards 20% efficient large-area screen-printed rear-passivated silicon solar cells**. *IEEE Journal of Photovoltaics*, **1**(1):16 – 21, 2011. 89

[89] M. Tucci, E. Talgorn, L. Serenelli, E. Salza, M. Izzi, and P. Mangiapane. **Laser fired back contact for silicon solar cells**. *Proceedings on Advanced Materials and Concepts for Photovoltaics EMRS 2007 Conference, Strasbourg, France*, **516**(20):6767 – 6770, 2008. 89

[90] D. Reinwand, J. Specht, D. Stuwe, S. Seitz, J. Nekarda, D. Biro, R. Preu, and R. Trassi. **21.1% efficient perc silicon solar cells on large scale by using inline sputtering for metallization**. *Conference Record of the 35th IEEE Photovoltaic Specialists Conference (PVSC), 2010*, pages 3582 – 3586, 2010. 89, 93

[91] P. Ortega, A. Orpella, I. Martin, M. Colina, G. Lopez, C. Voz, M. I. Sanchez, C. Molpeceres, and R. Alcubilla. **Laser-fired contact optimization in c-Si solar cells**. *Prog. Photovolt: Res. Appl.*, **20**(2):173 – 180, 2011. 89

[92] P. Ortega, G. Lopez, A. Orpella, I. Martin, M. Colina, C. Voz, S. Bermejo, J. Puigdollers, M. Garca, and R. Alcubilla. **Crystalline silicon solar cells beyond 20% efficiency**. *Conference on Electron Devices (CDE), 2011 Spanish*, 2011. 89

[93] M. Kerr, J. Schmidt, and A. Cuevas. **Comparison of the Open Circuit Voltage of Simplified PERC Cells Passivated with PECVD Silicon Nitride and Thermal Silicon Oxide**. *Prog. Photovolt: Res. Appl.*, **8**(5):529 – 536, 2000. 89

[94] S. Dauwe, L. Mittelsta, A. Metz, and R. Hezel. **Experimental Evidence of Parasitic Shunting in Silicon Nitride Rear Surface Passivated Solar Cells**. *Prog. Photovolt: Res. Appl.*, **10**(4):271 – 278, 2002. 91

[95] W. Brendle, V. X. Nguyen, A. Grohe, E. Schneiderlchner, E. Rau, G. Palfinger, and J. H. Werner. **20 .5% Efficient Silicon Solar Cell with a Low Temperature Rear Side Process Using Laser-Fired Contacts**. *Prog. Photovolt: Res. Appl.*, **14**(7):653 – 662, 2006. 91

[96] G. Heiser, P. P. Altermatt, A. Williams, A. Sproul, and M. A. Green. **Optimisation Of Rear Contact Geometry Of High Efficiency Silicon Solar Cells Using Three Dimensional Numerical Modelling**. *Proc. of 13th European Photovoltaic Solar Energy Conference*, pages 447 – 450, 1995. 91

[97] J. Renshaw, M. H. Kang, V. Meemongkolkiat, A. Rohatgi, D. Carlson, and M. Bennett. **3D-modeling of a back point contact solar cell structure with a selective emitter**. *Conference record of 34th IEEE Photovoltaic Specialists Conference (PVSC), 2009*, pages 375 – 379, 2009. 91

[98] H. Plagwitz, M. Schaper, J. Schmidt, B. Terheiden, and R. Brendel. **Analytical model for the optimization of locally contacted solar cells**. *Conference record of 31st IEEE Photovoltaic Specialists Conference (PVSC), 2005*, pages 999 – 1002, 2005. 91

[99] P. Saint-Cast, M. Rudiger, A. Wolf, M. Hofmann, J. Rentsch, and R. Preu. **Advanced analytical model for the effective recombination velocity of locally contacted surfaces**. *J. Appl. Phys.*, **108**(1):013705 – 013711, 2010. 91

[100] A. G. Aberle, G. Heiser, and M. A. Green. **Two dimensional numerical optimization study of the rear contact geometry of high efficiency silicon solar cells**. *J. Appl. Phys.*, **75**(10):5391 – 5405, 1994. 91, 96

[101] D. Kray and S. Glunz. **Investigation of Laser-fired Rear-side Recombination Properties Using an Analytical Model**. *Prog. Photovolt: Res. Appl.*, **14**(3):195 – 201, 2006. 91

[102] S. W. Glunz, E. Schneiderlchner, D. Kray, A. Grohe, M. Hermle, H. Kampwerth, R. Preu, and G. Willeke. **Laser-fired contact silicon solar cells on p- and n-substrates**. *Proc. of 19th European Photovoltaic Solar Energy Conference*, pages 3 – 6, 2004. 91

[103] S. Sterk and S. W. Glunz. **Simulation of semiconductor devices and processes**. *Simulation in High Efficiency Solar Cell Research*, **5**, 1993. 91

[104] K. Kotsovos and K. Misiakos. **Two dimensional numerical optimization study of the rear contact geometry of high efficiency silicon solar cells**. *J. Appl. Phys.*, **89**(4):2491 – 2496, 2001. 91

[105] A. Wolf, E. A. Wotke, A. Walczak, S. Mack, B. Bitnar, C. Koch, R. Preu, and D. Biro. **Pilot line processing of 18.6% efficient rear surface passivated large area solar cells**. *Conference record of 35th IEEE Photovoltaic Specialists Conference (PVSC), 2010*, pages 1014 – 1018, 2010. 96

[106] A. Wolf, D. Biro, J. Nekarda, S. Stumpp, A. Kimmerle, S. Mack, and R. Preu. **Comprehensive analytical model for locally contacted rear surface passivated solar cells**. *J. Appl. Phys.*, **108**(12):124510 – 124522, 2010. 96

[107] R. H. Cox and H. Strack. **Ohmic contacts for GaAs devices**. *Solid-state Electron.*, **10**(1213), 1967. 102

[108] J. M. Jin. *The Finite element method in electromagnetics*. Wiley, New York, 1993. 112

[109] M. D. Feit and J. A. Jr. Fleck. **Light propagation in graded-index optical fibers**. *Applied Optics*, **17**(24):3990 – 3998, 1978. 112

[110] M. G. Moharam, E. B. Grann, D. A. Pommet, and T. K. Gaylord. **Formulation for stable and efficient implementation of the rigorous coupled-wave analysis of binary gratings**. *Opt. Soc. Am. A.*, **12**(5):1068 – 1076, 1995. 112, 114

[111] M. G. Moharam and T. K. Gaylord. **Rigorous coupled-wave analysis of planar grating diffraction**. *J. Opt. Soc. Am.*, **71**(7):811 – 818, 1981. 112

[112] M. G. Moharam and T. K. Gaylord. **Diffraction analysis of dielectric surface relief gratings**. *J. Opt. Soc. Am.*, **72**(10):1385 – 1392, 1982. 112

[113] M. G. Moharam and T. K. Gaylord. **Rigorous coupled-wave analysis of metallic surface relief gratings**. *J. Opt. Soc. Am. A*, **3**(11):1780 – 1787, 1986. 112

[114] S. Peng and G. M. Morris. **Resonant scattering from two-dimensional gratings**. *J. Opt. Soc. Am. A*, **13**(5):993 – 1005, 1996. 112

[115] D. Delbeke, P. Bienstman, R. Bockstaele, and R. Baets. **Rigorous electromagnetic analysis of dipole emission in periodically corrugated layers: the grating-assisted resonant cavity light emitting diode**. *J. Opt. Soc. Am. A*, **19**(5):871 – 880, 2002. 112

[116] P. Lalanne and Silberstein. E. **Fourier-modal methods applied to waveguide computational problems**. *Opt. Lett.*, **25**(15):1092 – 1094, 2000. 112

[117] M. Agrawal, M. Frei, Y. Bhatnagar, T. Repmann, K. Witting, J. Schroeder, and C. Eberspacher. **Comprehensive experimental and numerical optimization of surface morphology of transparent conductive oxide films for tandem thin film photovoltaic cells**. pages 301 – 304, 2010. 112

[118] J. J. Hench and Z. Strakos. **The RCWA method - A case study with open questions and perspective of algebraic computations**. *Electr. Trans. Numerical Analysis*, **31**:331 – 357, 2008. 112, 113, 115, 118, 121

[119] A. Orlikovsky, V. Vyurkov, V. Lukichev, I. Semenikhin, and A. Khomyakov. **All-quantum simulation of ultrathin SOI MOSFET**. *Nanoscaled Semiconductor-on-Insulator Structures and Devices, NATO Science for Peace and Security Series B: Physics and Biophysics*, 2007. 114

[120] Li L. *Mathematical reflections on the Fourier modal method in grating theory*, **22**. SIAM, Philadelphia, PA, 2001. 116, 121

[121] H. Wu, D. W. L. Sprung, and J. Martorell. **Periodic quantum wires and their quasi-one-dimensional nature**. *Am. Journal of Physics*, **61**(5):798 – 803, 1993. 122

[122] D. Delbeke, P. Bienstman, R. Bockstaele, and R. Baets. **New formulation of the Fourier modal method for crossed surface-relief gratings**. *J. Opt. Soc. Am. A*, **14**(10):2758 – 2767, 1997. 132

[123] *Sentaurus Device Electromagnetic Wave Solver User Guide, Version C-2009.06*. Synopys, Inc., 2009. 139

[124] J. Krc, M. Zeman, Smole F., and Topic M. **Optical modeling of a-Si:H solar cells deposited on textured glass/SnO_2 substrates**. *J. Appl. Phys.*, **92**(2):749 – 755, 2002. 145

[125] M. Kaelin, D. Rudmann, and A. N. Tiwari. **Low cost processing of CIGS thin film solar cells**. *Solar Energy*, **77**(6):749 756, 2004. 159

[126] M. M. Gmez, J. Lu, J. L. Solis, E. Olsson, A. Hagfeldt, and C. G. Granqvist. **Dye-Sensitized Nanocrystalline Titanium-Oxide-Based Solar Cells Prepared by Sputtering: Influence of the Substrate Temperature During Deposition**. *J. Phys. Chem. B.*, **104**(36):8712 8718, 2000. 159

[127] R. E. I. Schropp and M. Zeman. **New developments in amorphous thin-film silicon solar cells**. *IEEE Transactions on Electron Devices*, **46**(10):2086 – 2092, 1999. 159, 160

[128] N. Romeo, A. Bosio, V. Canevari, and A. Podest. **Recent progress on CdTe/CdS thin film solar cells**. *Solar Energy*, **77**(6):795 801, 2000. 159

[129] B. E. Pieters, J. Krc, and M. Zeman. **Advanced Numerical Simulation Tool for Solar Cells - ASA5**. *Conference Record of the 2006 IEEE 4th World Conference on Photovoltaic Energy Conversion*, **2**:1513 – 1516, 2006. 159

[130] J. Krc, A. Campa, G. Cernivec, J. Malmstrom, M. Edoff, F. Smole, and M. Topic. **Optical modeling and simulation of thin-film Cu(In,Ga)Se2 solar cells**. *International Conference on Numerical Simulation of Semiconductor Optoelectronic Devices, 2006. NUSOD '06.*, pages 33 – 34, 2006. 159

[131] H. Zhu, A. K. Kalkan, J. Hou, and S. J. Fonash. **Applications of AMPS-1D for solar cell simulation**. *AIP Conference Proceedings.*, **462**:309 – 314, 1999. 159

[132] T. Brammer, W. Reetz, N. Senoussaoui, O. Vetterl, O. Kluth, B. Rech, H. Stiebig, and Wagner H. **Optical properties of silicon-based thin-film solar cells in substrate and superstrate configuration**. *Solar Energy Materials and Solar Cells*, **74**(1-4):629 – 641, 2002. 160

[133] L. Changwoo, H. Efstathiadis, J. E. Raynolds, and P. Haldar. **Two-dimensional computer modeling of single junction a-Si:H solar cells**. pages 1118 – 1122, 2009. 160, 169

[134] J.-S. Cho, J. K. Young, C. L. Jeong, H. P. Sang, H. J. Ji, S. Jinsoo, and H. Y. Kyung. **Study on light scattering of rf sputtered ZnO:Al thin films as a front electrode of amorphous silicon thin film solar cells**. *Conference Record of the 34th IEEE Photovoltaic Specialists Conference (PVSC), 2009*, pages 660 – 663, 2009. 160

[135] O. Isabella, K. Jager, J. Krc, and M. Zeman. **Light scattering properties of surface-textured substrates for thin-film solar cells**. *Proceedings of the 23rd European Photovoltaic Solar Energy Conference and Exhibition (EU PVSEC) 2008*, page 476 481, 2008. 160

[136] M. Zeman, R. A. C. M. M. van Swaaij, J. W. Metselaar, and R. E. I. Schropp. **Optical modeling of a-Si:H solar cells with rough interfaces: Effect of back contact and interface roughness**. *J. Appl. Phys.*, **88**(11):6436 6443, 2000. 160

[137] S. J. Fonash. *Solar Cell Device Physics, 2nd Edition*. Elsevier Academic Press, 2010. 160

[138] R.A. Street. *Hydrogenated Amorphous Silicon*. Cambridge University Press, 2005. 161

[139] Dhariwal S. R. and Rajvanshi S. **Theory of amorphous silicon solar cell (a): numerical analysis**. *Solar Energy Materials and Solar Cells*, **79**(2):199 – 213, 2000. 161, 169, 170

[140] Shimizu T. **Staebler-Wronski Effect in Hydrogenated Amorphous Silicon and Related Alloy Films**. *Japanese Journal of Applied Physics*, **43**(6A):3257 – 3268, 2004. 161

[141] M. Zeman. **New trends in thin-film silicon solar cell technology**. *The Fourth International Conference on Advanced Semiconductor Devices and Microsystems, 2002.*, pages 353 – 362, 2002. 161

[142] A. Fantoni, M. Vieira, and R. Martins. **Simulation of hydrogenated amorphous and microcrystalline silicon optoelectronic devices**. *Mathematics and Computers in Simulation*, **49**(4-5):381 401, 1999. 162, 170

[143] S. Olibet, E. Vallat-Sauvain, and C. Ballif. **Model for a-Si:H/c-Si interface recombination based on the amphoteric nature of silicon dangling bonds**. *Phys. Rev. B*, **76**:035326, 2007. 163

[144] *A manual for AMPS-1D, A One-Dimensional Device Simulation Program for the Analysis of Microelectronic and Photonic Structures*. The Center for Nanotechnology Education and Utilization, The Pennsylvania State University. 164, 169

[145] J. Springer, A. Poruba, and Vanecek M. **Improved three-dimensional optical model for thin-film silicon solar cells**. *J. Appl. Phys.*, **96**:5329 – 5332, 2004. 164

[146] J. Krc, Smole F., and Topic M. **Potential of light trapping in microcrystalline silicon solar cells with textured substrates**. *Progress in Photovoltaics Research and Applications*, **11**(7):429 – 436, 2003. 165

[147] J. Krc, M. Zeman, O. Kluth, Smole F., and Topic M. **Effect of surface roughness of ZnO:Al films on light scattering in hydrogenated amorphous silicon solar cells**. *Thin Solid Films*, **426**(1-2):296 304, 2003. 165, 167, 168

[148] H.-P. Pillai, J. Krc, and M. Zeman. **Optical Modeling of a-Si:H Thin Film Solar Cells with Rough Interfaces**. *Proceedings of SAFE 2001, Veldhoven, The Netherlands, November 28-29, 2001*, pages 159 – 162, 2001. 165

[149] G. Lrondel and R. Romestain. **Fresnel coefficients of a rough interface**. *Appl. Phys. Lett.*, **74**(19):1740 – 2742, 1999. 168

[150] P. Stulik and Singh J. **Calculation of collection efficiency for amorphous silicon solar cells**. *Journal of Non-Crystalline Solids*, **242**(2-3):115 121, 1998. 169

[151] F. Smole, M. Topic, and Furlan J. **Analysis of TCO/p(a-Si:C:H) heterojunction and its influence on p-i-n a-Si:H solar cell performance**. *Journal of Non-Crystalline Solids*, **194**(3):312 – 318, 1996. 170